Direct numerical simulation of bubbly flows : coupling with scalar transport and turbulence

Aurore Loisy

N° d'ordre NNT : 2016LYSE1142

THÈSE DE DOCTORAT DE L'UNIVERSITÉ DE LYON
opérée au sein de
l'Université Claude Bernard Lyon 1

École Doctorale ED162
MEGA : Mécanique, Énergétique, Génie civil, Acoustique

Spécialité de doctorat : Mécanique des Fluides

Soutenue publiquement le 15/09/2016, par :

Aurore LOISY

Direct numerical simulation of bubbly flows : coupling with scalar transport and turbulence

---

Devant le jury composé de :

LANCE Michel	Professeur des Universités, UCBL	Président
BEC Jérémie	Chargé de recherche, CNRS	Rapporteur
LEGENDRE Dominique	Professeur des Universités, INP Toulouse	Rapporteur
CARTELLIER Alain	Directeur de recherche, CNRS	Examinateur
POULIQUEN Olivier	Directeur de recherche, CNRS	Examinateur
NASO Aurore	Chargée de Recherche, CNRS	Co-directrice de thèse
SPELT Peter	Professeur des Universités, UCBL	Co-directeur de thèse

UNIVERSITE CLAUDE BERNARD - LYON 1

Président de l'Université	**M. François-Noël GILLY**
Vice-président du Conseil d'Administration	M. le Professeur Hamda BEN HADID
Vice-président du Conseil des Etudes et de la Vie Universitaire	M. le Professeur Philippe LALLE
Vice-président du Conseil Scientifique	M. le Professeur Germain GILLET
Directeur Général des Services	M. Alain HELLEU

COMPOSANTES SANTE

Faculté de Médecine Lyon Est – Claude Bernard	Directeur : M. le Professeur J. ETIENNE
Faculté de Médecine et de Maïeutique Lyon Sud – Charles Mérieux	Directeur : Mme la Professeure C. BURILLON
Faculté d'Odontologie	Directeur : M. le Professeur D. BOURGEOIS
Institut des Sciences Pharmaceutiques et Biologiques	Directeur : Mme la Professeure C. VINCIGUERRA
Institut des Sciences et Techniques de la Réadaptation	Directeur : M. le Professeur Y. MATILLON
Département de formation et Centre de Recherche en Biologie Humaine	Directeur : Mme. la Professeure A-M. SCHOTT

COMPOSANTES ET DEPARTEMENTS DE SCIENCES ET TECHNOLOGIE

Faculté des Sciences et Technologies	Directeur : M. F. DE MARCHI
Département Biologie	Directeur : M. le Professeur F. FLEURY
Département Chimie Biochimie	Directeur : Mme Caroline FELIX
Département GEP	Directeur : M. Hassan HAMMOURI
Département Informatique	Directeur : M. le Professeur S. AKKOUCHE
Département Mathématiques	Directeur : M. le Professeur Georges TOMANOV
Département Mécanique	Directeur : M. le Professeur H. BEN HADID
Département Physique	Directeur : M. Jean-Claude PLENET
UFR Sciences et Techniques des Activités Physiques et Sportives	Directeur : M. Y.VANPOULLE
Observatoire des Sciences de l'Univers de Lyon	Directeur : M. B. GUIDERDONI
Polytech Lyon	Directeur : M. le Professeur E.PERRIN
Ecole Supérieure de Chimie Physique Electronique	Directeur : M. G. PIGNAULT
Institut Universitaire de Technologie de Lyon 1	Directeur : M. le Professeur C. VITON
Ecole Supérieure du Professorat et de l'Education	Directeur : M. le Professeur A. MOUGNIOTTE
Institut de Science Financière et d'Assurances	Directeur : M. N. LEBOISNE

Thèse préparée au sein du

Laboratoire de Mécanique des Fluides et d'Acoustique

École Centrale de Lyon
36, avenue Guy de Collongue
69134 Écully cedex
France

Abstract

This thesis is devoted to the study of homogeneous bubbly flows and their coupling with scalar transport and turbulence. It focuses on the effects of finite size, hydrodynamic interactions, liquid inertia, and suspension microstructure, which are investigated using direct numerical simulations at the bubble scale. The dynamics of laminar buoyancy-driven bubbly suspensions is first revisited. More specifically, the effect of volume fraction on the bubble drift velocity is clarified by connecting numerical results to theory for ordered arrays of bubbles, and similarities between bubbly suspensions and ordered arrays are evidenced. The modeling of scalar mixing in laminar suspensions, as described by an effective diffusivity tensor, is then addressed. A rigorous framework for the computation of the effective diffusivity is provided, and it is shown that scalar mixing induced by a homogeneous swarm of bubbles fundamentally differs from that induced by an ordered array of bubbles. Lastly, turbulence is included in the simulations, and the dynamics of a finite-size bubble is characterized. In particular, it is shown that the bubble undergoes, on average, stronger decelerations than positive accelerations. Besides, the behavior of a large bubble shares a number of common features with that of a microbubble, most notably, the flow sampled by the bubble is biased. A definition of the liquid flow seen by the bubble, as it enters in usual models of added mass and lift forces, is finally proposed.

Keywords: bubbly flow, bubble dynamics, suspension, scalar transport, effective diffusivity, finite size, turbulent multiphase flow.

Résumé

Cette thèse est consacrée aux écoulements homogènes de bulles, ainsi qu'à leur couplage avec le transport de scalaire et la turbulence. Elle s'intéresse plus spécifiquement aux effets de taille finie, des interactions hydrodynamiques, de l'inertie du liquide et de la microstructure de la suspension. Ces effets sont étudiés à l'aide de simulations numériques directes à l'échelle d'une bulle. La dynamique d'une suspension laminaire de bulles induite par la seule gravité est d'abord revisitée. L'influence de la fraction volumique sur la vitesse de dérive des bulles est établie analytiquement et numériquement pour un réseau ordonné de bulles, puis des ressemblances entre suspensions de bulles et réseaux ordonnés sont mises en évidence. Le mélange d'un scalaire au sein d'une suspension laminaire est ensuite étudié et modélisé par une diffusivité effective tensorielle. Un cadre rigoureux permettant le calcul de la diffusivité effective est proposé, puis il montré que le mélange induit par un nuage de bulles diffère fondamentalement de celui généré par un réseau ordonné de bulles. Enfin, la turbulence est prise en compte dans les simulations et la dynamique d'une bulle de taille finie est caractérisée. Il est notamment montré qu'en moyenne, les accélérations négatives subies par la bulle sont plus fortes que les accélérations positives. Par ailleurs, le comportement d'une grosse bulle ressemble qualitativement à celui d'une microbulle, avec, notamment, une préférence pour certaines régions caractéristiques de l'écoulement. Une définition de l'écoulement vu par la bulle compatible avec les modèles standards de forces de portance et de masse ajoutée est finalement proposée.

Mots-clés : écoulement à bulles, dynamique de bulle, suspension, transport de scalaire, diffusivité effective, taille finie, écoulement diphasique turbulent.

Résumé long

Introduction générale

Les écoulements à bulles, qui font partie de la classe plus générale des écoulements diphasiques, consistent en une phase gazeuse distribuée sous la forme de bulles dans une phase liquide. Ces deux phases peuvent correspondre à deux fluides de compositions chimiques différentes, par exemple des bulles d'air dans de l'eau. Ce premier type d'écoulement se rencontre fréquemment dans l'industrie chimique, biochimique et pétrochimique (synthèse de produits chimiques, captage du dioxyde de carbone, etc.). Les procédés alors mis en jeu impliquent généralement le transfert ou le mélange des espèces chimiques en présence. Un écoulement à bulles peut aussi être constitué d'un unique fluide coexistant sous la forme de deux phases thermodynamiques différentes, par exemple des bulles de vapeur dans de l'eau. Ce second type d'écoulement trouve ses applications dans les domaines de la conversion d'énergie et de l'évacuation de la chaleur (générateur de vapeur, condensateur, etc.). L'usage répandu des écoulements à bulles dans le monde industriel tient au fait que ces derniers possèdent d'excellentes propriétés de mélange et de transfert en raison, d'une part, de l'agitation du liquide induite par le mouvement des bulles, et d'autre part, de l'importante surface de contact entre les deux phases.

L'efficacité, l'impact environnemental, mais aussi la sûreté de ces équipements industriels dépendent de la vitesse des processus de dissolution, d'évaporation ou de mélange, ceux-ci étant intrinsèquement liés à la dynamique des bulles et aux perturbations qu'elles induisent dans le liquide environnant. Cependant, d'un point de vue pratique, le détail des processus ayant lieu à l'échelle d'une bulle n'a généralement que peu d'intérêt, l'enjeu principal étant la prédiction des propriétés de l'écoulement à l'échelle du système. À ce jour, le lien entre dynamique à petite échelle et propriétés à grande échelle des écoulements à bulles est loin d'être entièrement compris.

Par ailleurs, les écoulements à bulles sont souvent turbulents. Le couplage entre écoulement diphasique et turbulence, deux des problèmes les plus difficiles de la mécanique des fluides, pose un formidable défi scientifique. La modélisation des écoulements dispersés turbulents est actuellement limitée aux systèmes très dilués et aux particules (fluides ou solides) de taille négligeable par rapport à la plus petite échelle de l'écoulement porteur. De plus, la déformation des particules fluides est généralement négligée.

Cette thèse s'intéresse à la dynamique des écoulements à bulles, aux processus de mélange au sein de ces écoulements et à leur couplage avec la turbulence environnante. Les interactions entre bulles, ainsi que la taille et la déformation de ces dernières, sont prises en compte dans cette étude, contrastant ainsi avec les travaux précédents. Pour cela, l'approche choisie ici est la simulation numérique directe d'une suspension homogène infinie et à l'échelle d'une seule bulle. Cette suspension est représentée par la répétition périodique tridimensionnelle d'une cellule unitaire cubique dans laquelle se déplacent librement plusieurs bulles. On parle alors de « réseau libre » de bulles. Dans la limite d'une cellule ne contenant qu'une seule bulle, le système obtenu correspond à un réseau cubique de bulles. Ce système est appelé « réseau ordonné ».

Chapitre 1. Simulation numérique directe d'écoulements à bulles : développement d'un code de calcul DNS tridimensionnel

Le développement d'un code de calcul de type DNS (pour *Direct Numerical Simulation*, en français Simulation Numérique Directe), initié par A. Naso, a été poursuivi dans le cadre de cette thèse. Ce code résout les équations de Navier-Stokes incompressibles au sein d'un domaine spatial périodique contenant deux fluides séparés par une interface mobile. À l'interface, le couplage entre les deux fluides se traduit par des conditions de continuité des vitesses, de continuité de la contrainte tangentielle, et de saut de la contrainte normale égal à la force de tension superficielle exercée par unité de surface. La seule force extérieure s'exerçant sur les fluides est la gravité.

Les équations gouvernant le mouvement des fluides sont écrites sous une forme valide dans les deux phases à la fois (Brackbill, Kothe, & Zemach, 1992) et sont résolues par une méthode de projection (Chorin, 1968). Pour le suivi de l'interface, une méthode de type surfaces de niveau, ou *level-set*, est utilisée (Osher & Sethian, 1988; Sussman, Smereka, & Osher, 1994). Des modifications à la méthode de base ont été implémentées afin d'améliorer sa précision (Russo & Smereka, 2000; Sabelnikov, Ovsyannikov, & Gorokhovski, 2014). De plus, afin d'assurer une conservation parfaite de la masse des deux phases sur des temps très longs, les surfaces de niveau sont corrigées à chaque pas de temps (Sussman & Uto, 1998). Afin d'éviter des instabilités numériques liées à la présence de discontinuités à l'interface, une épaisseur finie est donnée à cette dernière, ce qui permet, d'une part, de lisser les sauts interfaciaux de masse volumique et de viscosité, et d'autre part, de transformer la tension de surface en une force volumique localisée à l'interface.

L'algorithme d'intégration temporelle est basé sur un schéma de Runge-Kutta TVD du troisième ordre pour l'équation des surfaces de niveau, et sur un schéma mixte de Crank-Nicolson et Adams-Bashforth à l'ordre trois pour les équations de Navier-Stokes. La discrétisation spatiale des équations est réalisée sur une grille cartésienne uniforme décalée. Des schémas de type différences finies et volumes finis d'ordre cinq pour les termes advectifs et d'ordre deux pour les autres termes sont utilisés.

Le code a été validé pour des réseaux ordonnés et libres de bulles en ascension par comparaison à de précédents travaux numériques (Esmaeeli & Tryggvason, 1999). Dans ces cas tests, les bulles sont légèrement déformées et les nombres de Reynolds rencontrés sont de l'ordre de 10. Par ailleurs, une attention particulière a également été apportée aux potentiels effets indésirables liés à la conservation forcée de la masse des deux phases. Il est montré que, pour les régimes d'écoulement étudiés, ces effets sont négligeables, et ce même pour des bulles très déformées présentant une fine jupe (*skirt*).

Chapitre 2. Dynamique des écoulements à bulles : suspensions de bulles soumises à la seule gravité

Dans ce chapitre nous nous intéressons à la dynamique d'une suspension laminaire de bulles en ascension sous l'effet de la gravité. L'observable macroscopique sur lequel nous focalisons notre attention est la vitesse de dérive moyenne des bulles, notée U, et sa dépendance vis-à-vis de la fraction volumique de gaz, notée ϕ. Cette étude est motivée par l'absence de consensus sur la forme fonctionnelle de cette dépendance du fait de désaccords persistants entre théories (Batchelor, 1972; Keh & Tseng, 1992), simulations (Esmaeeli & Tryggvason, 1998; Bunner & Tryggvason, 2003; Yin & Koch, 2008) et expériences (Zenit, Koch, & Sangani, 2001; Garnier, Lance, & Marié, 2002; Colombet, Legendre, Risso, Cockx, & Guiraud, 2015).

Nous examinons dans un premier temps l'ascension d'un réseau ordonné de bulles déformables. Cette ascension est le plus souvent verticale et stationnaire. À partir de simulations numériques pour différents régimes (nombre de Reynolds compris entre 0 et 40, formes de bulle sphérique, ellipsoïdale, ou présentant une jupe) et d'une analyse théorique dans le cadre d'un écoulement d'Oseen, nous démontrons que l'évolution de U en fonction de ϕ n'est pas monotone en présence d'effets inertiels. Alors que pour des fractions volumiques modérées à élevées, U décroît avec ϕ, conformément à ce qui est communément admis, il s'avère que U croît avec ϕ lorsque la suspension est suffisamment diluée. Ce comportement s'explique par la compétition entre les interactions de sillage qui accélèrent l'ascension et les interactions visqueuses qui la ralentissent. Une expression explicite de la fonction $U = f(\phi)$, dont la forme découle de l'analyse théorique et dont les coefficients sont obtenus à partir des données numériques, est proposée. Par ailleurs, l'influence des interactions hydrodynamiques sur la forme des bulles est analysée. Une tendance générale des bulles déformées à devenir sphériques lorsque la fraction volumique augmente est notamment mise en évidence. Ces observations sont expliquées à partir du comportement d'une paire de bulles (Legendre, Magnaudet, & Mougin, 2003; Hallez & Legendre, 2011).

Dans certains cas, des bulles arrangées en réseau ordonné ne suivent pas une trajectoire verticale. La possibilité d'un mouvement oblique stationnaire est démontrée analytiquement pour un écoulement d'Oseen, et confirmée numériquement. Ce mouvement oblique stationnaire trouve son origine dans l'interaction de sillage entre deux bulles voisines qui se suivent, le

sillage de la bulle en amont induisant une force de portance sur la bulle en aval, et préfigure d'une transition vers un mouvement oblique oscillant puis chaotique. Une dynamique chaotique est obtenue lorsque des interactions de sillage non linéaires s'installent entre une bulle et ses voisines appartenant aux plans horizontaux situés en amont. Un scénario complet expliquant la transition de l'ascension stationnaire verticale vers l'ascension oblique chaotique est proposé.

Dans un second temps, une étude numérique de la dynamique d'une suspension de bulles libres est entreprise. Celle-ci révèle que les bulles très déformées possédant une jupe subissent rapidement des coalescences par paire. L'étude des mécanismes de la coalescence n'est pas poursuivie, car cette dernière ne peut pas, *a priori*, être simulée de manière rigoureuse par les méthodes numériques utilisées dans ce travail. *A contrario*, les bulles moins déformées ne coalescent pas même sur des temps d'évolution très longs, ce qui permet de définir un état statistiquement stationnaire atteint par le système. Cet état partage un certain nombre de caractéristiques avec l'état stationnaire atteint par une suspension ordonnée : les bulles libres deviennent de plus en plus sphériques avec l'augmentation de la fraction volumique, et la dépendance de U à ϕ est différente à faible et à forte fractions volumiques. Ce changement de comportement est compatible avec les résultats expérimentaux disponibles (Garnier et al., 2002; Martinez-Mercado, Palacios-Morales, & Zenit, 2007; Riboux, Risso, & Legendre, 2010; Colombet et al., 2015) et constitue une explication plausible à la confusion actuelle existant dans la littérature. Les similitudes entre suspensions de bulles et réseaux ordonnés sont expliquées par la présence d'un certain degré d'ordre au sein de ces suspensions. En effet les simulations numériques montrent que les bulles ne se distribuent pas aléatoirement dans l'espace, mais restent à une distance quasi-constante de leurs voisines.

Chapitre 3. Mélange de scalaire dans les écoulements à bulles : diffusivité effective d'une suspension de bulles

Dans ce chapitre nous abordons la modélisation du mélange d'un scalaire passif au sein d'un écoulement à bulles laminaire. Ce scalaire peut représenter, sous certaines hypothèses, la concentration d'une espèce chimique ou la température d'un fluide. À ce jour, les études dédiées au mélange induit par un nuage de bulles sont extrêmement limitées. En effet, la seule étude notable de ce sujet est celle, expérimentale, d'Alméras et al. (2015). Il est cependant opportun de mentionner que des analyses théoriques conséquentes ont été menées sur le mélange de scalaire au sein de matériaux poreux et des lits tassés (Koch & Brady, 1985, 1987b; Koch, Cox, Brenner, & Brady, 1989). Nous nous proposons ici d'adapter et d'étendre ces travaux au cas des écoulements à bulles.

L'équation gouvernant le transport de scalaire à l'échelle macroscopique, c'est-à-dire celle de la suspension, est obtenue en moyennant les équations locales qui régissent le transport de scalaire dans chacune des phases. Lorsque le système est homogène, l'équation macroscopique prend la forme d'une loi de Fick (ou de Fourier) dans laquelle apparaît une diffusivité effective

tensorielle (Batchelor, 1974; Koch & Brady, 1985, 1987b). Afin de fermer cette équation, il nous faut exprimer cette diffusivité effective en fonction des paramètres macroscopiques intervenant dans le problème. Nous avons pour cela développé une méthode originale permettant de calculer la diffusivité effective d'une suspension de bulles par simulation numérique directe.

La diffusivité effective d'une suspension peut être écrite comme la somme de diverses contributions reflétant différents mécanismes de transport à l'échelle macroscopique. Notre étude se concentre sur la contribution convective, c'est-à-dire celle qui décrit le mélange induit par les fluctuations de vitesses locales engendrées par le mouvement des bulles. La contribution convective de la diffusivité effective dépend, a priori, de nombreux paramètres macroscopiques, tels que le nombre de Reynolds des bulles, la fraction volumique de gaz ou encore le nombre de Péclet. Ce dernier est particulièrement important puisque qu'il compare les effets d'advection aux effets de diffusion, et détermine donc le mode de transport dominant.

Le mélange au sein de suspensions ordonnées pour lesquelles le mouvement des bulles est parallèle à un axe de symétrie du réseau a d'abord été étudié analytiquement sous l'approximation de bulles ponctuelles en écoulement d'Oseen. Il s'agit en fait d'une extension de la théorie de Koch et al. (1989) établie pour des particules solides en écoulement de Stokes. Dans la limite d'un écoulement de Stokes, Koch et al. (1989) ont montré que le mélange se fait par dispersion diffusive renforcée par convection à petit nombre de Péclet et par dispersion dite « de Taylor » à grand nombre de Péclet. La dispersion de Taylor est caractérisée par le fait que le mélange de scalaire ne peut se faire qu'en présence d'un transport, nécessairement diffusif, perpendiculaire aux lignes de courant. Notre analyse en écoulement d'Oseen révèle que ces deux régimes sont inchangés en présence d'effets inertiels. Les prédictions théoriques, supposément valides sous des conditions particulièrement strictes, se sont montrées en bon accord qualitatif avec les simulations numériques bien au-delà de leur domaine de validité attendu, y compris à des nombres de Reynolds modérés.

Des simulations du transport de scalaire au sein d'un réseau libre de bulles à nombre de Reynolds modéré ont ensuite été réalisées pour des nombres de Péclet variant sur six décades. À petit nombre de Péclet, la diffusion contribue au mélange convectif induit par les bulles, comme dans le cas des réseaux ordonnés. À grand nombre de Péclet, le mélange est purement advectif : la dispersion est dite « mécanique », et diffère donc de la dispersion de Taylor obtenue pour les réseaux ordonnés. Les mécanismes de mélange à grand nombre de Péclet changent de nature dès lors que du désordre est introduit dans le système. En effet, la transition entre dispersion de Taylor et dispersion mécanique s'effectue dès que deux bulles sont présentes dans le domaine. Alors que la dynamique des suspensions de bulles ressemble à celle des réseaux ordonnés, la dispersion au sein de ces suspensions se rapproche de celle obtenue pour des systèmes possédant une microstructure aléatoire. Par ailleurs, les simulations numériques suggèrent que la convergence de la diffusivité effective avec la taille du système est très rapide. Ce dernier résultat, qui devra être confirmé par l'étude de systèmes de plus grande taille, est particulièrement encourageant quant à la possibilité de calculer à peu de frais la diffusivité

effective des suspensions de bulles. Signalons enfin que des mesures expérimentales sur une vaste gamme de nombres de Péclet seraient les bienvenues afin de valider nos résultats.

Ce travail constitue la première étude numérique de la diffusivité effective des suspensions de bulles, et l'influence de nombreux paramètres reste à étudier, notamment celles du nombre de Reynolds et de la fraction volumique, mais aussi celle du rapport des diffusivités du gaz et du liquide et celle du saut de scalaire à l'interface, ce saut traduisant la loi de Henry dans le contexte du transport d'espèces chimiques. Un telle étude est d'ores et déjà possible avec notre code, mais la multiplicité des paramètres fait que les ressources numériques nécessaires à telle étude sont conséquentes.

Chapitre 4. Vers les écoulements à bulles turbulents : interaction entre une grosse bulle et une turbulence homogène isotrope

L'étude présentée dans ce chapitre est une exploration numérique de l'interaction entre une bulle isolée de taille finie en ascension et une turbulence homogène isotrope. Alors que la dynamique d'une bulle sphérique ponctuelle dans un écoulement turbulent est relativement bien comprise (Wang & Maxey, 1993; Maxey, Chang, & Wang, 1994; Spelt & Biesheuvel, 1997; Mazzitelli, Lohse, & Toschi, 2003b, 2003a; Snyder, Knio, Katz, & Le Maître, 2007), celle d'une bulle déformable de taille finie, c'est-à-dire de dimension caractéristique supérieure à l'échelle de Kolmogorov, demeure largement inexplorée. Les études expérimentales du sujet sont en effet peu nombreuses (Volk et al., 2008; Ravelet, Colin, & Risso, 2011; Prakash et al., 2012), quant aux simulations numériques, elles sont quasi-inexistantes puisqu'elles se résument à des simulations des grandes échelles (*large eddy simulations*) d'une bulle sphérique maintenue fixe dans un écoulement en conduite faiblement turbulent (Merle, Legendre, & Magnaudet, 2005; Legendre, Merle, & Magnaudet, 2006). Récemment, l'interaction entre une particule solide et un écoulement homogène isotrope a été simulé par DNS par différents groupes (Naso & Prosperetti, 2010; Cisse, Homann, & Bec, 2013; Chouippe & Uhlmann, 2015). L'extension de ces travaux au cas des bulles n'est cependant pas triviale car la déformation de l'interface et la recirculation interne du gaz doivent alors être prises en compte.

Nous nous proposons ici d'examiner l'ascension d'une grosse bulle déformable dans un écoulement turbulent et initialement homogène isotrope. Nous utilisons pour cela notre code de calcul diphasique dans lequel est implémenté le forçage linéaire de Lundgren (2003) qui permet de maintenir une turbulence statistiquement stationnaire au sein du liquide porteur. Il est à noter que l'utilisation d'un forçage se fait toujours au risque de modifier la physique de l'écoulement, et que des tests complémentaires seront nécessaires pour consolider nos résultats.

Le seul paramètre variable de notre étude est l'intensité turbulente, notée β et définie comme la moyenne quadratique des fluctuations de vitesse du liquide divisée par la vitesse terminale de la bulle dans un liquide au repos. Trois simulations correspondant à trois valeurs de β ont été menées sur des périodes de temps suffisamment longues pour obtenir des statistiques

eulériennes du liquide et lagrangiennes de la bulle raisonnablement convergées.

La turbulence de l'écoulement de base induit des fluctuations de la forme des bulles qui peuvent mener celles-ci à se rompre lorsque la tension superficielle est trop faible. La vitesse d'ascension moyenne des grosses bulles est fortement réduite par la turbulence, de manière analogue à ce qui est observé pour des bulles plus petites. Ce ralentissement est maximum lorsque β est proche de 1. La réduction de la vitesse d'ascension n'est cependant pas entièrement déterminée par la seule intensité turbulente, et l'influence des autres paramètres sans dimension doit maintenant être élucidé.

Le moyennage conditionnel des propriétés du liquide au voisinage des bulles a permis de mettre en évidence le fait que ces dernières ne parcourent pas l'écoulement de base de manière uniforme. Lorsque $\beta \lesssim 1$, les bulles résident préférentiellement dans les zones d'écoulement descendant alors que pour $\beta \gtrsim 1$, les bulles ont une préférence statistique pour les régions tourbillonnantes. Ce comportement, qui est qualitativement similaire à celui des bulles ponctuelles, peut être à l'origine de la réduction de la vitesse d'ascension des bulles (Spelt & Biesheuvel, 1997; Mazzitelli et al., 2003b, 2003a). Les mécanismes sous-jacents, en particulier le rôle joué par la force de portance, ne sont cependant pas forcément identiques, et leur élucidation nécessite de plus amples investigations.

Concernant les statistiques lagrangiennes, il est montré que la vitesse et l'accélération d'une grosse bulle partagent de nombreuses caractéristiques avec celles d'un traceur et d'une particule solide inertielle (Toschi & Bodenschatz, 2009; Mordant, Crawford, & Bodenschatz, 2004; Qureshi et al., 2008). Par ailleurs, la distribution de la composante verticale de l'accélération est négativement désaxée. Cette asymétrie est interprétée comme une conséquence de l'alignement préférentiel de la direction du mouvement avec la direction verticale et de l'asymétrie négative de la distribution de l'accélération longitudinale de la bulle. Cette dernière propriété, récemment découverte dans le cas des traceurs (Lévêque & Naso, 2014), a été mise en évidence pour la première fois par nos simulations dans le cas d'un objet de taille finie et traduit le fait qu'en moyenne, une grosse bulle décélère plus fortement qu'elle n'accélère.

Enfin, une forte corrélation entre l'accélération de la bulle et l'écoulement liquide « vu » par la bulle, lorsqu'adéquatement défini, a été mise en évidence. Plus précisément, la vitesse et la vorticité du liquide telles qu'elles apparaissent dans les expressions usuelles des forces de masse ajoutée et de portance peuvent être définies à partir de l'écoulement local moyenné sur une coquille enveloppant la bulle. Ces résultats constituent une fondation solide à l'élaboration d'une équation du mouvement pour les bulles de taille finie en écoulement turbulent.

Conclusion générale

Ce travail de thèse, consacré à l'étude des écoulements à bulles, contribue à la compréhension de leur dynamique, de leurs propriétés de mélange et de leur couplage avec la turbulence. Un certain nombre de résultats originaux, obtenus essentiellement par la simulation numérique

directe d'un système à échelle réduite, et complétés par des analyses théoriques dans le cadre des réseaux périodiques de bulles, ont été présentés.

Ces résultats ne s'appliquent qu'aux régimes d'écoulement correspondant à un nombre de Reynolds modéré et pour lesquels l'ascension d'une bulle isolée dans un liquide au repos est verticale et génère un sillage laminaire. Cette limitation est liée au coût des simulations qui augmente considérablement avec le nombre de Reynolds du fait de la finesse croissante des couches limites à résoudre. Par ailleurs, les bulles considérées dans ce travail sont parfaitement propres. En présence de tensioactifs, les conditions de saut à l'interface gaz-liquide sont modifiées et la dynamique des bulles peut en être notablement affectée.

La question des propriétés du liquide porteur n'a pas été abordée au cours de cette thèse, et pourra constituer une continuation naturelle de cette dernière. L'agitation du liquide générée par des bulles en ascension dans un liquide au repos a été étudiée au travers d'expériences (Cartellier & Rivière, 2001; Garnier et al., 2002; Cartellier, Andreotti, & Sechet, 2009; Riboux et al., 2010) et de simulations numériques directes (Esmaeeli & Tryggvason, 1999, 2005; Bunner & Tryggvason, 2002b, 2003). Mais, curieusement, l'agitation prédite par les simulations est souvent beaucoup plus faible que celle mesurée expérimentalement. Plusieurs explications sont envisageables, par exemple la présence de cisaillement dans les expériences ou bien des systèmes trop petits dans les études numériques. De nouvelles simulations sont donc nécessaires pour mettre en évidence un éventuel problème de convergence et expliquer l'origine de ce désaccord. Par ailleurs, s'il est largement reconnu qu'un écoulement turbulent peut être considérablement altéré par la présence de bulles (Lance & Bataille, 1991; Mazzitelli et al., 2003b; Lelouvetel, Tanaka, Sato, & Hishida, 2014), les mécanismes de cette modulation ne sont toujours pas clairement établis (Balachandar & Eaton, 2010). La simulation d'écoulements turbulents à bulles avec résolution de toutes les échelles est désormais à notre portée, et apportera certainement des éclairages nouveaux sur la physique de ces écoulements particulièrement complexes.

Remerciements

Je tiens en premier lieu à adresser mes plus sincères remerciements à Aurore Naso et Peter Spelt pour avoir encadré ces travaux de thèse qui n'auraient pas été ce qu'ils sont sans leurs précieux conseils et leur implication constante tout au long de ces années de doctorat. J'exprime toute ma gratitude à Aurore Naso pour m'avoir fait partager sa connaissance de la turbulence et sa vision de la physique, et pour m'avoir encouragée à communiquer sur mes travaux en de maintes occasions. Je suis particulièrement reconnaissante à Peter Spelt pour m'avoir incitée à développer des approches théoriques et m'avoir fait profiter de sa vaste connaissance du sujet. Enfin merci à eux deux pour leur gentillesse et pour leurs discours respectifs lors de ma soutenance.

Je souhaite remercier Jérémie Bec et Dominique Legendre, rapporteurs de ce manuscrit, pour leur lecture attentive et leurs remarques pertinentes. Je remercie également Alain Cartellier, Michel Lance et Olivier Pouliquen d'avoir accepté d'être membres de mon jury. Merci à eux cinq d'avoir transformé ce moment particulièrement stressant de la soutenance en un échange scientifique enrichissant et constructif.

Je remercie chaleureusement Christophe Pera et Dan-Gabriel Calugaru pour la disponibilité et la sympathie dont ils ont su faire preuve lors de mes irruptions récurrentes et souvent intéressées dans leurs bureaux respectifs.

Merci à Bernard pour sa bonne humeur inébranlable et communicative. Bernard, tes visites impromptues me manqueront.

Merci à mes parents de m'avoir soutenue dans des choix professionnels obscurs à leurs yeux. Sachez que je vous en suis infiniment reconnaissante.

Maurin, merci de partager ma vie.

Contents

General introduction

Bubbly flows are two-phase flows that consist of a disperse gaseous phase distributed within a liquid continuum in the form of bubbles. They are commonly employed in the industry because they offer excellent transfer and mixing characteristics owing to the increased contact area between the two phases and to the liquid agitation induced by bubble motion.

One may distinguish between two types of bubbly flows, based on the nature the two phases and the associated transport processes. The two phases may consist of different chemical species in different states, such as carbon dioxide bubbles in water. Such bubbly flows have widespread applications in chemical, biochemical, and petrochemical engineering (e.g., synthesis of chemical products, gas purification, wastewater treatment, carbon capture). In these systems, the transport of chemical species plays a crucial role. Alternatively, the two phases may represent different thermodynamic phases of the same species, such as vapor bubbles in water. These bubbly flows are intrinsically linked to energy conversion and heat removal (e.g., steam generators, boilers, condensers) which critically depend upon heat transfer and phase change processes.

These industrial systems have in common that their efficiency, environmental impact, and possibly safety depend on the rate of dissolution or evaporation which is, as a matter of fact, strongly coupled to the dynamics of the bubbles and to the disturbances they create in the surrounding liquid. In these systems, the primary interest is often not in the detailed processes occurring at the scale of one bubble, but rather in the conservation equations and constitutive relations governing transfer and mixing over much larger scales. But to date, the relation between small-scale dynamics and macroscale transport properties in bubbly suspensions is far from being thoroughly understood, and most available models are purely empirical.

Besides, bubbly flows encountered in practice are often turbulent. Turbulence and multiphase flows are two of the most challenging topics in fluid mechanics, and when combined they pose a formidable challenge. Up to now, the modeling of turbulent bubbly flows is mostly limited to systems sufficiently dilute to assume that hydrodynamic interactions are negligible, and to systems wherein the bubble size is smaller than the smallest length scale of the flow. In addition, bubble deformation is usually neglected.

From a mathematical standpoint, bubbly flow problems are most often intractable. The equations governing fluid motion are highly nonlinear and the position of the phase boundary must generally be found as a part of the solution. Exact analytical solutions, therefore, exist only for dilute systems in the Stokes flow limit. Experimental studies are not easy either. Bubbly flows are very sensitive to disturbances caused by intrusive measuring probes, and optical access to much of the flow becomes rapidly limited as the gas volume fraction increases. In addition, controlling basic parameters such as the bubble size remains a difficult task.

With the advance of computational methods, interface-resolved numerical simulation is becoming a viable option to explore the physics of bubbly flows and associated transport processes in the much more realistic case of large deformable bubbles, and to go beyond the limit of very small volume fractions of the disperse phase. Direct numerical simulations of real-size industrial systems remain however way out of reach due to the broad spectrum of temporal and spatial scales present in bubbly flows. One must therefore assume somewhat idealized configurations.

Unbounded homogeneous bubbly suspensions are conveniently represented by the periodic repetition of a unit cell containing a finite number of freely-moving bubbles, so that the solution of governing equations only needs to be determined within a computational domain, usually of cubic shape, with periodic boundary conditions. This periodic configuration is referred to as an "array" of bubbles. When the unit cell contains a single bubble, one effectively obtains a cubic lattice of bubbles. In this case the bubbles move with the same velocity, deform in the same way, and have a fixed position relative to their neighbors. We call this arrangement an "ordered array" (some authors also use the term "regular array"). When the unit cell contains several bubbles, these bubbles can move relatively to each others and deform independently. This configuration is referred to as a "free array". In addition to their computational convenience, ordered and free arrays provide an efficient mean of evaluating the role of and sensitivity to the suspension microstructure.

This thesis is devoted to the study of homogeneous bubbly flows, and their coupling with turbulence and passive scalar transport. It focuses on the effects of finite size, hydrodynamic interactions, liquid inertia, and suspension microstructure, which are investigated using direct numerical simulations of ordered and free arrays of deformable bubbles. The numerical methods employed for the simulation of bubbly flows at the bubble scale are first presented in chapter 1. Buoyancy-driven laminar bubbly suspensions are then revisited in chapter 2, where we clarify the effects of finite volume fraction and liquid inertia on their dynamics. The dispersion of a passive scalar, such as temperature or concentration, is considered in chapter 3, where the mixing properties of ordered and freely evolving bubbly suspensions are investigated. Turbulence is finally included in the simulations in chapter 4, and the effects of finite-size on interphase coupling in the presence of external agitation are characterized.

Chapter 1

Numerical simulation of bubbly flows

Development of a 3D DNS level-set code

Contents

1.1 Introduction

This first chapter is devoted to the description and assessment of the methods employed in the present thesis for the direct numerical simulation of homogeneous bubbly flows at the bubble scale. Numerical methods developed for single-phase flows, such as finite volumes, finite elements, and finite differences, can generally be used to solve the Navier-Stokes equations that govern the fluid motion in two-phase flows. The major challenge of multiphase flow simulation is twofold: to track and evolve interfaces on one hand, and to impose interfacial conditions on the other. Various methods have been developed for that purpose, each method having its own strengths and weaknesses.

One possibility is to use an adaptive, interface fitting grid and to solve the Navier-Stokes equations separately in each subdomain (Ryskin & Leal, 1984a; I. S. Kang & Leal, 1987). Governing equations are subsequently coupled explicitly through jump conditions at the interface. Another possibility is to use a stationary, structured grid for the whole computational domain. In this approach, the Navier-Stokes equations are most often rewritten as a single set of equations valid in both phases with variable density and viscosity, and surface tension is converted into a volume force distributed over an interfacial zone of finite thickness (Brackbill et al., 1992). It is however possible to enforce the interface jump conditions in a sharp manner by the construction of a ghost fluid (Fedkiw, Aslam, Merriman, & Osher, 1999; M. Kang, Fedkiw, & Liu, 2000). Then, the interface between the two phases can be tracked explicitly with marker points, resulting in so-called front-tracking methods (Peskin, 1977; Unverdi & Tryggvason, 1992). Alternatively, the interface can be implicitly captured using a marker function, as in volume-of-fluid methods (Noh & Woodward, 1976; Hirt & Nichols, 1981), level-set methods (Osher & Sethian, 1988; Sussman et al., 1994), and phase-field methods (Jacqmin, 1999; Ding, Spelt, & Shu, 2007). Detailed presentations of these various approaches can be found in, e.g., Prosperetti and Tryggvason (2007) and Tryggvason, Scardovelli, and Zaleski (2011).

The development of a two-phase flow DNS (Direct Numerical Simulation) code based on a level-set method has been initiated by A. Naso and pursued in the course of the present thesis. This code solves the Navier-Stokes equations in two fluid phases separated by a moving interface in a parallelepipedal domain with periodic boundary conditions. It is written in `C++`, and parallelized with MPI (Message Passing Interface). The code skeleton, the two-phase flow solver, and its parallelization, are owed to A. Naso.

During this thesis, the notorious problem of poor mass conservation, inherent to all level-set methods, has been addressed. Extensive optimization tests aiming at minimizing this issue for an acceptable computational cost were carried out. The choice of the time integration and spatial discretization schemes that will be presented hereinafter, as well as the modifications brought to the original level-set method used to capture the interface, result from these tests. The development of post-processing algorithms, the code validation, as well as the implementation of passive scalar transport and of turbulence forcing, were also part of this thesis work.

In this chapter we shall focus on the simulation of two-phase flows. The numerical methods employed for solving scalar transport and generating a turbulent background flow will be introduced in chapter 3 and chapter 4, respectively.

1.2 Mathematical formulation

1.2.1 Governing equations and jump conditions

We consider an unbounded two-phase system consisting of a fluid particulates (the disperse phase) distributed in a connected volume of an ambient fluid (the continuous phase). In what follows the subscripts d and c refer to the disperse and continuous phases, respectively. The two phases may represent different thermodynamic phases of the same species (e.g., steam-water), or consist of different chemical species that may be in the same state (e.g., oil-water), or in different states (e.g., air-water). Each phase consists of a viscous, immiscible, and incompressible Newtonian fluid which motion satisfies the Navier-Stokes equations. The physical properties of the two fluids, namely their densities (ρ_d, ρ_c), their viscosities (μ_d, μ_c), and surface tension (γ), are assumed to be constant.

Conservation of mass under the incompressibility condition results in a divergence-free velocity field, denoted $\boldsymbol{u}$, in each phase

$$\boldsymbol{\nabla} \cdot \boldsymbol{u}_n = 0 \tag{1.1}$$

where $n = \{c, d\}$ is used here to denote either phases. Conservation of momentum in each phase writes

$$\frac{\partial \rho_n \boldsymbol{u}_n}{\partial t} + \boldsymbol{\nabla} \cdot \rho_n \boldsymbol{u}_n \boldsymbol{u}_n = \boldsymbol{\nabla} \cdot \boldsymbol{T}_n + \boldsymbol{G}_n \quad \text{where } \boldsymbol{T}_n = -p_n \boldsymbol{I} + \mu_n (\boldsymbol{\nabla} \boldsymbol{u}_n + \boldsymbol{\nabla} \boldsymbol{u}_n^T), \tag{1.2}$$

where $\boldsymbol{T}$ is the stress tensor, $\boldsymbol{I}$ is the identity tensor, p is the pressure field, and $\boldsymbol{G}$ is the sum of external forces per unit volume. In the present context the only external body force is that due to gravity, so $\boldsymbol{G}_n = (\rho_n - \langle \rho \rangle)\boldsymbol{g}$ with $\boldsymbol{g}$ the gravitational acceleration vector. The first term in this last expression, $\rho_n \boldsymbol{g}$, is the weight of a unit volume of fluid. Because the system we consider is infinite, i.e. not bounded by walls, an additional body force $-\langle \rho \rangle \boldsymbol{g}$ (with $\langle \rho \rangle$ the volume-averaged density of the mixture) is required to prevent the entire system from accelerating in the downward vertical direction. This body force is equivalent to the average hydrostatic pressure gradient that would be generated by the base of a flow container to balance the total gravitational force on the mixture.

These equations are coupled through the appropriate boundary conditions at the interface. In the presence of viscous effects a no-slip condition is applied, which, combined with the absence of mass flux across the interface, leads to

$$[\boldsymbol{u}] = \boldsymbol{0} \tag{1.3}$$

where $[X] = X_c - X_d$ denotes the jump of a variable across the interface. Neglecting any variation of surface tension along the interface, the shear stress is continuous across it, and the jump of normal stress is balanced by the curvature force per unit area:

$$[\boldsymbol{n} \cdot \boldsymbol{T}] = \gamma \kappa \boldsymbol{n}, \tag{1.4}$$

where $\boldsymbol{n}$ is the unit vector normal to the interface and directed outward from the disperse phase, and κ is the interface curvature defined by $\kappa = \boldsymbol{\nabla} \cdot \boldsymbol{n}$ (e.g., Prosperetti and Tryggvason (2007), equation (1.23) therein). A non-zero tangential component in the stress balance would arise from the existence of surface tension gradients, as may result from gradients of temperature or chemical composition at the interface.

1.2.2 One-fluid formulation

When dealing with multiphase systems, governing equations may be conveniently rewritten as a single set of generalized equations valid for the entire flow. In this approach the different fluids are treated as one single fluid with discontinuous material properties and the jump conditions are incorporated by adding the appropriate source terms to the conservation laws. To identify each phase we introduce an indicator function, denoted H, and defined such that

$$H(\boldsymbol{x}, t) = \begin{cases} 1 & \text{if } \boldsymbol{x} \in \mathcal{V}_c(t), \\ \\ 0 & \text{if } \boldsymbol{x} \in \mathcal{V}_d(t), \end{cases} \tag{1.5}$$

and

$$\boldsymbol{\nabla} H(\boldsymbol{x}, t) \neq \boldsymbol{0} \quad \text{if } \boldsymbol{x} \in \mathcal{S}_i(t) \tag{1.6}$$

where $\mathcal{V}_c$ and $\mathcal{V}_d$ denote the sets of points that belong to the continuous and the disperse phases, respectively, and $\mathcal{S}_i$ contains the points lying at the interface.

Since the velocity is continuous across the interface, the generalized equation for mass conservation is simply

$$\boldsymbol{\nabla} \cdot \boldsymbol{u} = 0 \tag{1.7}$$

where $\boldsymbol{u}$ is now defined in the entire system. The one-fluid equation for momentum conservation is obtained by introducing generalized functions for the density, the viscosity and the pressure

$$\rho = H\rho_c + (1-H)\rho_d, \quad \mu = H\mu_c + (1-H)\mu_d, \quad \text{and} \quad p = Hp_c + (1-H)p_d, \tag{1.8}$$

and incorporating the normal stress jump condition as a singular volume force (Brackbill et al., 1992) to yield

$$\frac{\partial \rho \boldsymbol{u}}{\partial t} + \boldsymbol{\nabla} \cdot \rho \boldsymbol{u}\boldsymbol{u} = -\boldsymbol{\nabla} p + \boldsymbol{\nabla} \cdot \mu(\boldsymbol{\nabla}\boldsymbol{u} + \boldsymbol{\nabla}\boldsymbol{u}^T) + (\rho - \langle\rho\rangle)\boldsymbol{g} - \gamma\kappa\boldsymbol{\nabla} H. \tag{1.9}$$

(for the derivation of this last equation, see, e.g., section 3.1 in Prosperetti and Tryggvason (2007)). Equations (1.7) and (1.9) are solved numerically within a periodic unit cell using the methods described in the next section.

1.3 Numerical methods

1.3.1 Interface capturing

The deformable interface is captured by a level-set method (Osher & Sethian, 1988; Sussman et al., 1994). In this method the interface is implicitly defined by the zero-level

$$\mathcal{S}_i(t) = \{\boldsymbol{x} \mid \psi(\boldsymbol{x}, t) = 0\}. \tag{1.10}$$

of a continuous level-set function ψ, which is arbitrary chosen to be positive in the ambient liquid, and negative in the disperse gaseous phase. Level-set methods allow a straightforward and accurate representation of interfacial quantities that appear in the one-fluid formulation of the Navier-Stokes equation: the unit vector normal to the interface, and directed outward from the disperse phase, is given by

$$\boldsymbol{n} = \frac{\boldsymbol{\nabla}\psi}{|\boldsymbol{\nabla}\psi|}, \tag{1.11}$$

and the interface curvature is then easily computed from (e.g., Prosperetti and Tryggvason (2007), equation (3.56) therein)

$$\kappa = \boldsymbol{\nabla} \cdot \left(\frac{\boldsymbol{\nabla}\psi}{|\boldsymbol{\nabla}\psi|} \right). \tag{1.12}$$

The indicator step function H can also be defined as a function of ψ

$$H(\psi) = \begin{cases} 1 & \text{if } \psi(\boldsymbol{x}) > 0, \\ 0 & \text{if } \psi(\boldsymbol{x}) < 0, \end{cases} \tag{1.13}$$

and its gradient becomes

$$\boldsymbol{\nabla} H = \delta(\psi)\boldsymbol{\nabla}\psi \tag{1.14}$$

where δ denotes the Dirac delta function.

The level-set function is initialized as the signed normal distance to the interface, that is,

$$\psi(\boldsymbol{x}, t=0) = \begin{cases} +d & \text{if } \boldsymbol{x} \in \mathcal{V}_c(t=0), \\ -d & \text{if } \boldsymbol{x} \in \mathcal{V}_d(t=0), \end{cases} \tag{1.15}$$

with d the distance to the closest point lying on the interface, and its evolution is governed by the advection equation

$$\frac{\partial \psi}{\partial t} + \boldsymbol{u} \cdot \boldsymbol{\nabla}\psi = 0 \tag{1.16}$$

so that the zero-level of ψ is moved exactly as the actual interface moves. It must be noted that the level-set function will not, in general, remain a distance function. Its gradient may become very large or very small, resulting in a loss of accuracy when computing numerically the normal to the interface and the curvature (see (1.11) and (1.12)). It is therefore desirable that ψ satisfies the Eikonal equation

$$|\boldsymbol{\nabla}\psi| = 1 \tag{1.17}$$

at all times, that is, to maintain the level-set function as a signed distance function. This is achieved by the so-called reinitialization procedure. To reinitialize ψ, the iterative approach introduced by Sussman et al. (1994) is generally employed. It consists in solving for an artificial time τ

$$\frac{\partial d}{\partial \tau} = \mathrm{sgn}(\psi)(1-|\boldsymbol{\nabla} d|), \qquad \text{with } d(\boldsymbol{x},\tau=0)=\psi(\boldsymbol{x}) \tag{1.18}$$

where sgn is the sign function. The steady solution of (1.18) satisfies (1.17), and has the same zero-level as ψ, thus preserving the position of the interface.

In actual numerical computations however, the zero-contour of the discrete version of ψ may be displaced during the reinitialization process, thereby violating the principle of mass conservation. Their poor ability to conserve mass (or volume for incompressible flow) is the main drawback of level-set methods, and many efforts have been made since the nineties to improve the reinitialization algorithm in this respect (Sussman & Fatemi, 1999; Russo & Smereka, 2000; Hartmann, Meinke, & Schröder, 2008, 2010; McCaslin & Desjardins, 2014). Recently Sabelnikov et al. (2014) proposed to embed a source term in the level-set equation (1.16) in such a way that the Eikonal equation (1.17) is satisfied automatically, thereby eliminating the need for reinitializing the level-set function. From a numerical point of view though, this formulation is not convenient because it involves the computation of the normal velocity at the interface $(\boldsymbol{u}\cdot\boldsymbol{n})_{\psi=0}$ which requires, to be computed accurately, the implementation of specific procedures. To circumvent this problem they suggest to use an approximation of their modified level-set equation

$$\frac{\partial \psi}{\partial t} + \boldsymbol{u}\cdot\boldsymbol{\nabla}\psi = A(\boldsymbol{u},\psi)\,\psi \qquad \text{with } A(\boldsymbol{u},\psi)=\nabla_i\psi\nabla_i u_j \nabla_j\psi \tag{1.19}$$

where $A(\boldsymbol{u},\psi)$ is the local zero-order approximation of the source term in the region close to the interface, where $\psi\to 0$. Although the reinitialization procedure is still needed with this approximate formulation, the number of iterations needed to restore the level-set function as a distance function is significantly reduced compared to standard approach. Therefore both a reduction of the numerical cost and an improvement of the accuracy of zero-level of ψ and of interfacial geometrical quantities is expected. In our code the zero-order approximation of Sabelnikov et al. (2014) given by (1.19) is used together with the reinitialization algorithm of Russo and Smereka (2000).

Using this strategy, the volume change between two successive timesteps is negligible. It is, however, not zero, and may even become substantial when accumulated over very long integration times. Therefore a strict volume conservation is enforced by using the correction proposed by Sussman and Uto (1998): at the end of each timestep, the iso-contours of the level-set function are slightly shifted in such a way that the volume of each phase is exactly the same as its initial volume. Although this fix has been used in prior studies (Spelt, 2005, 2006; Couderc, 2007), the resort to such a rudimentary correction is clearly questionable, as the level-set function is modified everywhere while volume changes may occur locally, typically

in under-resolved regions and high-curvature zones. Nevertheless we will demonstrate that, for the applications we are interested in, its adverse effects are negligible.

1.3.2 Treatment of discontinuities

The price to pay for the simplicity of the one-fluid formulation is the introduction of singular functions, namely a Heaviside step function to represent the abrupt change in the fluid properties across the interface, and a Dirac delta function to model the action of surface tension. The numerical representation of these functions is challenging, as discontinuities can have a substantial adverse effect on the stability and the accuracy of numerical algorithms.

This problem can be circumvented by giving the interface a finite thickness proportional to the grid spacing. We substitute the smoothed Heaviside function, denoted H_ε,

$$H_\varepsilon(\psi) = \begin{cases} 1 & \text{if } \psi > \varepsilon, \\ 0 & \text{if } \psi < -\varepsilon, \\ \frac{1}{2}\left[1 + \frac{\psi}{\varepsilon} + \frac{1}{\pi}\sin\left(\frac{\pi\psi}{\varepsilon}\right)\right] & \text{if } |\psi| \leqslant \varepsilon, \end{cases} \tag{1.20}$$

for the step function, which allows material properties to vary continuously from one phase to the other. The delta function is then replaced by its smoothed version, which is defined as the derivative of H_ε with respect to ψ

$$\delta_\varepsilon(\psi) = \begin{cases} \frac{1}{2\varepsilon}\left[1 + \cos\left(\frac{\pi\psi}{\varepsilon}\right)\right] & \text{if } |\psi| \leqslant \varepsilon, \\ 0 & \text{otherwise,} \end{cases} \tag{1.21}$$

so that surface tension is treated as volume force distributed over several mesh points. The artificial thickness of the interface is equal to 2ε, and the standard value of $\varepsilon = 1.5\Delta x$, where Δx is the (uniform) grid spacing, is used.

1.3.3 Algorithm and discretization schemes

The position of the interface is evolved in time using the modified level-set method of Sabelnikov et al. (2014) combined with the reinitialization procedure of Russo and Smereka (2000) and an additional correction to enforce volume conservation. The integration of the incompressible Navier-Stokes equations is based on the projection method of Chorin (1968), which consists in a predictor step, where an intermediate velocity field is computed from the momentum conservation by ignoring the effect of pressure, and a corrector step, where the velocity field is corrected by the pressure gradient term computed from the solution of a density-weighted Poisson equation obtained from the divergence-free condition.

Spatial discretization relies on a finite difference/finite volume approach on a fixed, staggered, Cartesian grid. Scalar variables (level-set, pressure) are located at cell centers, which discrete coordinates are denoted with subscripts (i, j, k), and the three components of vector

variables (velocity) are stored on cell-face centers $(i+1/2, j, k)$, $(i, j+1/2, k$, and $(i, j, k+1/2)$, which allows a stronger coupling between velocity and pressure than with co-located grids.

The governing equations are integrated in a coupled manner using a time-staggered discretization: the velocity components are computed at integer time steps while the pressure and the level-set function are computed at half-integer time steps. In what follows, Δt is the time step, and the superscripts n and $*$ are used to denote the current time iteration and some intermediate iteration, respectively. After initial conditions have been defined for the level-set, velocity, and pressure fields, the time integration algorithm proceeds iteratively through the following steps.

At the beginning of timestep t^n, $\psi^{n-1/2}$, $\boldsymbol{u}^n$, $\boldsymbol{u}^{n-1}$, and $\boldsymbol{u}^{n-2}$ are known.

Step 1: Advection of the level-set function. ψ is advanced from $\psi^{n-1/2}$ to $\psi^{n+1/2}$ according to (1.19) using the three-stage third-order TVD Runge-Kutta scheme (Gottlieb & Shu, 1998)

$$\psi^* = \psi^{n-1/2} + \Delta t\big[-\mathscr{L}(\boldsymbol{u}^n, \psi^{n-1/2}) + \mathscr{S}(\boldsymbol{u}^n, \psi^{n-1/2})\,\psi^{n-1/2}\big], \tag{1.22a}$$

$$\psi^{**} = \frac{3}{4}\psi^{n-1/2} + \frac{1}{4}\psi^* + \frac{1}{4}\Delta t\big[-\mathscr{L}(\boldsymbol{u}^n, \psi^*) + \mathscr{S}(\boldsymbol{u}^n, \psi^*)\,\psi^*\big], \tag{1.22b}$$

$$\psi^{n+1/2} = \frac{1}{3}\psi^{n-1/2} + \frac{2}{3}\psi^{**} + \frac{2}{3}\Delta t\big[-\mathscr{L}(\boldsymbol{u}^n, \psi^{**}) + \mathscr{S}(\boldsymbol{u}^n, \psi^{**})\,\psi^{**}\big], \tag{1.22c}$$

where $\mathscr{L}(\boldsymbol{u}, \psi)$ and $\mathscr{S}(\boldsymbol{u}, \psi)$ are finite difference approximations of the advection term $\boldsymbol{u}\cdot\boldsymbol{\nabla}\psi$ and of the source term $A(\boldsymbol{u}, \psi)$, respectively. In $\mathscr{L}(\boldsymbol{u}, \psi)$, $\boldsymbol{u}$ is interpolated at the cell center with a second-order scheme and $\boldsymbol{\nabla}\psi$ is computed using a fifth-order WENO scheme (Jiang & Shu, 1996), as recommended by Salih and Ghosh Moulic (2009). In $\mathscr{S}(\boldsymbol{u}, \psi)$, $\nabla_i\psi$ is calculated through a fourth-order centered scheme and $\nabla_i u_j$ through a second-order centered scheme.

Step 2: Reinitialization of the level-set function. An interesting feature of (1.18) is that the reinitialization of the level-set function starts near the interface and propagates outward: when this equation is solved up to pseudo-time T, $d(\boldsymbol{x}, \tau = T)$ is the signed distance function for all points within distance T from the interface. Since it is important for ψ to be a signed distance function only inside the interfacial region of thickness 2ε, the reinitialization is not carried out to steady-state but only up to a given pseudo-time which must be at least equal to ε. Our algorithm is based on the second-order TVD Runge-Kutta scheme (Gottlieb & Shu, 1998) for the time integration of (1.18), which is carried out until $\tau = M\Delta\tau$, where $\Delta\tau$ is the artificial timestep, and M is a fixed number of iterations.

(i) Initially

$$d^0 = \psi^{n+1/2}.$$

(ii) Then for $m = 0$ to $m = M$:

$$d^* = d^m + \Delta\tau\mathscr{R}(d^m), \tag{1.23a}$$

$$d^{m+1} = \frac{1}{2}d^m + \frac{1}{2}d^* + \frac{1}{2}\Delta\tau\mathscr{R}(d^*). \tag{1.23b}$$

(iii) Finally

$$\psi^{n+1/2} = d^M.$$

In practice we use the standard value $\Delta\tau = 0.5\Delta x$, and set $M = 5$. In the above algorithm, $\mathscr{R}(d)$ represents the discretization of the spatial term $\mathrm{sgn}(\psi)(1-|\boldsymbol{\nabla} d|)$ devised by Russo and Smereka (2000), which reads in three dimensions

$$\mathscr{R}(d) = \begin{cases} -\dfrac{1}{\Delta x}\Big[\mathrm{sgn}\big(d^0_{i,j,k}\big)\big|d_{i,j,k}\big| - D_{i,j,k}\Big] & \text{if } (i,j,k) \in \Sigma_{\Delta x}, \\ -\mathrm{sgn}\big(d^0_{i,j,k}\big)G\big(d_{i,j,k}\big) & \text{otherwise,} \end{cases} \tag{1.24}$$

where $\Sigma_{\Delta x}$ is the set of points located within one grid point from the zero-level of d^0, where $D_{i,j,k}$ is computed by

$$D_{i,j,k} = \Delta x \frac{d^0_{i,j,k}}{\Delta d^0_{i,j,k}} \tag{1.25}$$

with

$$\begin{aligned} \Delta d^0_{i,j,k} = \max\Big\{ & \Delta x, \\ & 0.5\sqrt{\big(d^0_{i+1,j,k} - d^0_{i-1,j,k}\big)^2 + \big(d^0_{i,j+1,k} - d^0_{i,j-1,k}\big)^2 + \big(d^0_{i,j,k+1} - d^0_{i,j,k-1}\big)^2}, \\ & \Big|d^0_{i+1,j,k} - d^0_{i,j,k}\Big|, \Big|d^0_{i,j,k} - d^0_{i-1,j,k}\Big|, \Big|d^0_{i,j+1,k} - d^0_{i,j,k}\Big|, \\ & \Big|d^0_{i,j,k} - d^0_{i,j-1,k}\Big|, \Big|d^0_{i,j,k+1} - d^0_{i,j,k}\Big|, \Big|d^0_{i,j,k} - d^0_{i,j,k-1}\Big|\Big\}. \end{aligned} \tag{1.26}$$

and where $G\big(d_{i,j,k}\big)$ is an upwind discretization of $|\boldsymbol{\nabla} d| - 1$ computed with a finite-difference second-order ENO scheme (Harten, Engquist, Osher, & Chakravarthy, 1987).

Step 3: Correction of the level set function. To enforce volume conservation the iso-contours of $\psi^{n+1/2}$ are shifted. $\psi^{n+1/2}$ is then replaced by

$$\psi^{n+1/2} + \Delta\psi, \qquad \text{with } \Delta\psi = \frac{V_d^{n+1/2} - V_d^0}{2S_i^{n+1/2}}, \tag{1.27}$$

where V_d is the volume of the disperse phase calculated from

$$V_d = \int_{\mathcal{V}} (1 - H_\varepsilon(\psi))\,\mathrm{d}\boldsymbol{x}, \tag{1.28}$$

and S_i is the surface area of the interfaces between the two phases obtained from

$$S_i = \int_{\mathcal{V}} \delta_\varepsilon(\psi)\,\mathrm{d}\boldsymbol{x}, \tag{1.29}$$

where $\mathcal{V}$ is the computational domain.

Step 4: Predictor step for the velocity field. A provisional mid-step velocity $\boldsymbol{u}^*$ is computed from $\boldsymbol{u}^n$ by omitting the pressure gradient term in the momentum conservation equation and by using a mixed Crank-Nicolson/Adams-Bashforth time-stepping scheme:

$$\frac{\boldsymbol{u}^* - \boldsymbol{u}^n}{\Delta t} = -\mathscr{C}^{n+1/2} + \frac{1}{\rho^{n+1/2}}\mathscr{V}^{n+1/2} + \left(1 - \frac{\langle\rho\rangle}{\rho^{n+1/2}}\right)\boldsymbol{g} - \frac{1}{\rho^{n+1/2}}\mathscr{F}^{n+1/2} \tag{1.30}$$

where $\mathscr{C}$, $\mathscr{V}$, and $\mathscr{F}$, are spatial discretizations of the advection, viscous, and surface tension terms respectively. The advection term is extrapolated at $t^{n+1/2}$ using a third-order Adams-Bashforth scheme:

$$\mathscr{C}^{n+1/2} = \frac{23}{12}\mathscr{C}(\boldsymbol{u}^n) - \frac{16}{12}\mathscr{C}(\boldsymbol{u}^{n-1}) + \frac{5}{12}\mathscr{C}(\boldsymbol{u}^{n-2}) \tag{1.31}$$

where $\mathscr{C}$ is the discretization of $\boldsymbol{u}\cdot\boldsymbol{\nabla}\boldsymbol{u}$ based on a finite-difference fifth-order WENO scheme for $\boldsymbol{\nabla}\boldsymbol{u}$ with a second-order interpolation of $\boldsymbol{u}$ when needed. The contribution $\mathscr{V}$ is the discretized version of $\boldsymbol{\nabla}\cdot\mu(\boldsymbol{\nabla}\boldsymbol{u} + \boldsymbol{\nabla}\boldsymbol{u}^T)$, its component in the p-direction expands in

$$\mathscr{V}_p^{n+1/2} = \sum_{q=1}^{3}\Big\{D_q\big[\mu^{n+1/2}(D_q u_p)^{n+1/2}\big] + D_q\big[\mu^{n+1/2}(D_p u_q)^{n+1/2}\big]\Big\} \tag{1.32}$$

where D are discrete spatial derivatives calculated using second-order central-difference and interpolation schemes. The temporal discretization of the p-component of the viscous contribution employs a semi-implicit Crank-Nicolson scheme for the four terms involving the derivatives of u_p, and an explicit third-order Adams-Bashforth scheme for the two terms involving the derivatives of $u_{q\neq p}$. This writes

$$D_q\big[\mu^{n+1/2}(D_q u_p)^{n+1/2}\big] = D_q\left(\frac{\mu^{n+1/2}}{2}D_q u_p^n\right) + D_q\left(\frac{\mu^{n+1/2}}{2}D_q u_p^*\right) \tag{1.33}$$

and

$$D_q\big[\mu^{n+1/2}(D_p u_q)^{n+1/2}\big] = \begin{cases} D_q\left(\dfrac{\mu^{n+1/2}}{2}D_p u_q^n\right) + D_q\left(\dfrac{\mu^{n+1/2}}{2}D_p u_q^*\right) & \text{if } p = q, \\ D_q\left[\mu^{n+1/2}\left(\dfrac{23}{12}D_p u_q^n - \dfrac{16}{12}D_p u_q^{n-1} + \dfrac{5}{12}D_p u_q^{n-2}\right)\right] & \text{if } p \neq q. \end{cases} \tag{1.34}$$

The surface tension term is computed at $t^{n+1/2}$ directly from $\psi^{n+1/2}$, i.e.,

$$\mathscr{F}^{n+1/2} = \mathscr{F}(\psi^{n+1/2}) \tag{1.35}$$

where $\mathscr{F}$ is the space discretization of $\gamma\kappa\boldsymbol{\nabla}H_\varepsilon$: κ is obtained from a second-order centered finite-volume discretization of (1.12), and $\boldsymbol{\nabla}H_\varepsilon$ is computed using a second-order central differencing scheme. Note that the formulation of the singularity as $\boldsymbol{\nabla}H_\varepsilon$ is preferred over the usual form $\delta_\varepsilon(\psi)\boldsymbol{\nabla}\psi$ because it effectively reduces the amplitude of so-called spurious

currents (Meland, Gran, Olsen, & Munkejord, 2007), which are parasitic currents arising from an inconsistent discretization of the surface tension force and the pressure gradient. The resulting linear system is solved iteratively for $\boldsymbol{u}^*$ using a hybrid Jacobi/Gauss-Seidel algorithm with red-black coloring.

Step 5: Density-weighted Poisson equation for the pressure. The pseudo-pressure $\tilde{p}^{n+1/2}$ is obtained from

$$D_q\left(\frac{1}{\rho^{n+1/2}}D_q\tilde{p}^{n+1/2}\right) = \frac{1}{\Delta t}D_q u_q^* \tag{1.36}$$

where D are the second-order central-difference discretizations of the spatial derivatives. This system is solved by an over-relaxed red-black Gauss-Seidel method.

Step 6: Corrector step for the velocity field. The intermediate velocity $\boldsymbol{u}^*$ is corrected by the pressure gradient term to obtain $\boldsymbol{u}^{n+1}$ (Kim & Moin, 1985):

$$\boldsymbol{u}^{n+1} = \boldsymbol{u}^* - \frac{\Delta t}{\rho^{n+1/2}}D\tilde{p}^{n+1/2}. \tag{1.37}$$

The algorithm then proceeds to timestep t^{n+1}.

1.4 Validation and performance tests

The code presented hereinabove can be used for the simulation of any multiphase system consisting of two fluids separated by moving interface. As this thesis is concerned with buoyancy-driven bubbly flows, the validation tests presented here focus on this specific class of two-phase flows.

In these tests, the computational domain is a cube of linear size h with periodic boundary conditions and containing N_b bubbles of identical volume. This periodic configuration is referred to as an "array" of bubbles which fundamental "unit cell" is the computational domain. When the unit cell contains a single bubble ($N_b = 1$), one obtains a cubic lattice of bubbles, and we call this arrangement an "ordered array". When the unit cell contains several bubbles ($N_b > 1$), the bubbles can move relatively to each others. This latter configuration is termed a "free array".

In addition to N_b and to the initial conditions, the evolution of the system depends on

(i) the gas-to-liquid density ratio ρ_d/ρ_c,
(ii) the gas-to-liquid viscosity ratio μ_d/μ_c,
(iii) the gas volume fraction $\phi = (N_b\pi d_b^3)/(6h^3)$,
(iv) the Archimedes (or Galileo) number $Ar = \sqrt{\rho_c|\rho_d - \rho_c|g d_b^3}/\mu_c$ (g is the magnitude of the gravitational acceleration, which is aligned with a primary axis of the array), and
(v) the Bond (or Eötvös) number $Bo = |\rho_d - \rho_c|g d_b^2/\gamma$ (γ is the surface tension),

where we have introduced d_b, the characteristic size of the bubbles defined as the diameter of a sphere with the same volume as that of a bubble.

Five different flow regimes will be considered in the following. The corresponding parameters are listed in table 1.1. The regimes referred to as cases "WD-1" and "WD-8" correspond

case	Bo	Ar	ρ_d/ρ_c	μ_d/μ_c	N_b	ϕ
WD-1	1.8	28.4	0.100	0.100	1	0.1256
WD-8	1.9	29.2	0.050	0.050	8	0.0654
SD-1	219	14.5	0.100	0.100	1	0.0160
E1-1	2.0	29.9	0.001	0.010	1	0.0082
E1-8	2.0	29.9	0.001	0.010	8	0.0082

Table 1.1 Parameters used in the validation simulations: Bond (Bo) and Archimedes (Ar) numbers, gas-to-liquid density (ρ_d/ρ_c) and viscosity (μ_d/μ_c) ratios, number of bubbles in the periodic unit cell (N_b) and gas volume fraction (ϕ). Case code names: WD and SD stand for Weakly Deformed and Strongly Deformed bubbles, respectively, E1 correspond to the code name used in the subsequent chapters for ellipsoidal bubbles, and the digit appended after the dash corresponds to the number of bubbles in the unit cell.

to ordered and free arrays of weakly deformed (ellipsoidal) bubbles. They are identical to those simulated by Esmaeeli and Tryggvason (1999) and will be used for validation purposes. The regime referred to as case "SD-1" corresponds to an ordered array of strongly deformed (skirted) bubbles. It will be used to establish that shifting the level-set function in order to enforce volume conservation does not deteriorate the solution accuracy. In above mentioned cases, the gas-to-liquid density and viscosity ratios are closer to unity than those considered in the rest of this thesis in order to reproduce the conditions considered by prior workers and to allow the completion of the simulations in less than a week on 64 CPU cores (the computational time generally increases with increasing difference between the gas and liquid properties). The effect of the volume conservation fix will also be assessed for cases "E1-1" and "E1-8", which correspond to ordered and free arrays of ellipsoidal bubbles with density and viscosity ratios identical to those used in the subsequent chapters (this flow regime corresponds to that called "E1" in chapter 2 and chapter 3).

For each of these flow regimes, the bubbles were initially spherical and released from rest at time zero. The evolution of the system was monitored through frequent snapshots of the interface position and through time signals of the bubble Reynolds number $Re = \rho_c U d_b/\mu_c$, where U is the vertical component of the bubble drift velocity (the drift velocity is defined as the difference between the volume-averaged velocity of the gas phase minus the volume-averaged velocity of the whole system).

1.4.1 Validation against prior simulations

A standard benchmark test for the simulation of bubbly flows consists in comparing the terminal velocity and shape of an isolated bubble with those obtained experimentally in various regimes. A tempting idea to approach this ideal situation would be to introduce a single bubble in a very large computational domain, so that the influence of periodicity could be neglected.

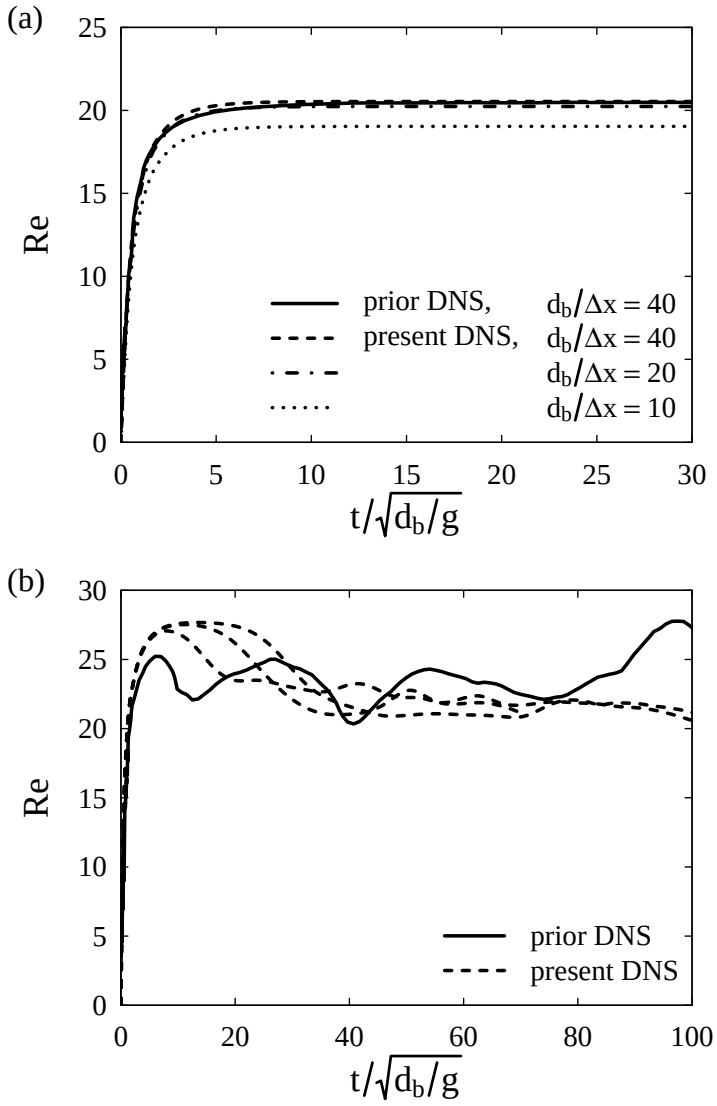

Figure 1.1 Time evolution of the drift velocity (given in the form of a Reynolds number) of arrays of weakly deformed bubbles. Solid line: prior DNS of Esmaeeli and Tryggvason (1999). Non-solid lines: present DNS. (a) Ordered array (case WD-1 in table 1.1), different resolutions (d_b is the bubble volume-equivalent diameter, Δx the grid spacing). (b) Free array (case WD-8 in table 1.1), with three realizations of the flow (before the first coalescence event).

We will see in chapter 2 that even at very low volume fractions (very large domains, in the limit of what is computationally feasible), the bubble rise velocity and shape are still significantly affected by their interactions, making such a comparison to experiments irrelevant. The code has therefore been validated against the numerical simulations of Esmaeeli and Tryggvason (1999), who computed the rise of arrays of nearly spherical bubbles in otherwise quiescent liquid at $O(10)$ Reynolds number using a finite difference/front-tracking method.

Esmaeeli and Tryggvason (1999) simulated the rise of an ordered array of bubbles with parameters corresponding to case WD-1 in table 1.1 (figure 2 of their paper, note that the Archimedes and Bond numbers mentioned therein differ from ours because they use different definitions for these). We repeated their simulation using an identical resolution of 40 grid cells per bubble diameter. As shown in figure 1.1a, both the transient evolution and the steady value of the bubbles drift velocity are accurately reproduced by our code. The effect of grid coarsening is also shown in the same figure. The steady drift velocities obtained with resolutions of 20 and 40 cells by diameter differ from each other by less than 1.5 %, and bubbles shapes are indistinguishable. A resolution of 20 grid cells seems therefore appropriate for this regime (a similar conclusion was drawn by Esmaeeli and Tryggvason (1999)).

We also simulated the rise of a free array by introducing 8 bubbles in the unit cell. The physical parameters are identical to that used by Esmaeeli and Tryggvason (1999) (case WD-8 in table 1.1, which corresponds to figure 5a of their paper), and the initial conditions are similar (the bubbles are placed on the nodes of a slightly perturbed simple cubic array). It must be mentioned that in the front-tracking simulations of Esmaeeli and Tryggvason (1999), bubbles are not allowed to coalesce, whereas with our level-set code, two bubbles automatically merge when the distance between their interfaces becomes smaller than the grid spacing. We repeated this simulation several times with slightly different initial conditions, but found that our bubbles inevitably coalesce sooner or later. The temporal development of the bubbles drift velocity (averaged over the 8 bubbles, before the first coalescence event) is shown in figure 1.1b for three realizations of the flow (dashed lines). Any quantitative comparison would be meaningless here, as the simulations have not been run for long enough, but our present results are in qualitatively agreement with that of Esmaeeli and Tryggvason (1999) (solid line).

Altogether, the behavior of ordered and free arrays of weakly deformed bubbles rising at $O(10)$ Reynolds number is well-reproduced by our code. Further comparison against prior work is included where prior work is available in chapter 2.

1.4.2 Volume conservation enforcement

It is important to stress that in our simulations, volume conservation is enforced at each timestep by (1.27). This trick allows us to run simulations for a virtually infinite amount of time: without it one phase would inescapably disappear. But it also displaces the interface in a somewhat arbitrary manner, thereby deteriorating the accuracy of the numerical solution. The excellent agreement we obtained with the results of Esmaeeli and Tryggvason (1999), who do

resolution	present DNS volume fix enabled		present DNS volume fix disabled		prior DNS (no volume fix)	
$d_b/\Delta x$	Re	$\frac{\max\lvert\Delta\psi\rvert}{\Delta x^{3.2}}$	Re	$\frac{(V_d^{\text{end}}-V_d^0)}{V_d^0}$	Re	$\frac{(V_d^{\text{end}}-V_d^0)}{V_d^0}$
40	20.53	0.11	20.53	0.0012	20.5	0.014
20	20.24	0.10	20.27	0.024	19.9	0.025
10	19.04	0.11	18.81	0.24	N/A	N/A

Table 1.2 Sensitivity analysis of the effects of resolution and volume conservation enforcement for an ordered array of weakly deformed bubbles (case WD-1 in table 1.1), and comparison to the prior DNS of Esmaeeli and Tryggvason (1999). Terminal bubbles drift velocities (given as a Reynolds number), maximum magnitude of the level-set correction, and volume relative variation between $t^0 = 0$ and $t^{\text{end}} = 30\sqrt{d_b/g}$ (d_b is the bubble volume-equivalent diameter, Δx is the grid spacing, V_d is the volume of the disperse phase).

not use such correction, is therefore reassuring in this respect.

Since it would be nonetheless desirable to evaluate the performance of our code without enforcing volume conservation, we disabled this fix and repeated the simulations of ordered arrays of ellipsoidal bubbles presented in figure 1.1a. The results are summarized in table 1.2. At $t^{\text{end}} = 30\sqrt{d_b/g}$, which corresponds to the time after which the bubbles have risen about twenty diameters, the bubbles volume has changed by 2.4 % when a resolution of 20 cells per diameter is used. For comparison, Esmaeeli and Tryggvason (1999) obtained in their simulation, with the same resolution and at a similar time, a volume variation of 2.5 %. Thanks to the improvements brought to the original level-set method, the difference between the numerical and the exact solution after one time iteration is small. As a consequence, the magnitude of the correction $\Delta\psi$ required for the strict conservation of volume is negligible compared to the overall error made in this region (our global numerical scheme is expected to exhibit a first-order spatial convergence in the smoothing region near the interface, while $\max|\Delta\psi| \approx 0.1\Delta x^{3.2}$).

It is not very surprising that our code performs well in this regime, because physical parameters are such that bubbles are weakly deformed (namely, they are oblate ellipsoids). We performed similar sensitivity tests with an ordered array of dimpled/skirted bubbles characterized by a very low surface tension (very high Bond number, case SD-1 in table 1.1). The temporal evolution of the bubbles drift velocities is shown in figure 1.2 for resolutions from 10 to 60 grid cells per bubble diameter, with and without volume conservation enforcement. Note that we do not include comparison to prior work because, to the best of our knowledge, no prior work reports the transient evolution of arrays of strongly deformed bubbles. The

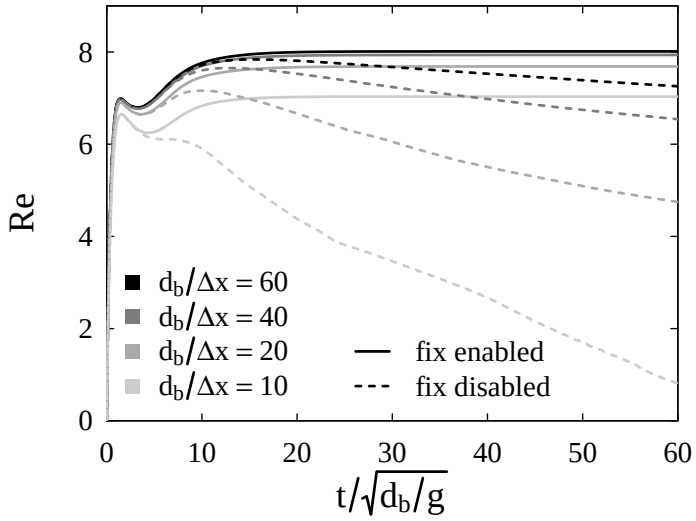

Figure 1.2 Effects of resolution (d_b is the bubble volume-equivalent diameter, Δx is the grid spacing) and of volume conservation enforcement on the rise of an ordered array of strongly deformed bubbles (case SD-1 in table 1.1).

resolution	volume fix enabled			volume fix disabled		
$d_b/\Delta x$	t^{mid}	t^{end}	$\frac{\max\lvert\Delta\psi\rvert}{\Delta x^{2.8}}$	t^{mid}	t^{end}	$\frac{(V_d^{\text{end}}-V_d^0)}{V_d^0}$
60			0.054			−0.21
40			0.049			−0.36
20			0.041			−0.67
10			0.055			−0.98

Table 1.3 Sensitivity analysis of the effects of resolution and of volume conservation enforcement on the shape of strongly deformed bubbles (case SD-1 in table 1.1). Bubble shape (2D cut-off in a symmetry plane) at $t^{\text{mid}} = 10\sqrt{d_b/g}$ and $t^{\text{end}} = 60\sqrt{d_b/g}$, maximum magnitude of the level-set correction, and volume relative variation between t^0 and t^{end} (Δx is the grid spacing, $\Delta\psi$ is the level-set correction, V_d is the disperse phase volume).

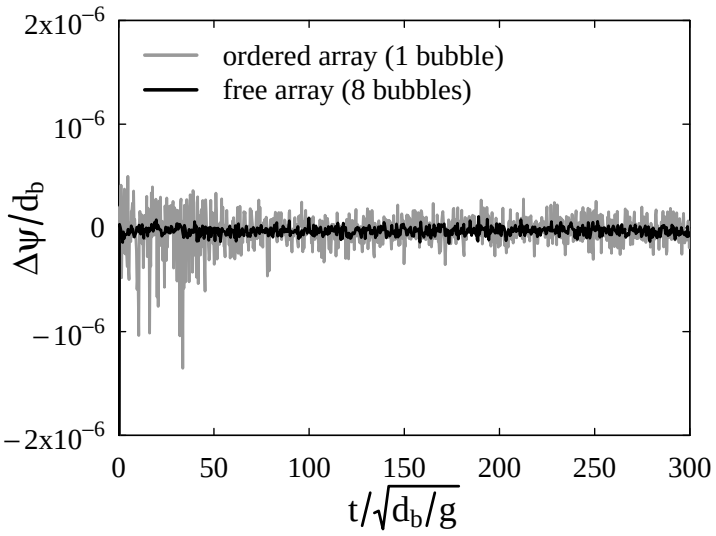

Figure 1.3 Time evolution of the level-set correction $\Delta\psi$, normalized by the bubble volume-equivalent diameter d_b, for free and ordered arrays of ellipsoidal bubbles in identical flow regimes (cases E1-1 and E1-8 in table 1.1).

shapes of the bubbles obtained at $t^{\text{mid}} = 10\sqrt{d_b/g}$ and $t^{\text{end}} = 60\sqrt{d_b/g}$ are reported in table 1.3 together with measurements of the volume variation (when the volume fix is not used) and of the volume correction (when the volume fix is used). When volume conservation is not imposed, the bubbles shrink inexorably, preventing the system to reach a steady-state. The rate of "numerical condensation" decreases as the grid refines: at t^{end}, the bubbles have almost completely disappeared with the coarsest grid (10 cells per bubble diameter), while the bubbles volume has reduced by 21 % with the finest grid (60 cells per diameter). But even with (reasonably) high resolutions, volume conservation remains problematic for long-time simulations. The volume correction we use to fix this issue is satisfactory, since it conserves the volume of the bubbles without affecting their dynamics: at short times (before volume loss becomes large), simulations with and without the volume fix yield the same results. The error made when modifying the location of the interface by an amount $\Delta\psi$ remains much smaller than the expected $O(\Delta x)$ global error in this region due to the finite thickness of the interface ($\max|\Delta\psi| \approx 0.05\Delta x$[2.8]).

Since the level-set correction is a global operation, its use may be legitimately questioned in the case of free arrays of bubbles, as the volume variation may be different for each bubble whereas the level-set correction is redistributed uniformly over the gas-liquid interface. As the interface position is captured implicitly, monitoring the individual bubble volumes is not straightforward. A dedicated bubble tracking algorithm could be implemented in the code, but this would increase the computational cost of the simulations, so the choice was made here not to do so. However, we shall demonstrate that the conclusions drawn for ordered arrays hold for free arrays, at least for the flow regimes considered in this thesis.

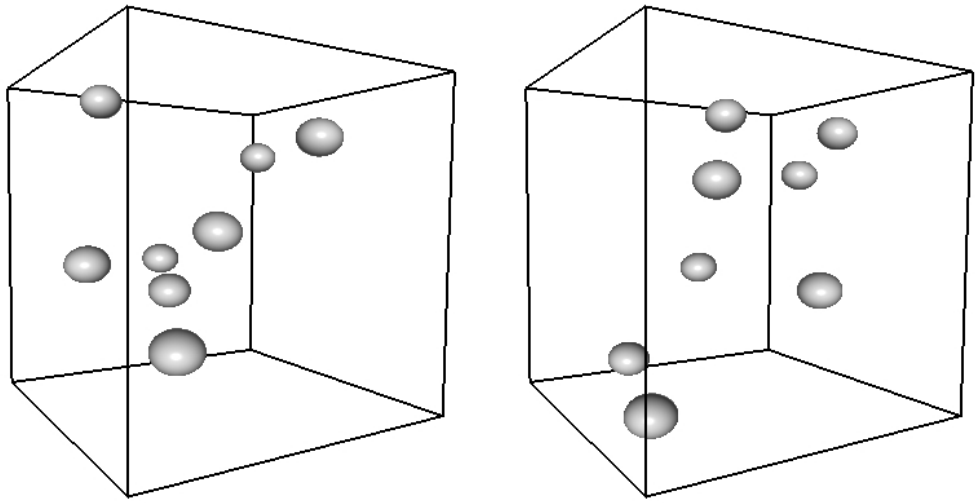

Figure 1.4 Instantaneous snapshots of the bubble shapes for a free array of 8 ellipsoidal bubbles (case E1-8 in table 1.1).

We show in figure 1.3 the time evolution of $\Delta\psi$ for a free array of 8 ellipsoidal bubbles, and compare it with that obtained for an ordered array in otherwise identical flow conditions. These flow conditions are representative of those considered in the subsequent chapters. The magnitude of $\Delta\psi$ is comparable in ordered and free arrays, and remains negligibly small ($|\Delta\psi|/d_b \lesssim 10^{-6}$). In addition, all bubbles exhibit similar shapes in the free array configuration, as illustrated in figure 1.4. It seems therefore reasonable to assume that all bubbles lose or gain identical volumes. We conclude that, for the applications we are interested in, the level-set correction can be safely used when the unit cell contains several free bubbles. We add that although only one simulation of freely moving bubbles has been examined here, the magnitude of the level-set correction has been monitored for all the simulations presented in the subsequent chapters, and found to be negligibly small in all cases, including the simulations with a background turbulent flow.

1.4.3 Code performance

The integration of the pressure equation is generally the most time-consuming part of any simulation of incompressible flows. In two-phase flow simulations, the ease by which the density-weighted Poisson equation (1.36) is solved depends generally on the density jump (Tryggvason et al., 2011). Although various advanced methods (such as multigrid methods) have been developed to solve efficiently the pressure equation for multiphase flows, they often fail to converge for vanishing gas-to-liquid density ratios, as encountered in bubbly flows. For this reason it is common practice to select relatively large density ratios (e.g., Lu and Tryggvason (2013) and Aboulhasanzadeh and Tryggvason (2014) used $\rho_d/\rho_c = 0.1$ in their recent DNS of bubbly flows). In the present simulations, a density ratio representative of most bubbly flows of practical interest is used ($\rho_d/\rho_c = 0.001$), and the pressure equation is solved by a

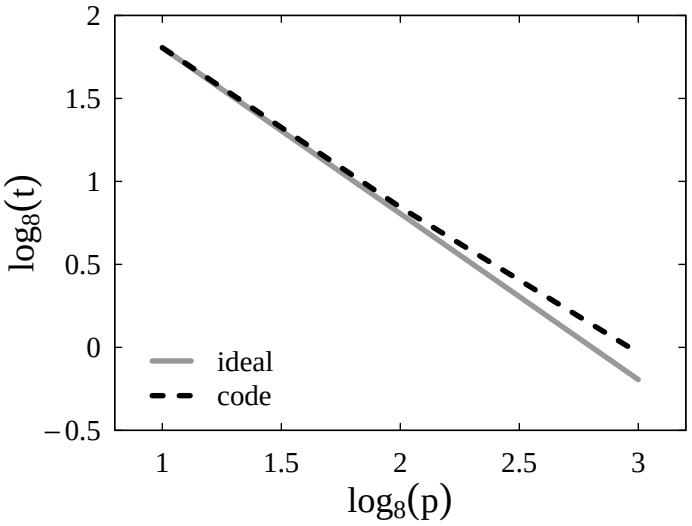

Figure 1.5 Code strong scalability: time elapsed vs. number of CPU cores for a problem of fixed size. Ideally, $t(p) = t(1)/p$.

Gauss-Seidel method with a low enough overrelaxation parameter. Convergence is therefore ensured, although it can be very slow (between $O(100)$ and $O(1000)$ iterations are typically needed).

As the time required to simulate a three-dimensional bubbly flow on a single CPU core would be exceedingly high, the code is parallelized with MPI: the computational domain can be decomposed, in the three space directions, into parallelepipoids of any aspect ratio, each processed on a single CPU core. As the objective is to minimize the time-to-solution, the code scalability is evaluated by fixing the problem size and increasing the number of cores ("strong scalability"). Ideal strong scalability is achieved if the computing time with a single core is divided by p when p cores are used in parallel. In practice, speedup is limited by synchronization barriers, interprocessor communications, and sequential I/O operations. The performance of our code has been assessed by solving a typical two-phase flow problem on 256^3 grid points with 2^3, 4^3, and 8^3 cores. The results, shown in figure 1.5, indicate that the code scalability is excellent (at least up to 512 cores).

1.5 Conclusions

The development of a parallelized DNS code for the resolution of the three-dimensional incompressible Navier-Stokes equations in a fluid-fluid system has been continued during this thesis. The numerical approach is based on a projection method to integrate the Navier-Stokes equations and on a level-set method to capture the interface.

At the beginning of this thesis, a major issue with the code was the violation of the mass conservation principle. This issue arises from the discretization of the level-set equation and

from the alteration of the zero contour of the level-set function during the reinitialization procedure. To date, no perfect solution to this problem exists, though improvements of the original level-set method and of the reinitialization algorithm are continuously proposed (e.g., McCaslin and Desjardins (2014), Luo, Shao, Yang, and Fan (2015)). The strategy we adopted for minimizing this problem consists in (i) using the high-order schemes recommended by Salih and Ghosh Moulic (2009) for the integration of the level-set equation; (ii) reducing the number of iterative steps needed in the reinitialization procedure by embedding a source term in the level-set equation as proposed by Sabelnikov et al. (2014); (iii) using the improved reinitialization algorithm of Russo and Smereka (2000).

With these modifications of the original method, the mass of each phase varies only by a negligible amount between successive time steps. These fluctuations are, however, not strictly zero, which may be problematic especially when simulations need to be run over very long times. For this reason, we also use the correction proposed by Sussman and Uto (1998), which consists in slightly shifting the level-set function such that strict mass conservation is enforced at each time step. This simple trick was shown not to deteriorate the solution accuracy in the present context of weakly to strongly deformed bubbles rising at moderate Reynolds number, and allows simulations to be carried out over virtually infinitely long times.

Chapter 2

Dynamics of laminar bubbly flows

Buoyancy-driven bubbly suspensions revisited

Contents

2.1 Introduction

This chapter is concerned with the dynamics of statistically homogeneous flows of monodisperse bubbles in the absence of external agitation. When this system is buoyancy-driven, one of the key interests lies in the prediction of the average bubble rise velocity, as it would be needed to estimate, for example, the average residence time in a bubble column.

The average bubble rise velocity relative to the average velocity of the entire suspension is termed herein the drift velocity and the magnitude of the drift velocity is denoted by U. In the dilute limit (wherein the bubble volume fraction is vanishingly small), if no clustering occurs, bubbles behave as if they were isolated, and the drift velocity approaches the terminal velocity U_0 of a single bubble in unbounded liquid under otherwise the same conditions, for which a number of correlations is available (Clift, Grace, & Weber, 1978; Loth, 2008). As volume fraction increases, U generally departs from U_0. This phenomenon can be represented by a correction function $G(\phi) = U/U_0$, where ϕ is the gas volume fraction; the dependencies of G on various other dimensionless groups (termed herein as 'flow conditions') are suppressed in the notation for G for brevity, but are not ignored.

A common form of the dependency on volume fraction used in empirical correlations is the Richardson-Zaki relation $G(\phi) = (1-\phi)^n$ (Richardson & Zaki, 1954; Ishii & Zuber, 1979), where n is an empirical parameter that depends on flow conditions. This expression provides a fairly satisfactory fitting for suspension of particles, bubbles and drops in a variety of flow regimes. However its physical interpretation is not clear, and deviations from this law are frequently reported. Various experiments have been carried out previously to determine $G(\phi)$ by injecting air or nitrogen bubbles of millimetric size in a vertical column filled with clean water. In their respective experiments, Zenit et al. (2001) found that their measurements could be approximately described by the Richardson-Zaki formula with exponent $n = 2.8$, Garnier et al. (2002) obtained instead $G(\phi) = 1 - \phi^{1/3}$, and Colombet et al. (2015) fitted their data by $G(\phi) = (0.28 + 0.72\exp(-15\phi))^{1/2}$. Typical experimental complexities may have arisen that could explain these differences. For example, it is challenging to purify water of surfactants, to rule out wall effects, and to obtain a truly monodisperse suspension. But a main inconvenience is that usually the bubble diameter cannot be kept constant if the volume fraction is changed. The terminal velocity, shape, and trajectory of a single air bubble in pure water strongly depends on its size (see, e.g., figure 7.3 and table 7.1 in Clift et al. (1978)). This renders difficult disentangling the dependency of drift velocity on hydrodynamic interactions - along with the microstructure - from that on bubble size, if the latter is varied simultaneously with volume fraction.

Theoretical predictions of the drift velocity of bubbles are available for asymptotic and ideal systems. The drift (or rather, sedimentation) velocity derived by Batchelor (1972) for rigid particles in Stokes flow, wherein a uniformly random sedimenting suspension of particles is considered, has been generalized to droplets and bubbles, yielding $G(\phi) = 1 - 4.44\phi + O(\phi^2)$

for bubbles whose viscosity can be ignored compared to that of the liquid (Keh & Tseng, 1992). The drift velocity strongly depends already on the microstructure in the dilute limit, though. If the probability of finding a particulate near a test particulate is uniform outside the excluded volume, as is assumed in the work cited above, interactions with nearby particulates result in $G(\phi) = 1 - O(\phi)$, whereas for a microstructure wherein a dominant contribution comes from particulates at a distance that corresponds to the mean separation $(V_p/\phi)^{1/3}$, with V_p the particulate volume, one expects $G(\phi) = 1 - O(\phi^{1/3})$ (e.g., Davis and Acrivos (1985)). A well-known example of the latter is a microstructure wherein particulates are arranged in a regular, ordered array. For bubbles arranged in an ordered array, $G(\phi) = 1 - b\phi^{1/3} + O(\phi^2)$, where the coefficient b is known for several cubic arrays, and the $O(\phi)$ term cancels if the gas viscosity is ignored compared to the liquid viscosity (Sangani & Acrivos, 1983a; Sangani, 1987). The microstructure is not known a priori, therefore these limiting cases of random and ordered arrays may provide the means to determine the possible magnitude of the effects of order of the microstructure.

Besides Stokes flows, a weakly-viscous theory based on potential-flow interactions has also been developed by Spelt and Sangani (1998). Exceptionally, the probability density function for a configuration of identical spherical bubbles is known in that case. The averaged drag coefficient could therefore be determined analytically in the dilute limit whilst accounting for the microstructure. In the present notation, this yielded $G(\phi) = 1 - \left(\frac{17}{8} + \frac{9}{20}A\right)\phi + O(\phi^2)$, where A is the ratio of U^2 and the root-mean-square bubble velocity. The dependency on A enters there because it affects the pair-probability density function in that analysis, this being nearly isotropic at low A whilst showing a preference for bubbles rising nearly side by side at large A.

Beyond these theoretical approaches, direct numerical simulations (DNS) of unbounded buoyancy-driven flows, in the sense of resolving the full Navier-Stokes equations coupled with the bubble dynamics and deformation, have been performed in prior work for cubic domains that contain a finite number of freely-moving bubbles, subject to periodic boundary conditions. It is generally hoped that as the number of bubbles in the cell becomes large, the statistically steady state reached by this system provides a faithful picture of real homogeneous bubbly flows, although convergence with the number of bubbles has to be verified. In the other extreme, the special case of one freely-rising bubble in the unit cell, one recovers a simple cubic lattice of bubbles. We refer to this setup with more than one bubble in the unit cell as a "free array", and to that with one bubble in the cell as an "ordered array".

For spherical bubbles rising at $O(1)$ ("low") Reynolds numbers, the DNS results of Esmaeeli and Tryggvason (1998), suggest that $G(\phi)$ for free arrays may be similar to that predicted for ordered arrays, but the system studied was concluded to be too small to draw definitive conclusions. Bunner and Tryggvason (2003) found that their results at $O(10)$ ("moderate") Reynolds numbers could be represented by $G(\phi) = 1 - \phi^{1/3}$ for spherical bubbles in free arrays, and a Richardson-Zaki expression with exponent $n = 3$ for deformable bubbles, but that no

theoretical justification for these scalings could be offered, beyond an observed difference in preferential spatial configurations of bubbles, discussed further below. Also, the expressions for $G(\phi)$ inferred in these pioneering studies could only be fitted from just a few different values of the volume fraction comprised between 2 and 12 %, their validity outside this range seems unclear. Further results for free arrays at moderate Reynolds numbers were obtained by Yin and Koch (2008), for volume fractions ranging from 1 to 25 %, using a lattice-Boltzmann method. They used $O(100)$ bubbles in a periodic cell, rather than $O(10)$ in most of the early studies cited above, and imposed a spherical shape, facilitated by a force balance that includes the surface integral of the traction acting on the bubble and the buoyancy force. Their results demonstrate that $G(\phi)$ is not well fitted by the Richardson-Zaki formula, and they suggest that this is associated with the anisotropic microstructure of bubbly suspensions in this regime. Gillissen, Sundaresan, and van den Akker (2011) conducted similar simulations using a combination of lattice-Boltzmann and immersed boundary methods, and obtained $G(\phi) = 1 - O(\phi^{1/3})$ for spherical bubbles rising at small to moderate Reynolds number, in qualitative agreement with earlier studies (Esmaeeli & Tryggvason, 1998; Bunner & Tryggvason, 2003).

From these prior studies, the microstructure, along with the drift velocity, is known to vary significantly with bubble Reynolds number and shape. For spherical bubbles rising at $O(100)$ ("high") Reynolds number, strong preference for horizontal alignment is observed in the simulated pair probability (Esmaeeli & Tryggvason, 2005), in agreement with the trends reviewed above for the idealized potential-flow interactions. The anisotropy in microstructure is larger than that observed in the experiments of Zenit et al. (2001), possibly because of bubble deformation: indeed the simulations of Esmaeeli and Tryggvason (2005) revealed that oblate ellipsoidal bubbles do not form horizontal rafts but instead are rather uniformly distributed. At $O(10)$ Reynolds number, the dynamics of bubble-bubble interactions is dominated by wake effects. A vertical pair of spherical bubbles changes its orientation to horizontal through a drafting-kissing-tumbling mechanism, resulting in preferential side by side alignment (Esmaeeli & Tryggvason, 1999; Bunner & Tryggvason, 2002a; Yin & Koch, 2008), whereas deformable bubbles tend to organize in vertical structures owing to the reversed lift force which attracts a bubble in the wake of its preceding neighbor (Bunner & Tryggvason, 2003). These effects decrease with decreasing Reynolds number, and nearly no preference is observed at $O(1)$ Reynolds number (Esmaeeli & Tryggvason, 1998; Cartellier & Rivière, 2001).

In the DNS studies cited thus far, the microstructure is allowed to develop naturally. For use of the results in general flows, wherein microstructure can be affected by weak gradients, it is necessary to know the role of and sensitivity to the microstructure. DNS results for rising deformable bubbles in an ordered arrangement have been conducted by Sankaranarayanan, Shan, Kevrekidis, and Sundaresan (2002), using a lattice-Boltzmann method, for a vast variety of flow regimes. While the rise velocity of spherical bubbles was found to decrease with volume fraction, highly distorted bubbles were observed to rise faster as the volume fraction increases. An empirical correlation of Richardson-Zaki form was used to represent these results, n being

positive for spherical bubbles, and negative for strongly deformed ones. One may however express some reservations regarding its general validity: (i) although they did not provide this information, it seems that most of their simulations were carried out at high volume fractions, typically between 5 and 25 %, so extrapolating outside of this range may not be appropriate; and (ii) the correlation does not reduce to the analytical result discussed above for creeping flows of ordered arrays.

Despite their apparent artificiality, ordered arrays of bubbles, as well as their relevance to real bubbly flows, certainly deserve further investigation. Firstly, a number of prior simulations and experiments reviewed above for $1 \lesssim Re \lesssim 1000$ found a bubble rise velocity scaling as $\phi^{1/3}$ (Esmaeeli & Tryggvason, 1998; Bunner & Tryggvason, 2003; Gillissen et al., 2011; Garnier et al., 2002). This scaling is the same as that obtained assuming a periodic arrangement of the bubbles, albeit under the Stokes flow approximation (Sangani & Acrivos, 1983a). The study of ordered arrays beyond the Stokes-flow limit is therefore of fundamental interest in order to connect theoretical, numerical, and experimental work. Secondly, prior experimental and numerical work on bubbly flows at moderate to high Reynolds number has shown that the magnitude of the bubble velocity fluctuations is substantially smaller than the bubble rise velocity (Bunner & Tryggvason, 2002b; Esmaeeli & Tryggvason, 2005; Zenit et al., 2001; Martinez-Mercado et al., 2007), at least when the gas volume fraction remains below approximately 10 %. This further motivates a study of a representation of bubbly suspensions by ordered arrays (zero bubble velocity fluctuations). Thirdly, only experimental investigations can assess the relevance (or lack thereof) of the ordered model to describe real bubbly suspensions. By re-examining prior experimental data (Garnier et al., 2002; Martinez-Mercado et al., 2007; Riboux et al., 2010; Colombet et al., 2015), we will show that available measurements support the idea that ordered arrays are indeed relevant to bubbly flows of practical interest.

In this chapter, we investigate the ordered and free rise of bubbles at low and moderate Reynolds numbers over a wide range of volume fractions, using DNS and analysis. The first objective is to determine the connection between the DNS results and theory for dilute ordered systems and, beyond the dilute limit, the connection between the DNS results and prior work on bubble pairs (e.g., Legendre et al. (2003), Hallez and Legendre (2011)). The second objective is to revisit arrays of free bubbles in light of our findings for ordered arrays, and to contrast and compare these two systems.

2.2 Methodology

2.2.1 Problem statement

We consider an infinite, homogeneous, monodisperse suspension of bubbles rising under the effect of buoyancy in otherwise quiescent liquid. The density and viscosity of each fluid, as well as the surface tension, are assumed to be constant. The suspension is represented by the periodic repetition of a cubic unit cell containing a given number of bubbles. The gravity

is aligned with a primary axis of the periodic array (due to the large number of parameters already involved in the problem, the influence of the orientation of gravity is not investigated here).

The behavior of this system depends on nine parameters: the number of bubbles N_b in the cell, the gas volume fraction ϕ, the gravitational acceleration g, the bubble volume or, more conveniently, its characteristic size d_b defined as the diameter of the volume-equivalent sphere, and the physical properties of the two fluids, namely their densities (ρ_d, ρ_c), their viscosities (μ_d, μ_c), and the surface tension (γ). The subscripts d and c refer to the disperse (gaseous) and continuous (liquid) phases, respectively.

In addition to the gas volume fraction and to the number of bubbles, four independent dimensionless groups can be constructed from the remaining parameters. Two of these are the ratios of the gas density and viscosity to those of the surrounding liquid. These are usually very small and of the same order for most gas-liquid systems of practical interest. As a consequence their influence will not be investigated, and unless otherwise mentioned, these parameters will be set to $\rho_d/\rho_c = 10^{-3}$ and $\mu_d/\mu_c = 10^{-2}$, which roughly corresponds to air bubbles in water. The last two dimensionless numbers are the Archimedes number

$$Ar = \frac{\sqrt{\rho_c|\rho_d - \rho_c|g d_b^3}}{\mu_c}, \tag{2.1}$$

or equivalently the Galilei number $Ga = Ar^2$, and the Bond number (also known as the Eötvös number),

$$Bo = \frac{|\rho_d - \rho_c|g d_b^2}{\gamma}. \tag{2.2}$$

The Archimedes and Bond numbers can be defined a priori, without the knowledge of the bubble velocity, and are therefore traditionally employed to describe the macroscopic conditions of buoyancy-driven bubbly flow (numerical) experiments.

At time zero, the bubbles are released from rest and start rising. The time evolution of the system is monitored through $\boldsymbol{U}(t)$, defined as the average drift velocity of the bubbles and computed at any time from

$$\boldsymbol{U} = \langle \boldsymbol{u} \rangle_d - \langle \boldsymbol{u} \rangle, \tag{2.3}$$

where $\langle\,\rangle$ denotes a volume average over the entire unit cell and $\langle\,\rangle_d$ denotes a volume average over the disperse phase only. In most situations $\boldsymbol{U}$ is parallel to gravity, so there is no need to distinguish between $|\boldsymbol{U}|$ and the vertical component of $\boldsymbol{U}$. For simplicity, and unless mentioned otherwise, U is used to denote the (positive) vertical component of $\boldsymbol{U}$. The drift velocity is used as the characteristic velocity scale to define the dynamic counterparts of the Archimedes and Bond numbers: the Reynolds number

$$Re = \frac{\rho_c U d_b}{\mu_c} \tag{2.4}$$

and the Weber number

$$We = \frac{\rho_c U^2 d_b}{\gamma} = \frac{BoRe^2}{Ar^2}, \tag{2.5}$$

which compare the effects of inertia, viscosity and surface tension. In a system at equilibrium for vertical rise, the hydrodynamic force acting on a bubble, whose magnitude is denoted f, equals the buoyancy force. It follows that the Reynolds number is related to the Archimedes number through

$$C_D = \frac{4}{3}\frac{Ar^2}{Re^2} \qquad \text{with } C_D = \frac{8f}{\pi d_b^2 \rho_c U^2}, \tag{2.6}$$

where C_D is the drag coefficient.

Assuming that a (possibly quasi-)steady state is reached independently of the initial conditions (which is not necessarily the case, but we will come to that later), the (quasi-)steady average bubble drift velocity can be written as $U = U(N_b, \phi, Ar, Bo)$. Similarly the (quasi-)steady average bubble shape, as described by a parameter χ (which will be specified later, typically an aspect ratio), reads $\chi = \chi(N_b, \phi, Ar, Bo)$. Our first goal is to characterize $U(\phi, Ar, Bo)$ and $\chi(\phi, Ar, Bo)$ when the bubbles have a fixed position relative to their neighbors ($N_b = 1$), and to understand how the imposed flow conditions (*Ar*,*Bo*) affect the dependency of these quantities on the volume fraction. Our second goal is to assess the effect of introducing additional degrees of freedom ($N_b > 1$) in the system, and to compare the behavior of freely evolving suspensions (sufficiently large N_b) with that of ordered suspensions ($N_b = 1$).

2.2.2 Flow regimes

Since we want to assess the effect of volume fraction under various conditions of Bond and Archimedes numbers, it seems natural to refer to the limiting case of a single bubble released in an unbounded quiescent liquid under the same conditions. At steady-state, this bubble is characterized by its shape (and an associated aspect ratio χ_0), and its terminal velocity U_0, usually expressed in the form of a terminal Reynolds number $Re_0 = \rho_c U_0 d_b / \mu_c$. The subscript 0 will be used hereafter when an isolated bubble is considered.

A rather general description of the equilibrium state reached by a buoyancy-driven bubble is given in the shape regime diagram of Grace (1973). This diagram splits the (Bo, Re_0) parameter space in a number of subregions and maps them onto the corresponding shape regimes. It also provides a graphical correlation between the Bond number, the Reynolds number, and the Morton number $Mo = (|\rho_d - \rho_c| g \mu_c^4)/(\rho_c^2 \gamma^3) = Bo^3/Ar^4$, which is often used in experimental work in place of the Archimedes number. In a simplistic manner, the terminal Reynolds number increases (non-linearly) with the Archimedes number, while the bubble departs from a spherical shape as the Bond number increases.

We considered nine different cases defined by the pair (*Ar*,*Bo*). A complete description of these cases and of the corresponding flow regimes is provided in table 2.1. They cover Reynolds numbers ranging from 0 to 60 and several shape regimes: spherical (cases “S”), ellipsoidal (cases “E”), and dimpled ellipsoidal-cap (case “C”). The parameters for case C correspond to a single-bubble experiment of Bhaga and Weber (1981), which was later reproduced numerically by Hua, Stene, and Lin (2008). The terminal Reynolds number and shape of the equivalent

case	Bo	Ar	Mo	shape	Re_0	We_0	χ_0
S0	0.38	0.15	1.00×10^{2}	spherical	0.00194	6.11×10^{-5}	1.000
S1	0.38	5.03	8.60×10^{-5}	spherical	1.80	4.88×10^{-2}	1.007
S2	0.38	10.0	5.49×10^{-6}	spherical	5.94	0.134	1.015
S3	0.38	15.3	1.00×10^{-6}	spherical	12.1	0.236	1.024
S4	0.38	27.2	1.00×10^{-7}	spherical	31.4	0.507	1.064
S5	0.38	40.7	2.00×10^{-8}	spherical	62.5	0.897	1.124
E1	2.0	29.9	1.00×10^{-5}	ellipsoidal	31	2.1	1.32
E2	5.0	30.0	1.54×10^{-4}	ellipsoidal	26	3.8	1.62
C	243	15.2	2.66×10^{2}	dimpled/skirted	7.77	63.2	1.89

Table 2.1 Simulated regimes: Bo, Ar, and $Mo = Bo^3/Ar^4$ are input parameters (with $\rho_d/\rho_c = 10^{-3}$ and $\mu_d/\mu_c = 10^{-2}$). The shapes, Re_0, $We_0 = Bo\,Re_0^2/Ar^2$, and χ_0 of an isolated buoyancy-driven bubble at steady-state are also given. Shapes are predicted by the diagram of Grace (1973). The values of Re_0 are estimated from the correlation of Mei, Klausner, and Lawrence (1994) for spherical bubbles (cases S0 to S5) and from the correlation of Loth (2008) for ellipsoidal bubbles (cases E1 and E2); the experimental value measured by Bhaga and Weber (1981) is reported for case C. The aspect ratio χ_0 is estimated from the correlation of Loth (2008) for all cases except case C, for which it is directly measured from visualizations of Hua, Stene, and Lin (2008).

isolated bubble have therefore been determined directly from their data. For the other cases, the single-bubble terminal Reynolds number and aspect ratio have been estimated using the correlations for spherical and ellipsoidal bubbles recommended in the review of Loth (2008).

2.2.3 Numerical methods

In both phases the fluid motion is governed by the incompressible Navier-Stokes equations which are coupled through fluid-fluid boundary conditions at the interface. This set of equations is provided in section 1.2.1. It is solved numerically within a periodic unit cell. A comprehensive description of our numerical strategy for the simulation of bubbly suspensions is provided in section 1.3. A brief overview of its salient features is recalled hereinafter.

Our approach relies on the one-fluid formulation of the governing equations. In this formulation, the different fluids are treated as a single phase with discontinuous density and viscosity, and surface tension is incorporated as a singular source term. This results in the standard continuum surface force model of Brackbill et al. (1992). To circumvent numerical difficulties due to the introduction of discontinuous and singular functions, the interface is given a finite thickness proportional to the grid spacing. Surface tension is therefore treated as a volume force distributed over several mesh points, and material properties vary continuously from one phase to the other.

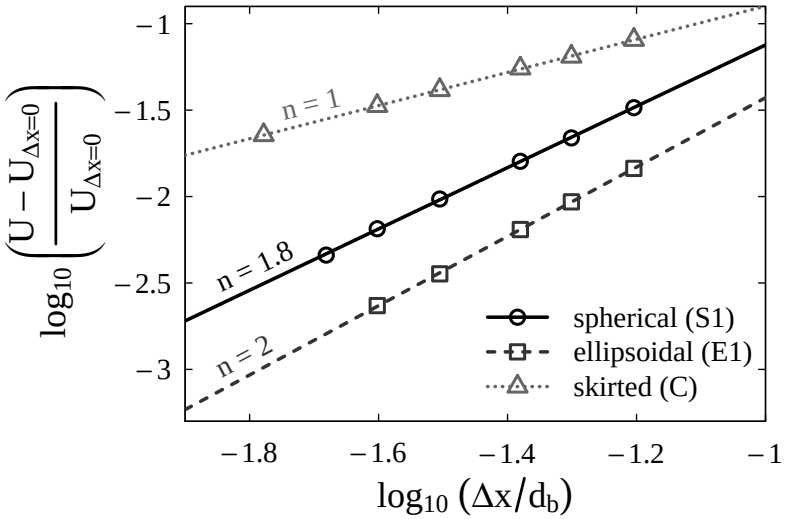

Figure 2.1 Spatial convergence for cases S1, E1, and C: relative error in the steady bubble drift velocity U as a function of the grid spacing Δx (d_b is the bubble volume-equivalent diameter; $U_{\Delta x=0}$ is extrapolated assuming $U = U_{\Delta x=0} - k\Delta x^n$, where k and n are case-specific positive constants fitted from numerical data).

The incompressible Navier-Stokes equations are integrated in their one-fluid form by a projection method (Chorin, 1968) and the moving interface separating the two fluids is captured by a level-set method (Osher & Sethian, 1988; Sussman et al., 1994). The zero-order approximation of the additional source term proposed by Sabelnikov et al. (2014) is embedded in the level-set equation, and the level-set function is reinitialized as a signed distance function at each time step using the procedure devised by Russo and Smereka (2000). In addition, strict volume conservation is enforced using the correction proposed by Sussman and Uto (1998).

Our time integration algorithm is based on third-order and second-order TVD Runge-Kutta schemes for the level-set advection and reinitialization equations, respectively, and on a mixed Crank-Nicolson/third-order Adams Bashforth scheme for the Navier-Stokes equations. For spatial derivatives, we employ a standard finite difference/finite volume discretization on a uniform Cartesian staggered grid: fifth-order WENO schemes are used for advection terms, and second-order centered schemes are used otherwise.

Grid convergence tests have been carried out systematically for all the cases reported in table 2.1, and for a single volume fraction. For each case, simulations of ordered arrays of rising bubbles have been performed for $d_b/\Delta x = \{16, 20, 24, 32, 40\}$. Higher resolutions have been considered when needed. The bubble shapes were found to be weakly affected by the spatial resolution, except for case C (skirted bubbles). The bubble drift velocities were found to decrease as Δx^n, where $n = 1.0$ for case C, $n = 1.8$ for cases S0 and S1, and $2 \leqslant n \leqslant 3$ for the other cases. Examples of convergence tests are provided in figure 2.1 for cases S1, E1, and C. A resolution of 20 grid cells per bubble diameter was concluded to be sufficient for all regimes

except for case S5, which requires a resolution of 30 grid cells per diameter because of the higher Reynolds numbers associated with this regime, and for case C, for which a resolution of 60 grid cells per diameter is needed for capturing the thin skirts of the bubbles.

In practice, resolutions of 40 and 20 nodes per diameter were used for ordered and free arrays, respectively, except for case C for which a resolution of 60 nodes per diameter was used in both configurations. With these resolutions, the error in the steady drift velocity due to the grid spacing in the ordered configuration is not larger than 2 % in case C and 1 % in the other cases. The choice of the time step is constrained by the condition of numerical stability, and the error due to time discretization is smaller than that due to spatial discretization.

2.3 Ordered arrays

We examine in this section the dynamics of cubic arrays of deformable bubbles ("ordered arrays") in the presence of liquid inertia. The main objective here is to connect DNS results, theoretical analysis for dilute systems, and prior work on bubble pairs.

Specifically, the effect of volume fraction on the rise velocity and shape of bubbles arranged in a simple cubic array is revisited here. Direct numerical simulations have been performed for the nine sets of flow conditions summarized in table 2.1. For each of these cases, the volume fraction $\phi = \pi/6(d_b/h)^3$ (where h is the linear size of the unit cell of the array) was varied from 0.1 to 30 % by changing the size of the computational domain (i.e., the lattice spacing) while keeping the bubble size constant.

Initially, the two fluids were at rest and separated by a spherical interface. A time zero, gravity was switched on. After a transient regime, various types of bubble motion could be observed: steady vertical rise, steady oblique rise, or unsteady oblique rise. The steady vertical rise is first examined in section 2.3.1. Other types of motions are then discussed in section 2.3.2.

Simulations were run until the bubble drift velocity became either constant or statistically stationary. This steady state is independent of the initial oblateness of the bubbles, and is reached when the velocity disturbances induced by bubbles' motion have diffused in all directions throughout the liquid, i.e., in a time of order $O(h^2\rho_c/\mu_c)$. As a consequence, from a numerical point of view, the investigation of small volume fractions (large domain sizes) is limited both by the needed number of grid points ($\sim h^3$) and by the computation time ($\sim h^2$).

2.3.1 Steady vertical rise of bubbles

The cubic lattice of bubbles is not only convenient from a computational point of view, it is also attractive from a theoretical standpoint since the solution only needs to be determined in a unit cell. When the bubbles rise steadily along straight paths parallel to an axis of the periodic array (as is the case in most of the cases presented here, since gravity is oriented along a lattice axis), the symmetries of the problem greatly simplify the analysis. In this context, we will first determine an analytical expression accounting for the first effect of inertial interactions in cubic

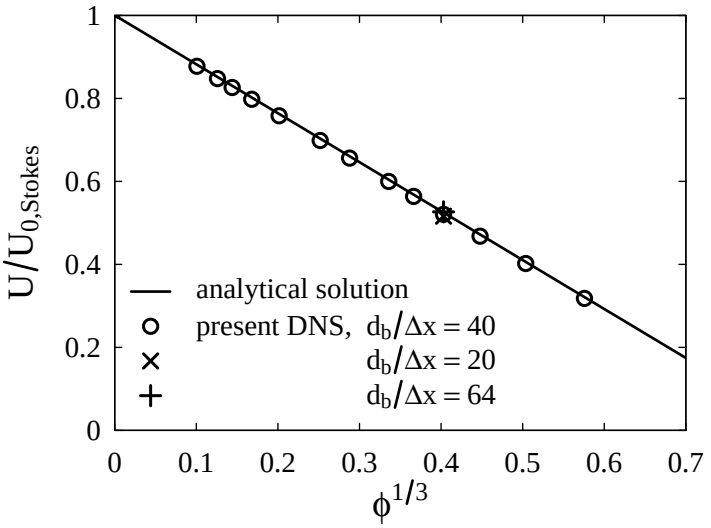

Figure 2.2 Steady drift velocity of an ordered array of spherical bubbles in the Stokes flow regime (case S0), normalized by that of an isolated bubble, as a function of volume fraction. ○: DNS; ——: analytical solution (Sangani, 1987). The crosses at $\phi^{1/3} = 0.4$ show the effect of resolution, with Δx the grid spacing and d_b the bubble diameter.

arrays of spherical bubbles (at small Reynolds numbers). Outside this narrow range of validity, the influence of the volume fraction on the steady rise velocity and shape of deformable bubbles will then be determined from our numerical simulations.

2.3.1.1 Spherical bubbles at low to moderate Reynolds number

The correction to the drift velocity due to finite volume fraction in the Stokes-flow regime has been determined by Sangani (1987) for cubic arrays of spherical fluid particles (bubbles or drops). The first term arises from a point-force approximation of the particles and reads, for a simple cubic array,

$$\frac{U}{U_{0,\text{Stokes}}} - 1 = -1.1734\mu^* \phi^{1/3} + O(\phi), \tag{2.7}$$

where $U_{0,\text{Stokes}}$ is the terminal velocity of a spherical fluid particle translating through an unbounded ambient fluid in Stokes-flow conditions (Hadamard, 1911; Rybczynski, 1911):

$$U_{0,\text{Stokes}} = \frac{1}{12}\frac{|\rho_c - \rho_d| g d_b^2}{\mu^* \mu_c}, \qquad \text{with } \mu^* = \frac{\mu_c + 3/2\mu_d}{\mu_c + \mu_d}. \tag{2.8}$$

The case of a rigid sphere ($\mu_d/\mu_c \to \infty$) is recovered as $\mu^* \to 3/2$, whereas the case of a clean bubble ($\mu_d/\mu_c \to 0$) corresponds to the limit $\mu^* \to 1$. Numerical simulations have been carried out for spherical bubbles rising at very small Reynolds numbers (case S0, $Re_0 = 1.94 \times 10^{-3}$), and excellent agreement with (2.7) has been obtained over a wide range of volume fractions, as shown in figure 2.2: the relative difference between the numerical and the analytical solutions

is less than 2 % and diminishes as volume fraction decreases (the effect of resolution is also shown on the same figure). Note that the relation between U and $\phi^{1/3}$ seems linear even at high volume fraction: indeed even though the analytical solution of Sangani (1987) includes $O(\phi)$ and $O(\phi^2)$ terms, for clean bubbles the $O(\phi)$ correction is zero and the $O(\phi^2)$ correction is negligible compared to the $O(\phi^{1/3})$ term (whereas these corrections are substantial for solid particles).

For small but non-zero Reynolds numbers, the Stokes equations are still valid near and inside the fluid particles, but should be replaced by the Oseen equations farther away, since inertial effects become comparable to viscous ones at distances from the particle of order $O(d_b/Re)$. The first correction to the drag force arising from inertial effects has been determined by Hill, Koch, and Ladd (2001) for a cubic array of solid spheres. The extension of their result to bubbles and drops is provided in appendix A. We show there that the correction to the bubble drift velocity due to liquid inertia and hydrodynamic interactions can be approximated at any $\phi \ll 1$ by

$$\frac{U}{U_{0,\text{Stokes}}} - 1 \approx -\frac{1}{8}\mu^* Re - 1.1734\mu^* \phi^{1/3} + \frac{25}{8}\mu^* \frac{Re\phi^{1/3}}{Re + 25\phi^{1/3}}. \tag{2.9}$$

The first term accounts for the effect of liquid inertia on an isolated bubble, the second term results from Stokes interactions, and the last term captures the effect of inertial interactions. The significance of each of these terms as a function of volume fraction can be understood as follows.

At zero volume fraction, the drag exerted on a single bubble normalized by the Stokes drag increases linearly with the Reynolds number (Brenner & Cox, 1963). This results in the negative correction to the drift velocity

$$\frac{U_0}{U_{0,\text{Stokes}}} - 1 = -\frac{1}{8}\mu^* Re, \tag{2.10}$$

where U_0 is the terminal velocity of the isolated bubble. At small volume fraction, inertial interactions result in a positive $O(\phi^{1/3})$ correction which overwhelms the negative $O(\phi^{1/3})$ Stokes-flow correction

$$\frac{U - U_0}{U_{0,\text{Stokes}}} \approx -1.1734\mu^* \phi^{1/3} + \frac{25}{8}\mu^* \phi^{1/3} \approx 2.0\mu^* \phi^{1/3} \qquad \text{when } \phi^{1/3} \ll Re, \tag{2.11}$$

so the net result is a drift velocity that increases with $\phi^{1/3}$. At large volume fraction (with respect to the Reynolds number), the drift velocity correction due to hydrodynamic interactions reads

$$\frac{U - U_0}{U_{0,\text{Stokes}}} = -1.1734\mu^* \phi^{1/3} + \frac{1}{8}\mu^* Re\left(1 - \frac{Re}{25\phi^{1/3}}\right) \qquad \text{when } Re \ll \phi^{1/3} \ll 1. \tag{2.12}$$

The $O(Re)$ contribution from inertia is negligible compared to the Stokes $O(\phi^{1/3})$ correction: the drift velocity therefore overall decreases linearly with $\phi^{1/3}$, as for creeping flows.

The drift velocity U can be computed, for any ϕ, by finding the positive root of (2.9) (quadratic in U). The solution for various Archimedes numbers is shown in figure 2.3. Note

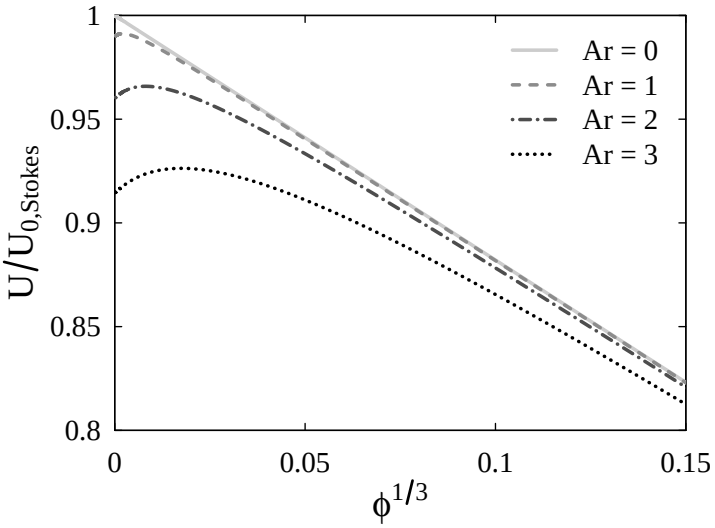

Figure 2.3 The effect of small but finite Archimedes number on the evolution of the steady drift velocity of an ordered array of spherical bubbles with volume fraction, as predicted from the analytical Oseen-flow solution (2.9). The drift velocity is normalized by the terminal velocity of an isolated bubble in Stokes flow conditions.

that higher Archimedes number corresponds to higher isolated-bubble Reynolds number: it can be shown from (2.1), (2.4), (2.8) and (2.10) that in this regime

$$Re_0 = \frac{1}{12}\frac{Ar^2}{\mu^*}\left(1+\frac{Ar^2}{96}\right)^{-1}. \tag{2.13}$$

The non-monotonicity of the function $U(\phi)/U_{0,\text{Stokes}}$ at finite Archimedes number contrasts with the case of Stokes flow, for which this function is strictly decreasing. This behavior results from the competition between "cooperative" long-range inertial interactions, which increase the drift velocity, and "hindering" viscous interactions which reduce it. At small volume fraction, inertial effects dominate, whereas at large volume fraction the liquid is more confined, inertial forces therefore cannot prevail over viscous ones and a Stokes-flow behavior is recovered.

The Oseen approximation is limited to $Re < 1$, which for an isolated clean bubble roughly corresponds to $Ar < 3.5$. For $Ar = 3$, the maximum of $U/U_{0,\text{Stokes}}$ is obtained for $\phi = 6\times10^{-6}$. Direct numerical simulation of such a small volume fraction is prohibitively expensive, so our analysis cannot be confirmed by numerical experiments in its expected range of validity. Nevertheless a comparison between the solution obtained from (2.9) and DNS for $Ar = 5.03$ is shown in figure 2.4, together with the numerical data obtained by Sankaranarayanan et al. (2002) for the identical flow regime using the lattice Boltzmann method. In their study, they found that the effect of volume fraction could be captured by a Richardson-Zaki type of (empirical) correlation $Re = 1.58(1-\phi)^{4.72}$. Although their data are well-fitted by this relation over the narrow range of volume fractions they investigated ($0.05 < \phi < 0.12$), our DNS results show that this expression cannot be used to extrapolate the effect of volume

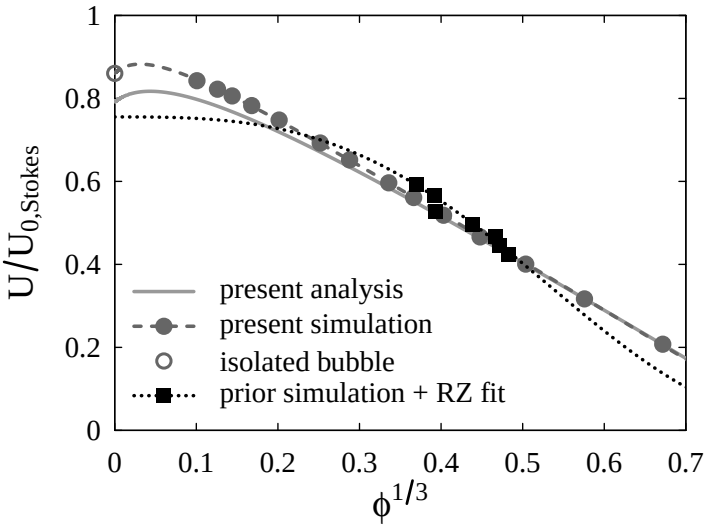

Figure 2.4 Steady drift velocity of an ordered array of spherical bubbles, normalized by the terminal velocity of an isolated bubble in Stokes flow conditions, as a function of volume fraction: comparison of analytical and numerical solutions for $Ar = 5.03$ (case S1). ——: analytical Oseen-flow solution obtained from (2.9); ●: DNS; ○: isolated bubble, estimated from Mei, Klausner, and Lawrence (1994); - - - -: numerical fit of the form of (2.15) matching DNS and isolated-bubble data; ■ and ·····: numerical data and fit by a Richardson-Zaki relation from Sankaranarayanan, Shan, Kevrekidis, and Sundaresan (2002).

fraction outside this range. In addition, their correlation gives a drift velocity at $\phi = 0$ that differs from the terminal velocity of an isolated bubble by more than 10 %. In contrast, the functional dependency of the drift velocity on volume fraction given by our analysis is in very good agreement with numerical simulations; the modest difference at small volume fractions arises from the limitation of Oseen theory to Reynolds numbers less than unity: for an isolated bubble rising in still liquid, the Oseen-flow solution yields $Re_0 = 1.66$ whereas the empirical correlation of Mei, Klausner, and Lawrence (1994) gives $Re_0 = 1.80$.

We now turn to ordered arrays of spherical bubbles rising at moderate Reynolds numbers. The bubble drift velocity has been determined for Archimedes numbers ranging from 0 to 40 (case S0 to S5). The numerical results for $U(\phi)/U_{0,\mathrm{Stokes}}$ are shown in figure 2.5a (symbols) together with those of our analysis for small Archimedes numbers (solid lines). It is remarkable that the evolution of the drift velocity with volume fraction for Archimedes numbers up to approximately 30 is consistent with the Oseen-flow analysis carried out for Archimedes numbers that are, at best, $O(1)$. In particular, for $Ar = 27.2$ (case S4), the predicted increase of the drift velocity at low volume fraction is confirmed numerically. For Archimedes numbers greater than 30 (case S5), the drift velocity of a cubic array of spherical bubbles does not necessarily remain parallel to gravity; we postpone discussion of this to section 2.3.2.

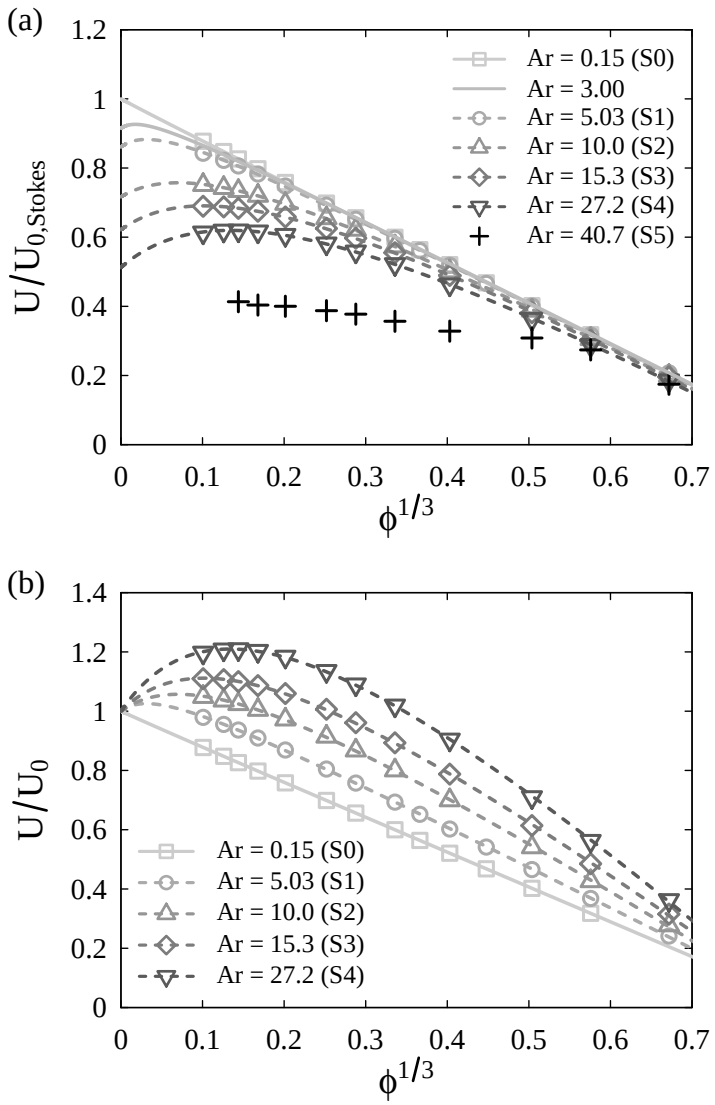

Figure 2.5 Steady drift velocity of an ordered array of spherical bubbles as a function of volume fraction for a large range of Archimedes numbers. The drift velocity is normalized by the terminal velocity of an isolated bubble, either in Stokes flow conditions (a) or in the same conditions of *Ar* and *Bo* (b). Symbols: DNS; ——: analytical Oseen-flow solution obtained from (2.9) for small *Ar*; - - - -: numerical fits of the form of (2.15) matching DNS and isolated-bubble data for larger *Ar*. In case S5, for which the bubbles motion is not steady or not parallel to gravity, the crosses are time-averaged vertical drift velocities.

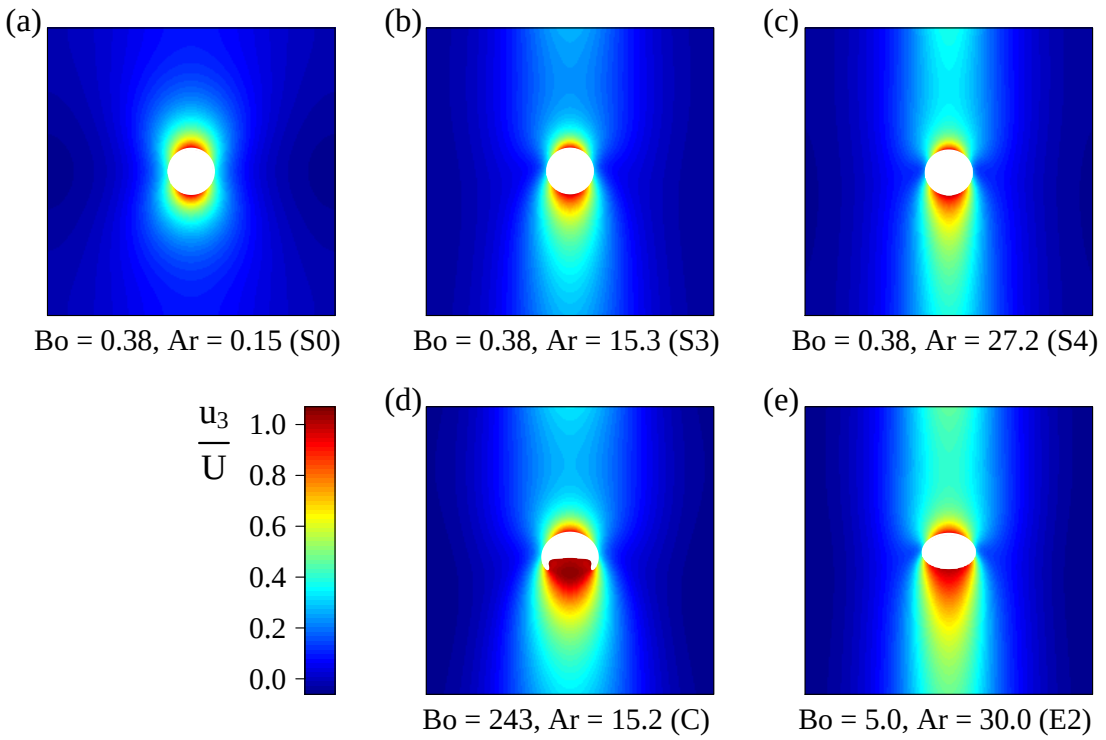

Figure 2.6 Vertical component of the liquid velocity normalized by the bubble drift velocity in a vertical symmetry plane passing through the center of a bubble in an ordered array configuration at $\phi = 0.2$ %. Gravity is pointing downward ($\boldsymbol{g} = -g\boldsymbol{e}_3$). Increasing Archimedes numbers from left to right, and increasing Bond numbers from top to bottom. The bubble interior is colored in white.

The function $U(\phi)/U_{0,\text{Stokes}}$ contains a constant contribution $U(0)/U_{0,\text{Stokes}}$ which is not due to the interactions between the bubbles but only to inertia. To visualize more distinctly the sole effect of hydrodynamic interactions, and for consistency with prior work, the ratio $U(\phi)/U_0$, with $U_0 = U(0)$ the terminal velocity of the equivalent isolated bubble, is plotted against volume fraction in figure 2.5b. At small volume fractions, and for non-zero Archimedes numbers, a cubic array of bubbles rises faster than a single bubble, and this acceleration is stronger at higher Archimedes numbers. At large volume fractions, the drift velocity of the array is drastically reduced, down to 20 to 30 % of its value for a single bubble.

Figure 2.6 shows the vertical component of the liquid velocity in a vertical symmetry plane passing through the center of a bubble at $\phi = 0.2$ %. The first row corresponds to spherical bubbles ($Bo = 0.38$) with increasing Archimedes numbers from left to right. It reveals that the region of liquid dragged up by each bubble extends quite far downstream. Since the bubble motion is parallel to a primary axis of the array, each bubble benefits from this upwards motion by its 'upstairs' neighbor(s). This effect is stronger at larger Archimedes numbers, corresponding to higher Reynolds numbers and for which the wakes of the bubbles therefore extend further

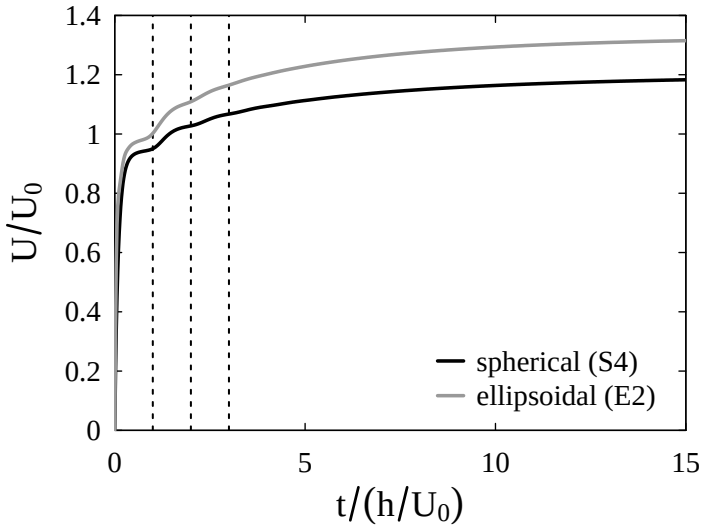

Figure 2.7 Time signal of the drift velocity of an ordered array of spherical and ellipsoidal bubbles at $\phi = 0.1$ %. The drift velocity is normalized by U_0, the terminal velocity of the same bubbles in isolated conditions. The dashed vertical lines denote $t = nh/U_0$, the characteristic times at which the bubbles enter into the wake of their n^{th} preceding neighbor. Only short times are shown for clarity (the steady-state is reached for $t \approx 50\,h/U_0$).

downstream. Cooperative rise is thus due to the strong wake interactions between vertically aligned bubbles. Wake interactions are also visible in the transient evolution of the drift velocity shown in figure 2.7. This quantity first levels off after an initial transient, then the bubbles experience a significant acceleration at $t \approx h/U_0$, that is as they enter into the wake of their first preceding neighbor. At the smallest volume fraction considered, the time scales separation and the wakes strength are sufficient to distinguish the same phenomenon at $t \approx 2h/U_0$: the bubbles rise is then influenced by the wake of their second preceding neighbor, they accelerate again, and so on until convergence.

To complete this analysis we now evaluate how a simple prediction based on pair interaction compares with our results. We estimate for this the drag coefficient of the trailing bubble of a vertically-aligned pair separated by a distance h (our lattice spacing) and translating with a velocity U identical to that of the array of bubbles at the corresponding volume fraction $\phi = \pi/6(d_b/h)^3$ using the model of Hallez and Legendre (2011) (equation (6.7) therein). Their expression, which accounts for potential and wake interactions, has been established for $Re \geqslant 20$, so we show in figure 2.8 the results obtained for case S4 and $\phi^{1/3} < 0.55$, where this condition is met. At very small volume fraction ($\phi^{1/3} \lesssim 0.13$), the drag acting on a bubble of the array is comparable to that exerted on the trailing bubble of pair rising in line, as expected since in dilute conditions wake interaction between vertically-aligned neighbors dominates. At elevated volume fraction, the dimensionless distance between vertically-aligned bubbles

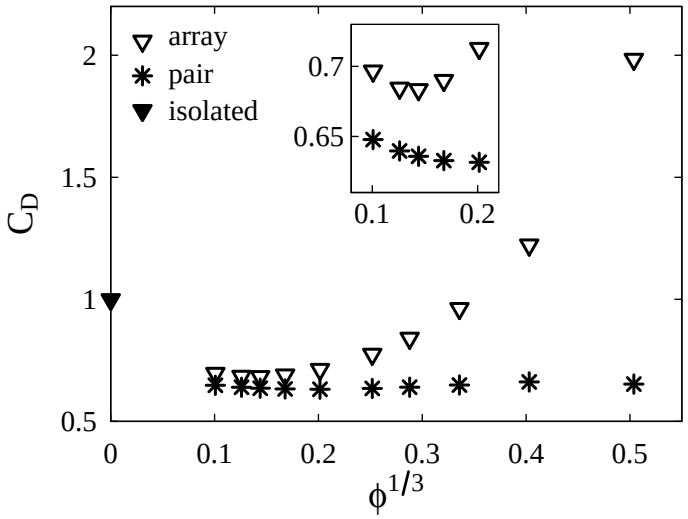

Figure 2.8 Drag coefficient as a function of volume fraction for case S4. $\triangledown$: ordered array; $*$: trailing bubble of a vertically-aligned pair within the same conditions (Reynolds number, separation distance), from Hallez and Legendre (2011); $\blacktriangledown$: isolated bubble, estimated from Mei, Klausner, and Lawrence (1994). Inset: zoom at small volume fractions.

h/d_b is smaller, but the drag is no longer governed primarily by such pair interactions, as the departure from the pair-interaction results is seen to be substantial in figure 2.8.

2.3.1.2 Deformed bubbles at moderate Reynolds numbers

We now examine the effect of the Bond number on bubble deformation and on hydrodynamic interactions. The effect of volume fraction on U/U_0 is first shown, for different values of the Bond number and comparable Archimedes numbers, in figure 2.9a ($Ar \approx 30$) and figure 2.9b ($Ar \approx 15$). The data points that are apparently missing at some intermediate volume fractions for case E1 actually correspond to bubbles that do not rise steadily and vertically (discussion of these is postponed to section 2.3.2 and figure 2.18a), and only small volume fractions are shown for case C because bubbles cannot exist at higher ϕ (instead, unsteady elongated bodies of gas are obtained). We have also included in figure 2.9a the numerical data obtained by Bunner and Tryggvason (2002a), who noticed that normalized drift velocities could be larger than unity at low volume fraction (black crosses). In their study, they estimated $Re_0 = 36$ by interpolating the data of Ryskin and Leal (1984b). Using the correlation of Loth (2008), as we did for our own sets of parameters, we obtained $Re_0 = 33$. For consistency we kept this value for re-plotting their data. Their results follow approximately the same trend as ours, although their normalized drift velocities are slightly lower. This is probably because the effect of the gas viscosity is assumed to be zero when estimating Re_0, a hypothesis better approached by our DNS than by that from Bunner and Tryggvason (2002a), who used a gas viscosity twice as

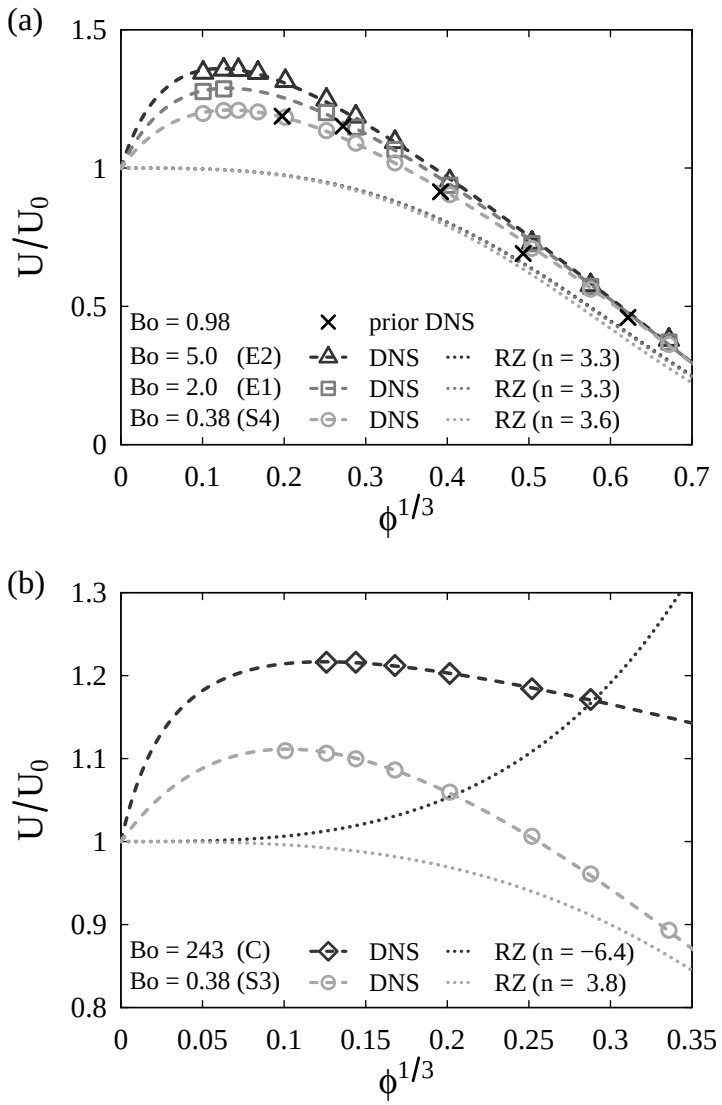

Figure 2.9 Normalized steady drift velocity of an ordered array of deformable bubbles as a function of volume fraction for various Bond numbers. (a) $Ar \approx 30$: spherical and ellipsoidal bubbles. (b) $Ar \approx 15$: spherical and dimpled ellipsoidal-cap bubbles. Open symbols: present DNS. Black crosses: prior DNS of Bunner and Tryggvason (2002a) ($Ar = 29.7$, $Bo = 0.98$, $\rho_d/\rho_c = \mu_d/\mu_c = 0.02$). Dashed lines: numerical fits of the form of (2.15) matching DNS and isolated-bubble data. Dotted lines: Richardson-Zaki relation $Re = Re_0(1-\phi)^n$, with n given by (2.14) from Sankaranarayanan and Sundaresan (2002).

large.

The shape of $U(\phi)/U_0$, specifically its non-monotonicity, is similar to that obtained for spherical bubbles, but the faster rise at small volume fraction is more pronounced at higher Bond numbers. The origin of this behavior becomes clear if one examines the effect of the Bond number on bubbles wakes in figure 2.6, in which the vertical component of the liquid velocity is represented in a vertical symmetry plane, at small volume fraction ($\phi = 0.2$ %). Each column corresponds to comparable Archimedes numbers ($Ar \approx 15$ and $Ar \approx 30$ for the second and third columns, respectively) with increasing Bond numbers from top to bottom. As the Bond number increases, the bubbles flatten (as discussed below) and their drag coefficient increases (for a given Re) as a result of the increase of their frontal area (e.g., Loth (2008)). This induces greater upward liquid velocities in their wakes and therefore stronger cooperative interactions between in-line objects. The transient evolution of the drift velocity is shown in figure 2.7. It is similar to that of spherical bubbles, with accelerations at time intervals $O(h/U_0)$ but a slightly different initial transient in which the time dependence of acceleration is non-monotonic, a feature related to the bubble deformation from a sphere to an ellipsoid.

These results can be directly compared with those of Sankaranarayanan et al. (2002), who found that the evolution of the drift velocity with the volume fraction follows a Richardson-Zaki law $Re = Re_0(1-\phi)^n$ (Richardson & Zaki, 1954), where n is given by an empirical closure relation in terms of $Re_0 Bo^{1/4} Ar^{-1}$ (in the present notation):

$$n = \begin{cases} 3.3 - 1.7\log_{10}(Re_0 Bo^{1/4} Ar^{-1}/1.3), & \text{if} \quad Re_0 Bo^{1/4} Ar^{-1} < 1.3, \\ 3.3 - 51\log_{10}(Re_0 Bo^{1/4} Ar^{-1}/1.3), & \text{if} \quad Re_0 Bo^{1/4} Ar^{-1} \geqslant 1.3. \end{cases} \tag{2.14}$$

The trends predicted by this relation, shown with the dotted lines in figure 2.9, strongly disagree with our numerical results. Once again, it appears that this power law dependency on volume fraction may be used to obtain a coarse estimate of the drift velocity at high volume fraction, but does not capture the complex influence of hydrodynamic interactions on the rise of cubic arrays of deformable bubbles for low values of ϕ.

To formulate a semi-empirical law for the function $U(\phi)/U_0$ consistent with the Oseen-flow analysis and that would be valid for smaller ϕ values and very deformed bubbles, we note that the positive root of (2.9) for U can be written in the form

$$\frac{U}{U_0} = 1 + \frac{U_{0,\text{Stokes}}}{U_0}\mu^* \frac{C_0 - (1.1734 + C_1)\phi^{1/3}}{1 + C_{m1}\phi^{-1/3}}, \tag{2.15}$$

where $U_{0,\text{Stokes}}$ is given by (2.8). We have introduced in this expression three fitting parameters C_0, C_1, and C_{m1} that we have computed for each case by a least-squares fit of DNS data at finite volume fraction and isolated-bubble data at zero volume fraction. The fitted values are shown in figure 2.10. These parameters account for the effect of inertial interactions (they are zero in the Stokes-flow regime, $Ar = 0$), and are monotonic functions (increasing and decreasing, respectively) of the Archimedes and Bond numbers. The fitted expression of the normalized

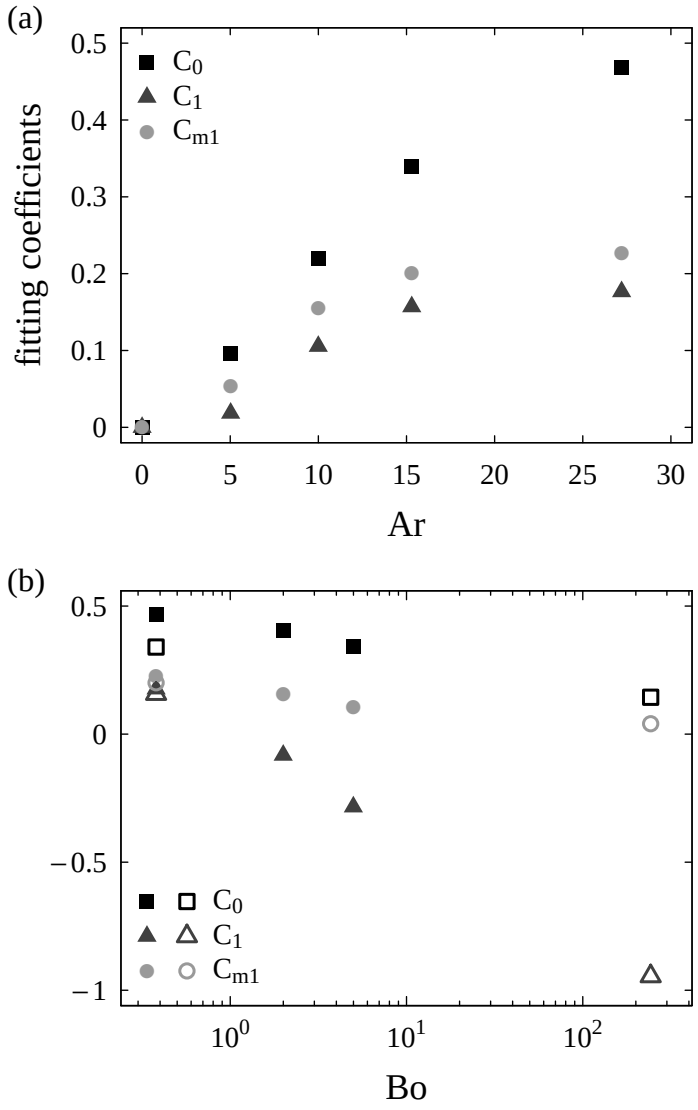

Figure 2.10 Fitted coefficients for $U(\phi)/U_0$ as given by (2.15): (a) as a function of the Archimedes number for $Bo = 0.38$, (b) as a function of the Bond number for $Ar \approx 15$ (open symbols) and for $Ar \approx 30$ (filled symbols). The coefficients are obtained by least-squares fits of DNS and isolated-bubble data.

drift velocity is shown with dashed lines for each case in figure 2.4, figure 2.5 and figure 2.9, where it is seen that the effect of volume fraction is well described by this law for all the flow regimes considered.

We now investigate the bubbles' shape. At low Bo (not shown here), the bubbles remain approximately spherical as volume fraction is varied; the aspect ratio χ (the maximum bubble width W divided by the maximum bubble height H, see figure 2.11) does not deviate from 1 by more than 5 %, due to the low value of the Weber number. At $Bo \geqslant O(1)$, the bubble shape strongly depends on volume fraction, and is investigated below. For intermediate Reynolds numbers, say $1 < Re < 100$, no theoretical expression of χ is available. At low Re and We a theoretical result is available (T. D. Taylor & Acrivos, 1964) for the shape modes introduced below, but this has been found not to predict accurately results of numerical simulations for an isolated bubble if We is increased to unity (Ryskin & Leal, 1984b). The analysis by Moore (1959) is for values of Re well over 100. Therefore, as a starting point in the following, the results of numerical simulations of an isolated bubble by Ryskin and Leal (1984b) are used.

We first focus on ellipsoidal bubbles (cases E1 and E2). Note that denomination "ellipsoidal bubble" refers to a bubble that is approximately spheroidal with weak fore-and-aft asymmetry, but does not mean that the bubble shape is strictly ellipsoidal. In all the simulations reported here, bubbles are virtually axisymmetric, but may exhibit significant fore-and-aft asymmetry. In figure 2.11, we present the aspect ratio as a function of volume fraction for these cases. We also show in figure 2.12 the first two shape coefficients $a_{2,3}$ defined by writing the local bubble radius $R(\theta)$ as

$$R(\theta) = \sum_n a_n P_n(\cos\theta), \tag{2.16}$$

where P_n is the Legendre polynomial of order n and θ is the angle between the position vector at the bubble surface and the bubble velocity (a_0 is the radius of the sphere with the same volume). The coefficients were obtained from a distribution of points (at least 500) on the bubble surface and integrating the orthogonality relation for each Legendre polynomial.

In figure 2.11 and figure 2.12, for both cases E1 and E2, as the volume fraction is increased, χ decreases monotonically to unity, and a_2 goes to zero, from about their respective values for isolated bubbles. The corresponding single bubbles (for which results are shown in the figures with filled symbols), are of oblate-ellipsoid shape. This shape is expected for isolated bubbles at large Re, through a Bernoulli suction effect in the vicinity of the bubble rim, and is expected also at low Re (T. D. Taylor & Acrivos, 1964). It may be anticipated that the demise of this shape at elevated volume fraction is partly due to the dependencies of Re and We on volume fraction. We have verified, however, that the empirical correlation by Loth (2008) for the aspect ratio of isolated bubbles:

$$\chi^{-1} = 1 - \left[1 - \left(0.25 + 0.55\exp(-0.09\,Re)\right)\right]\tanh\left[\left(0.165 + 0.55\exp(-0.3\,Re)\right)We\right], \tag{2.17}$$

using the values of Re and We obtained from the simulations, gives a very poor prediction of the results presented in figure 2.11 (shown with the dotted lines). The reduction of suction

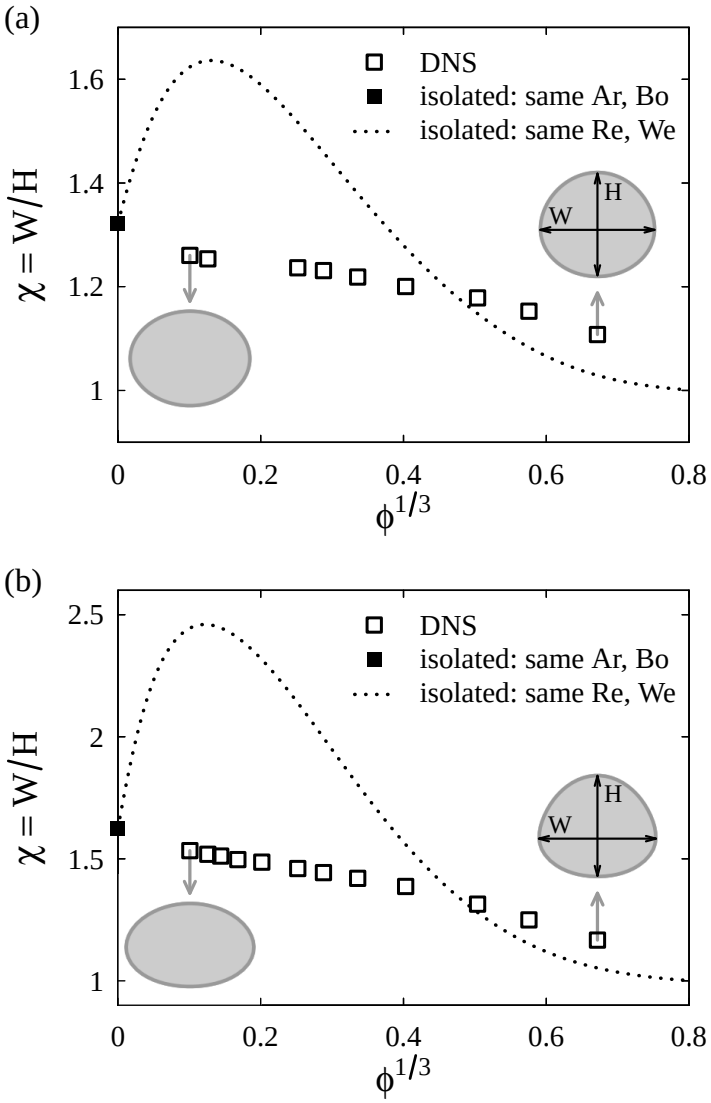

Figure 2.11 Steady aspect ratio of ellipsoidal bubbles in an ordered array configuration as a function of volume fraction for (a) case E1 ($Bo = 2.0$, $Ar = 29.9$), (b) case E2 ($Bo = 5.0$, $Ar = 30.0$). Bubbles shapes are shown in gray for the highest and the lowest simulated volume fractions. Open symbols: DNS. Filled symbols: isolated bubble with the same *Ar* and *Bo*, estimated from Loth (2008). Dotted lines: isolated bubble with the same *Re* and *We*, estimated from (2.17).

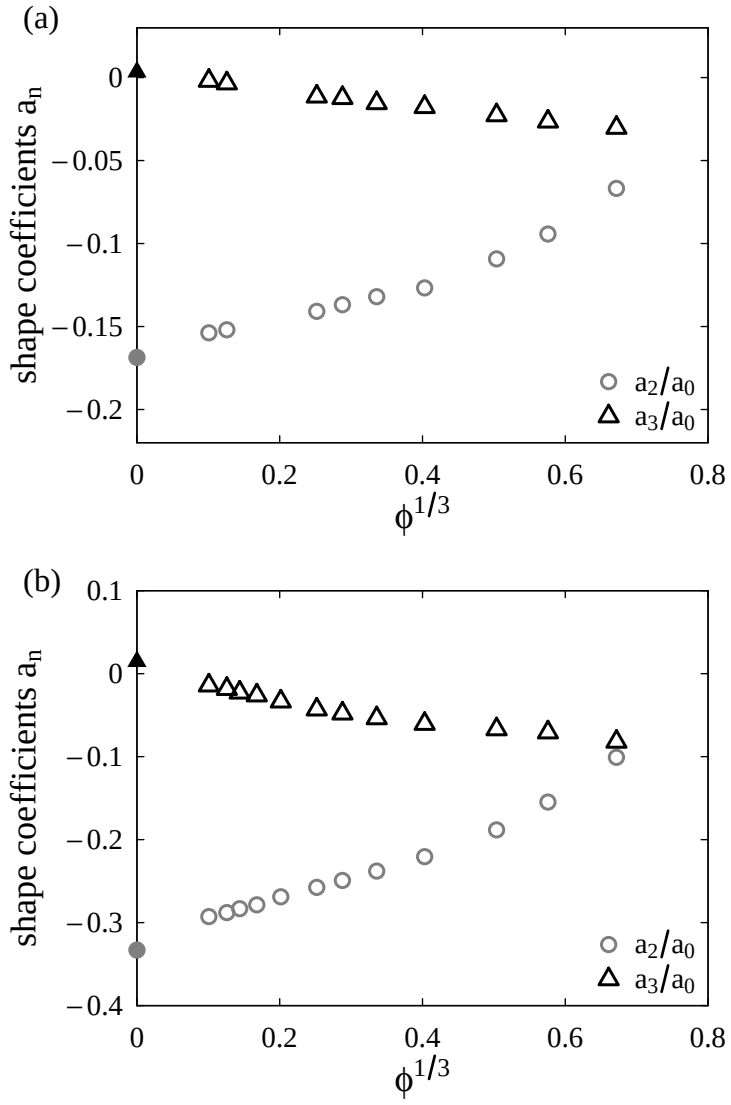

Figure 2.12 Steady shape coefficients (as defined from (2.16)) of ellipsoidal bubbles in an ordered array configuration as a function of volume fraction for (a) case E1 ($Bo = 2.0$, $Ar = 29.9$), (b) case E2 ($Bo = 5.0$, $Ar = 30.0$). Open symbols: DNS. Filled symbols: isolated bubble, estimated from Ryskin and Leal (1984b).

at the bubble rim is therefore due to the detailed bubble interactions. In their study of the hydrodynamic interactions between two spherical bubbles rising side by side, Legendre et al. (2003) showed that at small to moderate Reynolds number ($Re \lesssim 30$, as encountered in our study), the transverse force is repulsive and increases when the separation decreases. Such a reduction or elimination of suction between bubbles suggests the liquid downflow due to a bubble pair occurs around the pair as a whole. In a 3D cubic array, although the room for liquid to flow down with little opposition is reduced further (at four sides along a bubble rim), some remains present along vertical edges of each cell in the array. This is illustrated in figure 2.13 (top row), where we show the vertical relative liquid velocity in a horizontal plane cutting through the center of the bubble. Therefore, any suction effect normally arising at the rim of a bubble would be reduced in between bubbles lying in the same horizontal plane. This may be somewhat countered by an increase elsewhere along the bubble periphery (if not at a greater distance from the bubble), but a variation in curvature is opposed by surface tension.

In addition to this reduction in aspect ratio, the fore-and-aft asymmetry of the shape of an isolated bubble is altered significantly by the finite volume fraction. For single bubbles, cases E1 and E2 are near the boundary between a low-*Re* regime of bubbles with a blunt tail and, at the same *We* but larger *Re*, a regime of bubbles with a flat nose (Ryskin & Leal, 1984b); only a slightly flattened nose is observed, mostly in case E2, resulting in a positive value of a_3 in (2.16). The results in figure 2.12 show that already at small but finite volume fraction, this asymmetry is reversed. The bubble nose becomes rather pointed and the tail blunt as the volume fraction is increased further. This tendency for oblate ellipsoidal bubbles arranged in regular arrays to have their nose pulled upwards at finite volume fraction has been observed previously by Sankaranarayanan et al. (2002), and attributed to a wake effect. Indeed Hallez and Legendre (2011) showed that in the present range of Reynolds numbers, two spherical bubbles rising in line are attracted toward each other for separation distances greater than approximately 1.3 bubble diameter, which would be equivalent to $\phi^{1/3} = 0.62$, a value close to the upper bound of the range of volume fractions we consider. To investigate this further, the amplitude of the P_3 mode in (2.16) is included in figure 2.12. It is seen that in concentrated arrays this becomes as significant as that of the P_2 mode. The presence of successive bubbles in each others' wakes does reduce the variation in velocity magnitude between them, as can be seen in figure 2.13 (middle row). The significance of the stagnation-point flow at the bubble nose is thereby reduced as volume fraction is increased, and the large dynamic pressure at a stagnation point in the liquid is reduced (the pressure field is shown in figure 2.13, bottom row), along with the magnitude of normal deviatoric stress. Both these result in an increase in the jump in normal stress and hence an increase in interface curvature.

Finally we note that the results for aspect ratio and shape coefficients for cases E1 and E2 differ by a factor of approximately two, which roughly corresponds to the ratio of the bubble Weber numbers at all volume fractions. As we have not undertaken to extend our parametric study even further to confirm, it is concluded that the results for $(\chi - 1)$ and $a_{2,3}$ versus Weber

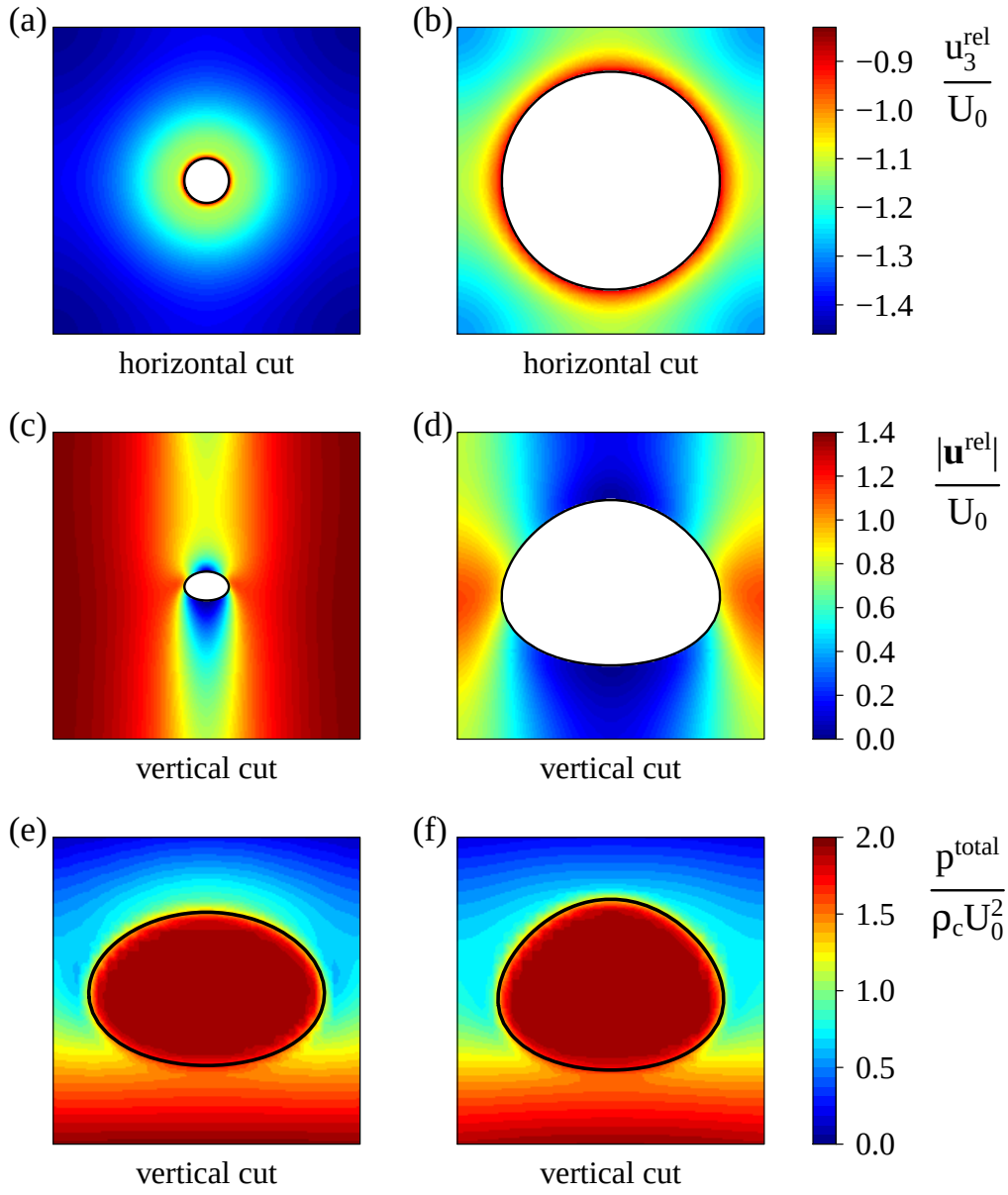

Figure 2.13 Influence of volume fraction on the deformation of an ordered array of oblate ellipsoidal bubbles (case E2): relative velocity ($\boldsymbol{u}^{\mathrm{rel}} = \boldsymbol{u} - \langle \boldsymbol{u} \rangle_d$) and pressure fields in symmetry planes passing through the center of a bubble. Increasing volume fractions from left to right: (a,c,e) $\phi = 0.1$ %, $U/U_0 = 1.34$, and (b,d,f) $\phi = 13$ %, $U/U_0 = 0.73$. Top row: vertical component of the liquid relative velocity in a horizontal plane. Middle row: magnitude of the liquid relative velocity in a vertical plane. Bottom row: total pressure (including the mixture-average hydrostatic component) in a vertical plane (only the region near and inside a bubble is shown). Gravity is pointing downward ($\boldsymbol{g} = -g\boldsymbol{e}_3$) in vertical cuts, and backward in horizontal cuts. The black lines show the interface location.

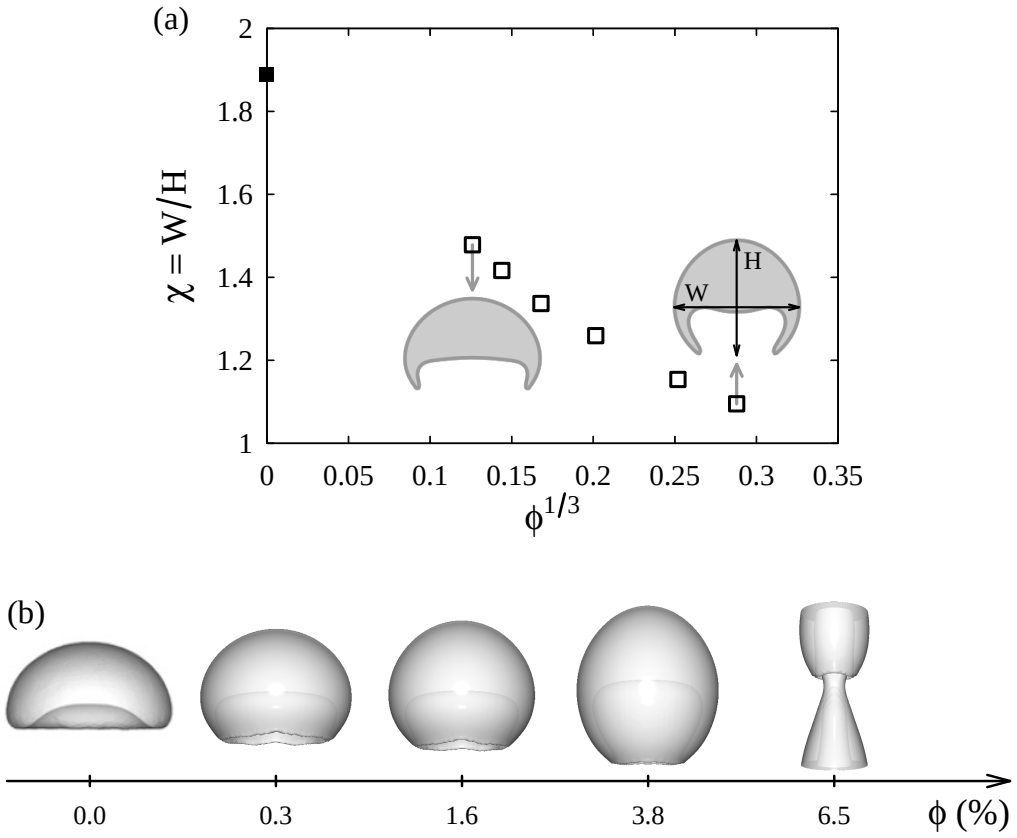

Figure 2.14 Effect of volume fraction on the steady shape of indented/skirted bubbles in an ordered array configuration (case C, $Bo = 243$, $Ar = 15.2$). (a) Bubble aspect ratio (open symbols: DNS, filled symbol: isolated bubble, estimated from Hua, Stene, and Lin (2008)). Bubbles shapes are shown in gray for the highest and the lowest simulated volume fractions. (b) Bubble shape visualizations. The shape of the isolated bubble at zero volume fraction is taken from Hua, Stene, and Lin (2008). At $\phi = 6.5$ %, the bubble is so deformed that it catches up with its preceding neighbor.

number, in the present range of $We < 7$, are consistent with a linear dependency.

We have also investigated a regime characterized by a very high Bond number (case C, $Bo = 243$). The evolution of the bubbles' "aspect ratio" and shape with volume fraction is shown in figure 2.14a. The qualitative effect of volume fraction on the bubbles shape is further illustrated in figure 2.14b. The corresponding bubbles in isolation (leftmost picture) are indented ellipsoidal caps (Bhaga & Weber, 1981; Hua et al., 2008). As the volume fraction increases, the upside-down crown of gas issuing from the bubble rim becomes thinner and longer to form a skirt with an inward curvature (in the direction of the bubble axis of symmetry). The range of ϕ values that can be considered in this case is relatively narrow, since for $\phi \gtrsim 6$ % the bubbles become so elongated that they catch up with their preceding neighbor (rightmost picture). The aspect ratio of the skirted bubble decreases towards unity as the volume fraction

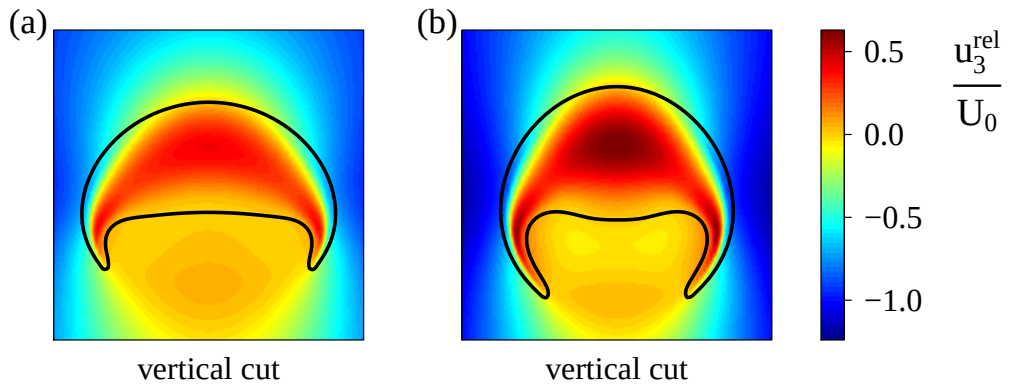

Figure 2.15 Influence of volume fraction on the deformation of an ordered array of dimpled/skirted ellipsoidal-cap bubbles (case C): vertical component of the relative velocity ($\boldsymbol{u}^{\mathrm{rel}} = \boldsymbol{u} - \langle \boldsymbol{u} \rangle_d$) in a vertical symmetry plane passing through the center of a bubble (only the region near and inside a bubble is shown). Increasing volume fractions from left to right: (a) $\phi = 0.2$ %, $U/U_0 = 1.22$, and (b) $\phi = 2.4$ %, $U/U_0 = 1.17$. Gravity is pointing downward ($\boldsymbol{g} = -g\boldsymbol{e}_3$). The black lines show the interface location.

is increased, even if the skirt is not included in the height. Indeed given the moderate value of the Reynolds number ($Re \approx 10$), the same reasoning as above for ellipsoidal bubbles is expected to apply, that is, a decrease of the suction effect as the size of the gap between side neighbors decreases. At low volume fraction, an extrapolation of the results to zero volume fraction appears consistent with the corresponding result for a single bubble.

The theory of Ray and Prosperetti (2014) indicates that the finite length of the skirt is dictated by the thinning of the skirt downstream of its point of formation. According to their model, the skirt thickness is proportional to $\sqrt{-u_s}$, where u_s is the (negative) vertical component of the relative velocity (that is, the liquid velocity in the bubble frame of reference) at the outer side of the skirt at a given altitude (the inward curvature of the skirt being neglected). We show in figure 2.15 the vertical relative velocity $u_3^{\mathrm{rel}} = u_3 - \langle u_3 \rangle_d$ in the vicinity of bubble (with gravity pointing in the $-\boldsymbol{e}_3$ direction). It can be observed that as the distance from the rim increases, $|u_s|$ ($\left|u_3^{\mathrm{rel}}\right|$ along the outer side of the skirt) decreases and the skirt tapers, until the skirt ends for a critical value of $|u_s|$, in (qualitative) agreement with the model of Ray and Prosperetti (2014). By comparing the left and right panels of figure 2.15, one remarks that at high volume fractions a significant downflow of liquid develops outside of bubbles wakes. This backflow of liquid, which is particularly strong because the bubbles rise velocity is not substantially reduced for large values of ϕ, increases the value of $|u_s|$ at a given altitude. Therefore, at higher volume fraction, the skirt must extend further downstream to reach the critical value of $|u_s|$ at which the skirt ends, as observed in our simulations.

2.3.2 Steady and unsteady oblique rise of bubbles

In the range of parameters considered thus far, the motion of a single bubble in unbounded liquid is straight, steady, and parallel to gravity. Bubble motion that is oblique (i.e., not aligned with gravity) was observed, however, for cases E1 and S5 at certain volume fractions. Such oblique motion has been reported previously for two-dimensional square arrays of bubbles (Sankaranarayanan et al., 2002; Sankaranarayanan & Sundaresan, 2002; Theodoropoulos, Sankaranarayanan, Sundaresan, & Kevrekidis, 2004), but their triggering and their stability remain essentially unexplained. We analyze oblique flows further here. In this subsection the bubble drift velocity vector is denoted by $\boldsymbol{U} = U_i \boldsymbol{e}_i$ and the gravity vector by $\boldsymbol{g} = -g\boldsymbol{e}_3$, where $\boldsymbol{e}_i$ are the unit primary vectors of the periodic array.

First, existence of such oblique solutions is demonstrated at Reynolds numbers that are small but finite. The Oseen analysis in appendix A yields the system of equations (A.17) that involve the bubble velocity and the force exerted by the fluid on the bubble. As this force is prescribed (it balances buoyancy), (A.17) yields the bubble velocity. The main solution is naturally a velocity vector aligned with gravity, as studied in section 2.3.1. Equation (A.17) does, however, allow for other solutions which satisfy the nonlinear system of equations (A.26). We have found these non-trivial solutions at values of Ar around 20. The most convenient way to obtain these solutions was found to be, for a given inclination of the bubble velocity (with respect to the upward vertical direction), to reduce the problem to a single nonlinear equation for the Reynolds number based on the lattice spacing and the magnitude of the bubble velocity (Re_h in appendix A), and to obtain the volume fraction from the remainder of the system of equations. Two types of non-trivial solutions were studied: either the horizontal bubble velocity component was aligned with one of the lattice unit vectors, or it was diagonal to the lattice. The results are presented in figure 2.16. It is seen that these exist below a critical value of the volume fraction (which we have found to increase rapidly with the value of Ar), the inclination angle strongly increasing as the volume fraction is reduced.

We now return to numerical results. After an initial transient during which they accelerate from rest under the effect of buoyancy, the bubbles may be deflected from their original vertical trajectories. At this point, the horizontal components of the bubble velocity grow in magnitude while the rise velocity drops off. After that, velocity fluctuations set in. Three types of dynamic behaviors have been identified depending on the evolution of these fluctuations: (i) the fluctuations may rapidly dampen out, and the bubbles finally rise steadily on a straight (but skewed to gravity) path; (ii) they may take the form of oscillations, so that the bubbles motion is oscillatory around a straight oblique path; (iii) they may become aperiodic, so the bubble rise is chaotic and, on average, not aligned with gravity. These regimes are exemplified in figure 2.17, and will be respectively referred to as steady oblique rise (a,b), oscillatory oblique rise (c), and chaotic oblique rise (d).

The bubble drift velocities are in all cases either steady or statistically stationary, so mean drift velocities can be defined by averaging over a sufficient time period. The horizontal and

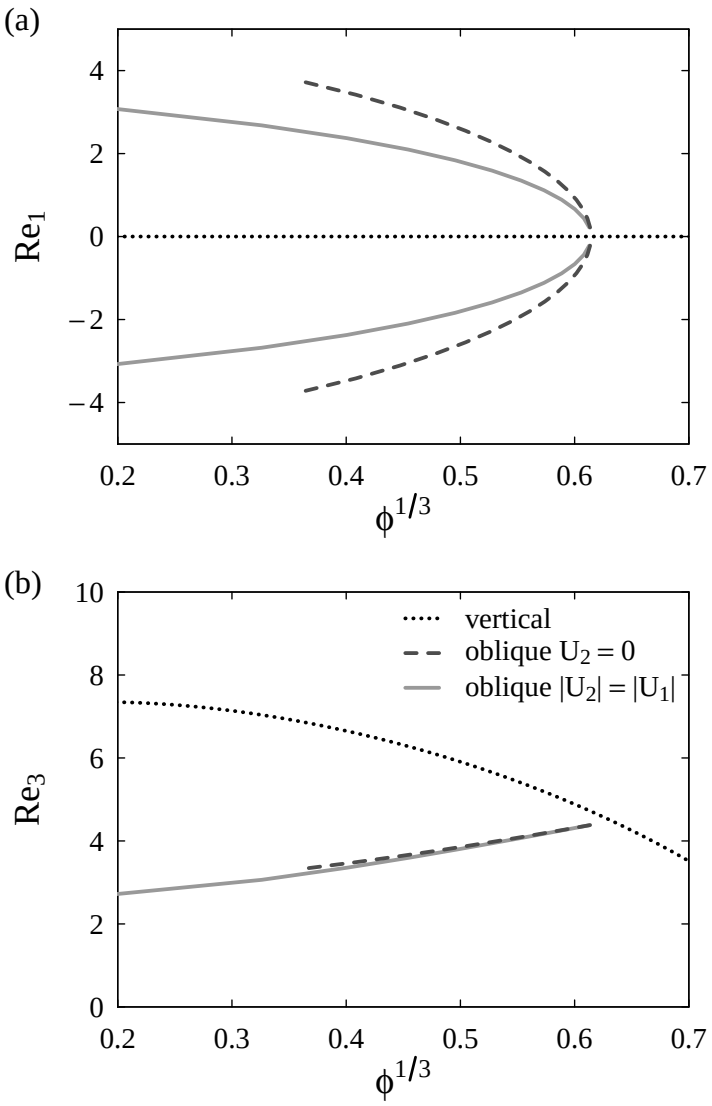

Figure 2.16 Subset of analytical solutions obtained from solving (A.17) for $Ar = 20$ and $\rho_d/\rho_c = \mu_d/\mu_c = 0$: bubble drift velocity horizontal (a) and vertical (b) components, given as Reynolds numbers $Re_i = U_i \rho_c d_b/\mu_c$, as a function of volume fraction. Gravity is pointing in the $-\boldsymbol{e}_3$ direction. ·····: vertical rise ($U_1 = U_2 = 0$); - - - -: oblique rise with $U_2 = 0$; ——: oblique rise with $|U_2| = |U_1|$.

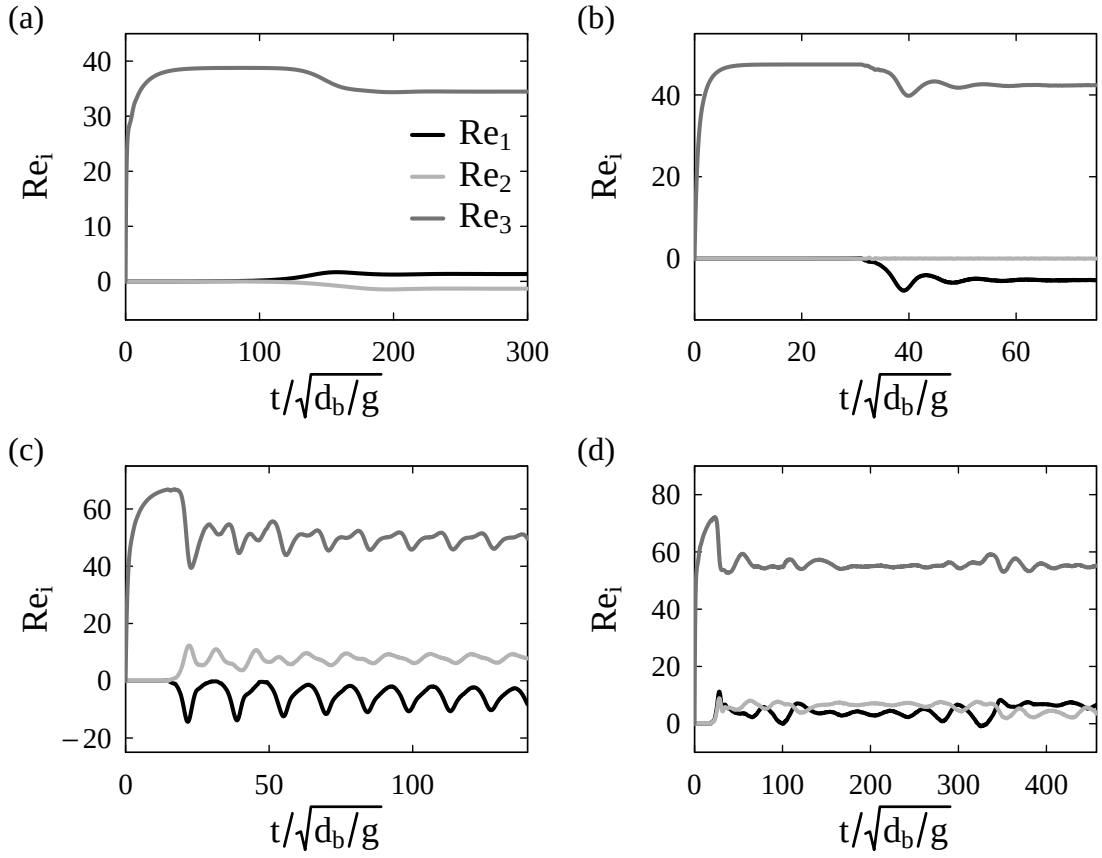

Figure 2.17 Time signals of the bubble drift velocity components (given as Reynolds numbers $Re_i = \rho_c U_i d_b / \mu_c$), with $\boldsymbol{U} = U_i \boldsymbol{e}_i$ and gravity pointing in the $-\boldsymbol{e}_3$ direction, in the three regimes of motion: steady oblique rise (a,b), oscillatory oblique rise (c), and chaotic oblique rise (d). These regimes are obtained for (a) case E1 at $\phi = 0.8$ %, (b) case S5 at $\phi = 13$ %, (c) case S5 at $\phi = 3.8$ %, (d) case S5 at $\phi = 0.5$ %.

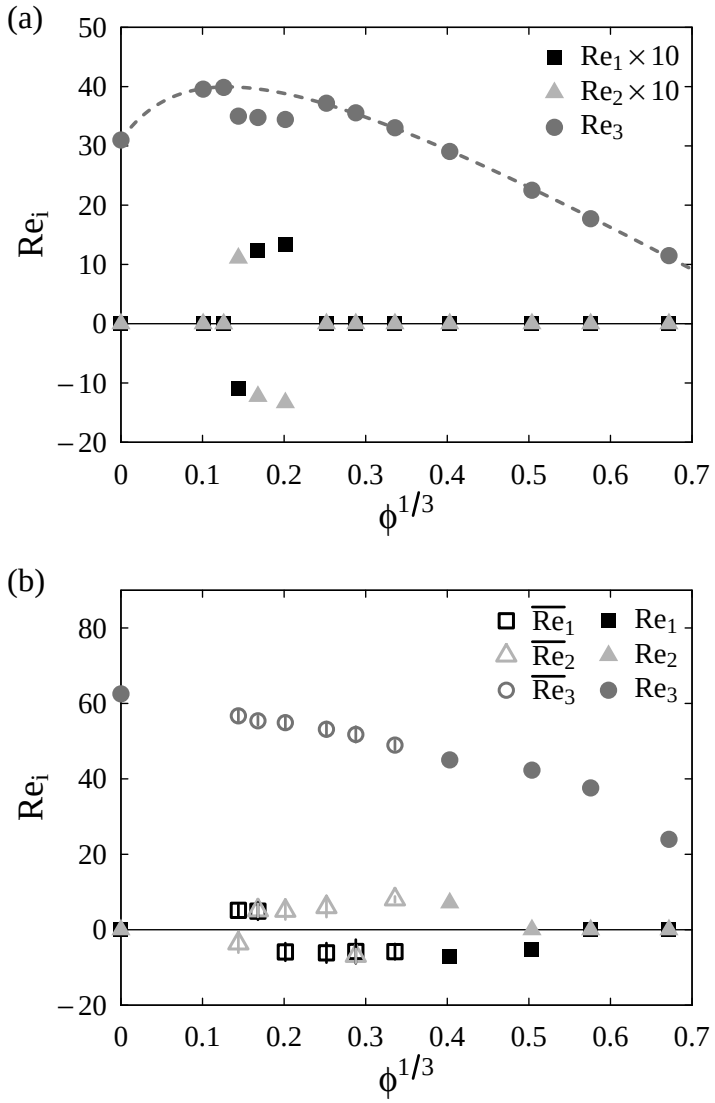

Figure 2.18 Quasi-steady drift velocity components ($\boldsymbol{U} = U_i \boldsymbol{e}_i$) in the form of Reynolds numbers ($Re_i = \rho_c U_i d_b / \mu_c$) as a function of volume fraction for an ordered array of bubbles in the cases where bubbles exhibit non-vertical motions. Gravity is pointing in the $-\boldsymbol{e}_3$ direction. (a) Case E1 ($Bo = 2.0$, $Ar = 29.9$, note that the horizontal components have been multiplied by 10 for clarity). (b) Case S5 ($Bo = 0.38$, $Ar = 40.7$). Filled symbols are used when the bubbles motion is steady (oblique or vertical). Open symbols and vertical bars are used when the bubbles motion is unsteady: symbols indicate the mean drift velocity, and bars show its root mean square. The dashed line is a numerical fit of the form of (2.15) matching DNS and isolated-bubble data for the vertical rise only.

vertical components of the (statistically-)steady drift velocity are plotted against volume fraction in figure 2.18 for cases E1 and S5. Filled symbols are used for steady bubbles motion, vertical or oblique. For unsteady bubble motion, the time-averaged drift velocity is shown with open symbols, and the standard deviation is represented using vertical bars. In case E1 (figure 2.18a), steady vertical rise is obtained at low and high volume fractions, whereas at intermediate volume fractions the bubbles rise steadily along an oblique path with an inclination angle of about 3°. This figure shows that three solutions exist in this regime: a symmetric vertical solution ($U_1 = U_2 = 0$), and two asymmetric oblique solutions consisting of horizontal velocity components of equal magnitude ($|U_1| = |U_2| \neq 0$), as predicted from the Oseen-flow analysis (figure 2.16). In case S5 (figure 2.18b), steady vertical rise, steady oblique rise, oscillatory oblique rise, and chaotic oblique rise are obtained in that order as volume fraction is decreased. Inclination of the velocity with respect to the upward vertical direction is between 6 and 13° (maximum for $\phi^{1/3} = 0.4$). As volume fraction approaches zero, the steady vertical rise of the isolated bubble must be recovered, although the occurrence of this transition cannot be evidenced by numerical simulations owing to their prohibitive cost.

It is possible to obtain insight in this behavior by using prior results for bubble pairs. At steady-state, the integral of fluid stresses over the bubble surface, denoted by $\boldsymbol{f}$, is balanced by the buoyancy force $\boldsymbol{f}_{\text{buoy}}$: $\boldsymbol{f} = -\boldsymbol{f}_{\text{buoy}}$, with $\boldsymbol{f}_{\text{buoy}} = f_{\text{buoy}}\boldsymbol{e}_3 = \frac{1}{6}\pi d_b^3(\rho_c - \rho_d)g\boldsymbol{e}_3$. The total surface force $\boldsymbol{f}$ acting on the bubble can be decomposed into a drag force $\boldsymbol{f}_{\text{drag}}$ and a lift force $\boldsymbol{f}_{\text{lift}}$, defined by

$$\boldsymbol{f}_{\text{drag}} = (\boldsymbol{f}\cdot\boldsymbol{U})\frac{\boldsymbol{U}}{|\boldsymbol{U}|^2}, \qquad \boldsymbol{f}_{\text{lift}} = \boldsymbol{f} - \boldsymbol{f}_{\text{drag}}, \tag{2.18}$$

and corresponding to longitudinal and transverse components of $\boldsymbol{f}$ with respect to the direction of motion, respectively (these definitions can be used for unsteady but statistically stationary systems by replacing $\boldsymbol{U}$ and $\boldsymbol{f}$ by their time averages). The persistence of a (possibly average) oblique motion implies the existence of a net (average) lift force exerted on the bubble. The magnitude of this lift force is classically presented in the form of a dimensionless lift coefficient C_L defined by

$$C_L = \frac{|\boldsymbol{f}_{\text{lift}}|}{0.125\pi d_b^2 \rho_c |\boldsymbol{U}|^2}. \tag{2.19}$$

The (average) lift coefficient is plotted as a function of volume fraction in figure 2.19 for case E1 (open gray triangles) and case S5 (open black squares).

Since the tilt angle remains small (not larger than 13° in our simulations), each bubble is in the wake of its predecessor, and the oblique path is expected to originate from the vorticity produced by the preceding bubble. We therefore investigate whether the lift force induced by the preceding bubble can be estimated from prior work on bubble pairs separated by a fixed distance equal to the present lattice spacing, both rising at a constant velocity $\boldsymbol{U}$ and where the angle between $\boldsymbol{U}$ and the vertical line joining their centers is the inclination angle measured from our simulations. The model proposed by Hallez and Legendre (2011) for bubble pairs (equation (6.12) therein) is used here for this purpose. A spherical bubble shape appears a

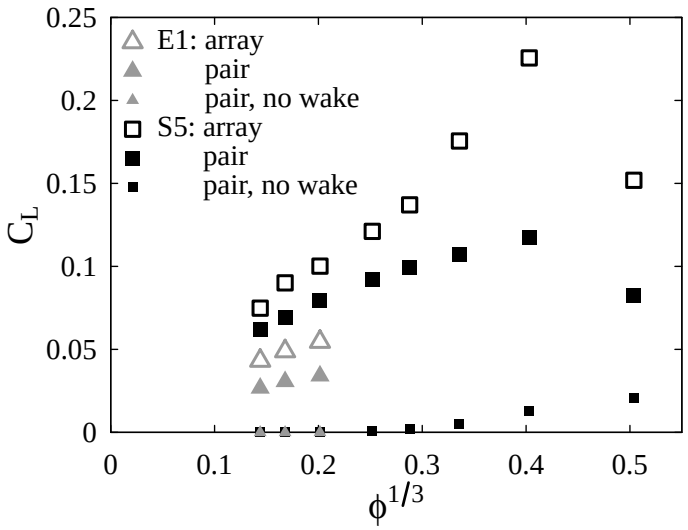

Figure 2.19 Average lift coefficient as a function of volume fraction for case E1 (gray triangles) and case S5 (black squares). Open symbols: for a bubble of an ordered array, present DNS. Filled symbols: for the trailing bubble of a pair of spherical bubbles within the same conditions (orientation, Reynolds number, separation distance) as two vertically-aligned bubbles of the ordered array, with (large symbols) and without (small symbols) accounting for the interaction with the wake of the leading bubble, from Hallez and Legendre (2011).

reasonable approximation given that in our simulations the aspect ratio does not exceed 1.3 for case E1, and 1.1 for case S5. The results are shown in figure 2.19 with larger filled symbols. To assess the influence of the leading bubble wake, the lift coefficient obtained for bubble pairs without the contribution from the wake is shown on the same figure with smaller filled symbols. The trend obtained by considering the pair interaction is in excellent adequacy with our numerical results for periodic arrays when the wake of the top bubble is accounted for, thereby demonstrating that oblique rise is essentially a wake-induced effect. The lift coefficient in ordered suspensions is found to be larger than that due to the interaction with the wake of a single bubble, and the difference is more pronounced at higher volume fractions, since in the periodic configuration the bubble has an infinite number of top neighbors that may contribute to the lift force.

This reasoning can even be made more precise by considering the expression of the lift force acting on a single spherical bubble moving in a (e.g. wake-induced) rotational flow (Auton, 1987; Legendre & Magnaudet, 1998; Hallez & Legendre, 2011):

$$\boldsymbol{f}_{\text{lift}} \propto d_b^3 \rho_c \boldsymbol{\Omega} \times \boldsymbol{U}. \tag{2.20}$$

In this expression, $\boldsymbol{\Omega} = |\boldsymbol{\Omega}|\boldsymbol{e}_h$ is the liquid vorticity "seen" by the bubble and produced by the motion of all the other bubbles. No clear definition of this quantity is available if vorticity

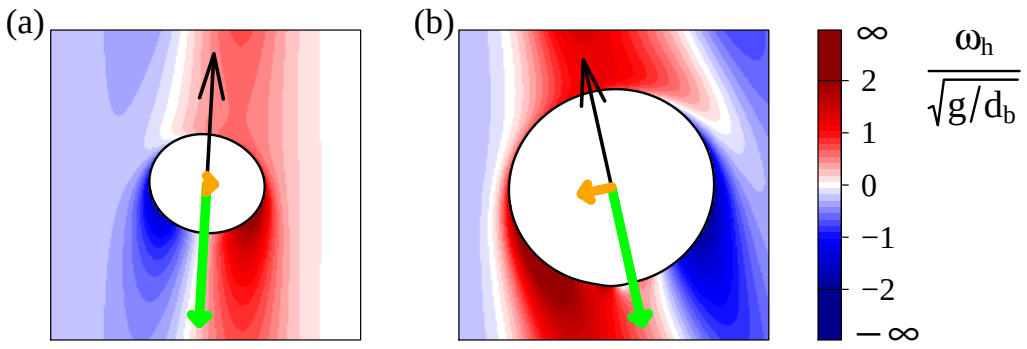

Figure 2.20 Liquid vorticity horizontal component $\omega_h = \boldsymbol{\omega} \cdot \boldsymbol{e}_h$ in the vertical plane passing through the center of a bubble and containing its drift velocity, for ordered arrays of bubbles rising steadily in an oblique direction: (a) case E1, $\phi = 0.8$ %; (b) case S5, $\phi = 6.5$ %. Positive (negative) values upstream of the bubble would give a positive (negative) contribution to the lift force as modeled by (2.20). The thin black arrow shows the direction of bubble drift velocity. The thick arrows show the magnitudes and directions of the drag (green arrows) and lift (orange arrows) forces scaled by the buoyancy force.

is not uniform at the bubble scale, as is the case in the present study, but it is reasonable to assume that it can be qualitatively estimated by examining vorticity profiles in the bubble vicinity. In turbulent flows, Merle et al. (2005) and Naso and Prosperetti (2010) approximated the velocity and vorticity "seen" by bubbles and solid particles respectively, by the average of these quantities over shells of different sizes. In order to show that our results are qualitatively consistent with (2.20), it is thus convenient to introduce an orthonormal direct basis $(\boldsymbol{e}_\parallel, \boldsymbol{e}_\perp, \boldsymbol{e}_h)$, defined by the unit vectors

$$\boldsymbol{e}_\parallel = \frac{\boldsymbol{U}}{|\boldsymbol{U}|}, \qquad \boldsymbol{e}_\perp = \frac{\boldsymbol{f}_{\text{lift}}}{|\boldsymbol{f}_{\text{lift}}|}, \qquad \boldsymbol{e}_h = \boldsymbol{e}_\parallel \times \boldsymbol{e}_\perp. \tag{2.21}$$

The bubble steady motion is contained in the vertical plane defined by $(\boldsymbol{e}_\parallel, \boldsymbol{e}_\perp)$ and $\boldsymbol{e}_h$ is the horizontal unit vector that completes the basis. We now examine the sign and magnitude of the liquid vorticity component $\omega_h = \boldsymbol{\omega} \cdot \boldsymbol{e}_h$ ahead of the bubble, where it should overall give a positive contribution to $|\boldsymbol{\Omega}|$ for the above model to be correct. We show in figure 2.20 the liquid vorticity field projected onto $\boldsymbol{e}_h$ in the vertical plane normal to $\boldsymbol{e}_h$ for two examples of steady oblique rise. The bubble in the right panel experiences a stronger lift force (indicated by the thick orange arrow) than the bubble in the left panel. This is consistent with (2.20) and the fact that, upstream of the bubble (its drift velocity being shown with the black arrow), ω_h is positive, and its magnitude is larger than that in the left panel (although only two examples are shown here the same result holds for all our simulations). In addition it is seen from figure 2.20 that ω_h is transported from the surface of preceding bubbles, hence confirming the key role played by the wakes and the associated lift force for the stability of oblique motion.

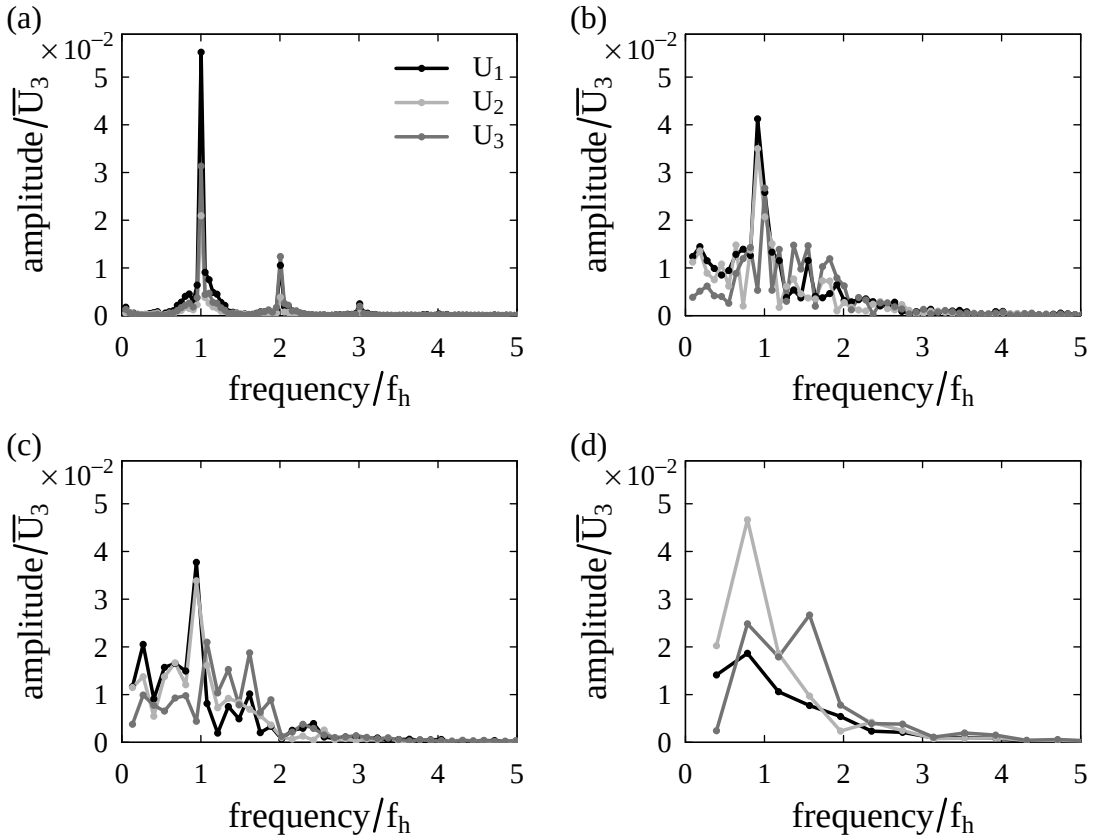

Figure 2.21 Single-sided amplitude spectra of discrete Fourier transforms of the drift velocity components time signals for case S5. Transition from oscillatory (a) to chaotic (d) motion for decreasing values of the volume fraction: (a) $\phi = 3.8$ %, (b) $\phi = 1.6$ %, (c) $\phi = 0.8$ %, (d) $\phi = 0.3$ % (). The amplitude is normalized by the average vertical drift velocity $\overline{U}_3$, the frequency is normalized by $f_h = (\overline{U}_1 + \overline{U}_2)/(2h)$. Note that due to computational cost the simulation for the lowest ϕ (d) could be not run over a large number of time periods.

We will now examine the time dependence of bubbles motion in the unsteady regimes. As illustrated in figure 2.21, which depicts the single-sided amplitude spectra of the discrete Fourier transforms of the drift velocity components time signals from the oscillatory (a) to the chaotic (d) rise regimes, a spectral analysis of the unsteady velocity signals reveals clear peaks at a frequency equal to $f_h = (\overline{U}_1 + \overline{U}_2)/(2h)$ (where the bar denotes a time-average). Normalizing frequencies by $f_3 \equiv \overline{U}_3/h$ (not shown here) does not lead to a collapse of the curves. This suggests that the force fluctuations experienced by a bubble are also driven by the interaction with the wakes of the preceding bubbles that are not on the same vertical axis. As a consequence, the dynamic behavior of a bubble in an ordered array, although greatly influenced by the direct interaction with its top neighbor, is also dictated by longer-range nonlinear interactions with other bubbles located in above horizontal planes.

In light of these results, we are now in a position to propose the following scenario for explaining the transitions between the various regimes of motion reported in figure 2.18. First, non-vertical motion can only occur when the flow conditions allow sufficiently high Reynolds numbers to be attained (here, cases E1 and S5). Vorticity then becomes significant in the vicinity of each bubble due to the wake of its predecessor; an infinitesimal asymmetry can then result in a lift force that is sufficient to result in oblique motion (Koch, 1993). If each bubble is only influenced by the wake of its immediate predecessor, this motion is steady. When the wakes extend horizontally over distances large compared to the lattice spacing, each bubble interacts with the wakes of a great number of neighbors, including some that are not located on the same vertical axis, and the motion becomes chaotic. Then, for a given flow regime, the volume fraction is in the first place related to the distance between the bubbles, but also affects the Reynolds number in a non-monotonic manner. At low volume fraction, when the Reynolds number increases with volume fraction, steady vertical rise, steady oblique rise, and unsteady oblique rise occur in that order at increasing volume fraction. At higher volume fraction, the situation becomes more complex because the Reynolds number decreases with ϕ. It appears that the dominant effect of increasing volume fraction is then not to bring the bubbles closer to each other, but to reduce their velocity, so that steady oblique rise is first recovered, and is replaced by steady vertical rise at the highest volume fractions.

2.4 Free arrays

We examine in this section the behavior of freely evolving bubbly flows as represented by the repetition of a unit cell containing several independent bubbles ("free arrays"). This problem, studied previously by several groups (e.g., Bunner and Tryggvason (2002a), Esmaeeli and Tryggvason (2005), Yin and Koch (2008)) but only at moderate and high volume fractions, is revisited here following the insights gained in the previous section for ordered arrays. Our main objective here is to investigate the dynamics of free arrays at small and intermediate volume fractions, and to compare the observed trends with those obtained for ordered suspensions.

Simulations of free arrays of bubbles have been undertaken for cases E1 and C (table 2.1). The two fluids were initially at rest, N_b identical spherical bubbles were introduced in a cubic periodic unit cell of size h (which results in a gas volume fraction $\phi = (\pi N_b d_b^3)/(6h^3)$), and gravity was switched on at time zero. It was found that the transient evolution of the system can follow either of two routes: one with successive pair coalescence events until an ordered array configuration is recovered, and the other one in which the number of bubbles remains constant throughout the simulation. The transient rise of free arrays is first described in section 2.4.1. We then focus in section 2.4.2 on systems in which coalescence is absent.

The drift velocities $\boldsymbol{U}$ reported in this section are defined at any time by (2.3), as for ordered arrays, and are therefore equal to the individual bubble drift velocities averaged over the N_b bubbles. In all simulations, the instantaneous horizontal components of $\boldsymbol{U}$ were found to be

negligibly small, so we shall hereinafter simply use U to denote the vertical component of the drift velocity vector.

2.4.1 Initial conditions and transient evolution

We first examine how the initial spatial configuration of the bubbles may affect in an irreversible manner the structure of a bubbly suspension. The N_b bubbles were initially spherical, and their positions inside the periodic computational domain was determined as follows. We first computed the locations of the M_b nodes ($M_b > N_b$) of a simple cubic lattice fitting in the periodic box and containing at least N_b nodes, that is, $M_b^{1/3} = \lceil N_b^{1/3} \rceil$ where $\lceil\ \rceil$ denotes the ceiling function. The bubbles were then placed on N_b nodes selected among the M_b available nodes by a random draw without replacement. Finally the positions of the N_b bubble centers were slightly perturbed in the three directions. For each bubble and in each direction, the perturbation was randomly drawn from a uniform distribution in the $\pm\epsilon$ interval, with ϵ chosen so that bubble interfaces were sufficiently separated to avoid immediate coalescence (with the numerical method used to capture interfaces, two bubbles automatically merge when the distance between their interfaces becomes smaller than the grid spacing). To evaluate the role played by the initial conditions on the fate of the system, several simulations of free arrays of bubbles differing only in the initial relative positions of the bubbles were conducted for each values of N_b and ϕ.

In case C, which corresponds to highly deformable bubbles of dimpled or skirted ellipsoidal-cap shapes, the bubbles were invariably found to undergo successive pair coalescence events until only one bubble remains in the unit cell, even at relatively low volume fractions (the lower simulated volume fraction is $\phi = 0.8$ %). Coalescence was also observed by Sankaranarayanan et al. (2002) for two-dimensional arrays of strongly distorted bubbles. An example of the transient evolution of the bubbles drift velocity is shown in figure 2.22 (solid and dashed lines are used before and after the first coalescence event, respectively), where it can be seen that the bubbles experience an significant acceleration prior to coalescence. This behavior can be explained as follows. When a strongly deformable bubble moves in shear flow at moderate Reynolds number, it migrates towards the region of maximum upward velocity owing to the deformation-induced lift force acting on it (Ervin & Tryggvason, 1997; Sankaranarayanan & Sundaresan, 2002; Tomiyama, Tamai, Zun, & Hosokawa, 2002; Magnaudet, Takagi, & Legendre, 2003). As a consequence, at finite volume fraction, a strongly deformable bubble feeling the flow disturbance induced by any of its above neighbors is driven towards the center of the wake of that neighbor under the effect of the lift force to form a vertically-aligned pair of bubbles. The trailing bubble is then drafted by the leading bubble until the two bubbles collide and coalesce to form a larger bubble, as exemplified by the insets in figure 2.22.

With our numerical approach, two colliding bubbles cannot bounce and as a consequence necessarily merge on contact. In this context, one may object that coalescence rates might be overestimated (the opposite applies to numerical studies based on a method that does not

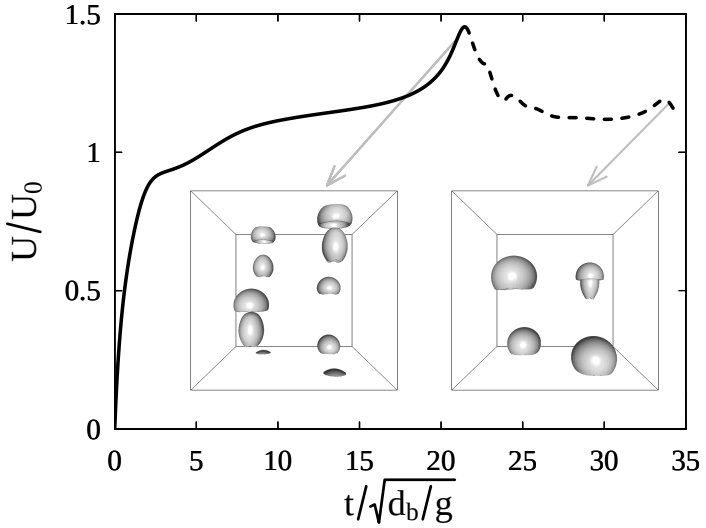

Figure 2.22 Time evolution of the average vertical drift velocity of strongly deformable bubbles, normalized by the terminal velocity of the equivalent isolated bubble, in a suspension of free bubbles for case C at $\phi = 1.6$ %. The unit cell initially contains 8 bubbles. Solid and dashed lines are used respectively before and after the first coalescence event. Insets: instantaneous location of the interfaces in the unit cell right before the first coalescence event (left) and at later times (right).

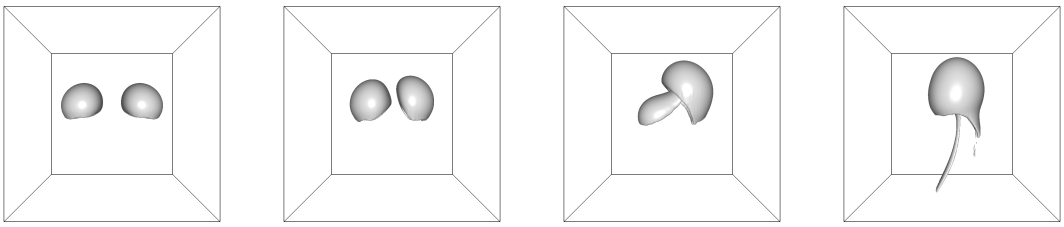

Figure 2.23 Time evolution (from left to right) of the location of the interfaces in the unit cell for an array containing initially two free bubbles at $\phi = 1.6$ % in case C.

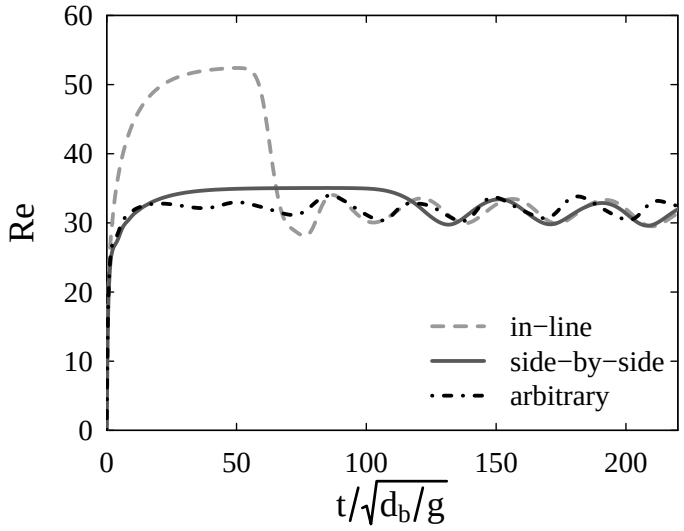

Figure 2.24 Time signals of the vertical drift velocity (given in the form of a Reynolds number) of a free array of two bubbles for various initial relative positions (case E1, $\phi = 1.6$ %).

allow deformable bubbles to merge, as in Bunner and Tryggvason (2003)). Prior experimental investigations showed that two ellipsoidal-cap bubbles rising in line at moderate Reynolds numbers always coalesce as a result of wake-induced attraction (Crabtree & Bridgwater, 1971; Narayanan, Goossens, & Kossen, 1974; Bhaga & Weber, 1980), thereby giving some confidence in our numerical predictions. The occurrence of coalescence can be delayed by choosing a different initial spatial distribution (e.g., by placing at time zero the N_b bubbles in the same horizontal plane), but cannot be avoided. The evolution of a free array of two identical bubbles initially lying in the same horizontal plane and aligned along a primary axis of the array is shown in figure 2.23: the two bubbles first rise side-by-side, but the vertical mirror symmetry is later broken and the bubbles finally coalesce. Overall our results suggest that a suspension of strongly deformed bubbles rising at low to moderate Reynolds numbers (that is, in conditions corresponding to our case C) is not stable at finite volume fraction and in practice would result in the formation of large gas slugs. We must however stress that the question whether or not the onset of coalescence is simulated accurately cannot be resolved well in the present method for these grid spacings. Moreover such a study should include validation against prior collision work. As a consequence coalescence is not studied further in the present thesis.

In contrast, coalescence was never observed for case E1 (weakly ellipsoidal bubbles), provided that the bubbles interfaces were initially sufficiently separated from each other and that the volume fraction remained below approximately 5 % (we shall elaborate on this last point in section 2.4.2.2). Examination of the suspension evolution revealed that bubbles never come into close contact, as previously observed by Esmaeeli and Tryggvason (1999) for a comparable system. After a transient regime, the flow was found to become independent of

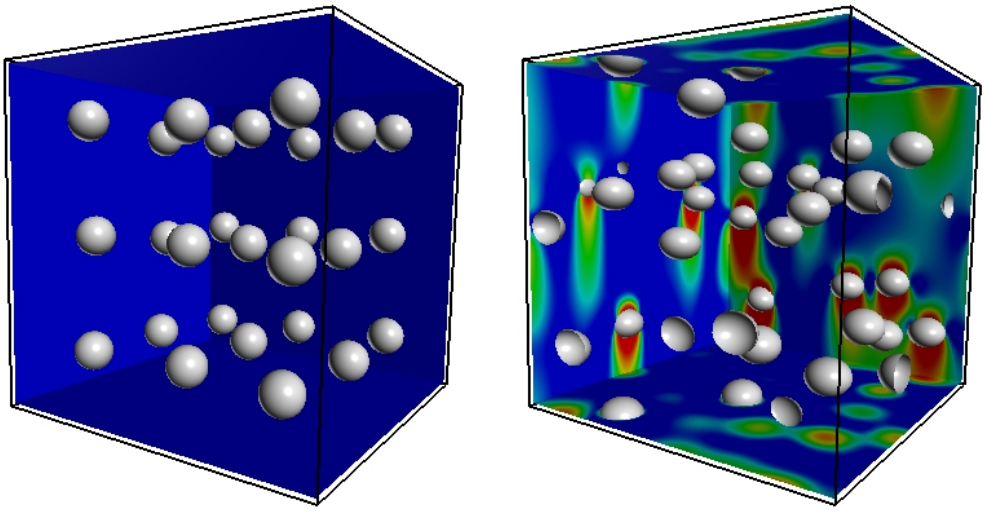

Figure 2.25 Instantaneous snapshots of a free array of 27 bubbles (case E1, $\phi = 2.4\,\%$). Left: initial state (slightly perturbed cubic array of spherical bubbles in a liquid at rest). Right: statistically steady state. Color scale: liquid vertical velocity (blue to red: lower to higher values).

the initial positions of the bubbles, and a well-defined statistically steady state was reached.

We compare in figure 2.24 the time signals of the drift velocity for an array of two free bubbles evolving from three different initial configurations: at time zero, the two bubbles were uniformly distributed along a primary axis of the periodic box, either vertical ("in-line", dashed line) or horizontal ("side-by-side", solid line), or were arbitrarily placed in the domain ("arbitrary", dashed-dotted line). In-line and side-by-side bubbles keep their relative positions for a relatively long time before reaching a statistically steady state that seems to be independent of the initial placement of the objects inside the unit cell. More generally, we found the final state reached by the system to be unique and independent of the initial positions and oblateness of the bubbles for all the values of N_b and ϕ considered in this study. Visualizations of initial and statistically steady states for a free array of 27 bubbles are presented in figure 2.25 for illustration purposes.

2.4.2 Statistically steady rise

We now examine the statistically stationary rise of free, non-coalescing, deformable bubbles at moderate Reynolds number. All the results presented below have been obtained for case E1 (table 2.1), which corresponds to weakly ellipsoidal bubbles rising at $O(10)$ Reynolds number. About fifty simulations of free arrays were run in total, corresponding to different initial conditions, numbers of bubbles, and volume fractions. For each of these, the transient evolution of the system was monitored through the time signals of the bubble drift velocity and of the interface surface area A (which is a measure of the average deformation of the N_b bubbles). Each simulation was continued until U and A became statistically stationary. Their

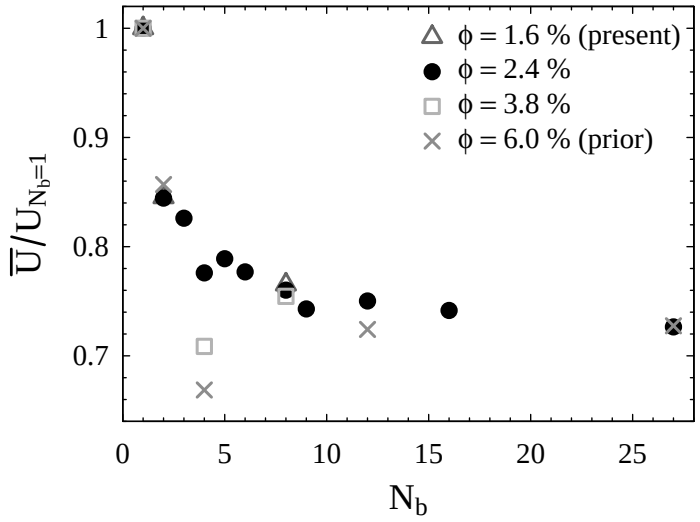

Figure 2.26 Influence of the number of bubbles on the average bubbles drift velocity for various volume fractions. The drift velocity is normalized by that obtained in the ordered configuration ($N_b = 1$). Symbols other than crosses: present DNS for case E1 ($Ar = 29.9$, $Bo = 2.0$). Crosses: prior DNS of Bunner and Tryggvason (2002a) for a comparable flow regime ($Ar = 29.7$, $Bo = 0.98$).

time averages, denoted by overbars in what follows, were then computed by averaging over a sufficient time interval.

2.4.2.1 Convergence with the number of bubbles

The influence of the number of free bubbles in the unit cell is evaluated by varying N_b from 2 to 27 while keeping the volume fraction (and all other parameters) constant. The evolution of the bubbles drift velocity with the number of bubbles is shown in figure 2.26 for $\phi = 2.4$ % (filled circles). The main effect of additional degrees of freedom is to slow down the bubbles: the drift velocity drops by 15 % when the relative motion between two bubbles is allowed, and is reduced further (up to ≈ 30 %) if the number of bubbles in the unit cell is increased. For $N_b \geqslant O(10)$, the drift velocity becomes nearly independent of the number of bubbles. The rate of convergence and the maximal relative decrease in drift velocity with the number of bubbles appear to be essentially independent of the volume fraction, at least in the limited range considered here, as shown in figure 2.26 (open triangles and squares).

The drift velocities obtained by Bunner and Tryggvason (2002a) for a similar flow regime have been reported on the same figure (crosses). It is worth mentioning that although the maximum number of bubbles shown in figure 2.26 is $N_b = 27$, Bunner and Tryggvason (2002a) have performed simulations for $1 \leqslant N_b \leqslant 216$ (see Figure 8a in their paper), and also concluded that the effect of the system size on the drift velocity becomes negligible for $N_b \geqslant O(10)$ in this flow regime. Overall the agreement between the two data sets is excellent, including in the

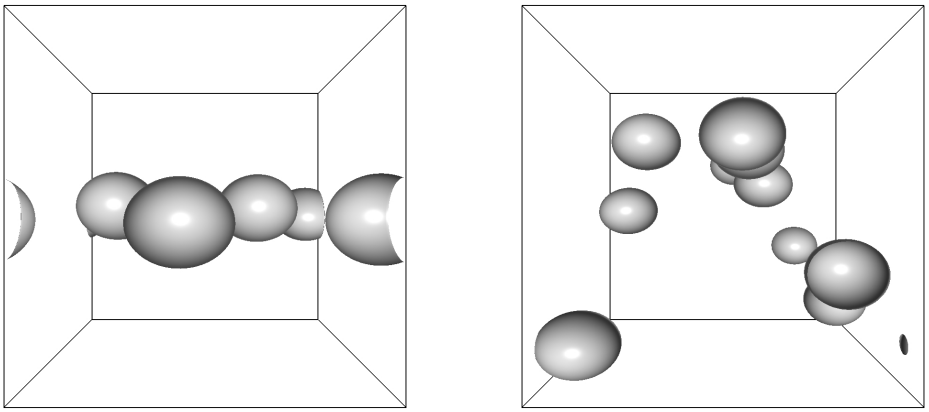

Figure 2.27 Influence of the number of free bubbles on their spatial distribution within a periodic unit cell: typical instantaneous snapshots for $N_b = 4$ (left) and $N_b = 8$ (right), for case E1 at $\phi = 3.8$ %.

peculiar case $N_b = 4$.

It can indeed be noticed in figure 2.26 that convergence is not monotonic, and that the rise is abnormally slow for $N_b = 4$. Visual inspection of the spatial distribution of the bubbles reveals a significant preference for horizontal alignment in that case. This bias is particularly pronounced for values of ϕ that are not very small and is therefore illustrated in figure 2.27 for $\phi = 3.8$ %: while the bubbles are rather uniformly distributed within the periodic cell for $N_b = 8$ (right), as is the case for other typical values of N_b, they all remain in the same horizontal plane when $N_b = 4$ (left), so that in the latter case the suspension actually consists of successive horizontal layers of bubbles. As shown by Hallez and Legendre (2011), side-by-side alignment maximizes the drag force acting on a pair of bubbles, resulting in lower drift velocities than with other types of spatial distributions.

This particular behavior for $N_b = 4$ demonstrates that an ordered microstructure is not always unstable. Such arrangements in horizontal planes are indeed possible if the number of free bubbles possesses an integer square root, due to periodicity and system symmetries. For $N_b = 9$, the bubbles also tend to arrange within a single horizontal plane, but this arrangement rapidly breaks up and is only observed intermittently. This results in the small but noticeable anomalous reduction of the drift velocity visible for $N_b = 9$ in figure 2.26. For $N_b = 16$, no horizontal layer of bubbles is formed during the simulation, and no anomaly is detectable in figure 2.26. We conclude that the artificial effects of symmetry and periodicity observed when N_b is an exact square rapidly vanish as the number N_b of independent bubbles is increased.

2.4.2.2 The effect of volume fraction on bubble drift velocity and deformation

The volume fraction has been varied from 0.2 to 3.8 % by reducing the size of the unit cell while keeping all the other parameters constant, for a number of freely moving bubbles set to $N_b = 8$. For volume fractions greater than 5 %, numerical coalescence (that is, coalescence due

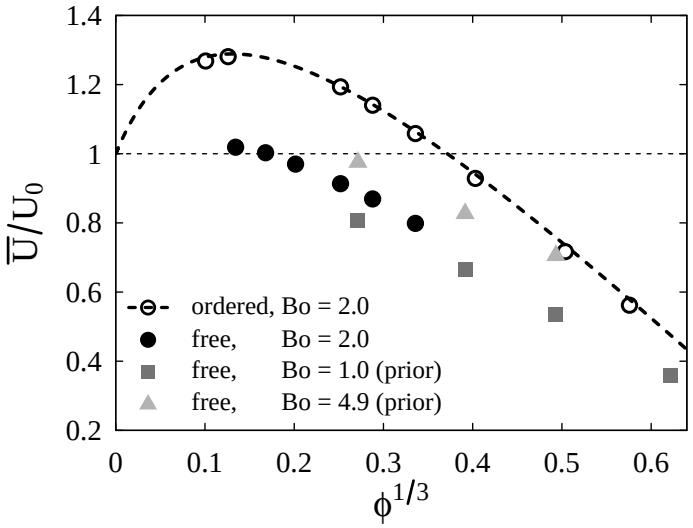

Figure 2.28 Influence of volume fraction on the bubbles drift velocity in ordered and freely evolving suspensions, with comparable Ar (≈ 30) and various Bo. The drift velocity is normalized by the terminal velocity of an isolated bubble for the same Archimedes and Bond numbers (estimated from Loth (2008)). ○ and - - - -: present DNS data, and their numerical fit, for $N_b = 1$ (ordered arrays) and $Bo = 2.0$; ●: present DNS for free arrays of 8 bubbles with $Bo = 2.0$; ■: prior DNS of Bunner and Tryggvason (2002a) for free arrays of 27 bubbles with $Bo = 0.98$; ▲: prior DNS of Bunner and Tryggvason (2003) for free arrays of 27 bubbles with $Bo = 4.9$.

to the spacing between bubble interfaces being less than the grid spacing) occurs during the transient evolution of the flow, therefore no data could be obtained for high volume fractions.

Data for fairly high volume fractions are however available from prior studies of Bunner and Tryggvason (2002a) and Bunner and Tryggvason (2003) who performed simulations of free arrays of bubbles using a front-tracking method that does not allow coalescence. In their simulations, the Archimedes numbers are similar to ours ($Ar \approx 30$) but the Bond numbers (and hence the bubble shapes) are different: the bubbles are nearly spherical ($Bo = 0.98$) in Bunner and Tryggvason (2002a), they are oblate ellipsoids ($Bo = 5.0$) in Bunner and Tryggvason (2003), our present flow conditions ($Bo = 2.0$) corresponding to an intermediate case. In order to present their results together with ours, we first estimate the terminal velocity of the corresponding isolated bubbles. We proceed for that purpose in the same manner as we did for our own simulations, that is by using the correlation of Loth (2008) for single ellipsoidal bubbles, which leads to $Re_0 = 33$ for $Bo = 0.98$, and $Re_0 = 26$ for $Bo = 5.0$.

The influence of volume fraction on the drift velocity normalized by the terminal velocity of the same bubble in unbounded liquid is shown in figure 2.28. Squares and triangles correspond to prior simulations of nearly spherical and oblate ellipsoidal bubbles, respectively. Filled circles correspond to our present simulations of weakly ellipsoidal bubbles. For comparison,

the results we obtained for the corresponding ordered arrays are shown in the same figure with open circles. Remarkably, the evolution of the drift velocity with ϕ seems to be different in dilute and fairly dense suspensions of free bubbles, as is the case when bubbles are perfectly ordered. We have checked that neither a linear evolution with ϕ nor a Richardson-Zaki law is compatible with the data presented in figure 2.28.

At moderate to fairly high volume fractions (say, $0.015 \leqslant \phi \leqslant 0.25$, that is, $0.25 \leqslant \phi^{1/3} \leqslant 0.63$), the drift velocity of free bubbles decreases approximately linearly in $\phi^{1/3}$. This scaling, which is also independent of the bubble oblateness (in the limit of the range of shapes considered here), agrees with that obtained for ordered suspensions in the same conditions.

The drift velocity dependence on volume fraction is radically different at vanishing ϕ: although we cannot approach the dilute limit in the simulations, it is clear that a simple extrapolation to $\phi = 0$ from results at larger ϕ is not feasible. In the absence of inertial effects and in this dilute limit, a linear reduction of the drift velocity with ϕ would be expected, according to the analytical solution from Keh and Tseng (1992), derived for random bubbly suspensions in the Stokes flow regime. At finite Reynolds numbers, however, inertial effects are expected to dominate far from the bubbles. The results for free arrays at low ϕ in figure 2.28 suggest strongly that bubbles in dilute suspensions rise faster than their isolated counterpart, as in ordered arrays, due to cooperative wake interactions. Such interactions would be much weaker than in ordered suspensions due to the less likely occurrence of vertical alignments (since a spherical or slightly oblate bubble lying in the wake of one of its neighbor experiences a transverse lift force directed away from the wake so that two weakly ellipsoidal bubbles cannot remain in line), but they might still play a role in the suspension dynamics. The uncertainty of the terminal velocity of isolated bubbles prevents us from drawing definitive conclusions on this point, as that would require simulations at even lower volume fractions, beyond the reach of the computational capabilities at our disposal.

The effect of volume fraction on bubble deformation is now evaluated, both qualitatively from visualizations of the flow, and quantitatively through the measurement of their interfacial surface area, larger surface areas being associated with a stronger departure from the spherical shape. We show in figure 2.29 the volume fraction dependence of the bubbles sphericity, defined as the ratio between the total surface areas of a set of N_b volume-equivalent spheres and that of the bubbles. The trends obtained for ordered and free arrays are qualitatively similar, ellipsoidal bubbles becoming more spherical as volume fraction increases. A plausible explanation of the larger oblateness (smaller sphericity) of freely moving bubbles is the weaker role of wake-induced nose elongation, due to the less likely occurrence of vertically-aligned pairs, as explained above.

The observed similarities between freely evolving suspensions and ordered arrays at small to intermediate volume fractions may be explained by the fact that in the former, the bubbles spatial distribution is nonrandom and possesses a certain degree of order. The presence of order in suspensions is classically evaluated using the structure factor or pair distribution

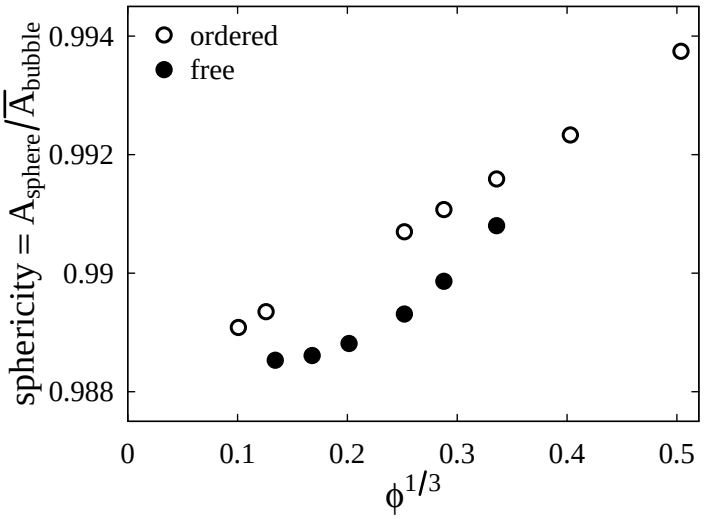

Figure 2.29 Influence of volume fraction on the bubbles sphericity in ordered (open circles) and free (filled circles) arrays for case E1. The sphericity is defined as the ratio between the total surface areas of a set of N_b volume-equivalent spheres and that of the bubbles.

function, as in the experiments of Cartellier and Rivière (2001) and Cartellier et al. (2009), and in the simulations of Bunner and Tryggvason (2002a) and Yin and Koch (2008), among others. With our numerical approach based on the level-set method, the bubble centers of mass are not tracked explicitly, so gathering statistical information about their relative positions during the course of the simulations is not straightforward and would actually requires the implementation of a dedicated tracking algorithm. For this reason the microstructure has not been evaluated quantitatively in our simulations. Nevertheless flow visualizations have been used for a qualitative evaluation of the bubble spatial distribution.

Visualizations of bubble motion revealed that free bubbles rise at comparable velocities with very weak horizontal displacements and never get close to each other for the entire range of volume fractions we considered. Their spatial distribution within the cell is fairly uniform, and their relative positions remain more or less constant as they rise, in agreement with prior observations by Esmaeeli and Tryggvason (1999), who also found, for similar flow conditions, that bubbles dispersion in the horizontal direction is almost absent.

These observations are consistent with prior quantitative evaluations of the microstructure of dilute and moderately concentrated suspensions of (nearly) spherical bubbles at $Re = O(10)$. On the experimental side, Cartellier and Rivière (2001) evidenced that in the range $10^{-4} < \phi < 10^{-2}$, a test bubble experiences a deficit of neighbors in its immediate vicinity and an excess of neighbors at the border of the deficit zone, or in other words, that a certain degree of order is present in the suspension. The magnitude and extent of the deficit zone decrease with increasing ϕ, but a clear nonrandom microstructure has been shown by Cartellier et al. (2009)

to persist at least up to $\phi = 0.08$. On the numerical side, Bunner and Tryggvason (2002a) and Yin and Koch (2008) identified analogous deficits of bubbles at short distances and excesses of bubbles farther away from a test bubble for $0.02 \leqslant \phi \leqslant 0.12$ and $\phi = 0.05$ in their respective simulations.

Although bubbles are free to sample the entire liquid, they stay with the same neighbors for long times, which explains why suspensions of free bubbles share some properties with perfectly ordered ones, at least up to moderately high volume fraction.

2.4.2.3 Comparison with experiments

Finally, we investigate the relation of our results and prior experimental data. A direct comparison between direct numerical simulations and experiments is often impossible because the typical flow conditions differ strongly between these two approaches (moderate vs. high Reynolds numbers, nearly spherical vs. wobbling bubbles, absence vs. presence of surfactants, monodispersity vs. polydispersity, constant vs. varying bubble diameter at varying ϕ, etc.). To the best of our knowledge, the only experiments carried out under conditions comparable to those in the present work are those of Martinez-Mercado et al. (2007), who measured the average velocity of nearly monodisperse air bubbles rising in a mixture of water and glycerin (50 % mass fraction), for volume fractions ranging from 0.4 to 6.5 %. Importantly, they found the bubble equivalent diameter to be almost independent of the gas volume fraction, so that comparison with our numerical data is relevant. According to the physical properties of the fluids and bubble equivalent diameter ($d_b = 1.20 \pm 0.05$ mm) reported in their paper, their experimental conditions correspond to $Ar = 26.3 \pm 1.6$ and $Bo = 0.25 \pm 0.02$. In this regime bubbles are nearly spherical (as confirmed by the photographs in their paper), so the terminal Reynolds number of the equivalent isolated bubble can be estimated from the correlation of Mei et al. (1994) (as we did for our simulations of spherical bubbles), which yields $Re_0 = 29.7 \pm 3.1$. These experimental conditions are therefore comparable to our case E1 ($Ar = 29.9$, $Bo = 2.0$, $Re_0 = 31$) in terms of Archimedes and Reynolds numbers, but not in terms of Bond numbers.

The evolution of the bubble drift velocity with volume fraction is shown in figure 2.30, wherein experimental measurements are represented by crosses and the present numerical results by circles. Numerical and experimental trends are very similar, both exhibiting two different scaling laws at moderate and low volume fractions. In particular, experimental data are compatible, like the numerical ones, with a linear dependence of the rise velocity on $\phi^{1/3}$ in the case of moderately concentrated suspensions. This behavior suggests that ordered arrays are able to capture some properties of real bubbly suspensions. Besides, we note that experimental velocities are systematically lower than that predicted from our simulations. Although perfect agreement is not expected due to the differences in the flow conditions, as discussed below, we speculate this may also be partly due to our work being on perfectly homogeneous suspensions, whereas experiments may be affected by the presence of walls and of weak gradients.

The main difference between our simulations and the above-mentioned experiments is the

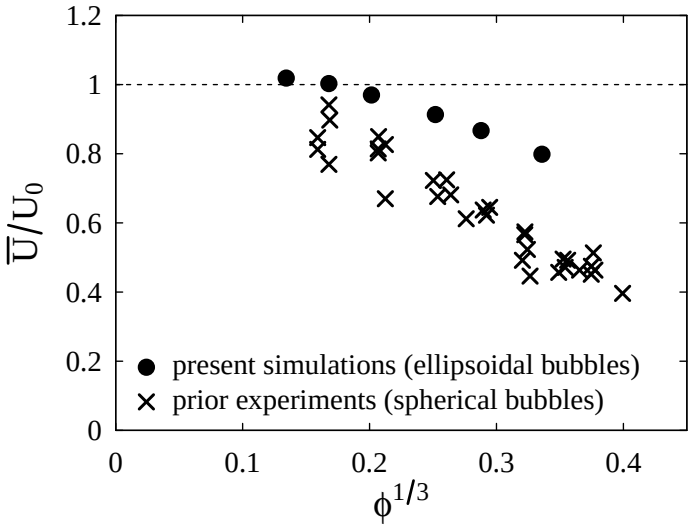

Figure 2.30 Influence of volume fraction on the normalized drift velocity of freely rising bubbles: comparison between simulations and experiments. •: present DNS ($N_b = 8$, $Ar = 29.9$, $Bo = 2.0$, $Re_0 = 31$); ×: experiments of Martinez-Mercado, Palacios-Morales, and Zenit (2007) ($Ar = 26.3 \pm 1.6$, $Bo = 0.25 \pm 0.02$, $Re_0 = 29.7 \pm 3.1$). The terminal velocities U_0 in unbounded liquid have been estimated from the correlation of Loth (2008) for numerical simulations (ellipsoidal bubbles) and from the correlation of Mei, Klausner, and Lawrence (1994) for experiments (spherical bubbles).

value of the Bond number which directly alters the bubble shape (ellipsoidal in the former, nearly spherical in the latter). It follows that a quantitative comparison of bubble shapes between our numerical results and experimental measurements is not possible. It is however worth mentioning that, in their experiment at high Reynolds number ($Re \approx 400$), Zenit et al. (2001) found the aspect ratio of ellipsoidal bubbles to decrease with increasing volume fraction (from $\chi = 1.5$ at $\phi \approx 0$ to $\chi = 1.2$ at $\phi \approx 0.05$). This trend is qualitatively similar to our numerical results presented in figure 2.11 for an ordered array of ellipsoidal bubbles with comparable aspect ratios, and more generally, is qualitatively similar to what we observe in our simulations of both ordered and free arrays of ellipsoidal bubbles.

To further support the idea that ordered arrays may be relevant to bubbly flows of practical interest, experimental data obtained by Garnier et al. (2002), Riboux et al. (2010), and Colombet et al. (2015) for the air-water system at high Reynolds number ($Re \gg 100$) are presented in figure 2.31 in the form $\overline{U}$ vs. $\phi^{1/3}$. Figure 2.31 bears a striking resemblance with figure 2.30: at moderate to fairly high volume fractions (say $0.2 \leqslant \phi^{1/3} \leqslant 0.5$, that is, $0.008 \leqslant \phi \leqslant 0.13$) the bubble velocity decreases linearly with $\phi^{1/3}$ whereas in the dilute limit a different scaling law seems to hold. We have checked that neither a linear evolution with ϕ nor a law of the form $\overline{U} \propto (1-\phi)^n$ (with n a constant, possibly different for each data set) is compatible with the data presented in figure 2.31. It is also worth mentioning that some of

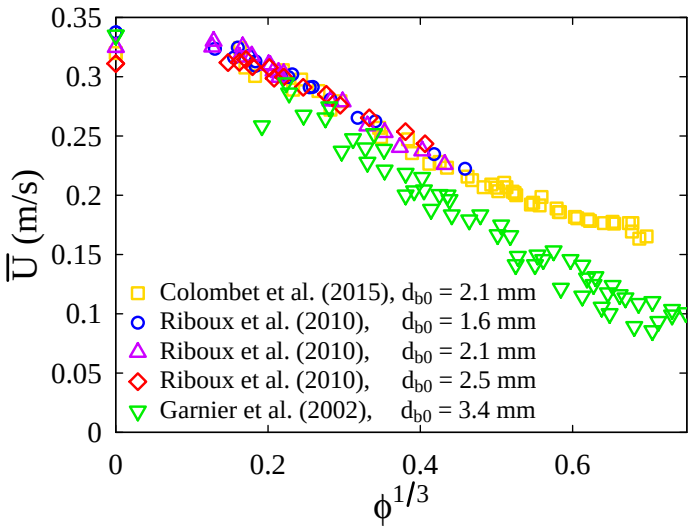

Figure 2.31 Prior experimental data for air bubbles rising in water: $\overline{U}$ (average drift velocity in meters per second) replotted versus $\phi^{1/3}$ (with ϕ the gas volume fraction). In the legend, d_{b0} is the experimentally-determined bubble diameter at zero volume fraction.

these data sets are consistent with the notion that, in dilute bubbly suspensions, the bubble drift velocity may be higher than that of a single bubble (although again definitive conclusions can hardly be drawn on this point owing to experimental uncertainty on the values of the isolated bubble velocity).

Overall our numerical results as well as prior experimental data suggest that some properties of bubbly flows are sensitive to the presence of order, and that modeling a bubbly suspension by a cubic lattice of bubbles to investigate such properties is not irrelevant, except maybe at very high volume fractions, and as long as clusters are not formed (whose dynamic may be quite different and that could lead to bubbly flows in the heterogeneous regimes).

2.4.2.4 Liquid agitation induced by bubble motion

As bubbles rise through a liquid at rest, they induce velocity fluctuations in the continuous phase. These fluctuations give rise to Reynolds stresses and play a crucial role for the mixing of chemical species or temperature. The properties of bubble-induced agitation, also called pseudo-turbulence, are beyond the scope of the present study. Nevertheless, for completeness, we provide in this section results for the liquid velocity fluctuations, denoted $\boldsymbol{u}' = (u', v', w')$, averaged over the liquid phase and over time (this double average is denoted by angular brackets hereinafter).

We show in figure 2.32 the evolution of the componentwise liquid velocity variance as a function of the number of bubbles in the unit cell ($2 \leqslant N_b \leqslant 27$) at $\phi = 2.4\,\%$. It appears that for $N_b \geqslant O(10)$, the liquid velocity fluctuations (especially the horizontal ones) are approximately constant, as is the case for the bubble rise velocity. For comparison, the results obtained by

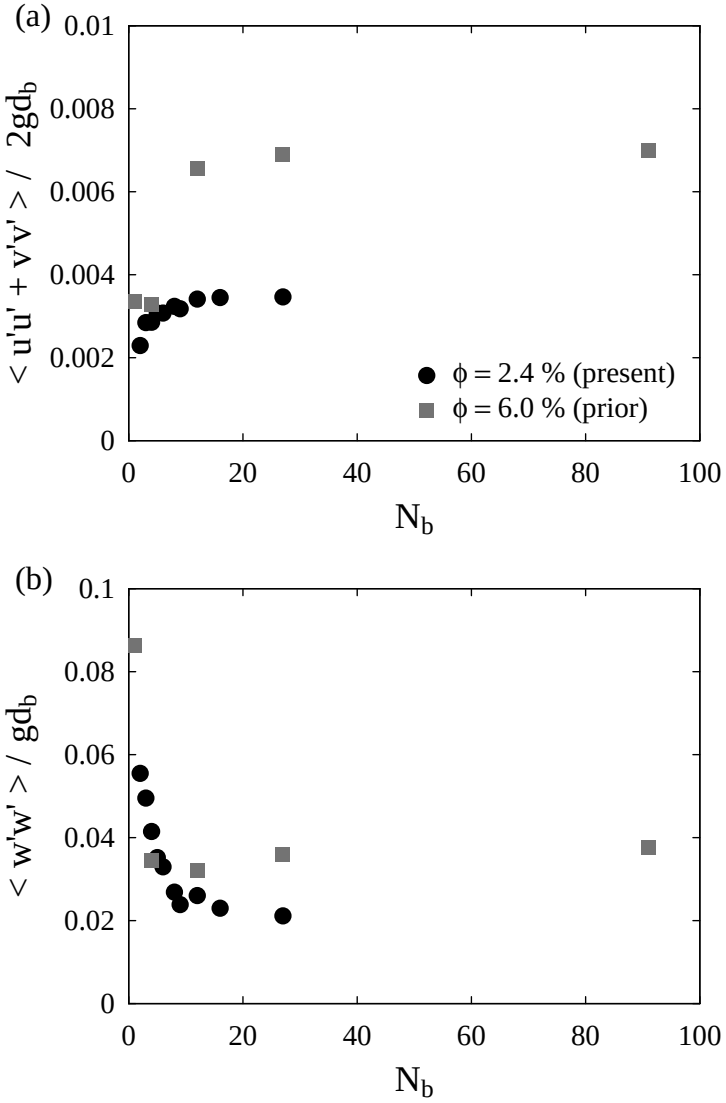

Figure 2.32 Influence of the number of bubbles on the componentwise liquid velocity variance: (a) horizontal components and (b) vertical component. ●: present DNS ($Ar = 29.9$, $Bo = 2.0$, $Re_0 = 31$) at $\phi = 2.4$ %; ■: prior DNS of Bunner and Tryggvason (2002a) for a comparable flow regime ($Ar = 29.7$, $Bo = 0.98$, $Re_0 = 33$) at $\phi = 6$ %.

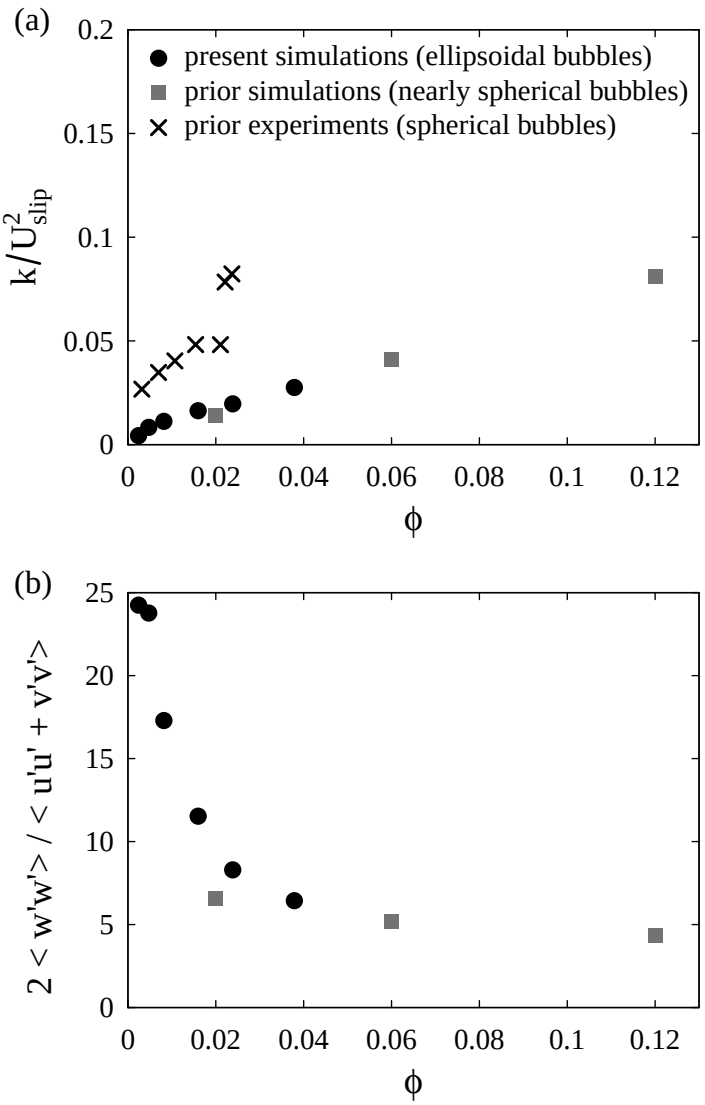

Figure 2.33 Influence of volume fraction on (a) the liquid fluctuating kinetic energy normalized by the bubble slip velocity squared, and (b) the associated anisotropy ratio. The bubble slip velocity is given by $U_{\text{slip}} = U/(1-\phi)$, with U the bubble drift velocity. ●: present DNS ($N_b = 8$, $Ar = 29.9$, $Bo = 2.0$, $Re_0 = 31$); ■: prior DNS of Bunner and Tryggvason (2002a) ($N_b = 27$, $Ar = 29.7$, $Bo = 0.98$, $Re_0 = 33$); ×: experiments of Martinez-Mercado, Palacios-Morales, and Zenit (2007) ($Ar = 26.3 \pm 1.6$, $Bo = 0.25 \pm 0.02$, $Re_0 = 29.7 \pm 3.1$).

Bunner and Tryggvason (2002b) in a comparable flow regime, albeit at $\phi = 6$ %, are plotted in the same figure. The convergence with the system size seems to be comparable in both studies for the horizontal fluctuations, but rather different for the vertical ones. A more in-depth study would be required to explain this discrepancy and to draw definitive conclusions.

A rigorous study of bubble-induced agitation may require more than 8 bubbles in the cell, however we only have information about the effect of volume fraction for $N_b = 8$. The effect of ϕ on the liquid velocity variance is presented in figure 2.33: the fluctuating kinetic energy $k = \langle u'u' + v'v' + w'w' \rangle / 2$ is shown in figure 2.33a, and the associated anisotropy ratio is shown in figure 2.33b. Our numerical data are depicted by circles, and those obtained by Bunner and Tryggvason (2002b) with $N_b = 27$ bubbles are represented by squares. Agreement between the two data sets appears to be good. Note that in figure 2.33a, we have normalized k by U_{slip}^2, where U_{slip} is the bubble slip velocity defined as the bubble velocity relative to the liquid velocity. The slip velocity relates to the bubble drift velocity U through $U_{\text{slip}} = U/(1-\phi)$. This normalization arises from the study of Bunner and Tryggvason (2002b), who found $k \propto \phi U_{\text{slip}}^2$. Our results indicate that this scaling does not hold at small volume fractions.

Finally, we compare these numerical results with experimental measurements. The fluctuating kinetic energy of the liquid phase determined experimentally by Martinez-Mercado et al. (2007) in a comparable flow regime is shown in figure 2.33a with crosses (the anisotropy ratio is not provided in their paper). As previously observed by Bunner and Tryggvason (2002b) and Martinez-Mercado et al. (2007), the experimental values are much higher than the numerical ones (by a factor of 3 to 4). However, it must be stressed that although the flow regimes are comparable, the Bond numbers are markedly higher in the simulations than in the experiments. A quantitative comparison is therefore not necessarily relevant (the same applies to the bubble rise velocity shown in figure 2.30, which was found to be smaller in the experiments than in the simulations). A further cause for the difference could be that agitation is increased in the experiments due to the presence of walls and of weak gradients. Further investigations, far beyond the scope of the present thesis, would be needed for definitively explaining this apparent discrepancy.

2.5 Conclusions

The effect of volume fraction ϕ on the drift velocity and deformation of bubbles has first been investigated when these are arranged in a cubic array. A non-monotonic behavior of the drift velocity U at increasing volume fraction has been obtained in the whole range of parameters considered from the DNS; this has been supported by an analysis in the limit of weakly inertial suspensions of spherical bubbles. For low values of ϕ, "cooperative" wake interactions dominate and lead to an increase of U at increasing volume fraction, whereas the opposite behavior occurs in the limit of large ϕ because of the predominance of "hindering" viscous interactions. These findings have been supported further by comparison with the drag

on a bubble behind another bubble when no other bubbles are present. A semiempirical law for the volume fraction dependence of the drift velocity, consistent with our numerical results even in the case of highly deformed bubbles, has also been proposed. The investigation of bubble shapes has shown that ellipsoidal and skirted bubbles tend to become spherical at increasing volume fraction, and that the fore-and-aft asymmetry of isolated ellipsoidal bubbles is reversed for non-vanishing values of ϕ. An oblique motion of the bubbles has been observed for certain parameter values, and has been supported by the above-mentioned analysis. In this regime, the lift coefficient can be approximated by that of bubble pairs that are aligned vertically. The behavior in this regime can be steady, oscillatory or chaotic, the latter arising if the horizontal extension of the bubbles wakes is large enough to allow interaction of bubbles with the wakes of neighbors which are not vertically aligned with them. A scenario explaining the transitions between these three regimes has been proposed.

The free rise of weakly deformed bubbles at moderate Reynolds number has then been investigated for small and intermediate volume fractions. Simulations of free arrays of bubbles revealed that these share some common properties with ordered ones. Most notably, the drift velocity of free bubbles decreases linearly in $\phi^{1/3}$ at moderately high ϕ whereas a different scaling law holds in the limit of low ϕ, as in ordered suspensions. This change of behavior is compatible with available experimental data, and is believed to be responsible for the confusion in the literature regarding the form of empirical correlations in the context of corresponding asymptotic expressions. In addition, deformable bubbles have been observed to become spherical as the volume fraction is increased, as in ordered arrays. We attribute the similarities between ordered and freely evolving suspensions to the fact that free bubbles were observed to keep the same neighbors for a long time, in agreement with prior work indicating that a certain degree of order is present in bubbly flows at comparable Reynolds number and volume fractions.

The present work is restricted to bubbles rising at a small to moderate Reynolds numbers. Beyond this, the dynamics of a bubble swarm will be enriched by the possibility of a single bubble already exhibiting path instabilities, shape oscillations, and turbulent wakes (e.g., Veldhuis (2007), Ern, Risso, Fabre, and Magnaudet (2012)). The simulation of such flow regimes would require substantially larger computational resources, as comparatively thin boundary layers would have to be resolved. In addition, the present conclusions apply to perfectly homogeneous systems, perfectly monodisperse suspensions, and perfectly clean bubbles. Weak shear, polydispersity, and interface contamination may all have significant effects in real bubbly flows (Magnaudet & Eames, 2000; Takagi & Matsumoto, 2011).

Chapter 3

Scalar mixing in laminar bubbly flows

The effective diffusivity of a bubbly suspension

Contents

3.1 Introduction

Bubble columns are widely employed in industry because they can offer excellent mixing characteristics without requiring any additional mechanical stirring. They are conceptually simple: a gas is sparged at the bottom of a liquid-filled vessel, and the bubbles rise under the effect of buoyancy. Mixing is then greatly enhanced owing to the liquid agitation induced by the bubble motion. The ability to predict the mixing properties of bubbly suspensions is crucial to design and operate such industrial equipment. However, most often, one is bound to rely on empirical correlations.

In this chapter we address the problem of scalar mixing in laminar bubbly suspensions. The scalar may represent, for example, the concentration of a chemical species, or the fluid temperature. In general, gradients of temperature and concentration can induce fluid motion and influence the velocity field through density and viscosity changes. When these gradients are small, such effects are sufficiently weak to be neglected. Temperature and solute concentration can then be considered as passive scalars, and are simply referred to as "scalars" hereinafter.

Our present interest is not in the detailed processes occurring at the scale of one bubble (termed hereinafter the "microscale") but rather in the conservation equations and constitutive relations governing the dispersion of a scalar in a bubbly suspension over much larger scales (termed hereinafter the "macroscale"). Under the assumption of macroscale homogeneity and stationarity, scalar dispersion in multiphase systems can be described by a macroscale version of Fick's (or Fourier's) law which relates the macroscale scalar flux to the macroscale scalar gradient through an effective diffusivity tensor (Batchelor, 1974; Koch & Brady, 1985, 1987b). This effective diffusivity is defined from an Eulerian perspective. Experimentally, scalar dispersion is usually investigated from a Lagrangian point of view. In the Lagrangian framework, the effective diffusivity is defined as the long-time limit of the time rate of change of a fluid tracer's mean-square displacement, that is, as a measure of spread about the mean position. Koch and Brady (1987b) demonstrated that the Lagrangian effective diffusivity is equivalent to the symmetric part of the Eulerian effective diffusivity, and that the antisymmetric part of the Eulerian effective diffusivity is associated with anisotropic microstructures.

Scalar dispersion in a suspension of particulates (bubbles, drops, or rigid particles) results from two processes of very different nature: the diffusion by the random Brownian motion of the molecules, and the convection by the fluid velocity disturbances induced by the particulate motion. The relative importance of these two processes is controlled by the Péclet number $Pe = Ud_b/D_c$, where U is the characteristic velocity of the particulates relative to that of the system, d_b is the characteristic size of the particulates, and D_c is the diffusivity of the bulk. When $Pe = 0$, the effective diffusivity is purely diffusive and depends only on the particulate-to-bulk diffusivity ratio, particulate volume fraction, and suspension microstructure (i.e., the positions, shapes, and orientations of the inclusions). This particular situation is essentially relevant to heat and electricity conduction in composite materials. When $Pe \gg 1$, the dominant

contribution to the effective diffusivity is due to convective mixing. This last regime is that generally met in bubbly flows.

Recently Alméras et al. (2015) investigated experimentally the dispersion of a low-diffusive dye within a homogeneous swarm of high-Reynolds-number rising bubbles at $Pe = O(10^6)$. They showed that scalar mixing primarily results from pseudo-turbulence, i.e., from the liquid agitation produced by bubble wake interactions, and can be modeled in a manner analogous to dispersion in real shear-induced turbulence (G. I. Taylor, 1922). Apart from the work of Alméras et al. (2015), the only other experimental investigation of mixing in homogeneous bubbly flows reported in the literature is the preliminary study of Mareuge and Lance (1995) which consists in a single data point. To the best of our knowledge, neither theoretical nor numerical investigations of scalar mixing in homogeneous bubbly flows have been reported so far. Theoretical work is, however, available for other types of multiphase systems, and we shall review these in the subsequent paragraphs.

A class of analytical work is devoted to the study of dilute systems with fixed random microstructure. In the absence of convection ($Pe = 0$), the analytical expression of the effective diffusivity is available in the dilute limit (e.g., Maxwell (1873), Jeffrey (1973)). In the presence of a bulk convective motion ($Pe > 0$), the problem of scalar dispersion has been analyzed by Koch and Brady (1985) for Stokes flow through a random bed of fixed solid spheres. Using the method of conditional averaging devised by Hinch (1977), Koch and Brady (1985) carried out an asymptotic analysis in low volume fraction of the effective diffusivity for all values of the Péclet number. Three mechanisms causing dispersion at high Péclet number have been identified: mechanical dispersion resulting from the stochastic velocity field in the bulk, which is independent of Brownian diffusion and grows as Ud_b, holdup dispersion in stagnant and recirculating regions which is proportional to $U^2 d_b^2/D_c$, and boundary-layer dispersion which grows as $Ud_b \ln(Ud_b/D_c)$ near the solid surfaces.

Another class of analytical studies assumes a periodic microstructure. For the pure diffusion problem ($Pe = 0$), analytical solutions have been derived for a composite material consisting of regularly arranged spheres embedded in a homogeneous matrix (Rayleigh, 1892; Sangani & Acrivos, 1983b), and the effect of anisotropy has been investigated by considering periodic arrangements of spheroidal inclusions (Kushch, 1997; Harfield, 1999). In the presence of convection ($Pe > 0$), the general theory of dispersion developed by Brenner (1980) and Brenner and Adler (1982) provides a consistent framework for determining the effective diffusivity in spatially periodic media. Koch et al. (1989) carried out explicit calculations for a periodic porous medium consisting of fixed solid particles arranged in a cubic lattice and embedded in a continuous phase which motion is governed by the Stokes equations. They showed that in ordered systems, the mechanical dispersion encountered in random media is absent, and that at high Péclet number, either Taylor dispersion, growing as $U^2 d_b^2/D_c$, or enhanced diffusion, which is proportional to D_c, is obtained depending on the direction of the mean flow relative to the lattice structure.

In bubbly flows, the spatial arrangement of the inclusions evolves in time, the microstructure of the suspension is unknown a priori, and Stokes flow conditions are rarely met. For these reasons, prior analyses are, a priori, not applicable to bubbly suspensions. Nevertheless, we showed in chapter 2 that the dynamics of freely evolving bubbly suspensions at moderate Reynolds number shares some common features with that of ordered arrays of bubbles. It is therefore of fundamental interest to investigate, contrast and compare the mixing properties of ordered and freely evolving bubbly suspensions in light of prior asymptotic analyses for ordered and random arrangements of rigid particles.

In this chapter we investigate scalar dispersion in ordered and freely evolving bubbly suspensions, with a focus on the contribution of bubble-induced velocity disturbances. The first objective is to provide a general framework for the macroscale description of scalar mixing by an effective diffusivity tensor, and to propose a practical mean to determine the effective diffusivity from direct numerical simulations. The second objective is to elucidate the role played by liquid inertia and hydrodynamic interactions in ordered suspensions, using simulation and analysis. The third objective is to investigate the effective diffusivity of freely evolving suspensions for a wide range of Péclet numbers, to compare it with that obtained for ordered suspensions, and to evaluate the effect of introducing additional degrees of freedom in the system.

3.2 Theoretical framework

The purpose of this section is to provide a theoretical framework for the macroscale description of scalar transport in suspensions. It builds on the work of Koch and Brady (1985) and Koch and Brady (1987b) on dispersion in porous media and packed beds. The macroscale we consider is the scale at which the suspension may be seen as a homogeneous continuum in a stationary state, without distinction between the two phases. We first derive an ensemble-average transport equation from the local transport equations that apply in each phase. Such a derivation is, to the best of our knowledge, not available in the literature. This average equation is closed, under the assumption of statistical homogeneity and time independence, by introducing an effective diffusivity tensor. In the context of monodisperse bubbly suspensions, this effective diffusivity is expected to depend on a limited number of crucial dimensionless groups. These are identified at the end of this section. Subscripts d and c are used throughout to refer to the disperse and continuous phases, respectively.

3.2.1 Local governing equations

The general problem we consider is that of heat or mass transfer through a monodisperse suspension of particulates (bubbles or drops) in the absence of phase change or chemical reactions. The fluid motion in each phase is governed by the incompressible Navier-Stokes equations, which are coupled at the interface by fluid-fluid boundary conditions. These are provided in section 1.2.1, and we shall focus here on scalar transport.

In each phase $n = \{c, d\}$, the conservation equation for a scalar c_n reads

$$\frac{\partial c_n}{\partial t} + \boldsymbol{\nabla} \cdot \boldsymbol{q_n} = 0 \qquad \text{if } \boldsymbol{x} \in \mathcal{V}_n \tag{3.1a}$$

where $\boldsymbol{q}_n$ is the flux of scalar given by

$$\boldsymbol{q}_n = \boldsymbol{u}_n c_n - D_n \boldsymbol{\nabla} c_n \tag{3.1b}$$

with $\boldsymbol{u}_n$ the solenoidal velocity field, D_n the diffusivity, and $\mathcal{V}_n$ the set of points that belong to phase n. In the context of heat transfer, (3.1) derives from the energy balance upon neglecting viscous heating, in this case c_n is the temperature and D_n is the thermal diffusivity as defined by Fourier's law. In the context of mass transfer, (3.1) describes the transport of a chemical species present at very low concentration so that Fick's law describes the conservation of mass, in that case c_n is the concentration and D_n is the molecular diffusivity.

At the interface, solute mass (for concentration) or thermal energy (for temperature) conservation yields

$$D_c \boldsymbol{\nabla} c_c \cdot \boldsymbol{n} = D_d \boldsymbol{\nabla} c_d \cdot \boldsymbol{n} \qquad \text{if } \boldsymbol{x} \in \mathcal{S}_i \tag{3.2}$$

where $\boldsymbol{n}$ is the unit vector normal to the interface and directed outward from the disperse phase, and $\mathcal{S}_i$ contains the points at the interface. It is further assumed that the fluid interface is maintained at thermodynamic equilibrium, which implies the equality of temperatures and chemical potentials on both sides of the interface. The condition of thermal and chemical equilibrium reads

$$c_d = m c_c \qquad \text{if } \boldsymbol{x} \in \mathcal{S}_i \tag{3.3}$$

where $m = 1$ if c_n stands for the temperature, and m is the dimensionless Henry's law constant (also known as the partition coefficient) if c_n is the solute concentration.

3.2.2 Average transport equation

In order to obtain a macroscopic equation for scalar transport, we consider an ensemble of realizations of the suspension, these realizations having the same macroscopic conditions (e.g., fluid properties, volume fraction) but different microscopic configurations (e.g., particulate individual positions and velocities), and average over those realizations. In concrete terms, ensemble averaging is realized by averaging over a large number of experiments run under identical macroscopic conditions. The ensemble-averaged transport equation is derived from local transport equations and interface boundary conditions in appendix B, we only provide here the resulting formulation.

We loosely introduce the following notations (for more rigorous definitions the reader is referred to appendix B.2):

- the ensemble average $\langle f \rangle(\boldsymbol{x}, t)$, which is the unconditional average of $f(\boldsymbol{x}, t)$ over an infinitely large number of realizations of the suspension, with f being defined in a generalized sense in the entire suspension;

- the phase average $\langle f \rangle_n(\boldsymbol{x}, t)$, with $n = \{c, d\}$, which is the conditional average of $f_n(\boldsymbol{x}, t)$ over the subset of realizations wherein $\boldsymbol{x}$ belongs to phase n at time t, with f_n being defined in phase n only;
- the volume fraction $\phi(\boldsymbol{x}, t)$, which is defined in the statistical sense: it is the fraction of realizations for which the point $\boldsymbol{x}$ lies inside the disperse phase at time t.

In what follows, unnecessary references to $\boldsymbol{x}$ and t are dropped.

The velocity fluctuations are defined in the usual manner in each phase by

$$\boldsymbol{u}_c' = \boldsymbol{u}_c - \langle \boldsymbol{u} \rangle \quad \text{and} \quad \boldsymbol{u}_d' = \boldsymbol{u}_d - \langle \boldsymbol{u} \rangle, \tag{3.4}$$

and the scalar fluctuations are defined by

$$c_c' = c_c - P\langle c \rangle \quad \text{and} \quad c_d' = c_d - mP\langle c \rangle, \tag{3.5}$$

with

$$P = \frac{1}{1 + \phi(m-1)}. \tag{3.6}$$

This particular definition arises from the unequal distribution of the scalar between the two phases when $m \neq 1$ (it is equivalent to $c_n' = c_n - \langle c \rangle$ when $m = 1$). By definition, the scalar fluctuations are zero when the system is at equilibrium, that is, in the absence of scalar gradient in each phase (see appendix B.2.1 for more details).

The ensemble-averaging procedure provides the conservation law for the average scalar field:

$$\frac{\partial \langle c \rangle}{\partial t} + \boldsymbol{\nabla} \cdot \langle \boldsymbol{q} \rangle = 0, \tag{3.7}$$

and the following expression of the average flux in statistically homogeneous systems:

$$\langle \boldsymbol{q} \rangle = \boldsymbol{U}_s \langle c \rangle - D_s \boldsymbol{\nabla} \langle c \rangle + (1-\phi)\langle \boldsymbol{u}' c' \rangle_c + \phi \langle \boldsymbol{u}' c' \rangle_d - (1-\phi) D_c \langle \boldsymbol{\nabla} c' \rangle_c - \phi D_d \langle \boldsymbol{\nabla} c' \rangle_d \tag{3.8}$$

where $\boldsymbol{U}_s$ and D_s are constants given by

$$\boldsymbol{U}_s = \langle \boldsymbol{u} \rangle + \phi(m-1)P\boldsymbol{U}, \tag{3.9}$$

$$D_s = D_c + \phi m P (D_d - D_c), \tag{3.10}$$

and where $\boldsymbol{U} = \langle \boldsymbol{u} \rangle_d - \langle \boldsymbol{u} \rangle$ is the disperse phase drift velocity. These terms can be understood as follows:

- $\boldsymbol{U}_s \langle c \rangle$ is the advection of the average scalar field at an average velocity $\boldsymbol{U}_s$ which is, in general, different from $\langle \boldsymbol{u} \rangle$ because of the unequal partitioning ($m \neq 1$) of the scalar between the two phases and of the relative motion (the drift) between the disperse phase and the entire system;
- $-D_s \boldsymbol{\nabla} \langle c \rangle$ is the diffusion of the average scalar field with an average diffusivity D_s which is equal to the average diffusivity of the suspension weighted by the scalar equilibrium distribution; in particular, when $m = 1$, D_s is simply the average diffusivity (not to be confused with the *effective* diffusivity defined in the next subsection) of the suspension;

- $(1-\phi)\langle \boldsymbol{u}'c'\rangle_c + \phi\langle \boldsymbol{u}'c'\rangle_d$ corresponds to the advection of the scalar fluctuations by the velocity fluctuations in both phases;
- $-(1-\phi)D_c\langle \boldsymbol{\nabla} c'\rangle_c - \phi D_d\langle \boldsymbol{\nabla} c'\rangle_d$ is the diffusive flux due to the perturbation of the scalar field in both phases induced by the presence of the particulates.

Various expressions of the average flux can be found in the literature, e.g., in Koch and Brady (1985) (equation (2.3b) therein, where the scalar fluctuation is defined as $c_n' = c_n - \langle c\rangle$) or in Koch and Brady (1987b) (equation (3b) therein, the scalar fluctuation being defined as in (3.5)). Our formulation is essentially equivalent to theirs, except that

(i) it does not assume a zero velocity inside the particulates (in their case, the particulates are rigid and fixed), and

(ii) it does not involve the product of generalized functions, the definition of which is ambiguous (in their expression a Heaviside step function is multiplied by a Dirac delta function).

Besides, although an alternative formulation has been preferred here, the diffusive part of the average flux can be written in a form in keeping with prior work on the conduction problem (Maxwell, 1873; Jeffrey, 1973), as explained in appendix B.2.3.

3.2.3 Effective diffusivity

When the suspension is statistically homogeneous and in a statistically stationary state, the linearity in c of the local flux (3.1b) results, in the presence of an imposed constant average scalar gradient, in a macroscale constitutive relation of the form (Batchelor, 1974; Koch & Brady, 1985, 1987b):

$$\langle \boldsymbol{q}\rangle = \boldsymbol{U}_s\langle c\rangle - \boldsymbol{D}^{\mathrm{eff}}\cdot\boldsymbol{\nabla}\langle c\rangle \tag{3.11}$$

where $\boldsymbol{U}_s$ is given by (3.9) and $\boldsymbol{D}^{\mathrm{eff}}$ is a constant effective diffusivity tensor. Comparison of the effective diffusivity definition (3.11) with the average flux expression (3.8) yields the expression of the effective diffusivity.

In section 3.2.2 we identified different transport mechanisms contributing to the average flux. In order to represent these, we split the effective diffusivity into average, convective, and diffusive contributions:

$$\boldsymbol{D}^{\mathrm{eff}} = D_s\boldsymbol{I} + \boldsymbol{D}^{\mathrm{conv}} + \boldsymbol{D}^{\mathrm{diff}}, \tag{3.12a}$$

where D_s is given by (3.10) and where the expressions of $\boldsymbol{D}^{\mathrm{conv}}$ and $\boldsymbol{D}^{\mathrm{diff}}$ in terms of microscopic quantities stem from identification with (3.8):

$$\boldsymbol{D}^{\mathrm{conv}}\cdot\boldsymbol{\nabla}\langle c\rangle = -(1-\phi)\langle \boldsymbol{u}'c'\rangle_c - \phi\langle \boldsymbol{u}'c'\rangle_d, \tag{3.12b}$$

$$\boldsymbol{D}^{\mathrm{diff}}\cdot\boldsymbol{\nabla}\langle c\rangle = (1-\phi)D_c\langle \boldsymbol{\nabla} c'\rangle_c + \phi D_d\langle \boldsymbol{\nabla} c'\rangle_d. \tag{3.12c}$$

Obviously in the absence of fluid motion, the scalar can only be transported by diffusion, and

$$\boldsymbol{D}^{\text{eff}} = D_s \boldsymbol{I} + \boldsymbol{D}^{\text{diff}} \qquad \text{when } \boldsymbol{u}_d = \boldsymbol{u}_c = \boldsymbol{0}.$$

On the other hand, when the particulates have the same transport properties as those of the surrounding fluid, only convection plays a role, and

$$\boldsymbol{D}^{\text{eff}} = D_c \boldsymbol{I} + \boldsymbol{D}^{\text{conv}} \qquad \text{when } D_d = D_c \text{ and } m = 1.$$

This last result is demonstrated in appendix B.2.3. We emphasize that although $\boldsymbol{D}^{\text{conv}}$ and $\boldsymbol{D}^{\text{diff}}$ arise from transport processes of different nature, they are not completely independent. For example, a diffusivity ratio $D_d/D_c \neq 1$ affects the convective contribution $\boldsymbol{D}^{\text{conv}}$ through the modification of c' in the particulates surroundings; and conversely the velocity disturbances induced by the presence of the particulates affect the scalar field c' and thus make an indirect contribution to $\boldsymbol{D}^{\text{diff}}$.

3.2.4 Dimensionless groups

The macroscale description proposed above would be complete if one could express $\boldsymbol{D}^{\text{conv}}$ and $\boldsymbol{D}^{\text{diff}}$ only in terms of macroscale parameters. The dimensionless parameters appearing in the problem are

(i) the gas volume fraction ϕ,
(ii) the gas-to-liquid diffusivity ratio D_d/D_c,
(iii) the partition coefficient m,
(iv) the Péclet number $Pe = Ud_b/D_c$, with U the bubble drift velocity and d_b the bubble volume-equivalent diameter,

together with additional parameters required to describe the two-phase flow, such as the Reynolds number and statistical information about the suspension microstructure.

The diffusive contribution to the effective diffusivity, $\boldsymbol{D}^{\text{diff}}$, arises from the fact that the scalar transport properties of the gas are different from that of the liquid, therefore $\boldsymbol{D}^{\text{diff}}$ is expected to depend primarily on m, D_d/D_c, and ϕ. The convective contribution to the effective diffusivity, $\boldsymbol{D}^{\text{conv}}$, is due to the velocity disturbances induced by the bubble motion, so $\boldsymbol{D}^{\text{conv}}$ is expected to depend primarily on Pe, ϕ, and flow properties. The Péclet number compares convective and diffusive transport, and is therefore expected to control the relative importance of $\boldsymbol{D}^{\text{diff}}$ and $\boldsymbol{D}^{\text{conv}}$. At high Péclet number, as often encountered in bubbly flows, $\boldsymbol{D}^{\text{conv}}$ is expected to be the dominant contribution to the effective diffusivity.

3.3 Numerical methodology

The expression of the effective diffusivity of a statistically homogeneous and stationary suspension is given in terms of microscopic quantities by (3.12). To determine the effective

diffusivity, we therefore need to impose a constant average scalar gradient $\boldsymbol{\nabla}\langle c\rangle$ and to compute the right-hand-side of (3.12b) and (3.12c). We present in this section a numerical method for the computation of $\boldsymbol{D}^{\mathsf{conv}}$ and $\boldsymbol{D}^{\mathsf{diff}}$.

3.3.1 One-fluid formulation

Our numerical approach for the simulation of bubbly flows, presented in chapter 1, relies on the one-fluid formulation of the incompressible Navier-Stokes equations which are solved within a periodic computational domain. In this context, one would like to obtain a governing equation for scalar transport which also applies to the entire domain and involves a spatially periodic variable. In addition, to avoid numerical difficulties, it would be preferable to solve for a variable that is continuous across the interface.

To comply with these requirements, the local scalar field is decomposed as follows:

$$c_c = P\bar{c} + \tilde{c}_c \quad \text{and} \quad c_d = mP\bar{c} + m\tilde{c}_d \tag{3.13}$$

where P is the constant defined in (3.6), where $\tilde{c}_{c,d}$ is the spatially periodic scalar disturbance, and where $\bar{c}$ is the imposed constant linear scalar field:

$$\bar{c} = \boldsymbol{G}\cdot\boldsymbol{x} \tag{3.14}$$

with $\boldsymbol{G} = \boldsymbol{\nabla}\langle c\rangle$ a constant vector. With these new variables, the condition (3.3) of thermodynamical equilibrium at the interface $\mathcal{S}_i$ becomes

$$\tilde{c}_d = \tilde{c}_c \qquad \text{if } \boldsymbol{x}\in\mathcal{S}_i.$$

The variable $\tilde{c}_{c,d}$ is therefore spatially periodic and continuous across the interface. In what follows we derive the one-fluid formulation of the transport equation for $\tilde{c}_{c,d}$.

The local scalar transport equation (3.1) reads in each fluid:

$$\frac{\partial c_c}{\partial t} + \boldsymbol{\nabla}\cdot(\boldsymbol{u}_c c_c) - \boldsymbol{\nabla}\cdot(D_c\boldsymbol{\nabla}c_c) = 0 \qquad \text{if } \boldsymbol{x}\in\mathcal{V}_c, \tag{3.15a}$$

$$\frac{\partial c_d}{\partial t} + \boldsymbol{\nabla}\cdot(\boldsymbol{u}_d c_d) - \boldsymbol{\nabla}\cdot(D_d\boldsymbol{\nabla}c_d) = 0 \qquad \text{if } \boldsymbol{x}\in\mathcal{V}_d. \tag{3.15b}$$

where $\mathcal{V}_c$ and $\mathcal{V}_d$ denote the sets of points that belong to the continuous and the disperse phases, respectively. To identify each phase we introduce an indicator function, denoted H, and defined such that

$$H(\boldsymbol{x},t) = \begin{cases} 1 & \text{if } \boldsymbol{x}\in\mathcal{V}_c(t), \\ \\ 0 & \text{if } \boldsymbol{x}\in\mathcal{V}_d(t). \end{cases} \tag{3.16}$$

In order to obtain a transport equation valid everywhere, we add the scalar transport equation (3.15a) that applies in the continuous phase multiplied by H to the equation (3.15b) that is

valid in the disperse phase multiplied by $(1-H)$. After some manipulations, identical to that used in appendix B.1.2, we obtain:

$$H\frac{\partial c_c}{\partial t}+(1-H)\frac{\partial c_d}{\partial t}+H\boldsymbol{\nabla}\cdot(\boldsymbol{u}_c c_c)+(1-H)\boldsymbol{\nabla}\cdot(\boldsymbol{u}_d c_d)-\boldsymbol{\nabla}\cdot[HD_c\boldsymbol{\nabla}c_c+(1-H)D_d\boldsymbol{\nabla}c_d]=0.$$

We shall now replace $c_{c,d}$ by its expression (3.13) in terms of $\bar{c}$ and $\tilde{c}_{c,d}$. Besides, since $\boldsymbol{u}_{c,d}$ and $\tilde{c}_{c,d}$ are continuous across the interface, we can define $\boldsymbol{u}=\boldsymbol{u}_{c,d}$ and $\tilde{c}=\tilde{c}_{c,d}$ in the entire domain. This yields:

$$\begin{aligned}&[H+(1-H)m]\frac{\partial\tilde{c}}{\partial t}+[H+(1-H)m]\boldsymbol{\nabla}\cdot(\boldsymbol{u}\tilde{c})-\boldsymbol{\nabla}\cdot\left\{[HD_c+(1-H)D_d m]\boldsymbol{\nabla}\tilde{c}\right\}\\&=-P[H+(1-H)m]\frac{\partial\bar{c}}{\partial t}-P[H+(1-H)m]\boldsymbol{\nabla}\cdot(\boldsymbol{u}\bar{c})+P\boldsymbol{\nabla}\cdot\left\{[HD_c+(1-H)D_d m]\boldsymbol{\nabla}\bar{c}\right\}.\end{aligned}$$

Using the definition (3.14) of $\bar{c}$, this equation becomes:

$$\begin{aligned}&[H+(1-H)m]\frac{\partial\tilde{c}}{\partial t}+[H+(1-H)m]\boldsymbol{\nabla}\cdot(\boldsymbol{u}\tilde{c})-\boldsymbol{\nabla}\cdot\left\{[HD_c+(1-H)D_d m]\boldsymbol{\nabla}\tilde{c}\right\}\\&=-P[H+(1-H)m]\boldsymbol{u}\cdot\boldsymbol{G}+P(D_c-D_d m)\boldsymbol{G}\cdot\boldsymbol{\nabla}H.\end{aligned}$$

Introducing

$$M=H+(1-H)m\quad\text{and}\quad K=HD_c+(1-H)D_d m,\tag{3.17}$$

we finally obtain

$$M\frac{\partial\tilde{c}}{\partial t}+M\boldsymbol{\nabla}\cdot(\boldsymbol{u}\tilde{c})-\boldsymbol{\nabla}\cdot(K\boldsymbol{\nabla}\tilde{c})=-PM\boldsymbol{u}\cdot\boldsymbol{G}+P(D_c-D_d m)\boldsymbol{G}\cdot\boldsymbol{\nabla}H\tag{3.18}$$

which is the equation we integrate in the code.

3.3.2 Numerical methods

The counterpart of the convenience of the one-fluid formulation (3.18) is the introduction, in the present case, of a Heaviside step function H and of its gradient $\boldsymbol{\nabla}H$. Similar difficulties were encountered with the one-fluid formulation of the incompressible Navier-Stokes equations. These have been circumvented in section 1.3.2 by introducing a smoothed indicator function H_ε, defined by (1.20), and used as a substitute for H. The same approach is used here for the scalar disturbance transport equation, which then reads

$$M\frac{\partial\tilde{c}}{\partial t}+M\boldsymbol{\nabla}\cdot(\boldsymbol{u}\tilde{c})-\boldsymbol{\nabla}\cdot(K\boldsymbol{\nabla}\tilde{c})=-PM\boldsymbol{u}\cdot\boldsymbol{G}+P(D_c-D_d m)\boldsymbol{G}\cdot\boldsymbol{\nabla}H_\varepsilon\tag{3.19a}$$

with

$$M=H_\varepsilon+(1-H_\varepsilon)m\quad\text{and}\quad K=H_\varepsilon D_c+(1-H_\varepsilon)D_d m.\tag{3.19b}$$

This equation is coupled with that governing the fluid motion and solved numerically, as explained hereinafter.

The numerical methods employed to solve the two-phase flow have been described in chapter 1. In short, we employ a standard projection method (Chorin, 1968) to integrate the incompressible Navier-Stokes equations in their one-fluid form, and a level-set method (Sussman et al., 1994) to capture the moving gas-liquid interface. Spatial discretization relies on a mixed finite difference/finite volume approach on a fixed, staggered, Cartesian grid. Second-order centered schemes are generally employed, except for advective terms which are discretized using fifth-order WENO schemes. Our time integration algorithm for the two-phase flow is provided in section 1.3.3. It is updated here to include the integration of the scalar disturbance transport equation (3.19).

The scalar field $\tilde{c}$ is stored at cell centers, together with the level-set function ψ, whereas the three components of the velocity field $\boldsymbol{u}$ are stored on cell-face centers. At the beginning of timestep t^n, $\psi^{n-1/2}$, $\tilde{c}^{n-1/2}$, and $\boldsymbol{u}^n$ are known. The algorithm then proceeds iteratively through the following steps.

Steps 1 to 3: Update of the level-set function. The position of the interface is first advanced in time according to the modified level-set method of Sabelnikov et al. (2014) using a third-order TVD Runge-Kutta scheme. The level-set function is then reinitialized using the procedure of Russo and Smereka (2000), and a correction is finally applied to enforce volume conservation. This yields $\psi^{n+1/2}$, the updated level-set function.

New step: Update of the scalar field. $\tilde{c}$ is advanced from $\tilde{c}^{n-1/2}$ to $\tilde{c}^{n+1/2}$ according to (3.19) using a Crank-Nicolson time-stepping scheme:

$$\begin{aligned} &M^n \frac{\tilde{c}^{n+1/2}}{\Delta t} - \frac{1}{2}\mathscr{D}(K^{n+1/2}, \tilde{c}^{n+1/2}) = \\ &M^n \frac{\tilde{c}^{n-1/2}}{\Delta t} + \frac{1}{2}\mathscr{D}(K^{n-1/2}, \tilde{c}^{n-1/2}) - M^n \mathscr{A}(\boldsymbol{u}^n, \tilde{c}^n) - PM^n \boldsymbol{u}^n \cdot \boldsymbol{G} + P(D_c - D_d m)\mathscr{H}(\psi^n) \end{aligned} \tag{3.20}$$

where $M^n = M(\psi^n)$, where ψ^n is linearly interpolated between $\psi^{n-1/2}$ and $\psi^{n+1/2}$, and where $\tilde{c}^n$ is evaluated using an explicit third-order Adams-Bashforth scheme:

$$\tilde{c}^n = \frac{23}{12}\tilde{c}^{n-1/2} - \frac{16}{12}\tilde{c}^{n-3/2} + \frac{5}{12}\tilde{c}^{n-5/2}. \tag{3.21}$$

In the above scheme, $\mathscr{D}$ and $\mathscr{H}$ are second-order centered finite difference approximations of the diffusive term $\boldsymbol{\nabla} \cdot (K \boldsymbol{\nabla} \tilde{c})$ and of the extra term $\boldsymbol{G} \cdot \boldsymbol{\nabla} H_\varepsilon$, respectively, and $\mathscr{A}$ is the spatial discretization of the advection term $\boldsymbol{\nabla} \cdot (\boldsymbol{u}\tilde{c})$ calculated using a fifth-order conservative WENO scheme (Jiang & Peng, 2000). This linear system in $\tilde{c}^{n+1/2}$ is solved iteratively using a parallel red-black Gauss-Seidel algorithm.

Steps 4 to 6: Update of the velocity field. The time integration of the incompressible Navier-Stokes equations is carried out using a mixed Crank-Nicolson/third-order Adams-Bashforth scheme and consists in a predictor step, where a temporary velocity field is estimated by ignoring the effect of pressure, and a corrector step, where the velocity field is corrected by the pressure gradient term computed from the divergence-free condition. This yields $\boldsymbol{u}^{n+1}$, the updated velocity field.

3.3.3 Computation of the effective diffusivity

Computing the effective diffusivity of the suspension amounts to the computation of $\boldsymbol{D}^{\text{conv}}$ and $\boldsymbol{D}^{\text{diff}}$ as defined by (3.12). For convenience we will use the following equivalent forms which involve the indicator function in place of phase averages (see appendix B.2.4 for the equivalence between the two formulations):

$$\boldsymbol{D}^{\text{conv}} \cdot \boldsymbol{\nabla}\langle c\rangle = -\langle H\boldsymbol{u}_c' c_c' + (1-H)\boldsymbol{u}_d' c_d'\rangle, \tag{3.22a}$$

$$\boldsymbol{D}^{\text{diff}} \cdot \boldsymbol{\nabla}\langle c\rangle = \langle HD_c\boldsymbol{\nabla}c_c' + (1-H)D_d\boldsymbol{\nabla}c_d'\rangle. \tag{3.22b}$$

We shall now establish (i) the relation between the average field $\langle c\rangle$ and the imposed field $\bar{c}$, and (ii) the relation between the fluctuation field c' and the periodic field $\tilde{c}$ with respect to the computation of the effective diffusivity.

We have

$$\langle c\rangle = \langle HP + (1-H)mP\rangle\bar{c} + \langle H\tilde{c}_c + (1-H)m\tilde{c}_d\rangle.$$

Defining

$$\langle\tilde{c}\rangle = \langle H\tilde{c}_c + (1-H)m\tilde{c}_d\rangle \tag{3.23}$$

and remarking that, by definition,

$$\langle HP + (1-H)mP\rangle = 1, \tag{3.24}$$

we obtain:

$$\langle c\rangle = \bar{c} + \langle\tilde{c}\rangle. \tag{3.25}$$

Since we have, by definition,

$$\boldsymbol{\nabla}\bar{c} = \boldsymbol{G} = \boldsymbol{\nabla}\langle c\rangle, \tag{3.26}$$

it follows that

$$\boldsymbol{\nabla}\langle\tilde{c}\rangle = \boldsymbol{0}. \tag{3.27}$$

The scalar fluctuation in the continuous phase c_c' is

$$\begin{aligned} c_c' &= c_c - P\langle c\rangle \\ &= P\bar{c} + \tilde{c}_c - P\langle c\rangle \\ &= P\bar{c} + \tilde{c}_c - P\bar{c} - P\langle\tilde{c}\rangle \\ &= \tilde{c}_c - P\langle\tilde{c}\rangle. \end{aligned}$$

Proceeding in a similar manner for c_d', we obtain the following relations:

$$c_c' = \tilde{c}_c - P\langle\tilde{c}\rangle \quad \text{and} \quad c_d' = m\tilde{c}_d - mP\langle\tilde{c}\rangle. \tag{3.28}$$

We have for the convective term:

$$\begin{aligned}\langle H\boldsymbol{u}_c'c_c' + (1-H)\boldsymbol{u}_d'c_d'\rangle &= \langle H\boldsymbol{u}_c'\tilde{c}_c + (1-H)m\boldsymbol{u}_d'\tilde{c}_d\rangle - \langle HP\boldsymbol{u}_c' + (1-H)mP\boldsymbol{u}_d'\rangle\langle\tilde{c}\rangle \\ &= \langle H\boldsymbol{u}_c'\tilde{c}_c + (1-H)m\boldsymbol{u}_d'\tilde{c}_d\rangle - (m-1)P\langle(1-H)\boldsymbol{u}_d'\rangle\langle\tilde{c}\rangle \\ &= \langle H\boldsymbol{u}_c'\tilde{c}_c + (1-H)m\boldsymbol{u}_d'\tilde{c}_d\rangle - \phi(m-1)P\boldsymbol{U}\langle\tilde{c}\rangle\end{aligned}$$

where we have used $P\langle H\boldsymbol{u}_c' + (1-H)\boldsymbol{u}_d'\rangle = \boldsymbol{0}$ to step from the first to the second line, and $\langle(1-H)\boldsymbol{u}_d'\rangle = \phi\boldsymbol{U}$ (see (B.27)) to step from the second to the third line. Besides, we have for diffusive term:

$$\begin{aligned}\langle HD_c\boldsymbol{\nabla}c_c' + (1-H)D_d\boldsymbol{\nabla}c_d'\rangle &= \langle HD_c\boldsymbol{\nabla}\tilde{c}_c + (1-H)D_dm\boldsymbol{\nabla}\tilde{c}_d\rangle - \langle HD_cP + (1-H)D_dmP\rangle\boldsymbol{\nabla}\langle\tilde{c}\rangle \\ &= \langle HD_c\boldsymbol{\nabla}\tilde{c}_c + (1-H)D_dm\boldsymbol{\nabla}\tilde{c}_d\rangle\end{aligned}$$

where we have used (3.27) to step from the first to the second line.

The effective diffusivity is therefore calculated from:

$$\boldsymbol{D}^{\mathrm{conv}}\cdot\boldsymbol{G} = -\langle H\boldsymbol{u}_c'\tilde{c}_c + (1-H)m\boldsymbol{u}_d'\tilde{c}_d\rangle + \phi(m-1)P\boldsymbol{U}\langle\tilde{c}\rangle, \tag{3.29a}$$

$$\boldsymbol{D}^{\mathrm{diff}}\cdot\boldsymbol{G} = \langle HD_c\boldsymbol{\nabla}\tilde{c}_c + (1-H)D_dm\boldsymbol{\nabla}\tilde{c}_d\rangle, \tag{3.29b}$$

where $\tilde{c}$ is the (statistically) steady solution of (3.18). In these expressions, $\langle\,\rangle$ has been defined so far as an ensemble average operator. For statistically homogeneous and stationary systems, the ergodicity hypothesis states that ensemble averaging is identical to volume and time averaging. As a consequence, $\boldsymbol{D}^{\mathrm{conv}}$ and $\boldsymbol{D}^{\mathrm{diff}}$ are computed from (3.29a) and (3.29b), respectively, with the ensemble average being replaced in practice by a volume average combined with a time average over an appropriate time period.

3.4 Mixing by bubble-induced agitation

In the present section, our interest lies in the macroscale modeling of scalar dispersion arising from bubble-induced agitation in buoyancy-driven bubbly suspensions. In what follows, subscripts d and c refer to the disperse (gas) and continuous (liquid) phases, respectively.

3.4.1 Problem statement

Under the conditions of statistical homogeneity and stationarity, scalar dispersion in a bubbly suspension can be described by a macroscale constitutive law which relates the average scalar flux to the average scalar gradient through an effective diffusivity tensor. This effective diffusivity captures both the effect of the bubbles having transport properties (diffusivity D_d and partition coefficient m) different from those of the liquid and the effect of the velocity disturbances induced by the bubbles. Our present interest goes to the latter. As a consequence,

in what follows, we assume equal gas and liquid diffusivities ($D_d = D_c$) and equal partitioning between both phases ($m = 1$) so that the effective diffusivity reduces to

$$\boldsymbol{D}^{\text{eff}} = D_c \boldsymbol{I} + \boldsymbol{D}^{\text{conv}}$$

where $\boldsymbol{D}^{\text{conv}}$ is the convective contribution to the effective diffusivity we wish to determine. It is defined by

$$\boldsymbol{D}^{\text{conv}} \cdot \boldsymbol{\nabla}\langle c \rangle = -(1-\phi)\langle \boldsymbol{u}' c' \rangle_c - \phi \langle \boldsymbol{u}' c' \rangle_d$$

where ϕ is the gas volume fraction, and where $\boldsymbol{u}'$ and c' are the velocity and scalar fluctuations defined in (3.4) and (3.5), respectively. Ultimately, the objective is to find a closure relation for $\boldsymbol{D}^{\text{conv}}$ in terms of other macroscopic quantities.

The bubbly suspensions we consider are monodisperse and buoyancy-driven. The characteristic length scale in this problem is the bubble size d_b. As the bubbles are deformable, d_b is defined as the diameter of a sphere with the same volume as that of a bubble. The characteristic velocity scale U is defined as the bubble rise velocity in the frame of the suspension (the so-called drift velocity). In addition to the gas volume fraction ϕ, the other key dimensionless group appearing in the scalar transport problem is the Péclet number

$$Pe = \frac{U d_b}{D_c} \tag{3.30}$$

which compares advective and diffusive transport. As scalar transport is coupled to momentum transport, the bubble Reynolds number

$$Re = \frac{U d_b}{\nu_c}, \tag{3.31}$$

with ν_c the liquid kinematic viscosity, and the suspension microstructure, loosely denoted $\mathscr{M}$ (which encompasses all the information about the statistical distribution of the bubble positions, shapes, orientations, etc.), are also expected be relevant. Our study aims at elucidating the effects of Re, ϕ, and $\mathscr{M}$ on the dependence of $\boldsymbol{D}^{\text{conv}}$ on Pe.

In our approach, bubbly suspensions are represented by the periodic repetition of a cubic unit cell containing a finite number N_b of freely moving bubbles. Conveniently, this setup allows variation between microstructures. In the one hand, when the unit cell contains a single bubble, one recovers a simple cubic array, which is of interest as a model of perfectly ordered suspensions. On the other hand, using a large number of bubbles in the unit cell is of interest as a model of real suspensions, although convergence with the number of bubbles would have to be verified. We shall herein refer to this setup with one bubble in the cell as an ordered array, and to that with more than one bubble in the unit cell as a free array.

The bubbles rise under the sole effect of gravity, which is oriented along a primary axis of the array (due to the large number of parameters already involved in the problem, the influence of the orientation of gravity has not been considered). Although we saw in chapter 2 that the rise of an array of bubbles is not necessarily parallel to gravity, we shall focus on the simplest case of bubbles rising vertically.

When the suspension microstructure is transversely isotropic, as is the case when the bubbles rise vertically along the primary axis (say $\boldsymbol{e}_3$) of the array, then, from symmetry arguments, we can write

$$\boldsymbol{D}^{\text{conv}} = \begin{bmatrix} D_{\perp}^{\text{conv}} & D_{12}^{\text{conv}} & D_{13}^{\text{conv}} \\ D_{12}^{\text{conv}} & D_{\perp}^{\text{conv}} & D_{13}^{\text{conv}} \\ D_{31}^{\text{conv}} & D_{31}^{\text{conv}} & D_{\parallel}^{\text{conv}} \end{bmatrix} \tag{3.32}$$

where we have introduced the longitudinal and transverse components of the convective contribution to the effective diffusivity, denoted $D_{\parallel}^{\text{conv}}$ and $D_{\perp}^{\text{conv}}$, respectively, and defined by

$$D_{\parallel}^{\text{conv}} = D_{33}^{\text{conv}} \qquad \text{and} \qquad D_{\perp}^{\text{conv}} = D_{11}^{\text{conv}} = D_{22}^{\text{conv}}. \tag{3.33}$$

Note that when the suspension has an isotropic microstructure, $\boldsymbol{D}^{\text{conv}}$ is symmetric (Koch & Brady, 1987b). This is not the case for bubbly flows with moderate Reynolds number, at least for low and intermediate volume fractions (Cartellier & Rivière, 2001; Cartellier et al., 2009; Bunner & Tryggvason, 2002a; Yin & Koch, 2008).

Our first goal is to characterize the effects of liquid inertia (through *Re*) and hydrodynamic interactions (through ϕ) on the dependence of $\boldsymbol{D}^{\text{conv}}$ on *Pe* for ordered suspensions ($N_b = 1$), thereby extending prior work on dilute ordered arrays of rigid spheres in Stokes flow conditions (Koch et al., 1989). Our second goal is to evaluate the effect of introducing additional degrees of freedom in the system (through increasing N_b), and to investigate the dependence of $\boldsymbol{D}^{\text{conv}}$ on *Pe* in freely evolving suspensions (sufficiently large N_b). As we found the off-diagonal components to be zero in all investigated configurations, only results for the longitudinal and the transverse components of $\boldsymbol{D}^{\text{conv}}$ will be presented.

3.4.2 Simulated flow regimes

As the bubbly flows we consider are buoyancy-driven, a further difficulty arises from the fact that U is a priori unknown, and depends in a complex manner on

(i) the number of bubbles in the unit cell N_b,
(ii) the gas volume fraction $\phi = (N_b \pi d_b^3)/(6h^3)$ (h is the linear size of the unit cell),
(iii) the gas-to-liquid density ratio, ρ_d/ρ_c,
(iv) the gas-to-liquid viscosity ratio μ_d/μ_c,
(v) the Archimedes (or Galileo) number $Ar = \sqrt{\rho_c |\rho_d - \rho_c| g d_b^3}/\mu_c$ (g is the magnitude of the gravitational acceleration),
(vi) the Bond (or Eötvös) number $Bo = |\rho_d - \rho_c| g d_b^2/\gamma$ (γ is the surface tension).

In most bubbly flows of practical relevance, the gas-to-liquid density and viscosity ratios are vanishingly small. Their precise values are not important from a physical point of view as long as they are small enough. In the simulations, the gas-to-liquid density and viscosity ratios were set to $\rho_d/\rho_c = 10^{-3}$ and $\mu_d/\mu_c = 10^{-2}$, respectively. The dependence of U on (Ar, Bo, ϕ, N_b) has been addressed in chapter 2 and is not further discussed here. In the present study, we shall assume that U is known.

case	Bo	Ar	shape	Re_0	N_b	ϕ
S0	0.38	0.15	spherical	0.00194	1	$[0.002-0.191]$
S1	0.38	5.03	spherical	1.80	1	$[0.002-0.191]$
C	243	15.2	dimpled/skirted	7.77	1	$[0.002-0.024]$
E1	2.0	29.9	ellipsoidal	31	1	$[0.002-0.191]$
E1	2.0	29.9	ellipsoidal	31	$[2,8]$	0.024

Table 3.1 Simulated flow configurations: Bo and Ar define the flow regime (for an easier interpretation the terminal shapes and Re_0 of the equivalent bubbles in isolated conditions are also given), N_b is the number of free bubbles in the unit cell, and ϕ is the gas volume fraction. Terminal shapes are those predicted by the diagram of Grace (1973). The values of Re_0 are estimated from the correlation of Mei, Klausner, and Lawrence (1994) for spherical bubbles (cases S0 and S1) and from the correlation of Loth (2008) for ellipsoidal bubbles (case E1); the experimental value measured by Bhaga and Weber (1981) is reported for case C.

For a given set of parameters, the components of $\boldsymbol{D}^{\mathrm{conv}}$ can be obtained from numerical simulations by imposing a constant linear scalar field $\bar{c}$ and determining the resulting periodic disturbance scalar field, as explained in section 3.3.3. Specifically, two distinct simulations are required to fully determine the five independent components of $\boldsymbol{D}^{\mathrm{conv}}$: in one simulation, $\boldsymbol{\nabla}\bar{c} = \boldsymbol{e}_3$, which yields D_{13}^{conv} and $D_{\parallel}^{\mathrm{conv}}$, in the other simulation, $\boldsymbol{\nabla}\bar{c} = \boldsymbol{e}_1$, which yields $D_{\perp}^{\mathrm{conv}}$, D_{12}^{conv}, and D_{31}^{conv}. The off-diagonal components of $\boldsymbol{D}^{\mathrm{conv}}$ were found to be zero (up to computer accuracy for ordered arrays, and statistical uncertainty for free arrays) for all the sets of parameters we considered, and therefore will not be shown.

We now describe the various configurations that have been investigated by direct numerical simulations. Four different flow regimes, as defined by the set (Ar, Bo), have been considered. These are described in table 3.1, and have been studied in chapter 2 (the same case code names are used). In case S0, the bubbles are spherical and the Reynold number is vanishingly small, in order to approach Stokes flow conditions. In case S1, the bubbles are (nearly) spherical, and in the dilute limit, $Re_0 = 1.80$ (the subscript 0 is used to refer to the limiting case of a single bubble released in an unbounded quiescent liquid under the same conditions of Ar and Bo). In case C, the bubbles are skirted, and $Re_0 = 7.77$. In case E1, the bubbles are ellipsoidal, and $Re_0 = 31$.

Ordered arrays of bubbles in these four flow regimes have been considered for a wide range of volume fractions (provided in table 3.1). All ordered suspensions considered here are in a strictly steady state. For free arrays, the number of bubbles N_b in the cell is an additional parameter. Simulations of scalar transport have been performed for $2 \leqslant N_b \leqslant 8$ in case E1 at $\phi = 2.4$ %. In these conditions, coalescence is absent, and the system is in an unsteady but statistically stationary state. For each of these configurations (Ar, Bo, ϕ, N_b), the drift velocity

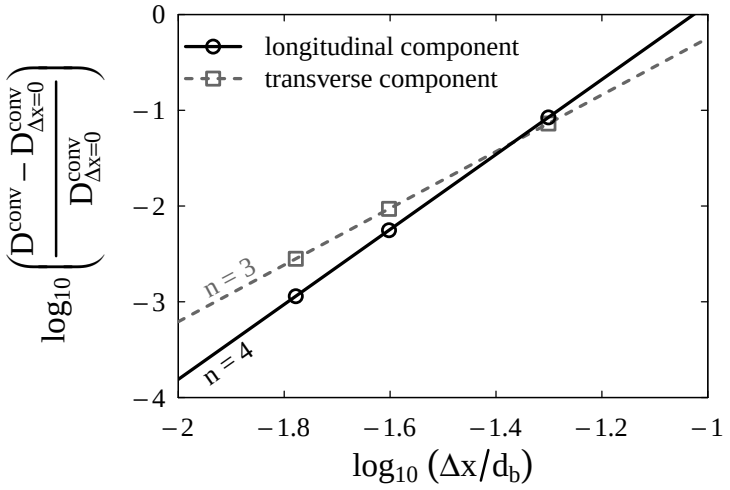

Figure 3.1 Spatial convergence for an ordered array of bubbles in case E1 at $Pe = 10^3$: relative error in $D_{\parallel}^{\mathrm{conv}}$ and $D_{\perp}^{\mathrm{conv}}$ as a function of the grid spacing Δx (d_b is the bubble volume-equivalent diameter; $D_{\Delta x=0}^{\mathrm{conv}}$ is extrapolated assuming $D^{\mathrm{conv}} = D_{\Delta x=0}^{\mathrm{conv}} - k\Delta x^n$, where k and n are constants fitted from numerical data)

(and then the Reynolds number) is known from chapter 2. This allowed us to impose the Péclet number a priori.

The effect of the grid spacing on $D_{\parallel}^{\mathrm{conv}}$ and $D_{\perp}^{\mathrm{conv}}$ has been assessed for case E1 at $Pe = 10^3$ for one value of the volume fraction ($\phi = 2.4$ %), in both ordered and free configurations. For ordered arrays, three different resolutions were tested, namely $d_b/\Delta x = \{20, 40, 60\}$ with Δx the grid spacing. The results are provided in figure 3.1. The error in the values of $D_{\parallel}^{\mathrm{conv}}$ and $D_{\perp}^{\mathrm{conv}}$ arising from spatial discretization is less than 1 % when a resolution of 40 grid cells per bubble diameter is used. This resolution is the same as that used for the simulation of the corresponding bubbly flow in chapter 2. In practice, we used for each configuration the same resolution as that selected for the simulation of the corresponding ordered bubbly suspensions (see section 2.2.3), namely 60 grid cells per diameter for case C and 40 grid cells per diameter for the other cases. For free arrays, due to the computational cost of the simulations, only two different resolutions were tested, namely 20 and 30 grid cells per bubble diameter, for an array of 8 bubbles. The values of $D_{\parallel}^{\mathrm{conv}}$ and $D_{\perp}^{\mathrm{conv}}$ obtained with $d_b/\Delta x = 20$ differ from those obtained for $d_b/\Delta x = 30$ by approximately 10 %. This difference is however believed to be essentially due to the relatively short time period over which statistically steady quantities were averaged for $d_b/\Delta x = 30$, as this simulation was too expensive to be continued over very long times. A resolution of 20 grid cells per diameter was therefore used for all simulations of free arrays. For a given case, the same resolution was used for all volume fractions and Péclet numbers. Note that for $D_d/D_c \gg 1$ (not considered here but frequently encountered in practice), finer resolutions may be required, as thin scalar boundary layers around the bubbles would need to be resolved.

3.4.3 Ordered arrays

We examine in this section the dispersion of a passive scalar in ordered suspensions of deformable bubbles. Our main objective here is to elucidate the effects of inertia and finite volume fraction on dispersion, using theoretical analysis and numerical simulation.

3.4.3.1 Asymptotic analysis

We first determine analytically the convective contribution to the effective diffusivity of ordered suspensions of spherical fluid particulates (bubbles or drops). The Reynolds number of the particulates is assumed to be small so that the Navier-Stokes equations can be approximated by the Oseen equations.

3.4.3.1.1 General solution

An ordered array of particulates translating at a drift velocity $\boldsymbol{U}$ is equivalent to an ordered array of fixed particulates immersed in a viscous fluid moving with an average system velocity $\langle \boldsymbol{u} \rangle = -\boldsymbol{U}$. The centers of the particulates are located on the nodes of a simple cubic lattice:

$$\boldsymbol{r_n} = h\,(n_1\boldsymbol{e}_1 + n_2\boldsymbol{e}_2 + n_3\boldsymbol{e}_3) \qquad n_1, n_2, n_3 = 0, \pm 1, \pm 2, \ldots \tag{3.34}$$

where h is the lattice spacing and $\boldsymbol{e}_i$ are the unit vectors aligned with the primitive axes of the cubic lattice. In the dilute limit ($d_b/h \ll 1$), these particulates can be represented by point forces $-\boldsymbol{f}$ acting on the fluid. The convective contribution to the effective diffusivity arising from the far field has been derived by Koch et al. (1989) for an ordered array of rigid spheres in the Stokes flow regime. In what follows we extend their result to an ordered array of spherical fluid particulates at small but finite *Re*.

When $Pe \ll 1$, the convective contribution to the effective diffusivity arising from the far field can be approximated by (Koch et al., 1989):

$$\frac{\boldsymbol{D}^{\mathrm{conv}}}{D_c} = \sum_{\boldsymbol{k}\neq\boldsymbol{0}} \frac{k^2 \hat{\boldsymbol{u}}'(\boldsymbol{k})\hat{\boldsymbol{u}}'(-\boldsymbol{k})}{(2\pi)^2 k^4 D_c^2 + (\boldsymbol{U}\cdot\boldsymbol{k})^2} \tag{3.35}$$

where the summation is over all vectors $\boldsymbol{k}$ in the reciprocal lattice

$$\boldsymbol{k} = \frac{1}{h}\,(n_1\boldsymbol{e}_1 + n_2\boldsymbol{e}_2 + n_3\boldsymbol{e}_3) \tag{3.36}$$

and where $\hat{\boldsymbol{u}}'$ is the three-dimensional Fourier transform of the velocity disturbance $\boldsymbol{u}' = \boldsymbol{u} - \langle \boldsymbol{u} \rangle$. In Oseen flow past an ordered array of point particulates, $\hat{\boldsymbol{u}}'$ is given by (A.10):

$$\hat{\boldsymbol{u}}'(\boldsymbol{k}) = \frac{\boldsymbol{f}\cdot(\boldsymbol{k}\boldsymbol{k}/k^2 - \boldsymbol{I})}{(2\pi k)^2 h^3 \mu_c + \mathrm{i}2\pi h^3 \rho_c \boldsymbol{U}\cdot\boldsymbol{k}} \qquad \boldsymbol{k} \neq \boldsymbol{0} \tag{3.37}$$

where $\boldsymbol{f}$ is the hydrodynamic force exerted by the ambient fluid on a particulate. In the dilute limit, $\boldsymbol{f}$ can be approximated by the Oseen drag exerted on a single spherical particulate:

$$\boldsymbol{f} = F\boldsymbol{f}_{0,\mathrm{Stokes}} \tag{3.38}$$

where $\boldsymbol{f}_{0,\text{Stokes}}$ is the Stokes drag on a spherical fluid particulate (Hadamard, 1911; Rybczynski, 1911):

$$\boldsymbol{f}_{0,\text{Stokes}} = -2\pi\mu^*\mu_c d_b \boldsymbol{U}, \qquad \text{with } \mu^* = \frac{\mu_c + 3/2\mu_d}{\mu_c + \mu_d}, \tag{3.39}$$

and where F accounts for the finite-Re correction to the Stokes drag (Brenner & Cox, 1963):

$$F = 1 + \frac{1}{8}\mu^* Re. \tag{3.40}$$

The convective contribution to the effective diffusivity of a dilute ordered array of fluid particulates in Oseen-flow conditions is therefore:

$$\frac{\boldsymbol{D}^{\text{conv}}}{D_c} = \frac{\mu^{*2}}{(2\pi)^2}\frac{d_b^2}{h^2}F^2\boldsymbol{C} \tag{3.41a}$$

where $\boldsymbol{C}$ is the dimensionless tensor:

$$\boldsymbol{C} = \sum_{\boldsymbol{k}^*\neq\boldsymbol{0}} \frac{\left[\boldsymbol{U}^*\cdot\left(\dfrac{\boldsymbol{k}^*\boldsymbol{k}^*}{k^{*2}} - \boldsymbol{I}\right)\right]^2}{k^{*2}\left[\dfrac{(2\pi)^2 k^{*4}}{Pe_h^2} + (\boldsymbol{U}^*\cdot\boldsymbol{k}^*)^2\right]\left[1 + \dfrac{Re_h^2(\boldsymbol{U}^*\cdot\boldsymbol{k}^*)^2}{(2\pi)^2 k^{*4}}\right]} \tag{3.41b}$$

with $\boldsymbol{U}^* = \boldsymbol{U}/U$, $\boldsymbol{k}^* = \boldsymbol{k}h$, $Re_h = \rho_c U h/\mu_c$, and $Pe_h = Uh/D_c$. The solution given by Koch et al. (1989) (equation (4.5) therein) for rigid spheres and Stokes flow is recovered in the limit $Re \to 0$ and $\mu_d/\mu_c \to \infty$.

The tensor $\boldsymbol{C}$ only depends on Pe_h, Re_h, and on the orientation of $\boldsymbol{U}$ relative to the reciprocal lattice (which structure is, for cubic arrays, identical to that of the direct lattice). As highlighted by Koch et al. (1989), the asymptotic behavior of $\boldsymbol{C}$ depends on whether there exists any $\boldsymbol{k}$ such that $\boldsymbol{U}\cdot\boldsymbol{k} = 0$, that is, on whether there exists any separation vector $\boldsymbol{r_n}$ in the real space which is perpendicular to $\boldsymbol{U}$. The asymptotic behavior of $\|\boldsymbol{C}\|$, where $\|\ \|$ denotes the tensorial Frobenius norm, is provided in table 3.2. From there we can immediately deduce the asymptotic behavior of $\|\boldsymbol{D}^{\text{conv}}\|$, which is summarized in terms of Pe and Re in table 3.3. The results show that the dependence of $\|\boldsymbol{D}^{\text{conv}}\|$ on Pe in the limits $Pe \ll d_b/h$ and $Pe \gg d_b/h$ is not affected by inertial effects.

3.4.3.1.2 Application to ordered arrays rising vertically

Let us now come back to our original problem of an ordered array of particulates rising under the effect of buoyancy. The gravitational acceleration is oriented along a primary axis of the array, say $\boldsymbol{g} = g\boldsymbol{e}_3$. We saw in chapter 2 that, in the presence of inertial effects and hydrodynamic interactions, the rise of such an array is not necessarily parallel to gravity. Nevertheless, we shall focus on the specific case where $\boldsymbol{U} = U\boldsymbol{e}_3$. This situation corresponds to that considered throughout the rest of this chapter.

regime		$\|\boldsymbol{C}\|$	
$Pe_h = Uh/D_c$	$Re_h = \rho_c U h/\mu_c$	if $\exists \boldsymbol{k} \mid \boldsymbol{U}\cdot\boldsymbol{k} = 0$	if $\nexists \boldsymbol{k} \mid \boldsymbol{U}\cdot\boldsymbol{k} = 0$
$Pe_h \ll 1$	$Re_h \ll 1$	Pe_h^2	Pe_h^2
	$Re_h \gg 1$	Pe_h^2	Pe_h^2/Re_h^2
$Pe_h \gg 1$	$Re_h \ll 1$	Pe_h^2	1
	$Re_h \gg 1$	Pe_h^2	$1/Re_h^2$

Table 3.2 Asymptotic behavior of $\|\boldsymbol{C}\|$ depending on Pe_h, Re_h, and on the orientation of the mean flow relative to the reciprocal lattice.

regime		$\|\boldsymbol{D}^{\mathrm{conv}}\|/D_c$	
$Pe = Ud_b/D_c$	$Re = \rho_c U d_b/\mu_c$	if $\exists \boldsymbol{r_n} \mid \boldsymbol{U} \perp \boldsymbol{r_n}$	if $\nexists \boldsymbol{r_n} \mid \boldsymbol{U} \perp \boldsymbol{r_n}$
$Pe \ll d_b/h \ll 1$	$Re \ll d_b/h$	F^2Pe^2	F^2Pe^2
	$Re \gg d_b/h$	F^2Pe^2	$F^2\phi^{2/3}Pe^2/Re^2$
$d_b/h \ll Pe \ll 1$	$Re \ll d_b/h$	F^2Pe^2	$F^2\phi^{2/3}$
	$Re \gg d_b/h$	F^2Pe^2	$F^2\phi^{4/3}/Re^2$

Table 3.3 Asymptotic behavior of $\|\boldsymbol{D}^{\mathrm{conv}}\|/D_c$ depending on Pe, Re, and on the orientation of the mean flow relative to the real lattice based on the solution (3.41), derived for an ordered array of point particulates in Oseen flow conditions (F is the Oseen drag divided by the Stokes drag).

As explained in appendix A.2.1, in this case the hydrodynamic force exerted by the fluid on a particulate is parallel to the drift velocity, and, since this force balances the buoyancy force at steady state, F is related to U through

$$F = \frac{U_{0,\text{Stokes}}}{U} \tag{3.42}$$

where $U_{0,\text{Stokes}}$ is the terminal velocity of an isolated spherical fluid particulate in Stokes flow:

$$U_{0,\text{Stokes}} = \frac{1}{12}\frac{|\rho_c - \rho_d| g d_b^2}{\mu^* \mu_c}, \qquad \text{with } \mu^* = \frac{\mu_c + 3/2\mu_d}{\mu_c + \mu_d}. \tag{3.43}$$

Note F can also be expressed in terms of commonly employed dimensionless groups:

$$F = \frac{1}{12\mu^*}\frac{Ar^2}{Re}. \tag{3.44}$$

In the "sedimentation" problem considered here, F is generally not known (as U is generally not known): it is a non-trivial function of the flow regime and volume fraction which reduces to (3.40) when $\phi \to 0$ and when Oseen-flow approximation is applicable.

The longitudinal and transverse components of the convective contribution, $D_{\parallel}^{\text{conv}}$ and $D_{\perp}^{\text{conv}}$ respectively, have been calculated from (3.41) for $d_b/h = 10^{-6}$ as a function of Pe for various $Re < 1$. This very low value of d_b/h is required to allow Pe to be either much smaller or much larger than d_b/h while satisfying the condition $Pe \ll 1$ under which the analytical solution has been derived. The results, shown in figure 3.2, indicate that the asymptotic dependences of $D_{\parallel}^{\text{conv}}$ and $D_{\perp}^{\text{conv}}$ on Pe are independent of Re. The sole effect of inertia is to modify the proportionality constants (by a substantial amount for the transverse component though).

In the limit of low Pe (with respect to d_b/h), both the transverse and the longitudinal components of $\boldsymbol{D}^{\text{conv}}$ exhibit a quadratic dependence on the Péclet number ($D_{\perp,\parallel}^{\text{conv}} \propto D_c Pe^2$). In this regime, diffusion is much faster than convection. As the scalar is advected by velocity disturbances, it rapidly spreads out owing to diffusion, and convective dispersion (measured through $\boldsymbol{D}^{\text{conv}}$) is influenced by both mechanisms. This regime is termed "convectively enhanced dispersion" (Koch et al., 1989).

In the limit of high Pe (with respect to d_b/h), the transverse component of $\boldsymbol{D}^{\text{conv}}$ is independent of the Péclet number ($D_{\perp}^{\text{conv}} \propto D_c$) whereas its longitudinal component grows quadratically with the Péclet number ($D_{\parallel}^{\text{conv}} \propto D_c Pe^2$). In this regime, convection dominates, but owing to the spatial periodicity of the flow, convective dispersion is obtained only if molecular diffusion across streamlines is considered (Koch et al., 1989). This regime is termed "Taylor dispersion" owing to the formal analogy, pointed out by Brenner (1980), with one-dimensional shear-induced Taylor dispersion in a capillary tube.

We emphasize that the expression (3.41) has been derived from the approximation (3.35), the validity of which is established only for $Pe \ll 1$ (which is, in practice, of limited use). Using symmetry arguments, Koch et al. (1989) (section 4.2 therein) showed that in the limit $Pe \gg 1$, Taylor dispersion is obtained if the average flow is perpendicular to a set of planes of both

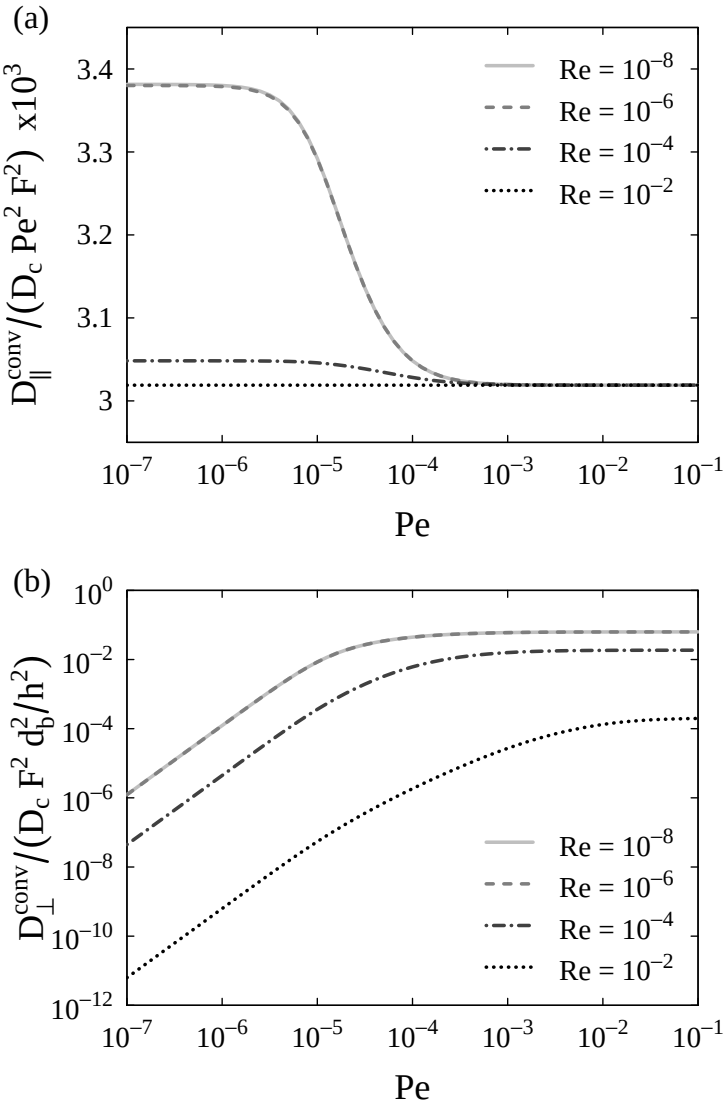

Figure 3.2 Longitudinal (a) and transverse (b) components of $\boldsymbol{D}^{\mathrm{conv}}$ as a function of the Péclet number for ordered arrays of point particulates at various small but finite Reynolds numbers ($\boldsymbol{U} = U\boldsymbol{e_3}$, $d_b/h = 10^{-6}$, and F is given by (3.42)).

translational and reflectional symmetry, such as Stokes flows parallel to the primary axis of an ordered array of spheres. Taylor dispersion is then easily understood by remarking that, owing to the symmetries of the flow, a fluid tracer particle entering the unit cell at one point, say $\boldsymbol{x}$, exits the cell at the equivalent point in the next cell, that is, $\boldsymbol{x} + h\boldsymbol{e}_3$), so that dispersion can only occur if diffusion across streamlines is present (Koch et al., 1989). In the presence of inertial effects, the reflectional symmetry is lost, hence this argument does not hold. Koch et al. (1989) also demonstrated that, for Stokes flow, the solution for $Pe \ll h/d_b$ is identical, at lowest order, to that obtained for $Pe \ll 1$ (section 4.3 therein, note that their Pe corresponds to Pe_h in our notations). Such a demonstration for Oseen flow will not be attempted here. Instead, the range $Pe \geqslant 1$ will be explored using direct numerical simulations.

3.4.3.2 Numerical results

The above analysis provides explicit expressions of $D_{\parallel}^{\mathrm{conv}}$ and $D_{\perp}^{\mathrm{conv}}$. These are valid for spherical bubbles rising at $Re < 1$ (strictly speaking, at a Reynolds number sufficiently small to assume Oseen flow, in terms of Archimedes and Bond numbers this regime would be reached for $Bo < 1$ and $Ar \lesssim 1$), and in the limits $\phi \to 0$ and $Pe \ll 1$. We shall now determine using numerical simulations whether these restrictions can be relaxed, and if so, to which extent.

3.4.3.2.1 Inertial effects at small volume fraction

We first examine the case of suspensions at low (but not vanishing) volume fraction in order to approach the dilute limit assumption, and to focus on the sole effect of inertia. The longitudinal and transverse components of the convective contribution to the effective diffusivity have been computed at $\phi = 0.2$ % for each of the four flow regimes listed in table 3.1, and the Péclet number has been varied from 10^{-1} to 10^3. The results are shown in figure 3.3, where the different colors, symbols and line styles depict the different flow regimes (the lines are drawn to guide the eyes). Qualitatively, figure 3.3 bears a striking resemblance to figure 3.2, even for case C (skirted bubbles). Specifically, the dependence on Pe as well as the effect of increasing Re are qualitatively similar in the analysis and in the simulations for both the longitudinal and the transverse components of $\boldsymbol{D}^{\mathrm{conv}}$: at low Péclet number, $D_{\parallel,\perp}^{\mathrm{conv}} \propto D_c Pe^2$, at high Péclet number, $D_{\parallel}^{\mathrm{conv}} \propto D_c Pe^2$ and $D_{\perp}^{\mathrm{conv}} \propto D_c$, and inertial effects and bubble deformation only affect the proportionality constants.

To allows a quantitative comparison between the DNS and the analysis, we present in figure 3.4 the ratio of $D_{\parallel,\perp}^{\mathrm{conv}}$ to $D_{\parallel,\perp}^{\mathrm{conv,anal}}$ where $D_{\parallel,\perp}^{\mathrm{conv,anal}}$ is given by (3.41) with F computed directly from its definition (3.42). For the longitudinal component, the numerical solution does not deviate by more than 5 % from the theoretical prediction, as can be seen from figure 3.4a. We conclude that, at small volume fraction, the asymptotic analysis yields the correct qualitative behavior and order of magnitude for $D_{\parallel}^{\mathrm{conv}}$ at any Péclet number up to 10^3 and any Reynolds number up to 40, even when the bubbles are strongly deformed. In contrast, the asymptotic analysis severely underpredicts the value of $D_{\perp}^{\mathrm{conv}}$ at high Péclet number, even for $Re \lesssim 1$. As a

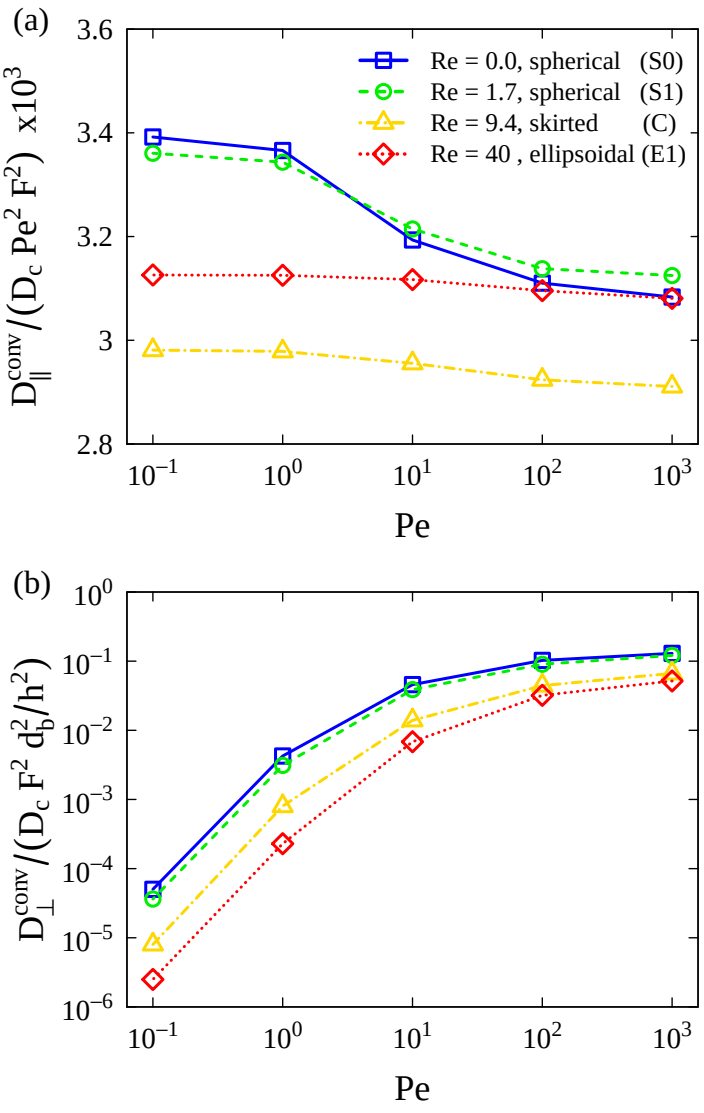

Figure 3.3 Longitudinal (a) and transverse (b) components of $\boldsymbol{D}^{\text{conv}}$ as a function of the Péclet number for ordered arrays in various flow regimes at small volume fraction ($\phi = 0.2$ %). The normalizations of $D_{\parallel}^{\text{conv}}$ by $D_c F^2 Pe^2$ and of $D_{\perp}^{\text{conv}}$ by $D_c F^2 d_b^2/h^2$ are those suggested by the asymptotic analysis. F is given by (3.42). The lines are drawn to guide the eyes.

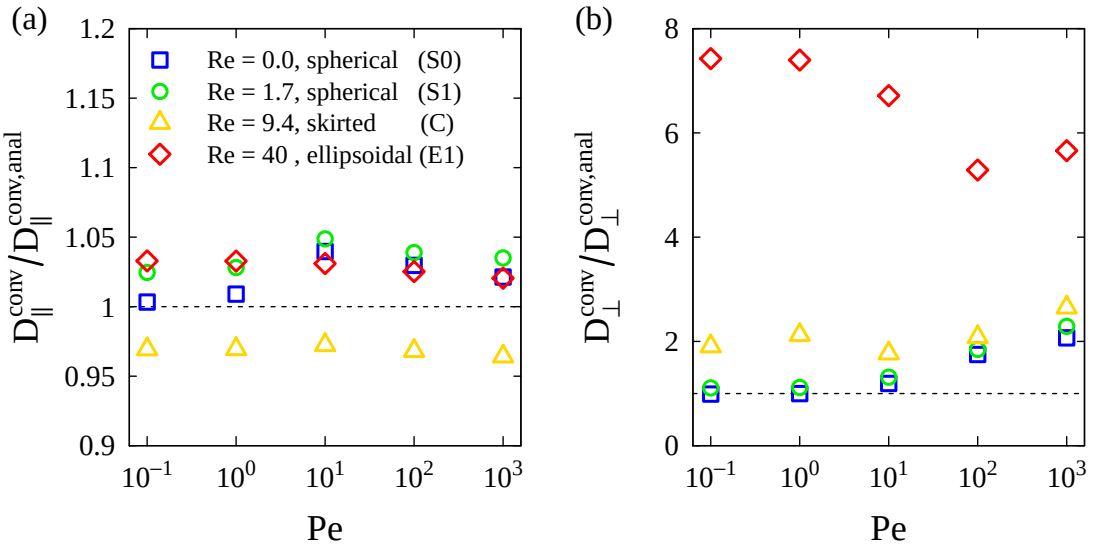

Figure 3.4 Numerical solution $\boldsymbol{D}^{\mathrm{conv}}$ divided by the analytical solution $\boldsymbol{D}^{\mathrm{conv,anal}}$ as a function of the Péclet number for ordered arrays in various flow regimes at small volume fraction ($\phi = 0.2$ %): longitudinal (a) and transverse (b) components. $\boldsymbol{D}^{\mathrm{conv,anal}}$ is given by (3.41).

consequence, $D_{\perp}^{\mathrm{conv}}$ cannot be estimated from our analytical solution when the assumptions underlying its derivation are not satisfied.

To illustrate the dispersion regimes at low and high Péclet number, we present visualizations of c' (the scalar fluctuation defined by (3.5)) used to compute $D_{\parallel}^{\mathrm{conv}}$ and $D_{\perp}^{\mathrm{conv}}$ in figure 3.5 and figure 3.6, respectively. In each of these figures, the field of c' is represented for each flow regime in a vertical symmetry plane passing through the center of a bubble for $Pe = 10^{-1}$ (left) and $Pe = 10^{3}$ (right), and the Reynolds number increases from top to bottom. The field of c' associated to $D_{\parallel}^{\mathrm{conv}}$, shown in figure 3.5, exhibits similar features at low and high Pe, resulting in $D_{\parallel}^{\mathrm{conv}} \propto Pe^2$ in both limits. In contrast, the field of c' associated to $D_{\perp}^{\mathrm{conv}}$, represented in figure 3.6, is qualitatively different at low and high Pe, resulting in the different scaling laws identified above. In addition, the Reynolds number and the bubble shape affect the fore-and-aft symmetry and the details of c', but not its essential features, resulting in quantitative but not qualitative effects on $D_{\parallel}^{\mathrm{conv}}$ and $D_{\perp}^{\mathrm{conv}}$.

3.4.3.2.2 Volume fraction effects at high Péclet number

We shall now focus on the effect of volume fraction. We computed the longitudinal and transverse components of $\boldsymbol{D}^{\mathrm{conv}}$ for volume fractions between 0.1 and 20 %, when possible, for each of the flow regimes and for $Pe = 10^{3}$. This choice of a high Péclet number is motivated by its practical relevance, as $Pe \gg 1$ is commonly encountered in real systems. For case C, results will

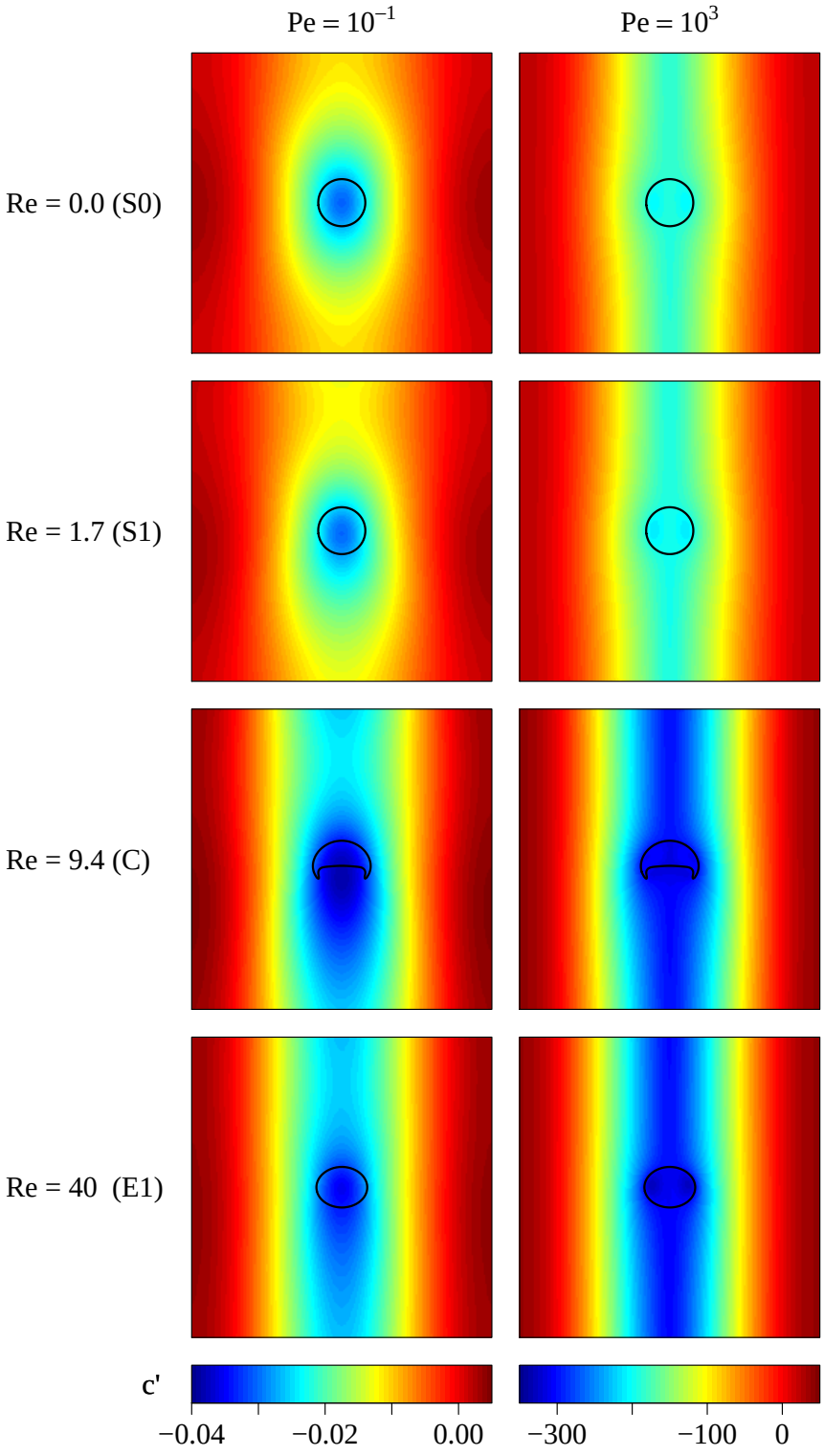

Figure 3.5 Scalar fluctuation field associated to $D_{\|}^{\mathrm{conv}}$, shown in a vertical symmetry plane passing through the center of a bubble (c' is defined by (3.5)), for ordered arrays in various flow regimes at $Pe = 10^{-1}$ (left) and $Pe = 10^{3}$ (right). The imposed scalar field $\bar{c}$ increases linearly within the cell from bottom to top ($\phi = 0.2$ %, the entire cell is shown, and gravity is pointing downward).

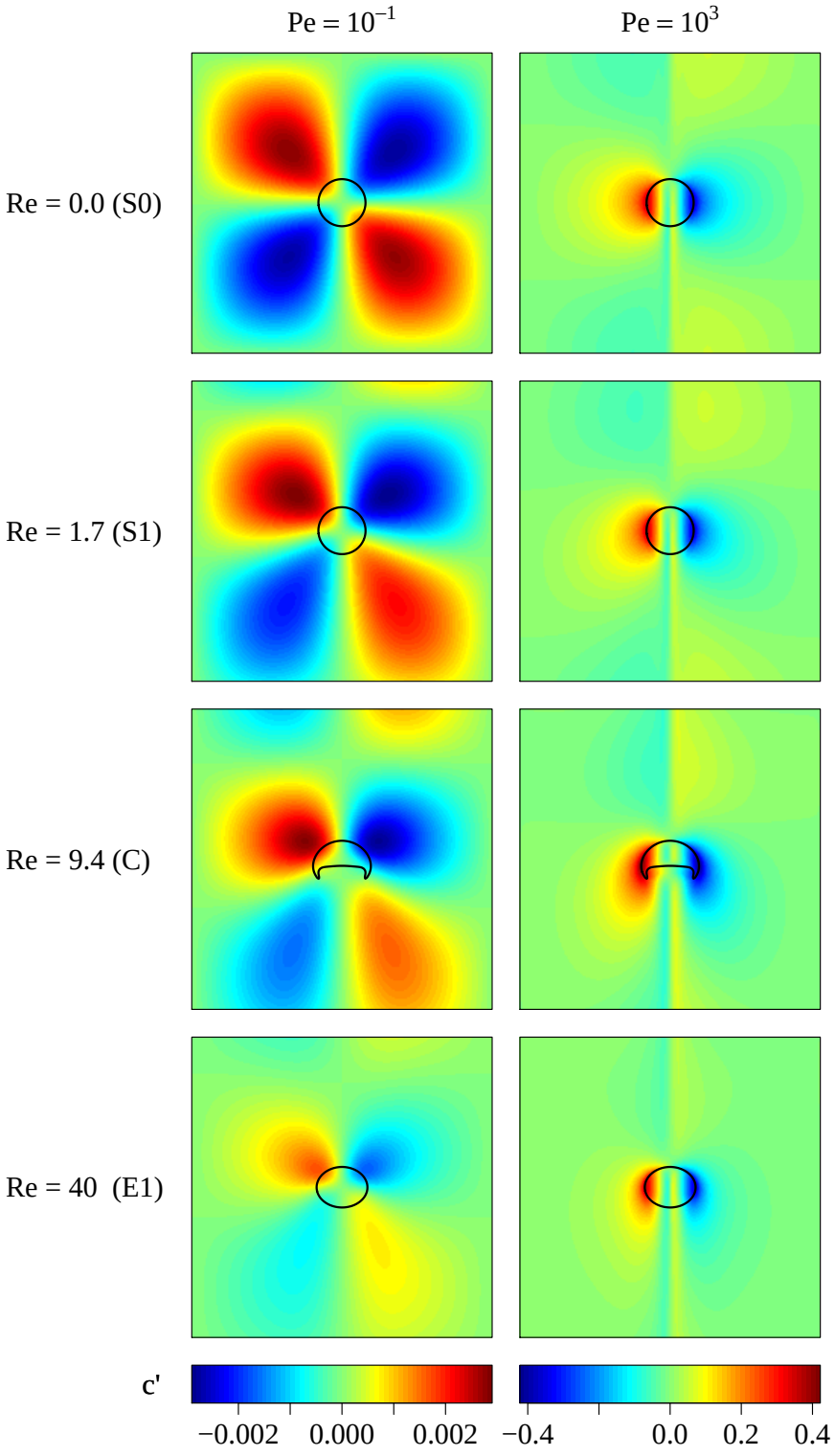

Figure 3.6 Scalar fluctuation field associated to $D_{\perp}^{\mathrm{conv}}$, shown in a vertical symmetry plane passing through the center of a bubble (c' is defined by (3.5)), for ordered arrays in various flow regimes at $Pe = 10^{-1}$ (left) and $Pe = 10^{3}$ (right). The imposed scalar field $\bar{c}$ increases linearly within the cell from left to right ($\phi = 0.2$ %, the entire cell is shown, and gravity is pointing downward).

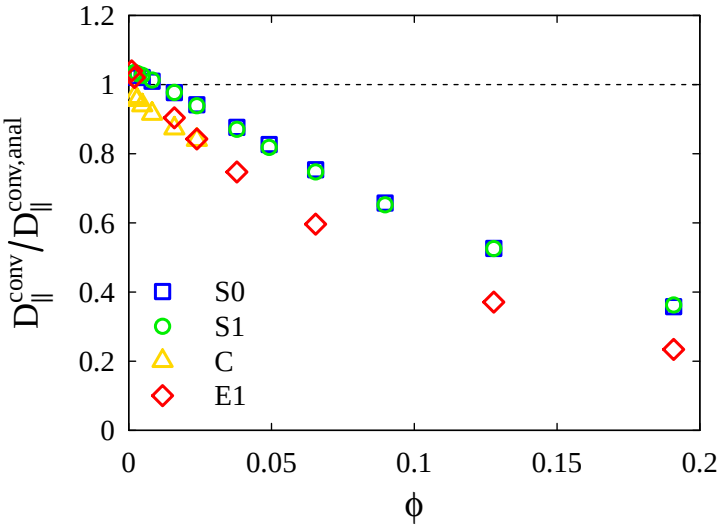

Figure 3.7 Deviation of the numerical solution with respect to the asymptotic analytical solution (3.41) as a function of volume fraction for ordered arrays at $Pe = 10^3$. The colors and symbols correspond to the different flow regimes listed in table 3.1.

only be shown for small volume fractions because the ordered array of bubbles does not exist at high volume fraction (instead unsteady elongated bodies of gas are obtained, see figure 2.14b). For case E1, some data points are apparently missing at some intermediate volume fractions, they actually correspond to bubbles rising in an oblique direction (see figure 2.18a). The study of this last configuration is beyond the scope of the present chapter.

We start with the effect of volume fraction on $D_{\parallel}^{conv}$, for which a good prediction can be obtained from the Oseen-flow analysis at small volume fraction. Figure 3.7 presents the evolution of $D_{\parallel}^{conv}/D_{\parallel}^{conv,anal}$ with ϕ, where $D_{\parallel}^{conv,anal}$ is the asymptotic analytical solution given by (3.41) with F computed from (3.42). The deviation of the numerical solution with respect to the analytical prediction increases with increasing volume fraction. Therefore the asymptotic solution needs to be corrected. When the volume fraction becomes large, the contribution from the gas phase is expected to be substantial and of a different nature from that arising from the bulk. We split $D_{\parallel}^{conv}$ into a contribution from the liquid (continuous phase) $D_{\parallel}^{conv,c}$ and a contribution from the bubble interior (disperse phase) $D_{\parallel}^{conv,d}$ as follows:

$$D_{\parallel}^{conv} = D_{\parallel}^{conv,c} + D_{\parallel}^{conv,d}, \tag{3.45a}$$

where

$$D_{\parallel}^{conv,c} = -(1-\phi)\langle u_3' c' \rangle_c, \tag{3.45b}$$

$$D_{\parallel}^{conv,d} = -\phi \langle u_3' c' \rangle_d, \tag{3.45c}$$

with u_3' the vertical component of $\boldsymbol{u}'$.

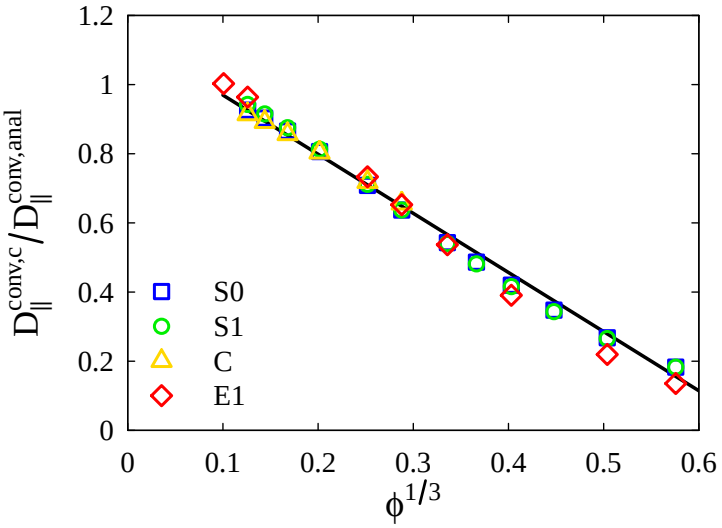

Figure 3.8 Contribution of the *continuous* phase $D_{\parallel}^{conv,c}$ as a function of volume fraction for ordered arrays at $Pe = 10^3$. $D_{\parallel}^{conv,anal}$ is the asymptotic solution given by (3.41). The slope of the black line is -1.71. The colors and symbols correspond to the different flow regimes listed in table 3.1.

We first discuss the contribution from the continuous phase $D_{\parallel}^{conv,c}$. In the analysis we have neglected the effect of the near field, which makes a contribution $O(\phi^{1/3})$ smaller than the one we have calculated (see remark below equation (4.2) in Koch et al. (1989)). Therefore we write $D_{\parallel}^{conv,c}$ as

$$D_{\parallel}^{conv,c} = D_{\parallel}^{conv,anal}\left[1 + O(\phi^{1/3})\right] \tag{3.46}$$

where $D_{\parallel}^{conv,anal}$ is given by (3.41). To determine the $O(\phi^{1/3})$ correction we plot $D_{\parallel}^{conv,c}/D_{\parallel}^{conv,anal}$ as a function of $\phi^{1/3}$ in figure 3.8. All data points approximately collapse on a single line, therefore the coefficient that multiplies $\phi^{1/3}$ is (nearly) constant (in particular, it does not depend, or very weakly, on the flow regime, which is rather unexpected). A linear regression yields a proportionality coefficient of -1.71, the corresponding linear relationship is shown as a black line in the figure. We conclude from figure 3.8 that the liquid contribution $D_{\parallel}^{conv,c}$ can be predicted for ϕ up to 20 % from the following expression:

$$D_{\parallel}^{conv,c} = \begin{cases} D_{\parallel}^{conv,anal} & \text{if } \phi^{1/3} < 0.1, \\ D_{\parallel}^{conv,anal}(1.14 - 1.71\phi^{1/3}) & \text{if } \phi^{1/3} \geqslant 0.1, \end{cases} \tag{3.47}$$

which is expected to apply to a variety of flow regimes (spherical to strongly deformed bubbles, Reynolds number from 0 to 40). Also note that $\phi^{1/3}$ is proportional to d_b/h, so the above relation is linear in the inverse of the distance between neighbor bubbles.

We now turn to the contribution $D_{\parallel}^{conv,d}$ arising from the bubble interior. The analysis of dispersion in porous media with random microstructure by Koch and Brady (1985) indicates

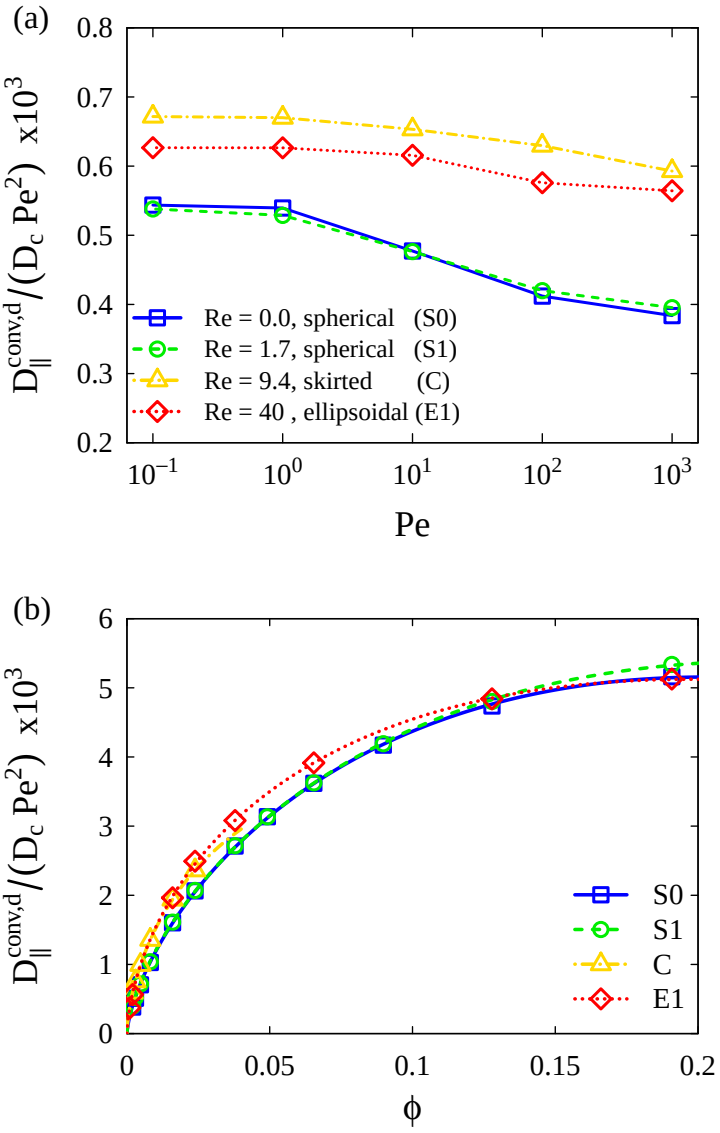

Figure 3.9 Contribution of the *disperse* phase $D_{\parallel}^{conv,d}$ for ordered arrays: (a) evolution with the Péclet number at $\phi = 0.2$ % (the lines are drawn to guide the eyes), and (b) evolution with the volume fraction at $Pe = 10^3$ (the lines are fits of the form of (3.48)). The colors and symbols correspond to the different flow regimes listed in table 3.1.

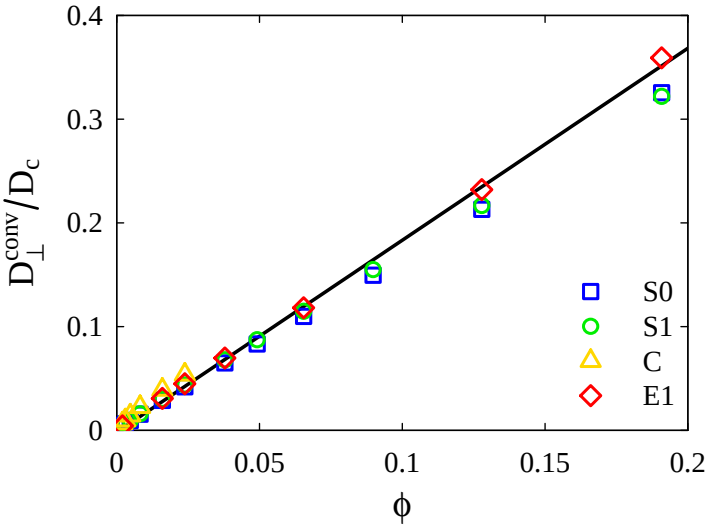

Figure 3.10 Evolution of $D_\perp^{conv}$ with volume fraction for ordered arrays at $Pe = 10^3$. The colors and symbols correspond to the different flow regimes listed in table 3.1. The slope of the black line is 1.85.

that regions of closed streamlines make an $O(\phi_{cs} Pe^2)$ convective contribution to the effective diffusivity, where ϕ_{cs} is the volume fraction of these regions (the Pe^2 scaling arises because a fluid tracer particle can only escape a closed streamline by diffusion normal to that streamline). By analogy we expect the recirculation within the bubble interior to yield a contribution $D_\parallel^{conv,d}/D_c = O(\phi Pe^2)$. The validity of the quadratic dependency on the Péclet number is assessed in figure 3.9a, where we show $D_\parallel^{conv,d}/(D_c Pe^2)$ as a function of Pe for $\phi = 0.2$ % (the lines are drawn to guide the eyes). The curves are not perfect straight lines (especially at low Re), so $D_\parallel^{conv,d}$ is not strictly proportional to Pe^2 over the entire range of Péclet numbers, however $D_\parallel^{conv,d}$ is indeed $O(Pe^2)$. We have checked that this statement holds at higher volume fraction (not shown). The effect of volume fraction on $D_\parallel^{conv,d}$ is shown in figure 3.9b, where $D_\parallel^{conv,d}/(D_c Pe^2)$ is plotted against ϕ. Clearly these two quantities are not linearly related. We found that instead $D_\parallel^{conv,d}$ can be expanded in a power series of $\phi^{i/3}$, starting at $i = 2$:

$$\frac{D_\parallel^{conv,d}}{D_c Pe^2} = \sum_{i \geqslant 2} a_i \phi^{i/3} \tag{3.48}$$

where a_i are constants that depend on the flow regime. The lines shown in figure 3.9b have been obtained by fitting the numerical data to (3.48) for $i = \{2, 3, 4\}$ for each case. The constants a_i depend weakly on the flow regime, and are all $O(10^{-2})$. No physical explanation can be offered beyond the fact that this type of expansion arises naturally in periodic configurations.

We finally present the results of a preliminary investigation of the effect of volume fraction on $D_\perp^{conv}$, for which the asymptotic analysis was found to yield quantitatively incorrect values beyond the dilute limit. The evolution of $D_\perp^{conv}$ with volume fraction, shown in figure 3.10, is

compatible with a linear dependence on ϕ for all the investigated flow regimes. Remarkably, the flow regime is of very minor importance here: for a given volume fraction, the values of $D_{\perp}^{\mathrm{conv}}$ are nearly identical whatever the Reynolds number (for $0 \leqslant Re \leqslant 40$) and the bubble shape (from spherical to strongly deformed). We conclude that the effect of ϕ must be accounted for to obtain a correct estimate of $D_{\perp}^{\mathrm{conv}}$, even at small volume fraction. The origin of the linear scaling with ϕ remains to be elucidated.

3.4.4 Free arrays

We examine in this section scalar mixing in freely evolving suspensions as represented by the periodic repetition of a unit cell containing several independent bubbles ("free arrays"). Our objective here is threefold: (i) to investigate the effective diffusivity of freely evolving suspensions at small and high Péclet numbers, (ii) to compare and contrast it with that obtained in ordered systems, and (iii) to evaluate the effect of the system size.

For that purpose, we considered a single flow regime (ellipsoidal bubbles at $Re = O(10)$, corresponding to case E1 in table 3.1) at intermediate volume fraction ($\phi = 2.4$ %) and explored the effect of varying the number of free bubbles N_b on the dependence of $\boldsymbol{D}^{\mathrm{conv}}$ on the Péclet number. Due to the multiplicity of simulations involved and to their duration (typically several months on 64 cores), only a few different values of N_b belonging to a rather limited range have been considered (namely $N_b = \{2, 3, 5, 8\}$ in the simulations for the determination of $D_{\parallel}^{\mathrm{conv}}$, and $N_b = \{2, 8\}$ in those for $D_{\perp}^{\mathrm{conv}}$). For the same reason, investigations of the effects of volume fraction and flow regime could not be undertaken as part of the present thesis.

The results for the longitudinal and transverse components of $\boldsymbol{D}^{\mathrm{conv}}$ are presented in figure 3.11, where we show their values for various N_b over a very wide range of Péclet numbers. Convergence of $D_{\parallel}^{\mathrm{conv}}$ with the system size is very fast: the values of $D_{\parallel}^{\mathrm{conv}}$ are essentially independent of the number of free bubbles for $2 \leqslant N_b \leqslant 8$ at all Péclet numbers. This suggests that $D_{\parallel}^{\mathrm{conv}}$ is independent of the system size, although this would need to be confirmed by considering larger values of N_b. Our data for $D_{\perp}^{\mathrm{conv}}$ suggest that convergence with N_b is slower for this quantity, especially at high Péclet number, although conclusions can hardly be drawn on this point due to the few values of N_b considered.

We first examine the dependence of $\boldsymbol{D}^{\mathrm{conv}}$ on the Péclet number in free arrays of bubbles. At small Pe, $D_{\parallel,\perp}^{\mathrm{conv}} \propto D_c Pe^2$, whereas at high Pe, $D_{\parallel,\perp}^{\mathrm{conv}} \propto D_c Pe = U d_b$. Note that the scaling at high Pe is expected from a simple dimensional analysis in a convection-dominated regime where diffusion plays no role. This regime is termed "mechanical dispersion" (Koch & Brady, 1985). The different dispersion regimes at low and high Pe can also be identified from the features of the scalar fluctuation field c' (defined by (3.5)). Instantaneous snapshots of c' associated to $D_{\parallel}^{\mathrm{conv}}$ and $D_{\perp}^{\mathrm{conv}}$ are shown in figure 3.12 and figure 3.13, respectively, for an array of 8 free bubbles at $Pe = 10^{-1}$ (left) and at $Pe = 10^{6}$ (right). For a given component, the isocontours of c' follow markedly different patterns at low and high Pe.

We now compare these results to those obtained for ordered arrays (black dots in figure 3.11)

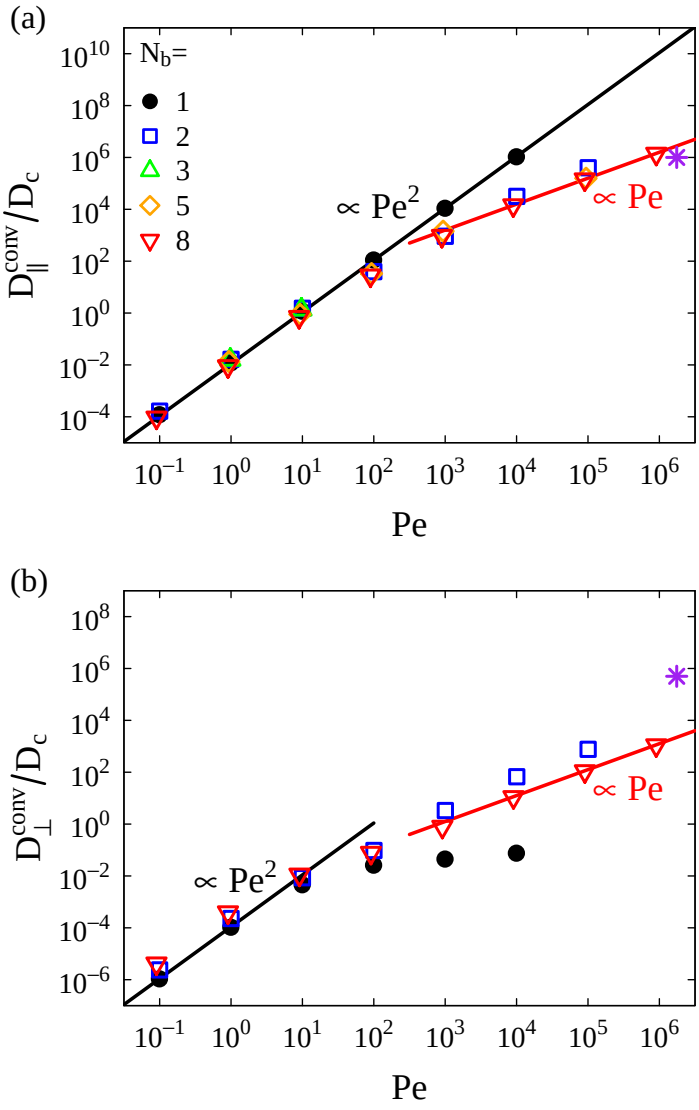

Figure 3.11 Longitudinal (a) and transverse (b) components of $\boldsymbol{D}^{\mathrm{conv}}$ as a function of the Péclet number for various numbers of free bubbles N_b in the unit cell ($N_b = 1$ corresponds to an ordered array). Symbols other than purple stars: DNS ($Re \approx 30$, $\phi = 2.4$ %); purple stars: experimental data of Alméras et al. (2015) ($Re \approx 700$, $\phi \approx 2.4$ %).

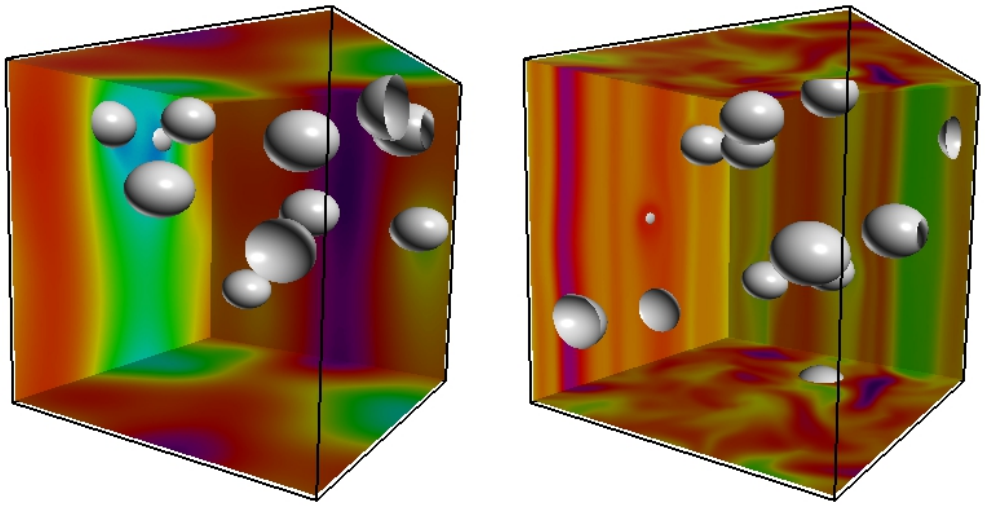

Figure 3.12 Instantaneous scalar fluctuation field associated to $D_{\parallel}^{\mathrm{conv}}$ (as is defined by (3.5)) for a free array of 8 bubbles, at $Pe = 10^{-1}$ (left) and $Pe = 10^{6}$ (right). The gradient of $\bar{c}$ is vertical (the entire cell is shown, and gravity is pointing downward).

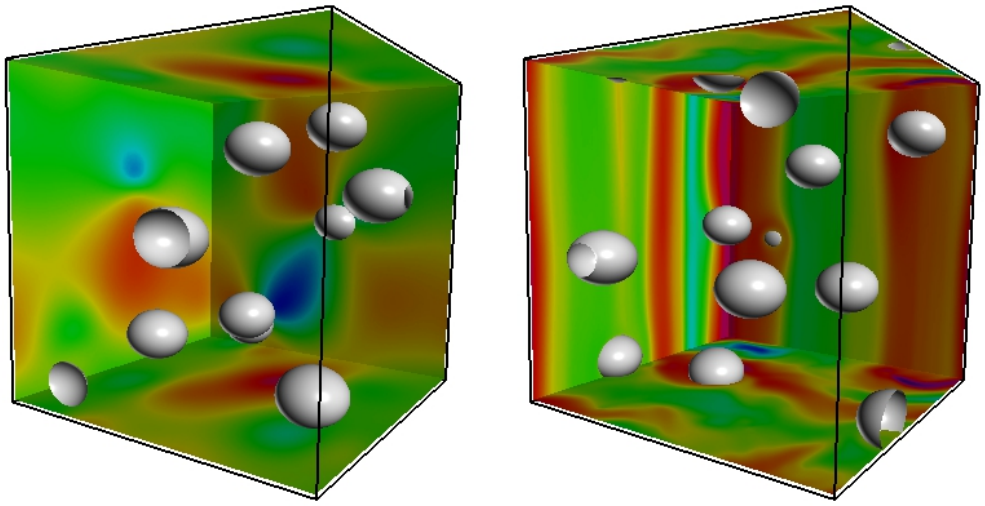

Figure 3.13 Instantaneous scalar fluctuation field associated to $D_{\perp}^{\mathrm{conv}}$ (as defined by (3.5)) for a free array of 8 bubbles, at $Pe = 10^{-1}$ (left) and $Pe = 10^{6}$ (right). The gradient of $\bar{c}$ is horizontal (the entire cell is shown, and gravity is pointing downward).

and discuss the effect of the microstructure. At small *Pe*, $D_{\parallel}^{\mathrm{conv}}$ and $D_{\perp}^{\mathrm{conv}}$ grow quadratically with *Pe* in both free and ordered arrays. This scaling was also obtained by Koch and Brady (1985) for low-*Pe* dispersion in porous media with random microstructure (albeit in the Stokes flow limit). Since in the low-*Pe* regime, diffusion by the random motion of molecules is much faster than convection by the flow, the microstructure has only a quantitative incidence on $\boldsymbol{D}^{\mathrm{conv}}$, and dispersion is qualitatively identical in ordered and freely evolving suspensions. Note that similar features in the spatial distribution of c' can be identified in ordered and free arrays at low *Pe* (see left side of figures 3.5 and 3.12 for $D_{\parallel}^{\mathrm{conv}}$, and of figures 3.6 and 3.13 for $D_{\perp}^{\mathrm{conv}}$).

At high *Pe*, Taylor dispersion obtained in ordered arrays is replaced by mechanical dispersion as soon as the relative motion between bubbles is allowed. Incidentally, mechanical dispersion is also obtained at high *Pe* in random media in Stokes flow conditions (Koch & Brady, 1985). Although the microstructure of the present bubbly suspensions has not been evaluated quantitatively, visual inspection and prior results on their dynamics (see in particular section 2.4.2.2) showed that it is not random, and is characterized by a certain "organization". Despite the fact that freely evolving suspensions resemble ordered ones with respect to their dynamics, scalar dispersion is extremely sensitive to the *introduction* of disorder, and is fundamentally different in perfectly ordered and weakly disordered suspensions at high Péclet number. It does not, however, seem to be sensitive to the *degree* of disorder, as suggested by the fact that the same scalings with *Pe* are obtained for random porous media and weakly disordered suspensions. We stress that this last statement is purely speculative, and would require a quantitative study of the effect of the microstructure to be confirmed.

We finally attempt a comparison of our results with the experimental data of Alméras et al. (2015), who measured the effective diffusivity of a homogeneous swarm of high-Reynolds-number rising bubbles at $Pe \approx 1.75 \times 10^6$ for gas volume fractions ranging from 1 % to 13 %. It is important to stress that in these experiments, $Re \approx 700$, whereas in the simulations, $Re \approx 30$, so the comparison is only indicative. Interpolation (by eye) of their data at $\phi \approx 2.4$ % (figure 10 in their paper) yields $D_{\parallel}^{\mathrm{eff}}/D_c = 1 \times 10^6$ and $D_{\perp}^{\mathrm{eff}}/D_c = 5 \times 10^5$. These experimental values are represented by purple stars in figure 3.11. Note that at such high Péclet number, the dominant contribution to $\boldsymbol{D}^{\mathrm{eff}}$ is due to $\boldsymbol{D}^{\mathrm{conv}}$, so it seems reasonable to assume that these are equivalent. The order of magnitude of $D_{\parallel}^{\mathrm{eff}}/D_c$ is comparable in the experiment and in the simulation, whereas $D_{\perp}^{\mathrm{eff}}/D_c$ is much higher in the experiment. This difference can be explained from the different properties of the bubble-induced liquid agitation in the horizontal direction. In our simulations of free arrays at moderate *Re*, the bubbles were observed to rise along nearly straight vertical lines, and the liquid velocity variance is characterized by an anisotropy ratio $2\langle u_3' u_3' \rangle / \langle u_1' u_1' + u_2' u_2' \rangle$ of approximately 8 (for $N_b = 8$), as can be seen in figure 2.33b, whereas in the experiment at high *Re*, the bubble motion is fully three-dimensional, and the anisotropy ratio is approximately 2. Finally, as only one value of the Péclet number was considered in the experiments of Alméras et al. (2015), no comparison can be offered regarding the dependence of the effective diffusivity on the Péclet number.

3.5 Conclusions

An average conservation equation for the macroscale scalar field in bubbly suspensions has first been derived from local governing equations. This equation has been complemented by a macroscale constitutive relation involving an effective diffusivity tensor which expression in terms of microscopic quantities stems directly from the averaging procedure. A general methodology has been developed for the computation of the effective diffusivity tensor from direct numerical simulations of scalar transport in bubbly suspensions as represented by arrays of bubbles. The longitudinal and transverse components of the convective contribution to the effective diffusivity, denoted $D_{\parallel}^{\mathrm{conv}}$ and $D_{\perp}^{\mathrm{conv}}$, respectively, have then been computed for bubbly suspensions in various flow regimes. This convective contribution is that associated with bubble-induced agitation, and is the dominant contribution to the effective diffusivity in commonly encountered bubbly flows.

The dispersion theory of Koch et al. (1989) indicates that convective mixing mechanisms in ordered suspensions in Stokes-flow conditions differ at low and high Péclet numbers. At low Péclet number, convectively enhanced dispersion is obtained, whereas at high Péclet number, Taylor dispersion dominates. In the present study, we have extended this theory to account for weak inertial effects, and we have shown that these two dispersion regimes are qualitatively unchanged in the presence of inertia. This result has been confirmed by direct numerical simulations for values of the Reynolds number ranging from vanishingly small to moderate. Theoretical predictions have been shown to yield the correct order of magnitude for $D_{\parallel}^{\mathrm{conv}}$ in a variety of flow regimes (spherical to strongly deformed bubbles with Reynolds numbers from 0 to 40) at small volume fraction. A simple correction obtained from the numerical simulations has been proposed to account for the effect of volume fraction up to 20 %. In contrast, $D_{\perp}^{\mathrm{conv}}$ is severely underpredicted by the theory when its underlying assumptions are not satisfied, and further investigations are required to fully elucidate the behavior of $D_{\perp}^{\mathrm{conv}}$ at finite volume fraction.

Simulations of scalar transport in freely evolving bubbly suspensions, as represented by free arrays of bubbles, have been carried out for a wide range of Péclet numbers, and the effect of introducing additional degrees of freedom in the system has been evaluated. At low Péclet number, dispersion in free arrays is convectively enhanced, as in ordered arrays. At high Péclet number, Taylor dispersion in perfectly ordered systems is replaced by purely mechanical dispersion, analogous to that encountered in random media, as soon as two bubbles are introduced in the unit cell. Besides, the effective diffusivity seems to be weakly sensitive to the system size. This last assertion requires more thorough investigations to be confirmed, but is encouraging regarding the possibility of computing the effective diffusivity of homogeneous bubbly flows from direct numerical simulations of systems of relatively small size.

The results presented in this chapter are restricted to bubbles having the same diffusivity as that of the surrounding liquid ($D_d = D_c$), and to scalar fields that are continuous across the

interface ($m = 1$). Ongoing simulations for $D_d \gg D_c$ indicate that the effect of a difference in diffusivities on $\boldsymbol{D}^{\text{conv}}$ is substantial only at high volume fraction and low Péclet number. The effect of $m \neq 1$, which represents Henry's law in the context of chemical species transport, should be investigated in the future. In addition, preliminary results for the diffusive contribution to the effective diffusivity, denoted $\boldsymbol{D}^{\text{diff}}$, indicate that a reasonable estimate of it is obtained from the first-order analytical solution of the conduction problem derived by Maxwell (1873), except maybe at very high volume fraction, and that the effects of order, anisotropy, and bubble deformation are only of secondary importance.

Besides the effective diffusivity, another quantity of practical importance is the rate of interfacial scalar transport in the presence of an average scalar gradient between the disperse phase and the bulk. Heat and mass exchanges across phase boundaries are traditionally expressed as dimensionless transfer coefficients called the Nusselt and the Sherwood numbers, respectively. Their functional dependences on suspension properties, in particular the volume fraction, have been the subject of analytical (Acrivos, Hinch, & Jeffrey, 1980), numerical (Aboulhasanzadeh & Tryggvason, 2014), and experimental (Colombet et al., 2011, 2015) studies. Formally, the Nusselt and the Sherwood numbers are closure coefficients for the conditionally averaged scalar transport equation, where the conditional average is defined as an ensemble average over the subset of realizations wherein a particulate is present at a given position. Less formally, the Nusselt and Sherwood numbers are related to a "mesoscale" description of scalar transfer between the two phases, whereas the effective diffusivity is associated with a "macroscale" description of scalar transport through a two-phase mixture seen as a continuum. They correspond to different closure problems, and one cannot be inferred from the other.

Chapter 4

Toward turbulent bubbly flows

The interaction between a large bubble and homogeneous isotropic turbulence

Contents

4.1 Introduction

In this chapter we investigate the dynamics of a bubble rising in a turbulent liquid flow. When the bubbles are smaller than the smallest length scales of the flow, their trajectories can be computed in a Lagrangian manner from the integration of an explicit equation of motion and their action on the surrounding flow can be modeled by point forces acting on the carrier phase. This approach has been extensively used to investigate the dynamics of microbubbles in three-dimensional homogeneous isotropic turbulence and their backreaction on the surrounding flow (Wang & Maxey, 1993; Maxey et al., 1994; Spelt & Biesheuvel, 1997; Mazzitelli et al., 2003b, 2003a; Snyder et al., 2007). These studies highlighted the crucial role played by the lift force in retarding the rise of small bubbles and on the modulation of turbulence by their presence.

But in many situations of practical interest, the characteristic size of the bubbles is in the inertial range of scales. In that case, the hydrodynamic forces acting on the bubble are influenced by all the length and time scales down to the Kolmogorov microscales (Merle et al., 2005) and their rapid fluctuations cannot be accurately captured by standard point-bubble models (Balachandar & Eaton, 2010). Hence, to properly capture the physics of turbulent flows laden with finite-size bubbles, all the scales of the carrier flow and of the disturbances induced by their motion must be resolved.

The question of the dynamics of finite-size particulates in a turbulent environment has drawn considerable attention within the last years. On the experimental side, this problem has been tackled by a number of investigators, essentially in the case of solid particles (e.g., Volk, Calzavarini, Leveque, and Pinton (2011), Zimmermann et al. (2011), Bellani and Variano (2012), Bellani, Byron, Collignon, Meyer, and Variano (2012), Klein, Gibert, Bérut, and Bodenschatz (2013), Mathai, Prakash, Brons, Sun, and Lohse (2015)), and, to a much lesser extent, in the case of bubbles (e.g., Volk et al. (2008), Ravelet et al. (2011), Prakash et al. (2012)). However the measurement of the carrier-phase velocity field in the immediate vicinity of the particulates remains a difficult task, and interface-resolved simulations are needed to complement laboratory experiments.

While the interaction between isotropic turbulence and large solid spherical particles has been recently simulated in increasingly complex configurations (fixed particle (Naso & Prosperetti, 2010), free non-buoyant particle (Homann & Bec, 2010; Cisse et al., 2013), settling particles (Chouippe & Uhlmann, 2015)), the case of clean bubbles still remains largely uncharted territory: the state-of-the-art amounts to the early large-eddy simulations of Merle et al. (2005) and Legendre et al. (2006) who considered a large bubble with imposed spherical shape held fixed on the axis of a weakly turbulent pipe flow. Compared to those of solid particles, direct numerical simulations of bubbly flows are even more challenging because internal gas circulation and interface deformation need to be accounted for, which in turn requires solving the Navier-Stokes equations in both phases and to treat the interface as a free

surface.

In this chapter we present the results of direct numerical simulations of a single, deformable, finite-size bubble freely rising in an otherwise homogeneous isotropic turbulent flow. These simulations have three objectives: (i) to characterize the kinematics of a large bubble rising in a turbulent environment, (ii) to evaluate whether the bubble acceleration can be correlated to appropriately defined liquid flow properties, and (iii) to characterize the liquid flow sampled by the bubble. For clarity and consistency with usual conventions in this field, the notations used in this chapter slightly differ from that used in preceding chapters.

4.2 Methodology

4.2.1 Physical parameters

We consider the statistically stationary rise of a single buoyant bubble in an otherwise homogeneous isotropic turbulent liquid flow. The primary dimensionless parameter characterizing the interaction between the bubble and turbulence is the turbulence intensity $\beta = u_0/V_T$, where u_0 is the root mean square of the liquid velocity fluctuations in the absence of the bubble (denoted by the subscript 0) and V_T is the terminal velocity reached by the bubble when rising in still liquid (denoted by the subscript T). In the present study, β is $O(1)$ and is modified through V_T as explained in the next paragraph. The characteristic length scales of the carrier flow are the Kolmogorov scale $\eta = (\nu^3/\varepsilon_0)^{1/4}$, the Taylor scale $\lambda = \sqrt{15\nu u_0^2/\varepsilon_0}$, and the integral scale $L = u_0^3/\varepsilon_0$, where ν is the kinematic viscosity of the liquid and ε_0 is the mean dissipation rate per unit mass of the single-phase flow. The bubble characteristic size d_b, defined as the diameter of the volume-equivalent sphere, is equal to Taylor length-scale size. Turbulence length scales with respect to bubble size, as well as Taylor-microscale Reynolds number $Re_\lambda = u_0\lambda/\nu$, were kept constant throughout the study. They are listed in table 4.1.

When a bubble is rising in a liquid at rest, the terminal bubble velocity depends on the ratios of the gas density and viscosity to that of the liquid, which are set to 10^{-3} and 10^{-2}, respectively, and on two dimensionless groups that measure the relative strengths of the buoyancy, viscous, and surface tension forces acting on the bubble. The first dimensionless group is the Bond number (also known as the Eötvös number) $Bo = g d_b^2 \Delta\rho/\gamma$, where g is the magnitude of the gravitational acceleration, $\Delta\rho$ is the density difference between the liquid and the gas phases, and γ is the surface tension. The Bond number was set to $Bo = 0.38$, which yields in quiescent conditions a nearly spherical (though deformable) bubble. This choice allows the bubble to deform without breaking-up in the presence of an intense background turbulent flow. The second dimensionless group is the Archimedes number (also known as the Galileo number) $Ar = \sqrt{\rho\Delta\rho g d_b^3}/\nu$, which is the variable parameter that determines the terminal velocity of the bubble V_T. This velocity is estimated herein using the correlation of Mei et al. (1994), and is used to define a characteristic bubble Reynolds number $Re_T = V_T d_b/\nu$. For the range of parameters considered here, Re_T is $O(10)$ so that in quiescent liquid the bubble motion is

Ar	Re_T	Re_0	β	Re_λ	$\frac{\eta}{d_b}$	$\frac{\lambda}{d_b}$	$\frac{L}{d_b}$	$\frac{h}{d_b}$	$\frac{\Delta x}{d_b}$	$\frac{\tau_\eta}{t_b}$	$\frac{T_L}{t_b}$	$\frac{\Delta t}{t_b}$
40.7	62.5	28.5	0.46	29.9	0.098	1.0	2.1	12	1/16	0.50	3.9	0.0007
27.2	31.4	28.4	0.90	29.7	0.098	1.0	2.1	12	1/16	0.45	3.4	0.0009
19.2	17.6	28.2	1.60	29.5	0.098	1.0	2.1	12	1/16	0.40	3.1	0.0011

Table 4.1 Parameters of the simulations. Ar: Archimedes number; $Re_T = d_b V_T/\nu$: terminal bubble Reynolds number based on V_T, the terminal velocity of the bubble in quiescent conditions estimated from Mei, Klausner, and Lawrence (1994); $Re_0 = d_b u_0/\nu$: bubble Reynolds number based on u_0, the root-mean-square liquid velocity fluctuations in the absence of the bubble; $\beta = u_0/V_T$: turbulence intensity; Re_λ: Taylor-microscale Reynolds number; d_b: bubble volume-equivalent diameter; η: Kolmogorov length scale; λ: Taylor length scale; L: integral length scale; h: computational domain size; Δx: mesh size; $t_b = V_T/(2g)$: bubble characteristic time scale with g the gravitational acceleration; τ: Kolmogorov time scale; T_L: large-eddy turnover time scale; Δt: time step.

steady, vertical, and its wake is laminar, steady, and attached to the bubble. In the asymptotic limit of Stokes or potential flow, the drag acting on the bubble is proportional to its velocity, and the bubble relaxation time is $t_b = V_T/(2g)$. Such a linear drag law does not hold for $O(10)$ Reynolds number, nevertheless for consistency with prior work we kept this definition to estimate a characteristic time scale for the bubble laminar rise. In the present setup $t_b \approx 2\tau_\eta$ and $t_b \approx 0.3T_L$, where $\tau_\eta = (\nu/\varepsilon_0)^{1/2}$ is the Kolmogorov time scale and $T_L = u_0^2/\varepsilon_0$ is the large-eddy turnover time scale. All above-mentioned parameters are summarized in table 4.1.

4.2.2 Two-phase flow simulation

The carrier flow varying over distances much smaller than the bubble size, the point-bubble approximation is not appropriate. Instead, all the scales present in the two-phase flow must be resolved. In our approach, the fluid motion is solved both in the liquid and the gas with the appropriate jump conditions at the fluid-fluid boundary, namely the continuity of velocity and of shear stress across the interface (owing to the absence of phase change and surface tension gradients, respectively), and a jump in normal stress equal to the surface tension force per unit area. These sets of equations coupled by interfacial jump conditions are integrated numerically using our three-dimensional DNS code, a detailed description of which is provided in chapter 1.

In short, the incompressible Navier-Stokes equations are integrated in physical space by a standard projection method (Chorin, 1968), surface tension is accounted for using the continuum surface force model (Brackbill et al., 1992), and the deformable gas-liquid interface is captured by a modified level-set method (Russo & Smereka, 2000; Sabelnikov et al., 2014). Our time integration algorithm is based on a third-order TVD Runge-Kutta scheme for the level-set equation and on a mixed Crank-Nicolson/third-order Adams-Bashforth scheme for the Navier-

Stokes equations. For spatial derivatives, we employ a standard mixed finite difference/finite volume discretization on a uniform Cartesian staggered grid: fifth-order WENO schemes are used for advection terms, and second-order centered schemes are used otherwise. The grid spacing was set to $\Delta x = 0.64\eta = d_b/16$ and the time step to $\Delta t = O(10^{-3}\tau_\eta)$, which allows the flow to be fully resolved.

With level-set methods, the mass (volume for incompressible flows) of each phase is not necessarily conserved. In our approach, volume conservation is enforced at each time step using the correction proposed by Sussman and Uto (1998). This correction consists in slightly shifting the level-set function ψ by an amount $\Delta\psi$ in such a way that the volume of each phase remains constant. We have checked that the magnitude of this correction is negligible ($\max|\Delta\psi|/\Delta x \lesssim 10^{-6}$ in the present simulations, see chapter 1 for more details and validation tests).

Periodic boundary conditions are applied at the boundaries of the cubic computational domain, of linear dimension $h = 12\,d_b$. This configuration effectively corresponds to a cubic array of bubbles with volume fraction of 0.03 %. We have seen in chapter 2 that even at very low volume fraction a bubble rising in quiescent liquid may be affected by the wakes of its preceding neighbors. The situation is however very different here. The carrier phase is now turbulent with velocity fluctuations u_0 comparable to the bubble velocity V_T ($\beta = u_0/V_T \sim 1$, see table 4.1). Prior work on spherical bubbles and particles set fixed in a weakly turbulent environment showed that the velocity defect in the (laminar) wake first decays as z^{-1} (z being the downstream distance to the particulate) and then follows a z^{-2} power law from the point where the magnitude of the velocity defect and that of the turbulent velocity fluctuations become of the same order (Legendre et al., 2006; Amoura, Roig, Risso, & Billet, 2010; Eames, Johnson, Roig, & Risso, 2011). Assuming a z^{-2} decay law, a coarse estimate of the wake velocity u_z at a downstream distance $z = h$ from the bubble is $u_z/u_0 \sim (V_T/u_0)(h/d_b)^{-2} \sim 10^{-2} \ll 1$. It seems therefore reasonable to consider that a bubble is not affected by the wakes of its periodic images. The negligible effect of periodicity will be confirmed a posteriori in section 4.3.3.

4.2.3 Turbulence forcing

Statistically stationary turbulence was sustained in our system using the linear forcing proposed by Lundgren (2003), which consists in a forcing term proportional to the velocity vector. This forcing scheme, which is formulated in physical space, has been shown to yield the same results as spectral implementations of low-wavenumber forcing for single-phase flow turbulence (Rosales & Meneveau, 2005), and has been used in prior studies of turbulent two-phase flows by Naso and Prosperetti (2010) (fixed solid sphere) and Duret et al. (2012) (interface-resolved gas-liquid flow). Gravity was however not included in these prior studies. The use of the linear forcing in two-phase systems where gravity is accounted for has been recently criticized by Chouippe and Uhlmann (2015) based on the argument that this scheme, due to its intrinsic instability, leads to an unbounded growth of the kinetic energy and hence

does not allow a stable stationary-state to be reached. This problem is however easily solved, as will be shown below.

In our numerical approach, a statistically stationary level of kinetic energy was maintained by forcing the carrier phase as follows. The liquid momentum conservation equation is supplemented by an additional body force $\rho \boldsymbol{f}$:

$$\frac{D\rho \boldsymbol{u}}{Dt} = \boldsymbol{\nabla} \cdot \boldsymbol{T} + (\rho - \langle \rho \rangle)\boldsymbol{g} + \rho \boldsymbol{f}, \qquad \text{with } \boldsymbol{f} = Q\boldsymbol{u}^*, \tag{4.1}$$

where ρ is the liquid density, $\boldsymbol{u}$ is the velocity, t is the time, $\boldsymbol{T}$ is the stress tensor, $\boldsymbol{g} = -g\boldsymbol{e}_z$ is the gravitational acceleration, and $\langle \rho \rangle$ is the system average density which must be subtracted from the local density to prevent the entire system from accelerating in the downward vertical direction. In the forcing term, Q is a positive constant, and, in a single-phase flow, $\boldsymbol{u}^*$ would be the local velocity. In two-phase flows a slightly different definition must be used for $\boldsymbol{u}^*$, as explained in the next paragraph. The forcing term is discretized in time using a third-order Adams-Bashforth scheme. For stationary single-phase turbulence, prescribing a value of Q is equivalent to imposing a large-eddy turnover time scale $T_L = 1/3Q$, and setting the size of the periodic box determines the integral length scale $L \approx 0.19h$ (Rosales & Meneveau, 2005). These two relations allow u_0 to be estimated a priori.

The introduction of the forcing term $\rho Q\boldsymbol{u}^*$ in (4.1) results in an additional net force $\boldsymbol{N}$ on the liquid:

$$\boldsymbol{N} = \rho Q \int_{\mathcal{V}_c} \boldsymbol{u}^* \, \mathrm{d}\boldsymbol{x} \tag{4.2}$$

where $\mathcal{V}_c$ denotes the set of points that belong to the continuous phase. If one sets $\boldsymbol{u}^* = \boldsymbol{u}$ as in single-phase flows, $\boldsymbol{N}$ is not zero, because the volume integral of $\boldsymbol{u}$ over the liquid phase is not strictly zero (the upward motion of the bubble must be compensated by a downflow of liquid). As a consequence, the liquid mean flow grows exponentially, as observed by Chouippe and Uhlmann (2015). This issue is removed by subtracting the instantaneous mean liquid velocity $\langle \boldsymbol{u} \rangle_c$ from the local velocity:

$$\boldsymbol{u}^* = \boldsymbol{u} - \langle \boldsymbol{u} \rangle_c \qquad \text{with } \langle \boldsymbol{u} \rangle_c = \frac{1}{V_c} \int_{\mathcal{V}_c} \boldsymbol{u} \, \mathrm{d}\boldsymbol{x} \tag{4.3}$$

with V_c the volume of the liquid phase. Now $\boldsymbol{N} = \boldsymbol{0}$ is satisfied, the forcing has no net effect on the liquid phase, and a statistically stationary state can be reached. Note that even in the absence of gravity it is generally desirable to subtract the residual mean flow to ensure stability (Naso & Prosperetti, 2010; Duret et al., 2012).

4.2.4 Simulation procedure

Our simulation procedure was as follows. A carrier turbulent flow with a Taylor-microscale Reynolds number $Re_\lambda = 30$ was first generated in the periodic computational domain. An initially spherical bubble with $d_b = \lambda$ was then introduced in the domain, and the two-phase

flow was evolved until a statistically stationary state was reached, as monitored by the time signals of the bubble velocity and liquid kinetic energy. The simulation was then continued over a time period of $O(400\,T_L)$, during which liquid Eulerian and bubble Lagrangian statistics were gathered. This procedure was repeated for each value of the turbulence intensity β.

As the center of mass of the bubble is not tracked explicitly with our numerical method, computing the bubble velocity in a Lagrangian manner would have been cumbersome. Instead the instantaneous bubble velocity $\boldsymbol{V}$ was computed from the gas phase velocity

$$\boldsymbol{V} = \langle \boldsymbol{u} \rangle_d \qquad \text{with } \langle \boldsymbol{u} \rangle_d = \frac{1}{V_d} \int_{\mathcal{V}_d} \boldsymbol{u}\, \mathrm{d}\boldsymbol{x} \tag{4.4}$$

where V_d the volume of the gas phase (that is, the bubble volume), and $\mathcal{V}_d$ is the set of points that belong to the gas phase. It has been checked numerically that this definition yields the same result as the direct computation of $\mathrm{d}\boldsymbol{X}/\mathrm{d}t$ where $\boldsymbol{X}$ is the position of the bubble center of mass. Also, since the computational domain is very large, the bubble velocity as defined by (4.4) is indistinguishable from the bubble drift velocity, denoted $\boldsymbol{U}$, used in previous chapters. Indeed in our simulations, $|\langle V_i \rangle - \langle U_i \rangle| / \langle V_i \rangle \leqslant 5 \times 10^{-4}$ for $i \in \{x, y, z\}$ at all times and for all β. Such a distinction would be relevant for much larger volume fractions only.

4.3 Results

4.3.1 Statistical description of the bubble motion and deformation

In quiescent liquid ($\beta = 0$), the bubbles considered here rise along straight vertical paths. As the turbulence intensity β is increased, their trajectories become more erratic, as illustrated in figure 4.1. This section is devoted to the characterization of the bubble kinematics. In what follows, $\boldsymbol{V}$ denotes the bubble velocity, and $\boldsymbol{A} = \mathrm{d}\boldsymbol{V}/\mathrm{d}t$ is the bubble acceleration. Subscripts x, y, and z, denote the two horizontal and the vertical components of a vector quantity, respectively, with buoyancy acting in the positive z-direction. Time averaging is denoted by brackets, and since the two horizontal directions are equivalent, Lagrangian statistics for the x and y components have been combined.

For information we first report in table 4.2 the average bubble Reynolds number $\langle Re_z \rangle = \langle V_z \rangle d_b / \nu$ based on the average bubble *rise* velocity for each value of β: these remain $O(10)$, and are lower than in the quiescent case. This result will be further discussed hereinafter. We emphasize that $\langle Re_z \rangle$ is *not* the average bubble Reynolds number based on the bubble *slip* velocity (i.e., the bubble velocity relative to that of the carrier flow), which is unknown. This crucial issue will be addressed in section 4.3.2.

4.3.1.1 Deformation

The bubble deformation is characterized here through the bubble sphericity, defined as the ratio between the surface of a volume-equivalent sphere and that of the bubble (lower sphericity

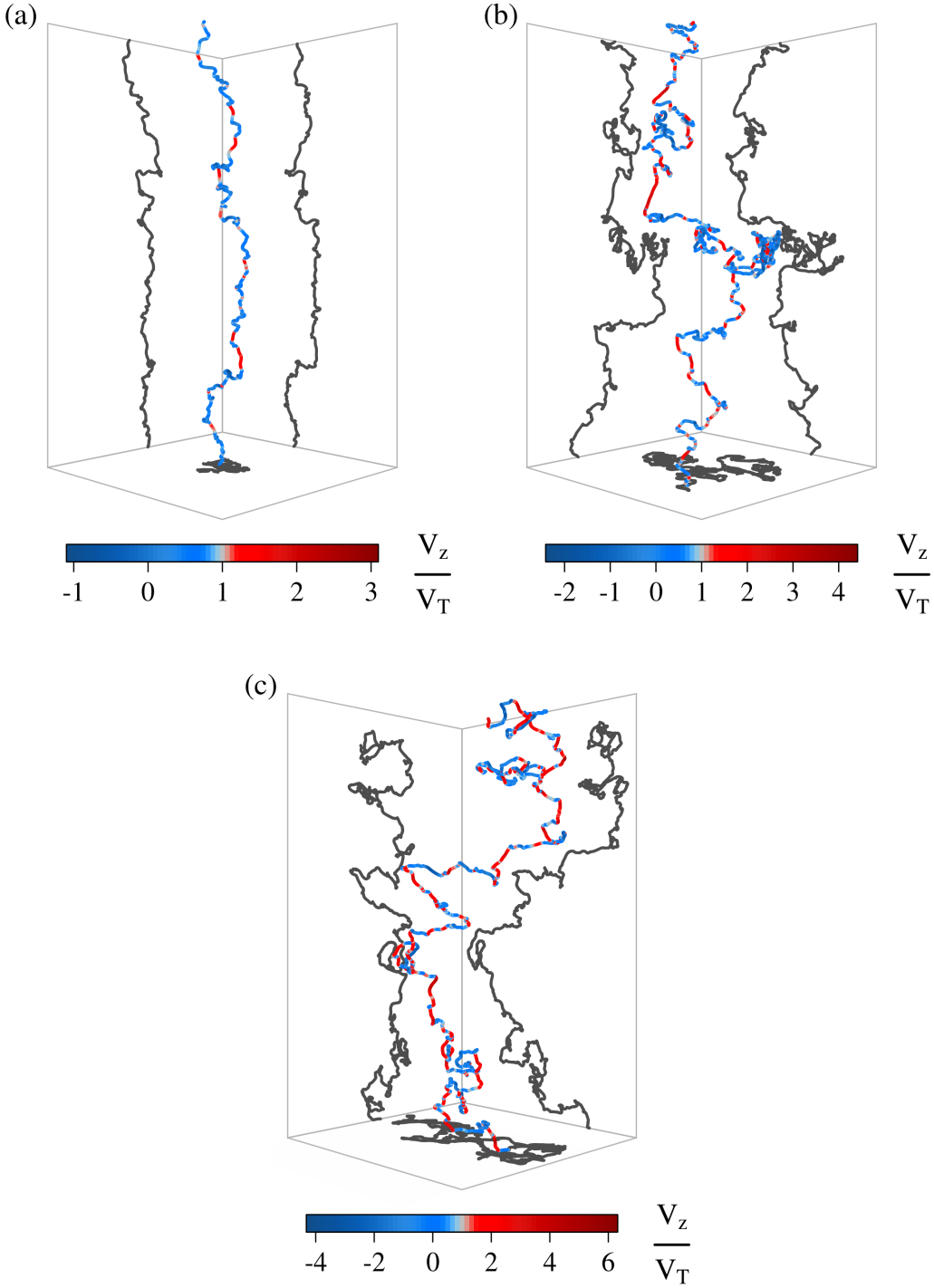

Figure 4.1 Sample bubble trajectories and their 2D projections on horizontal and vertical planes for (a) $\beta = 0.46$, (b) $\beta = 0.90$, (c) $\beta = 1.60$. Bubbles are rising upward, the outer "box" shown in light gray is a parallelepiped of width $7h$ and height $14h$, with h the size of the computational domain. Color code: instantaneous bubble vertical velocity normalized by the terminal velocity of the same bubble rising in still liquid.

β	Re_T	$\langle Re_z \rangle$	Ψ_T	$\langle \Psi \rangle$	χ_T^{eq}	$\langle \chi^{\mathrm{eq}} \rangle$
0.46	62.5	25.0	0.9944	0.9918 (± 0.0031)	1.19	1.23 (- 0.05, + 0.05)
0.90	31.4	7.2	0.9946	0.9919 (± 0.0040)	1.19	1.23 (- 0.07, + 0.06)
1.60	17.6	6.4	0.9948	0.9869 (± 0.0094)	1.18	1.31 (- 0.16, + 0.11)

Table 4.2 Bubble rise velocity and deformation in quiescent and turbulent conditions for each value of the turbulence intensity β. $Re_T = d_b V_T / \nu$: terminal bubble Reynolds number based on the terminal velocity of the bubble in quiescent conditions V_T; $\langle Re_z \rangle = \langle V_z \rangle d_b / \nu$: bubble Reynolds number based on the *average rise* velocity $\langle V_z \rangle$ (not to be confused with the bubble Reynolds number based on the *slip* velocity, which is unknown); Ψ: bubble sphericity, defined as the ratio between the surface of a volume-equivalent sphere and that of the bubble; χ^{eq}: aspect ratio of an oblate spheroid with sphericity Ψ. Subscript T is used for bubbles rising in quiescent conditions (Re_T estimated from Mei, Klausner, and Lawrence (1994), Ψ_T determined from numerical simulation without turbulence forcing, for explanations about the latter see the end of section 4.3.3.1). Brackets indicate time averaging for bubbles rising in turbulent conditions, the numbers in parentheses correspond to the root-mean-square fluctuation around the mean value.

corresponds to greater departure from a spherical shape). A spectral analysis of the sphericity time signals (not shown) revealed the absence of any dominant frequency: the bubbles do not experience periodic shape oscillations. The mean sphericity and the root mean square of the sphericity fluctuations around the mean value are provided in table 4.2 for each β. For an easier interpretation we also provide the aspect ratio of a spheroid with the same sphericity as that of the bubble for each case. The bubble is more deformed in turbulent conditions than in still liquid. The mean deformation and the shape fluctuations are greater for higher turbulence intensity. Nevertheless, owing to the relatively low value of the Bond number ($Bo = 0.38$), the bubble deformation remains overall modest: for $\beta = 1.60$, the aspect ratio of the equivalent spheroid is approximately 1.3 and its deviation from the mean (based on the root-mean-square sphericity fluctuation) is between 0.1 and 0.2. For the record, we mention that preliminary simulations of bubbles with higher Bond numbers (and with $Ar \approx 30$ and $\beta \approx 1$) showed that the bubbles inevitably break up when $Bo \gtrsim 3$, that is, when surface tension is sufficiently weak.

4.3.1.2 Velocity components

On average, the bubble motion is vertical. The vertical component of the mean bubble velocity $\langle V_z \rangle$ is reported in table 4.3 and compared with V_T, the bubble terminal velocity in quiescent conditions. The bubble mean rise velocity is found to be significantly lower than V_T: we obtain $0.23 \leqslant \langle V_z \rangle / V_T \leqslant 0.40$. In addition, the rise velocity reduction is a non-monotonic function of β, the maximum reduction occurring for $\beta = 0.90$. The reduction of the rise velocity by turbulence is well-known for much smaller bubbles (Wang & Maxey, 1993; Maxey et al.,

β	$\langle V_z \rangle / V_T$	$\langle v_{x,y}^2 \rangle / u_0^2$	$\langle v_z^2 \rangle / u_0^2$
0.46	0.40 ± 0.04	0.97 ± 0.03	0.98 ± 0.05
0.90	0.23 ± 0.12	0.73 ± 0.02	0.77 ± 0.04
1.60	0.37 ± 0.04	0.76 ± 0.02	0.70 ± 0.04

Table 4.3 Bubble velocity mean and variance for each value of the turbulence intensity β. $\boldsymbol{V}$: bubble velocity; $\boldsymbol{v} = \boldsymbol{V} - \langle \boldsymbol{V} \rangle$: bubble velocity fluctuation; V_T: terminal bubble velocity in quiescent conditions, estimated from Mei, Klausner, and Lawrence (1994); u_0^2: variance of the liquid velocity fluctuations in the absence of the bubble. Buoyancy acts in the positive z-direction. Brackets indicate time averaging.

1994; Spelt & Biesheuvel, 1997; Mazzitelli et al., 2003b, 2003a; Snyder et al., 2007; Poorte & Biesheuvel, 2002; Aliseda & Lasheras, 2011) (note that Poorte and Biesheuvel (2002) reported two measurements of slightly increased rise velocities for $\beta \leqslant 0.12$, but to the best of our knowledge these have not been reproduced thus far and remain unexplained). Quantitative comparison with these prior studies is however not possible, essentially because of the mismatch in the values of Re_λ and Re_T. Nevertheless, the order of magnitude of the present rise velocity reduction is comparable to that obtained for smaller bubbles at comparable β. For example, for higher Re_λ and Re_T than ours, Poorte and Biesheuvel (2002) measured $\langle V_z \rangle / V_T = 0.7$ for $\beta = 0.4$, Spelt and Biesheuvel (1997) obtained $\langle V_z \rangle / V_T = 0.6$ for $\beta = 0.4$ and $\langle V_z \rangle / V_T = 0.4$ for $\beta = 1.0$, and Snyder et al. (2007) reported $\langle V_z \rangle / V_T = 0.4$ for $\beta = 1.2$. Regarding the dependence on β, both non-monotonic and monotonic evolutions of $\langle V_z \rangle / V_T$ with β have been reported for point bubbles (the former by, e.g., Spelt and Biesheuvel (1997) and the latter by, e.g., Mazzitelli et al. (2003a) and Snyder et al. (2007)), thereby indicating that the value of β alone is not sufficient to predict the rise velocity reduction. We also provide in table 4.3 the componentwise variances of the bubble velocity. The variances of the horizontal and vertical components of the bubble velocity are found to be equal up to statistical convergence uncertainty. They are comparable to u_0^2 (the variance of the liquid velocity fluctuations in the absence of the bubble) for $\beta = 0.46$, and are smaller than u_0^2 for higher values of β.

The componentwise probability density functions (PDFs) of the bubble velocity fluctuation $v_i = V_i - \langle V_i \rangle$ normalized to unit variance are presented in figure 4.2. The distributions of the horizontal and vertical components of the velocity fluctuation are roughly Gaussian (up to statistical convergence uncertainty), as is the case for fluid tracers. For inertial particulates, a weak asymmetry (either positive or negative) in the distribution of the vertical velocity fluctuations has been reported by Spelt and Biesheuvel (1997) and Snyder et al. (2007) for point bubbles, by Poorte and Biesheuvel (2002) and Prakash et al. (2012) for finite-size bubbles (although smaller than in the present simulations), and by Chouippe and Uhlmann (2015) for large buoyant solid spheres. These prior results indicate that the shape of the vertical velocity PDF depends in a complex manner on β (and presumably on other factors). Since we follow a

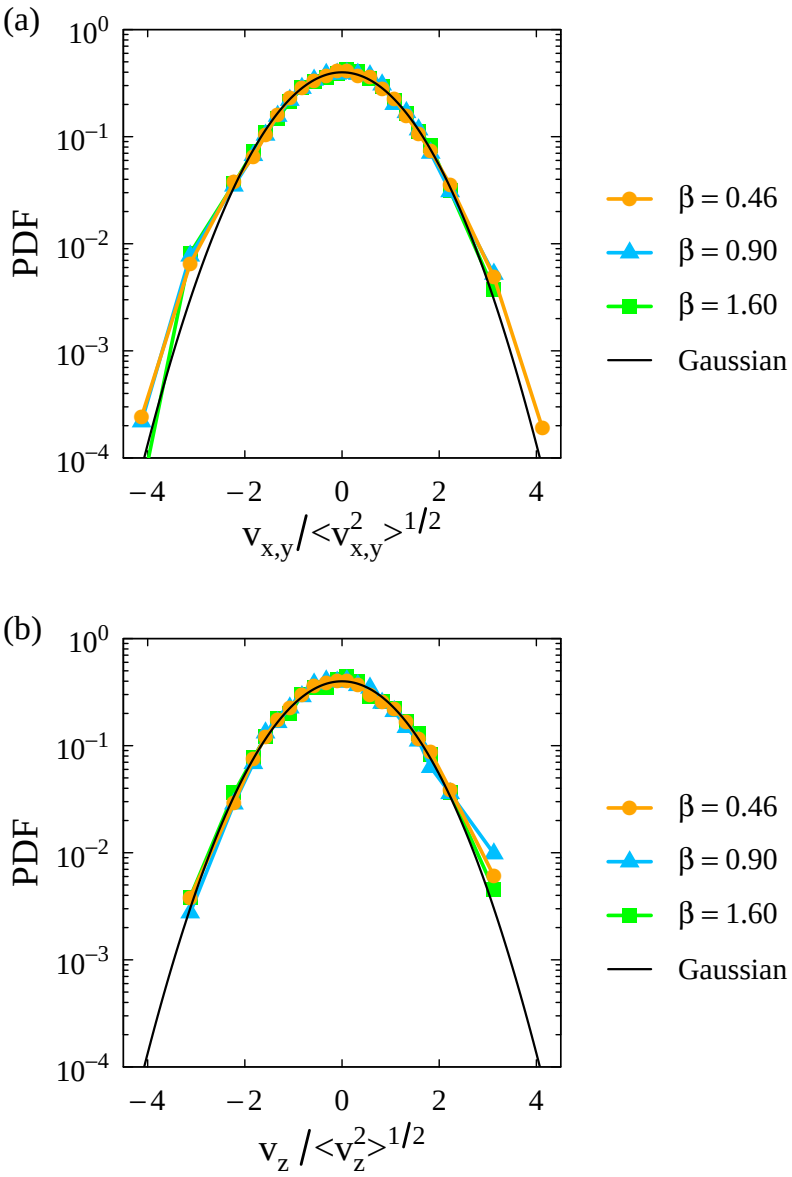

Figure 4.2 PDFs of the (a) horizontal and (b) vertical components of the bubble velocity fluctuation $v_i = V_i - \langle V_i \rangle$, normalized to unit variance. ——: Gaussian distribution of zero mean and variance one.

β	$\langle A_z\rangle/a_0$	$\langle a_{x,y}^2\rangle/a_0^2$	$\langle a_z^2\rangle/a_0^2$
0.46	0.022 ± 0.006	2.92 ± 0.02	2.55 ± 0.04
0.90	0.011 ± 0.003	1.43 ± 0.02	1.48 ± 0.03
1.60	0.004 ± 0.004	1.22 ± 0.05	1.15 ± 0.10

Table 4.4 Bubble acceleration mean and variance for each value of the turbulence intensity β. $\boldsymbol{A}$: bubble acceleration; $\boldsymbol{a} = \boldsymbol{A} - \langle \boldsymbol{A}\rangle$: bubble acceleration fluctuation; $a_0^2 = \varepsilon_0^{4/3}\eta^{-2/3}$: acceleration variance scaling according to the Heisenberg-Yaglom relation. Buoyancy acts in the positive z-direction. Brackets indicate time averaging.

single bubble, obtaining accurate high-order Lagrangian statistics from our simulations is nearly impossible. As a consequence, we cannot assess the effect of β on such an asymmetry in the distribution of the vertical velocity fluctuations. But in any case, the degree of departure from Gaussianity in our simulations, if any, is small for all β: the skewness is $\langle v_i^3\rangle/\langle v_i^2\rangle^{3/2} = 0.0 \pm 0.3$, and the flatness is $\langle v_i^4\rangle/\langle v_i^2\rangle^2 = 3.1 \pm 0.3$ for $i = x, y, z$. Finally, although direct comparison with prior work on small bubbles is not possible (again essentially because of very different Re_λ and Re_T), it is worth mentioning that nearly Gaussian vertical velocity distributions have also been obtained by Poorte and Biesheuvel (2002) and Spelt and Biesheuvel (1997) for $\beta \approx 0.5$, and by Snyder et al. (2007) for $\beta = 1.2$.

4.3.1.3 Acceleration components

We now turn to the statistics of the bubble acceleration components $A_i = \mathrm{d}V_i/\mathrm{d}t$. The componentwise acceleration mean and variance are reported in table 4.4. The mean bubble acceleration in the vertical direction is nearly zero (and is obviously zero in the two horizontal directions). The variances of the horizontal and vertical components of the acceleration are of the same order. They are comparable to $a_0^2 = \varepsilon_0^{4/3}\eta^{-2/3}$ (the variance of the acceleration of a fluid tracer according to the Heisenberg-Yaglom prediction) for $\beta = 1.60$, and increase with decreasing β.

The componentwise PDFs of the bubble acceleration fluctuation $a_i = A_i - \langle A_i\rangle$ normalized to unit variance are presented in figure 4.3. These PDFs are highly non-Gaussian and exhibit large tails, as is the case for fluid tracers and small particles (Toschi & Bodenschatz, 2009), as well as for finite-size solid spheres (e.g., Qureshi, Bourgoin, Baudet, Cartellier, and Gagne (2007, 2008), Homann and Bec (2010), Chouippe and Uhlmann (2015)). Qureshi et al. (2007, 2008) have shown that the shape of the horizontal acceleration PDF of finite-size rigid spheres is invariant with particle size and density ratio, and can be fitted by the following function associated with a lognormal distribution of the acceleration amplitude (Mordant et al., 2004):

$$p(a_i) = \frac{\mathrm{e}^{3\sigma^2/2}}{4\sqrt{3}}\left[1 - \mathrm{erf}\left(\frac{\ln(\left|a_i/\sqrt{3}\right|) + 2\sigma^2}{\sqrt{2}\sigma}\right)\right]. \tag{4.5}$$

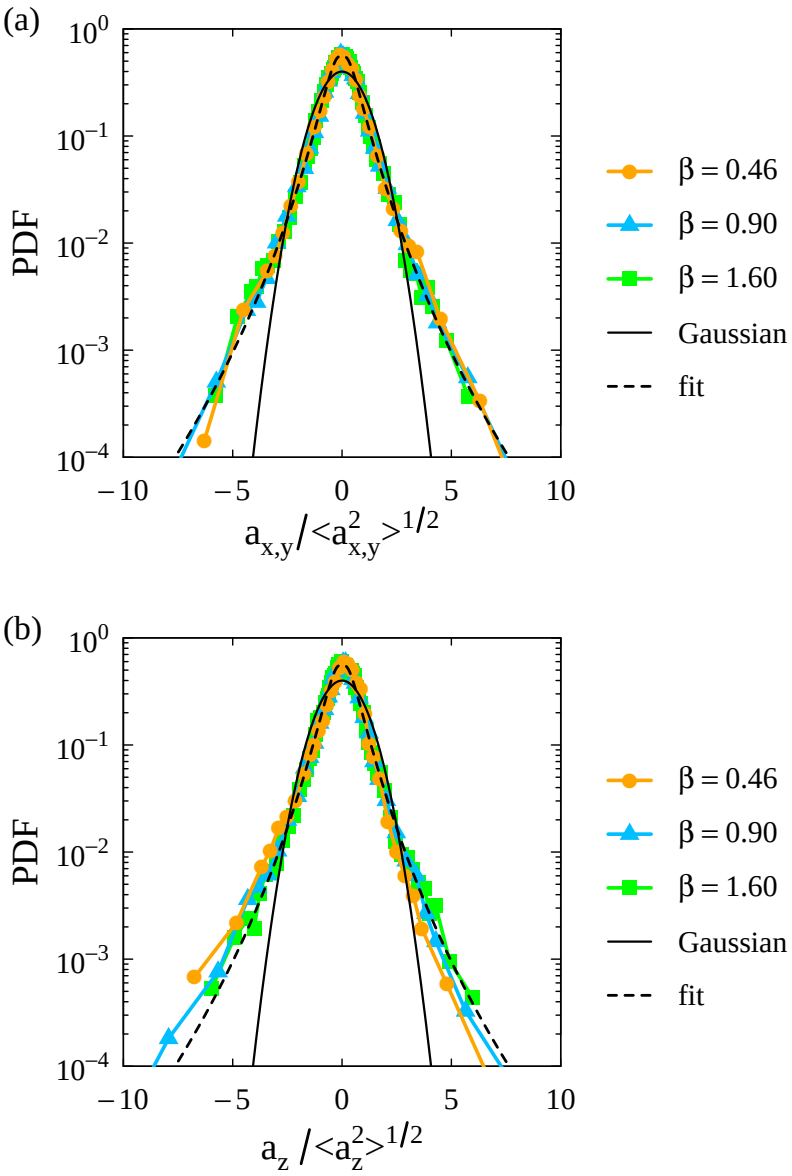

Figure 4.3 PDFs of the (a) horizontal and (b) vertical components of the bubble acceleration fluctuation $a_i = A_i - \langle A_i \rangle$, normalized to unit variance. ——: Gaussian distribution of zero mean and variance one; - - - -: fit of the horizontal component distributions by the relation (4.5) with $\sigma = 0.66$ which corresponds to a distribution flatness $\langle a_i^4 \rangle / \langle a_i^2 \rangle^2 = 10.3$.

Our data for the horizontal components of the bubble acceleration are well described by this relation, shown by the dashed line in figure 4.3a. The best fit (in the sense of least squares) is obtained for $\sigma = 0.66 \pm 0.01$; this corresponds to a distribution flatness $\langle a_i^4 \rangle / \langle a_i^2 \rangle^2 = \frac{9}{5} \mathrm{e}^{4\sigma^2} = 10.3$. As a comparison, the value of σ fitted from their experimental measurements with rigid spheres is 0.62, which yields a flatness of 8.4. Their fit would be nearly indistinguishable from ours in figure 4.3a, and is therefore not shown. In their numerical simulations, Homann and Bec (2010) and Chouippe and Uhlmann (2015) obtained acceleration flatnesses of the same order of magnitude (between 6 and 8.5) for non-buoyant solid particles of diameters $d_b \in [2\eta, 14\eta]$. For buoyant solid particles with $d_b = 6.7\eta = 0.42\lambda$, Chouippe and Uhlmann (2015) obtained a noticeably smaller flatness, namely 3.9, for the horizontal component of the particle acceleration, although no explanation could be offered for this unexpectedly low value.

An additional property evidenced by our simulations is the negative asymmetry in the distribution of the vertical component of the bubble acceleration, particularly visible for the most buoyant bubble ($\beta = 0.46$, orange dots). In quantitative terms, the skewness is $\langle a_z^3 \rangle / \langle a_z^2 \rangle^{3/2} = \{-1.0 \pm 0.3, -0.6 \pm 0.6, -0.5 \pm 0.2\}$ for $\beta = \{0.46, 0.90, 1.60\}$, although we must express some reservations regarding the reliability of these values given the limited amount of data from which they are computed. An interpretation of this asymmetry is proposed in the following subsection.

4.3.1.4 Longitudinal acceleration

We now examine the distribution of the bubble longitudinal acceleration, denoted $A_\parallel$ and defined by $A_\parallel = \boldsymbol{A} \cdot \boldsymbol{V} / |\boldsymbol{V}|$. The PDFs of $A_\parallel$ are shown in figure 4.4a for each value of β (the mean of $A_\parallel$ is zero). The distribution of $A_\parallel$ is clearly asymmetric for all the considered values of β: the skewness is $\langle A_\parallel^3 \rangle / \langle A_\parallel^2 \rangle^{3/2} = -0.6 \pm 0.1$ (with the same reservations about accuracy as above) and is virtually independent of β. From a kinematic viewpoint, the longitudinal acceleration represents the rate of change of the velocity magnitude ($A_\parallel = \mathrm{d}|\boldsymbol{V}|/\mathrm{d}t$). This negative asymmetry therefore means that a finite-size bubble undergoes, on average, stronger deceleration than positive acceleration.

Since the vertical direction is parallel to the average direction of motion, the negative skewness of the vertical acceleration PDF (figure 4.3b) is believed to originate from the negative skewness of the longitudinal acceleration PDF (figure 4.4a). As β decreases, the bubble path becomes closer to a vertical line (the bubble trajectories are shown in figure 4.1 for each β), the vertical direction becomes more likely to coincide with the longitudinal direction, and A_z becomes closer to $A_\parallel$. For this reason the skewness coefficient of the vertical acceleration PDF increases with decreasing β. This interpretation would also explain the positively-skewed shape (skewness of 0.63) of the vertical acceleration PDF reported by Chouippe and Uhlmann (2015) for finite-size spheres falling (in the negative vertical direction) under the effect of gravity.

As $A_\parallel$ is not invariant under Galilean transformations, it is also worthwhile to examine the bubble longitudinal acceleration in a frame moving at the bubble average velocity. We

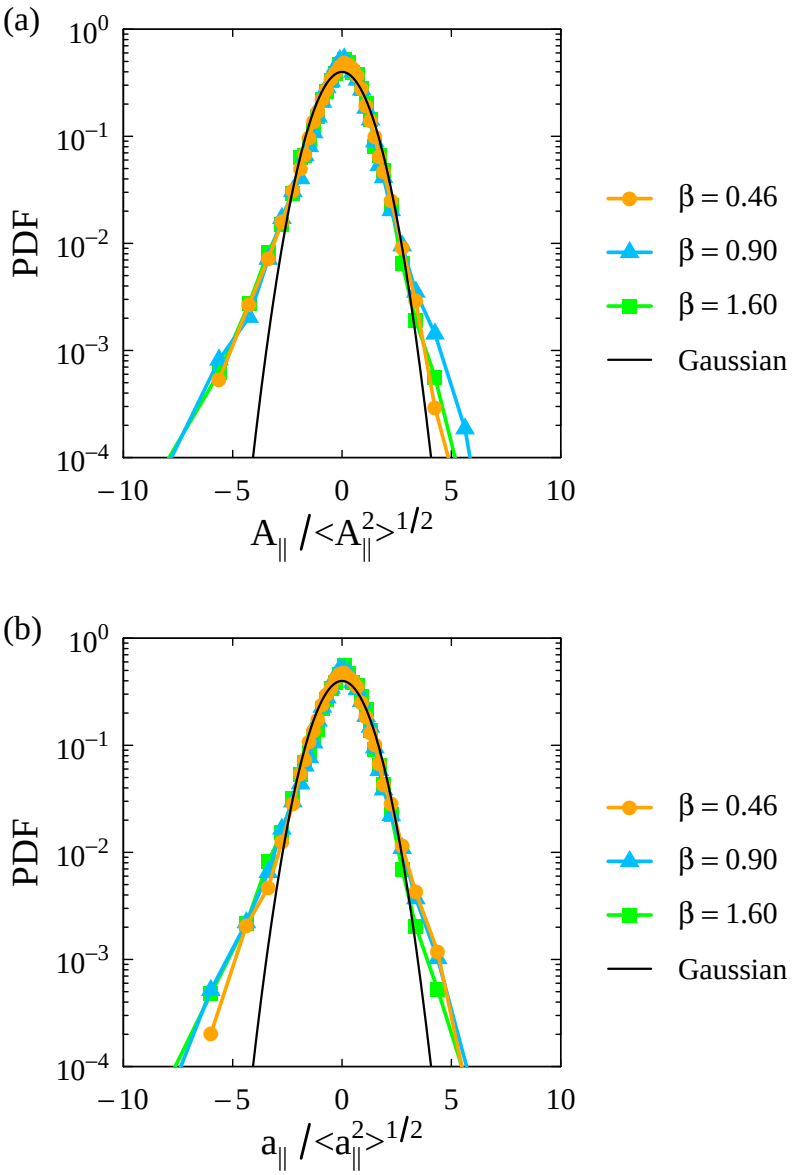

Figure 4.4 PDFs of the bubble longitudinal acceleration normalized to unit variance. (a) $A_{\|} = \boldsymbol{A} \cdot \boldsymbol{V}/|\boldsymbol{V}|$ (bubble acceleration projected on the bubble velocity direction) and (b) $a_{\|} = \boldsymbol{a} \cdot \boldsymbol{v}/|\boldsymbol{v}|$ with $\boldsymbol{v} = \boldsymbol{V} - \langle \boldsymbol{V} \rangle$ and $\boldsymbol{a} = \boldsymbol{A} - \langle \boldsymbol{A} \rangle$ (bubble acceleration fluctuation projected on the bubble velocity fluctuation direction, with $\langle \boldsymbol{A} \rangle$ being negligibly small). ——: Gaussian distribution of zero mean and variance one.

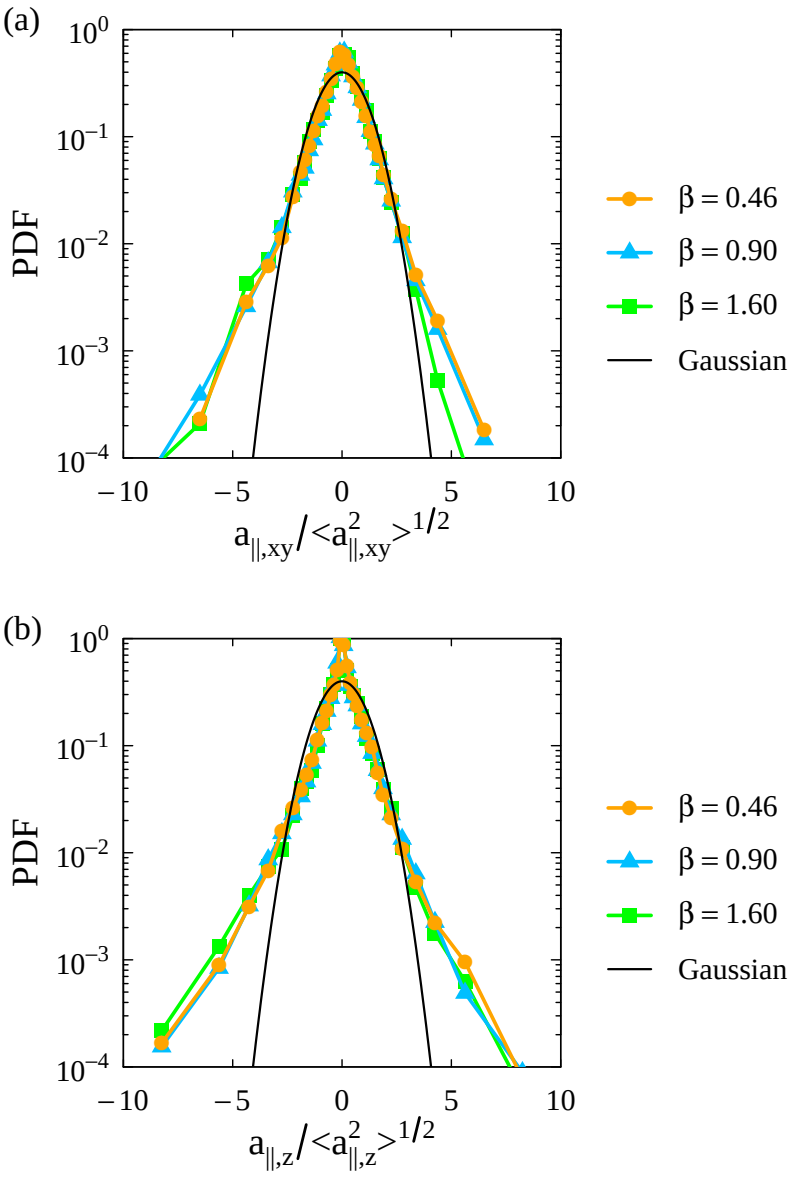

Figure 4.5 PDFs of the contributions to the bubble longitudinal acceleration, normalized to unit variance: (a) horizontal contribution $a_{\|,xy} = (a_x v_x + a_y v_y)/|\boldsymbol{v}|$ and (b) vertical contribution $a_{\|,z} = a_z v_z/|\boldsymbol{v}|$. ——: Gaussian distribution of zero mean and variance one.

define $a_{\parallel} = \boldsymbol{a}\cdot\boldsymbol{v}/|\boldsymbol{v}|$ with $\boldsymbol{v} = \boldsymbol{V} - \langle \boldsymbol{V}\rangle$ and $\boldsymbol{a} = \boldsymbol{A} - \langle \boldsymbol{A}\rangle$ (note that $\langle \boldsymbol{A}\rangle$ is negligibly small). The PDFs of $a_{\parallel}$, shown in figure 4.4b, are quantitatively similar to the PDFs of $A_{\parallel}$ (the mean of $a_{\parallel}$ is zero). As the bubble dynamics is strongly anisotropic owing to buoyancy, it may also be interesting to distinguish between horizontal and vertical directions. We introduce the horizontal contribution $a_{\parallel,xy} = (a_x v_x + a_y v_y)/|\boldsymbol{v}|$ and the vertical contribution $a_{\parallel,z} = a_z v_z/|\boldsymbol{v}|$ to $a_{\parallel}$ (with $a_{\parallel} = a_{\parallel,xy} + a_{\parallel,z}$). The PDFs of $a_{\parallel,xy}$ and $a_{\parallel,z}$ are provided in figure 4.5: both contributions are found to be negatively skewed (convergence uncertainty prevents us from attempting a quantitative comparison between their respective skewness coefficients). This is the very first time, to our knowledge, that the distribution of the longitudinal acceleration of a large, inertial object is shown to be negatively skewed: so far, this property had only been evidenced in the case of fluid tracers (Lévêque & Naso, 2014).

4.3.2 Modeling of hydrodynamic forces

In the present simulations, the bubble deformation is not substantial (see table 4.2). An often-used, though *approximate* and of *limited* use, equation of motion for a *spherical* bubble of size $d_b < \eta$ at moderately high Reynolds number is (Magnaudet & Eames, 2000):

$$\begin{aligned}\boldsymbol{A} = &\frac{\alpha-1}{\alpha+C_M}\boldsymbol{g} + \frac{1+C_M}{\alpha+C_M}\frac{D\boldsymbol{U}_0}{Dt} + \frac{C_L}{\alpha+C_M}(\boldsymbol{U}_0-\boldsymbol{V})\times\boldsymbol{\Omega}_0 \\ &+ \frac{1}{\alpha+C_M}\frac{3C_D}{4d_b}|\boldsymbol{U}_0-\boldsymbol{V}|(\boldsymbol{U}_0-\boldsymbol{V}) + \frac{1}{\alpha+C_M}\frac{18\nu}{d_b^2}\int_{-\infty}^{t} K(t-\tau)\frac{\mathrm{d}(\boldsymbol{U}_0-\boldsymbol{V})}{\mathrm{d}\tau}\,\mathrm{d}\tau\end{aligned} \tag{4.6}$$

where $\boldsymbol{A} = \mathrm{d}\boldsymbol{V}/\mathrm{d}t$ is the bubble acceleration, α is the gas-to-liquid density ratio, and $\boldsymbol{U}_0$ and $\boldsymbol{\Omega}_0$ are respectively the undisturbed liquid velocity and vorticity at the bubble position. This approximate equation derives from a force balance that includes buoyancy (yielding the first term on the right-hand side), unperturbed liquid acceleration and acceleration reaction (resulting, when combined, in the second term), lift (yielding the third term), steady drag (fourth term), and history effects (last term). C_M, C_L, and C_D are the added mass, lift, and steady drag coefficients, respectively, and K is the history kernel. Note that the validity of simply adding these various forces is not clear a priori.

When $d_b > \eta$, (4.6) is clearly not applicable. It may, however, provide a first approximation of the bubble dynamics. Assuming so, a subsequent issue lies in the fact that the notion of "unperturbed flow at bubble position" is meaningless when the base flow varies over length scales smaller than $O(d_b)$. Hence a first step toward the extension of (4.6) to a finite-size bubble consists of finding adequate definitions for $\boldsymbol{U}_0$ and $\boldsymbol{\Omega}_0$ that would characterize the flow "seen" by that bubble. A conceivable approach, first proposed by Merle et al. (2005), consists in averaging the flow properties in the bubble surroundings over an appropriate volume. This idea has been proven successful by Naso and Prosperetti (2010), who showed that the fluid angular velocity seen by a fixed solid particle can be defined in terms of the fluid vorticity averaged over a shell concentric with the particle. Besides, Cisse et al. (2013) constructed the

mean fluid velocity profile around a free rigid sphere based on an analogous definition of the particle direction of motion.

We undertake here an approach similar to that used by Naso and Prosperetti (2010): the idea is to replace $\boldsymbol{U}_0$ ($\boldsymbol{\Omega}_0$) in (4.6) by its counterpart $\langle \boldsymbol{u} \rangle_s$ ($\langle \boldsymbol{\omega} \rangle_s$, with $\boldsymbol{\omega} = \boldsymbol{\nabla} \times \boldsymbol{u}$) defined as the average of the local liquid velocity (vorticity) over a volume comprised between the bubble interface and a surface located at a distance s from the interface. Formally, this average reads

$$\langle \boldsymbol{q} \rangle_s(t) = \frac{1}{V_s(t)} \int_{\mathcal{V}(s,t)} \boldsymbol{q}(\boldsymbol{x}, t)\, \mathrm{d}\boldsymbol{x} \qquad \text{with } V_s(t) = \int_{\mathcal{V}(s,t)} \mathrm{d}\boldsymbol{x}, \tag{4.7}$$

where $\mathcal{V}(s,t)$ contains the points in the liquid phase such that $0 \leqslant \psi(\boldsymbol{x}, t) \leqslant s$ at time t, with ψ the normal distance to the interface. If this volume-averaging approach is appropriate, and if the equation of motion (4.6) provides a descent approximation (which is assumed as a starting point, but by no means expected for a large bubble in turbulence), it might be possible to find a value of s for which the bubble acceleration $\boldsymbol{A}$ is correlated to $\mathrm{d}\langle \boldsymbol{u} \rangle_s / \mathrm{d}t$, $(\langle \boldsymbol{u} \rangle_s - \boldsymbol{V})$, and $(\langle \boldsymbol{u} \rangle_s - \boldsymbol{V}) \times \langle \boldsymbol{\omega} \rangle_s$. Given that the adequate shell thickness s may depend on the nature of the force involved, we will treat each term on the right-hand-side (abbreviated r.h.s. hereinafter) of (4.6) separately. Owing to the lack of a reliable expression of the history kernel K for a bubble in nonrectilinear motion at finite Reynolds number, as discussed in Magnaudet and Eames (2000), the history term cannot be treated rigorously and is therefore not investigated.

The simpler contribution to the bubble acceleration is that arising from the combination of the acceleration reaction force and the effect of the undisturbed liquid acceleration (second term on the r.h.s. of (4.6)), as it involves only C_M and the Lagrangian derivative of $\boldsymbol{U}_0$. Under the assumption of a near-spherical shape, the added mass coefficient is a constant which actual value is unimportant for the present purpose. In our calculations we used $C_M = 0.5$.

We now need to determine the thickness s_M^u of the shell over which $\boldsymbol{u}$ should be averaged to obtain the best possible estimate of $\boldsymbol{U}_0$. Recalling that part of the inertia force arises from the undisturbed liquid acceleration integrated over the bubble volume, it seems reasonable to expect the shell volume to be comparable to the bubble volume. In terms of shell thicknesses, this expectation is $s_M^u \sim s_d$ where $s_d = 0.13\, d_b$ is the thickness of the spherical shell which volume $4/3\pi[(d_b/2 + s_d)^3 - (d_b/2)^3]$ is equal to the bubble volume $4/3\pi(d_b/2)^3$. The actual shell thickness s_M^u was determined from our simulations by maximizing the componentwise correlation between $\boldsymbol{A}$ and $\boldsymbol{F}^{\mathrm{acc}}$, the latter being defined by:

$$\boldsymbol{F}^{\mathrm{acc}} = \frac{1 + C_M}{\alpha + C_M} \frac{\mathrm{d}\langle \boldsymbol{u} \rangle_{s_M^u}}{\mathrm{d}t}. \tag{4.8}$$

The maximum correlation coefficients are between 0.85 and 0.9 and were obtained for $s_M^u/d_b = 0.15 \pm 0.05$ whatever β, in agreement with our expectations. This remarkably strong correlation is clearly visible in figure 4.6 where we show the componentwise joint PDFs of $\boldsymbol{A}$ and $\boldsymbol{F}^{\mathrm{acc}}$; the associated correlation coefficients are written in red in each plot. For completeness the mean and root-mean-square (rms) of $\boldsymbol{F}^{\mathrm{acc}}$ are reported in table 4.5.

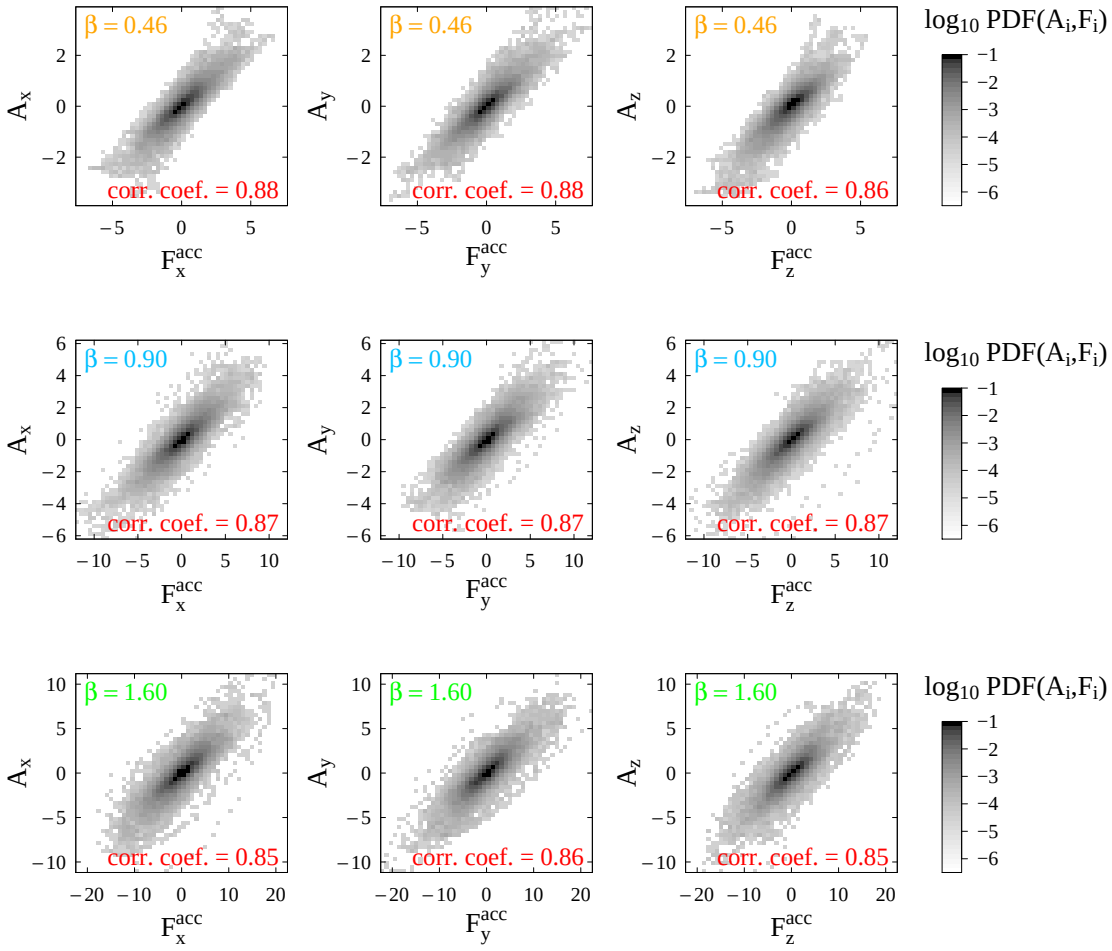

Figure 4.6 Componentwise joint PDFs (logarithmic color scale) of $\boldsymbol{A}$ and $\boldsymbol{F}^{\mathrm{acc}} = [(1+C_M)/(\alpha+C_M)]\,\mathrm{d}\langle\boldsymbol{u}\rangle_{s_M^u}/\mathrm{d}t$ for the three values of β (rows). $\boldsymbol{A}$: bubble acceleration; $\boldsymbol{F}^{\mathrm{acc}}$: undisturbed liquid acceleration/acceleration reaction term on the r.h.s. of (4.6). The added mass coefficient is $C_M = 0.5$, and the shell thickness is $s_M^u = 0.15\,d_b$. Associated correlation coefficients are written in red. All quantities have been normalized by the magnitude of the buoyancy contribution to the bubble acceleration $F^{\mathrm{buoy}} = [(\alpha-1)/(\alpha+C_M)]\,g$. Buoyancy acts in the positive z-direction.

We now turn to the lift contribution to the bubble acceleration (third term on the r.h.s. of (4.6)). It involves three unknown quantities: C_L, $\boldsymbol{U}_0$, and $\boldsymbol{\Omega}_0$. The lift coefficient of a spherical bubble depends on the bubble relative ("slip") Reynolds number Re_L, the shear rate Sr_L, and possibly other factors (Legendre & Magnaudet, 1998; Rastello, Marié, & Lance, 2011). Here the instantaneous Re_L and Sr_L are defined by:

$$Re_L = \frac{\left|\langle \boldsymbol{u} \rangle_{s_L^u} - \boldsymbol{V}\right| d_b}{\nu} \tag{4.9}$$

and

$$Sr_L = \frac{d_b \langle \boldsymbol{\omega} \rangle_{s_L^\omega}}{\left|\langle \boldsymbol{u} \rangle_{s_L^u} - \boldsymbol{V}\right|}. \tag{4.10}$$

We estimated an instantaneous lift coefficient using the empirical expression proposed by Legendre and Magnaudet (1998) (equation (18) therein, valid for a spherical bubble in steady flow at any Reynolds number and with shear rate not greater than unity):

$$C_L = \left\{ \left[\frac{6}{\pi^2} (Re_L\, Sr_L)^{-1/2} \frac{2.255}{(1 + 0.2\, Re_L / Sr_L)^{3/2}} \right]^2 + \left[\frac{1}{2} \frac{Re_L + 16}{Re_L + 29} \right]^2 \right\}^{1/2}, \tag{4.11}$$

which is believed to be sufficient given the coarse level of refinement of our present approach.

Using expression (4.11) for C_L, we determined the two shell thicknesses s_L^u and s_L^ω which maximize the correlation between $\boldsymbol{A}$ and $\boldsymbol{F}^{\text{lift}}$, the latter being defined by:

$$\boldsymbol{F}^{\text{lift}} = \frac{C_L}{\alpha + C_M} (\langle \boldsymbol{u} \rangle_{s_L^u} - \boldsymbol{V}) \times \langle \boldsymbol{\omega} \rangle_{s_L^\omega}. \tag{4.12}$$

The results are β-dependent, and are summarized in table 4.6. The maximum correlation coefficients are approximately $\{0.8, 0.7, 0.6\}$ for $\beta = \{0.46, 0.90, 1.60\}$. These have been obtained for $s_L^u = O(d_b)$ and $s_L^\omega = O(\delta_L)$, where δ_L is the thickness of a loosely defined "boundary layer" estimated as $\delta_L / d_b \sim \sqrt{2/\langle Re_L \rangle}$ (Moore, 1963). In this expression $\langle Re_L \rangle$ is the mean (time-averaged) relative Reynolds number defined by (4.9). The mean and rms of Re_L, Sr_L, and C_L are reported in table 4.6. Note that the lift coefficient C_L is nearly constant, its rms fluctuations being around 5 % of the mean value. We have checked that the present results do not depend upon the expression used for C_L: assuming C_L to be constant rather than using (4.11) does not affect the strength of the correlation nor the shell thicknesses. On a side note, we mention that an analogous result for the vorticity seen by a fixed solid particle in otherwise comparable conditions was obtained by Naso and Prosperetti (2010): they showed that the fluid angular velocity seen by the particle, as it appears in the torque equation, can be defined in terms of the fluid vorticity averaged over a shell extending from the particle surface to the edge of the viscous layer. The reasonable correlation between $\boldsymbol{A}$ and $\boldsymbol{F}^{\text{lift}}$ is also visible in figure 4.7, where we show their componentwise joint PDFs. The mean and rms of $\boldsymbol{F}^{\text{lift}}$ are provided in table 4.5. It is worthwhile to mention that, on average, $\boldsymbol{F}^{\text{lift}}$ is directed downward, and therefore opposes the bubble rise. This result is compatible with

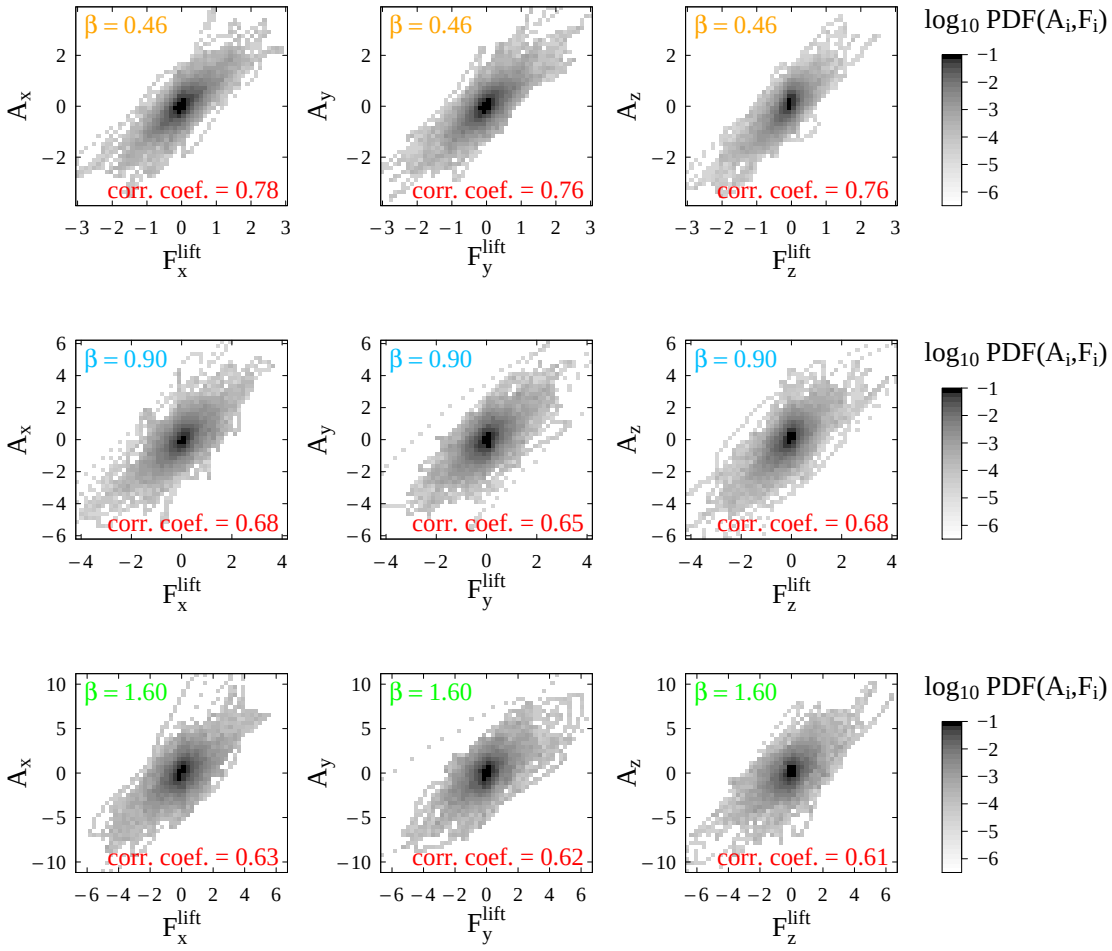

Figure 4.7 Componentwise joint PDFs (logarithmic color scale) of $\boldsymbol{A}$ and $\boldsymbol{F}^{\text{lift}} = [C_L/(\alpha + C_M)](\langle \boldsymbol{u} \rangle_{s_L^u} - \boldsymbol{V}) \times \langle \boldsymbol{\omega} \rangle_{s_L^\omega}$ for the three values of β (rows). $\boldsymbol{A}$: bubble acceleration; $\boldsymbol{F}^{\text{lift}}$: lift term on the r.h.s. of (4.6). The added mass coefficient is $C_M = 0.5$, the lift coefficient C_L is given by (4.11), and the shell thicknesses s_L^u and s_L^ω are that reported in table 4.6. Associated correlation coefficients are written in red. All quantities have been normalized by the magnitude of the buoyancy contribution to the bubble acceleration $F^{\text{buoy}} = [(\alpha - 1)/(\alpha + C_M)]\, g$. Buoyancy acts in the positive z-direction.

	$\beta = 0.46$			$\beta = 0.90$			$\beta = 1.60$		
$\boldsymbol{Q}$	$\langle Q_z \rangle$	$Q_{x,y}^{\mathrm{rms}}$	Q_z^{rms}	$\langle Q_z \rangle$	$Q_{x,y}^{\mathrm{rms}}$	Q_z^{rms}	$\langle Q_z \rangle$	$Q_{x,y}^{\mathrm{rms}}$	Q_z^{rms}
$\boldsymbol{A}$	0.008	0.56	0.52	0.007	0.88	0.89	0.006	1.60	1.54
$\boldsymbol{F}^{\mathrm{acc}}$	0.001	1.02	0.92	0.002	1.58	1.61	0.005	2.99	2.86
$\boldsymbol{F}^{\mathrm{lift}}$	-0.100	0.41	0.33	-0.103	0.56	0.51	-0.067	0.90	0.87

Table 4.5 Mean and root-mean-square (rms) of the bubble acceleration $\boldsymbol{A}$, and of the undisturbed liquid acceleration/acceleration reaction $\boldsymbol{F}^{\mathrm{acc}}$ and lift $\boldsymbol{F}^{\mathrm{lift}}$ terms as defined by (4.8) and (4.12), respectively. All quantities have been normalized by the magnitude of the buoyancy contribution to the bubble acceleration $F^{\mathrm{buoy}} = [(\alpha - 1)/(\alpha + C_M)]\, g$. Buoyancy acts in the positive z-direction. Brackets indicate time averaging, and $Q_i^{\mathrm{rms}} = \sqrt{\langle q_i^2 \rangle}$ with $q_i = Q_i - \langle Q_i \rangle$.

β	s_L^u/d_b	s_L^ω/d_b	δ_L/d_b	$\langle Re_L \rangle$	$\langle Sr_L \rangle$	$\langle C_L \rangle$
0.46	1.25	0.20	0.22	41.8 ± 16.5	2.13 ± 2.53	0.40 ± 0.02
0.90	1.25	0.25	0.27	26.6 ± 12.9	3.68 ± 4.38	0.38 ± 0.02
1.60	1.00	0.30	0.30	22.3 ± 10.9	4.59 ± 5.85	0.37 ± 0.02

Table 4.6 Relevant quantities for the modeling of the lift force acting on a large bubble based on shell-averaging of the local flow. s_L^u, s_L^ω: shell thicknesses for the liquid velocity and vorticity as they appear in (4.12), respectively (uncertainty on s_L^u/d_b is ±0.25, uncertainty on s_L^ω/d_b is ±0.05); δ_L: thickness of the viscous boundary layer, estimated from $\delta_L/d_b = \sqrt{2/\langle Re_L \rangle}$ (Moore, 1963); $\langle Re_L \rangle$, $\langle Sr_L \rangle$, $\langle C_L \rangle$: mean ± rms values of the Reynolds number, shear rate, and lift coefficient as defined by (4.9), (4.10), and (4.11), respectively.

the mechanisms of rise velocity reduction known for point bubbles. These mechanisms are summarized at the beginning of section 4.3.3.

We now focus on the drag contribution to $\boldsymbol{A}$ (fourth term on the r.h.s. of (4.6)), which involves two unknown quantities: C_D and $\boldsymbol{U}_0$. The drag coefficient of a spherical bubble depends strongly on the bubble relative Reynolds number Re_D, defined here by

$$Re_D = \frac{\left|\langle \boldsymbol{u} \rangle_{s_D^u} - \boldsymbol{V}\right| d_b}{\nu}. \tag{4.13}$$

An instantaneous C_D was estimated using the following correlation (Mei et al., 1994):

$$C_D = \frac{16}{Re_D}\left\{1 + \left[\frac{8}{Re_D} + \frac{1}{2}\left(1 + \frac{3.315}{\sqrt{Re_D}}\right)\right]^{-1}\right\} \tag{4.14}$$

which is valid for a spherical bubble in uniform flow at any Reynolds number (Loth, 2008).

Using expression (4.14) for C_D, we sought the shell thickness s_D^u which would maximize the correlation between $\boldsymbol{A}$ and $\boldsymbol{F}^{\text{drag}}$, the latter being defined by:

$$\boldsymbol{F}^{\text{drag}} = \frac{1}{\alpha + C_M}\frac{3C_D}{4d_b}\left|\langle \boldsymbol{u} \rangle_{s_D^u} - \boldsymbol{V}\right|(\langle \boldsymbol{u} \rangle_{s_D^u} - \boldsymbol{V}). \tag{4.15}$$

We found that $\boldsymbol{A}$ is not correlated to $\boldsymbol{F}^{\text{drag}}$ whatever s_D^u: the correlation coefficients are smaller than 0.1 for all $s_D^u \in [0, 4\,d_b]$. We have checked that this result holds for simpler drag laws, such as $C_D = 16/Re_D$ (Stokes drag) and $C_D = 2 + 16/Re_D$ (valid at small Reynolds number), and when a correction for shear is included (equation (15) from Magnaudet and Eames (2000)). A possible reason for this absence of correlation is the inadequacy of available expressions of C_D for strongly nonuniform flows. Another explanation is the inappropriateness of the shell-averaging approach for the drag term as modeled in (4.6). A third possibility is that the drag force essentially balances buoyancy and contributes only marginally to the bubble acceleration fluctuations. In any case, we stress once more that (4.6) is a priori not expected to hold in the present configuration.

4.3.3 Preferential sampling of the turbulent flow

Experiments on the motion of bubbles of small size ($d_b \lesssim \eta$) in homogeneous isotropic turbulent flow demonstrated that the rise velocity of bubbles is generally reduced by turbulence (Poorte & Biesheuvel, 2002; Aliseda & Lasheras, 2011), hence confirming predictions of point-bubble simulations (Wang & Maxey, 1993; Maxey et al., 1994; Spelt & Biesheuvel, 1997; Mazzitelli et al., 2003b, 2003a; Snyder et al., 2007). As shown in section 4.3.1, our simulations extend this result to the so far unexplored regime of large bubbles ($d_b \sim \lambda$). Two mechanisms retarding the rise of *small* bubbles have been identified depending on the value of β. For lower values of β, bubbles rise fast through the flow, and are transported toward downflow regions by lift forces, where their velocity is reduced owing to the increased viscous drag and to the downward lift force induced by the bubble lateral motion (Spelt & Biesheuvel, 1997). For

higher values of β, bubbles are trapped inside vortices (Wang & Maxey, 1993; Maxey et al., 1994; Sene, Hunt, & Thomas, 1994), and preferentially accumulate on the downflow side of eddies under the effect of the lift force (Spelt & Biesheuvel, 1997; Mazzitelli et al., 2003b, 2003a), which further reduces their rise velocity. Hence an important question to be answered is whether or not *large* bubbles sample the flow uniformly.

4.3.3.1 Characterization of the flow sampled by the bubble

Information about the local flow around the bubble is collected by a conditional averaging of the liquid flow in the vicinity of the bubble along its path. We introduce a polar coordinates system (r,θ) with its origin located at the bubble center of mass $\boldsymbol{X}$ and oriented along its instantaneous (absolute) direction of motion $\boldsymbol{V}$:

- $r = |\boldsymbol{r}|$ where $\boldsymbol{r} = \boldsymbol{x} - \boldsymbol{X}$ is the relative position vector, and
- $\theta = \arccos\left(\dfrac{\boldsymbol{r}}{|\boldsymbol{r}|}\cdot\dfrac{\boldsymbol{V}}{|\boldsymbol{V}|}\right)$ is the angle between $\boldsymbol{r}$ and the bubble instantaneous velocity $\boldsymbol{V}$.

For any quantity q of interest, its average conditioned on r_i and θ_i is computed as follows (T is the total duration of the simulation):

$$\langle q\rangle_{r=r_i,\theta=\theta_i} = \frac{1}{T}\int_0^T \left(\frac{1}{V_{r_i,\theta_i}(t)}\int_{\mathcal{V}(r_i,\theta_i,t)} q(\boldsymbol{x},t)\,\mathrm{d}\boldsymbol{x}\right)\mathrm{d}t \qquad \text{with } V_{r_i,\theta_i}(t) = \int_{\mathcal{V}(r_i,\theta_i,t)} \mathrm{d}\boldsymbol{x} \tag{4.16}$$

where $\mathcal{V}(r_i,\theta_i,t)$ is the set of points such that $r = r_i \pm \Delta x/2$ (with Δx the grid spacing) and $\theta = \theta_i \pm 1^\circ$ at time t. Since the bubble is deformable we also introduce the normal distance to the interface $\psi = \min(|\boldsymbol{x} - \boldsymbol{X}_{\text{interface}}|)$, with $\boldsymbol{X}_{\text{interface}}$ the set of points lying on the interface (ψ is actually the level-set function in the liquid, see section 1.3.1). This allows us to define the average of q conditioned on the distance to the bubble surface ψ_i:

$$\langle q\rangle_{\psi=\psi_i} = \frac{1}{T}\int_0^T \left(\frac{1}{V_{\psi_i}(t)}\int_{\mathcal{V}(\psi_i,t)} q(\boldsymbol{x},t)\,\mathrm{d}\boldsymbol{x}\right)\mathrm{d}t \qquad \text{with } V_{\psi_i}(t) = \int_{\mathcal{V}(\psi_i,t)} \mathrm{d}\boldsymbol{x} \tag{4.17}$$

where $\mathcal{V}(\psi_i,t)$ contains the points located at a distance $\psi = \psi_i \pm \Delta x/2$ from the interface at time t.

In point-bubbles simulations, increased residence time in downflow regions and accumulation in vortices is easily quantified by averaging the (unperturbed) liquid vertical velocity and enstrophy at the bubble's position (as in, e.g., Mazzitelli et al. (2003b)). When the bubble is much larger than the smallest length scale of the flow, two difficulties arise: first, the bubble might be larger than the regions of interest (as illustrated in figure 4.8), and second, because the presence of the bubble induces local disturbances in the ambient flow, it is not straightforward to distinguish this effect from that of preferential sampling. The present proposal to characterize the flow sampled by the bubble consists of two steps:

(i) a conditional averaging of the liquid flow in the vicinity of the bubble along its path (as defined above by (4.16) and (4.17)), which includes the contribution of preferential

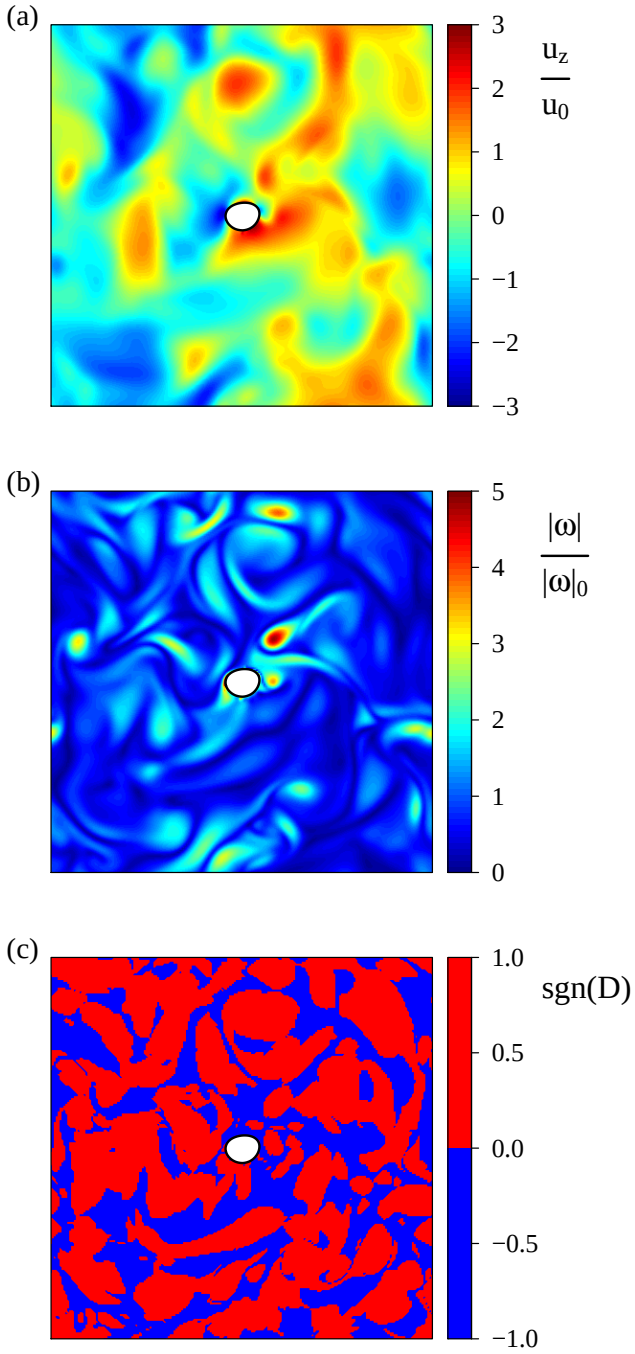

Figure 4.8 Simultaneous snapshots of the carrier flow in a 2D plane passing through the bubble center: (a) vertical component of the velocity u_z, (b) modulus of the vorticity $\boldsymbol{\omega}$, and (c) sign of D (defined in the main text), used to differentiate between strain-dominated ($D < 0$) and vorticity-dominated ($D > 0$) regions. Velocity and vorticity are normalized by their mean values in the absence of the bubble. The bubble interior is colored in white, and the gas-liquid interface is depicted by a black line. Note that the single-phase flow obtained without the bubble has similar characteristics.

sampling (if any) of flow regions larger than the bubble but also the contribution of the flow induced by the bubble, and

(ii) the computation of the same quantities in the case where the bubble rises steadily in still liquid (without turbulence forcing), so that the only contribution to the conditionally-averaged flow is that due to the bubble motion.

If the results of (i) and (ii) are sufficiently different (in magnitude or in sign), and if the characteristic size of the sampled regions is sufficiently large, then a qualitative estimate of the sole contribution of preferential sampling can be inferred by comparison.

Before going further we should clarify how we proceeded for step (ii). As mentioned in section 4.2, we actually simulate a periodic array of bubbles. In light of our findings in chapter 2, we know that such bubbles, when rising in otherwise quiescent liquid, may interact with the wakes of their neighbors even at very low volume fraction. Such wake interaction sets in at time $t^w \sim h/V_T$ (see figure 2.7), with h the size of the computational domain. Before t^w, an ordered array of bubbles released from rest behaves as if the bubbles were in isolation: a (temporary) "steady-state" is established at time $t^s \sim d^2/\nu$ and the bubble velocity then equals V_T. Reaching such a well-defined (temporary) "steady-state" requires $t^s < t^w$, that is, $h/d_b > Re_T$. This requirement is not met in our simulations, nevertheless the bubble velocity was observed to reach a first plateau at short times, so the simulation was stopped at this point and the flow around the bubble was stored to be used as reference for the quiescent case. The difference between the bubble velocity at the end of the simulation and the values of V_T estimated using the correlation of Mei et al. (1994) for an isolated spherical bubble is between 4 and 9 %, so this approach should be sufficient for the present purposes.

4.3.3.2 Preferential sampling of downflow and swirling regions

To assess whether the bubble spends more time in downward velocity regions (such as the blue zones in figure 4.8a), we averaged the vertical component of the liquid velocity u_z (defined in the laboratory frame) around the bubble. The average (axisymmetric) field $\langle u_z \rangle_{r,\theta}$ is shown in figure 4.9 (top row) for increasing β from left to right. The profile of u_z as a function of the distance to the interface ψ is presented in figure 4.10a; for comparison the results obtained without background turbulence are shown in the inset. A bubble rising in an otherwise quiescent liquid pushes the liquid aside and drags some liquid with it, this results in an average upflow in its immediate vicinity which can be seen in the inset of figure 4.10a. In the presence of a turbulent carrier flow, this bubble-induced upflow is still present (it is clearly visible at the bubble's rear in figure 4.9 for $\beta = 0.46$, which corresponds to the most buoyant/fastest bubble), and is responsible for the sharp increase in $\langle u_z \rangle_\psi$ with decreasing distance very close to the interface. We shall therefore ignore this effect. Farther from the interface, for $\beta = 1.60$, $\langle u_z \rangle_\psi$ and $\langle u_z \rangle_{r,\theta}$ are approximately zero, meaning that the bubble samples equally upflow and downflow regions. In contrast, for $\beta = 0.46$ and $\beta = 0.90$, the vertical velocity is, on average, clearly negative around the bubble, thereby revealing a

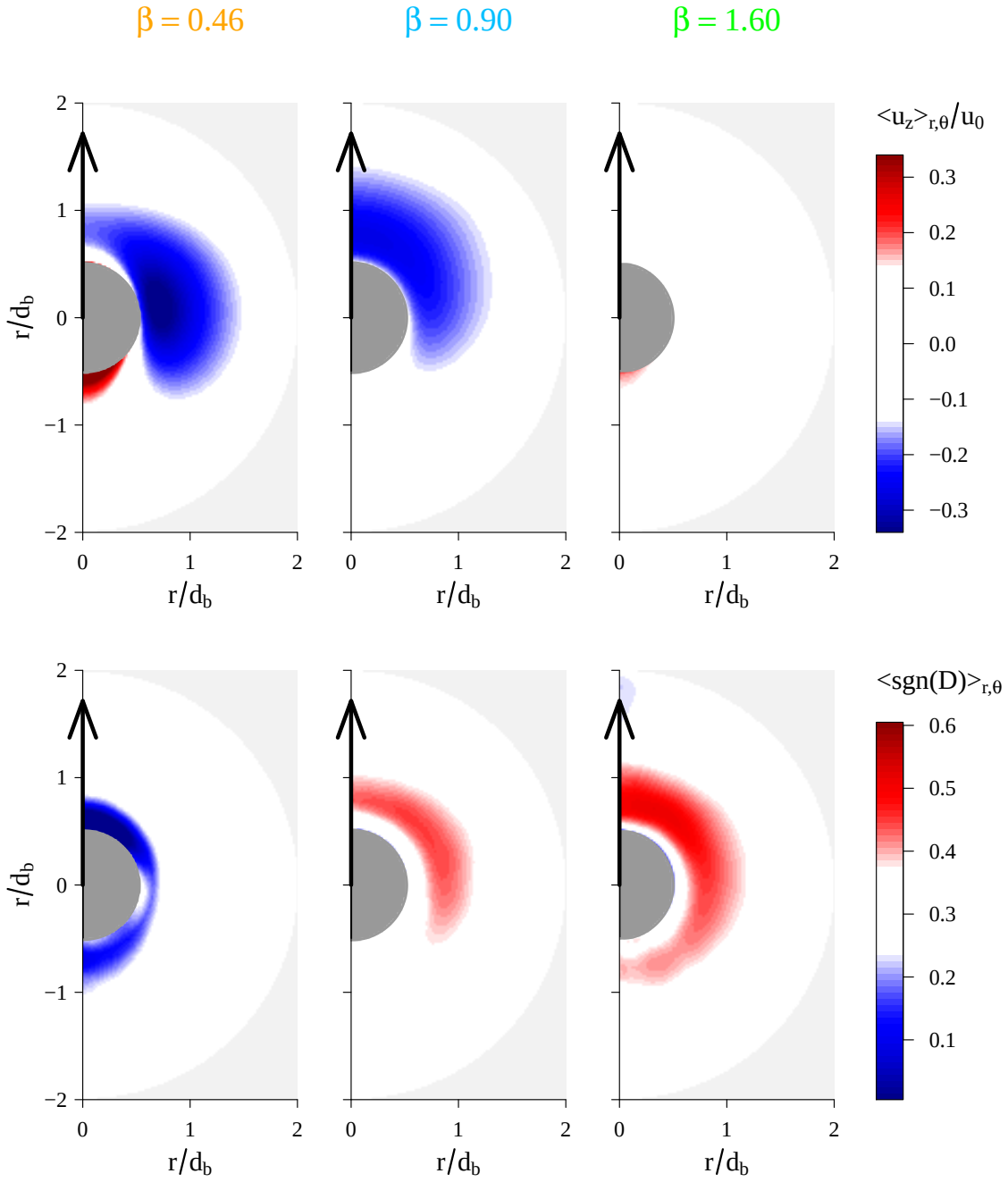

Figure 4.9 Average flow field around the bubble conditioned on r and θ, as defined by (4.16), for increasing β from left to right. Top row: vertical velocity normalized by the velocity fluctuations rms of the single-phase flow. Bottom row: sign of D (defined in the main text), used to differentiate between strain-dominated ($D < 0$) and vorticity-dominated ($D > 0$) regions. The color scale is centered on the single-phase flow value. The arrows indicate the bubble instantaneous direction of motion.

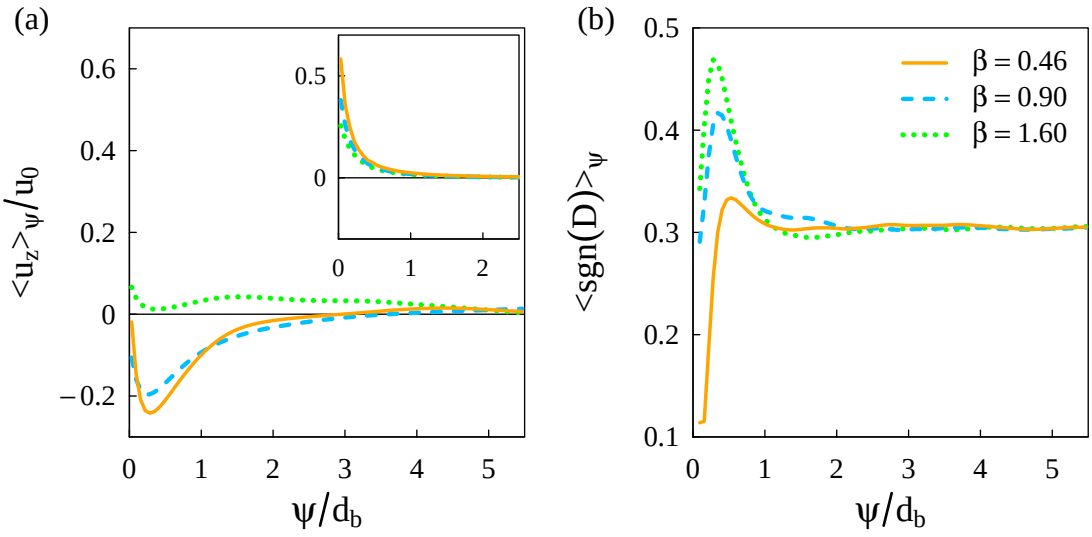

Figure 4.10 Average flow profile around the bubble (as given by (4.17), ψ is the distance to the interface): (a) vertical velocity normalized by the velocity fluctuations rms of the single-phase flow (inset: same quantity in the absence of turbulence), and (b) sign of D (defined in the main text), used to differentiate between strain-dominated ($D < 0$) and vorticity-dominated ($D > 0$) regions.

significant preference of the bubbles for downward velocity regions. The characteristic size of these regions is comparable to the integral length scale $L \approx 2\,d_b$.

Besides, small bubbles are known to be trapped in vortices. Since vorticity is a quantity varying over small scales (as illustrated in figure 4.8b), preferential sampling of vortical zones cannot be evidenced by averaging the vorticity around the bubble. Alternatively, the topology of the flow can be characterized by the eigenvalues of the velocity gradient tensor: if they are all real, the flow is locally dominated by strain, whereas if two of them are complex conjugates, the flow is locally swirling (Cantwell, 1992). In incompressible flows these eigenvalues λ are solutions of the characteristic equation $\lambda^3 + Q\lambda + R = 0$ with Q and R the second and third invariants of the velocity gradient tensor, respectively. It follows that the nature of the eigenvalues only depends on the sign of the discriminant $D = 27R^2 + 4Q^3$: if $D < 0$, the three eigenvalues are real, if $D > 0$, two of them are complex conjugates (Cantwell, 1992). It can be observed in figure 4.8c, where we show an instantaneous snapshot of sgn(D) (the sign of the discriminant), that strain-dominated ($D < 0$) and vorticity-dominated ($D > 0$) regions defined in that way can be of size comparable to or larger than that of the bubble. As a consequence, increased residence time in swirling regions can be evidenced by averaging sgn(D) in the bubble surroundings.

The conditionally-averaged field $\langle \mathrm{sgn}(D) \rangle_{r,\theta}$ is presented in figure 4.9 (bottom row), and the evolution of $\langle \mathrm{sgn}(D) \rangle_{\psi}$ with the distance to the interface ψ is shown in figure 4.10b. Far

from the bubble, $\langle \mathrm{sgn}(D) \rangle_\psi$ is equal to $\mathrm{sgn}(D)_0 = 0.3$, where $\mathrm{sgn}(D)_0$ is the mean value of $\mathrm{sgn}(D)$ in the single-phase flow (loosely speaking, $\mathrm{sgn}(D)_0 > 0$ means that swirling regions occupy a larger volume than strain-dominated regions in the base flow). As the distance to the bubble surface reduces, an increase in $\langle \mathrm{sgn}(D) \rangle_\psi$ is observed, followed by a sharp decrease at distances smaller than one bubble radius. Since for a single bubble rising in still liquid we obtain $-1.0 \leqslant \langle \mathrm{sgn}(D) \rangle_\psi \leqslant -0.8$ for all ψ, and since this sharp decrease occurs extremely close to the interface, we suspect that this local reduction of $\langle \mathrm{sgn}(D) \rangle_\psi$ results from the distortion of the flow by the bubble. Ignoring this effect, we remark that for $\beta = 0.46$, $\langle \mathrm{sgn}(D) \rangle_\psi$ and $\langle \mathrm{sgn}(D) \rangle_{r,\theta}$ are not significantly modified near the bubble. This means that the time spent by this bubble in regions dominated by strain and by vorticity is roughly proportional to the respective volumes of these regions. The situation is different for $\beta = 0.90$ and 1.60. A large red region around the bubble can be identified in figure 4.9 (bottom row), corresponding to $\langle \mathrm{sgn}(D) \rangle_{r,\theta}$ greater than $\mathrm{sgn}(D)_0$. This relative increase, which is also clearly visible in figure 4.10b, indicates that the flow sampled by the bubble is biased: for $\beta = 0.90$ and 1.60, the bubble preferentially resides in swirling regions ($\mathrm{sgn}(D) = 1$) of the flow. This preference is more pronounced for $\beta = 1.60$.

On a side note, we point out that the single-phase flow statistics of the quantities considered in figure 4.9 and figure 4.10 are recovered at distances from the bubble surface comparable to $3\,d_b$. Hydrodynamic interactions are therefore expected to be important if two bubbles are located within approximately $6\,d_b$ from each other. In the present setup, the separation distance between periodic neighbors (interface to interface) is $11\,d_b$. Hence, hydrodynamic interactions can reasonably be assumed to be completely negligible and the bubble can safely be considered as isolated.

Overall, our results suggest that the reduction of the rise velocity of finite-size bubbles is (primarily) related to preferential sampling of downflow regions of large extent when $\beta \lesssim 1$, whereas it is (primarily) associated with trapping in swirling zones when $\beta \gtrsim 1$, as is the case for point bubbles. In our present setup, it is difficult to establish clearly the role played by the lift force in the biased sampling of the flow (one cannot just switch it off to see what happens!). Our estimate of the lift force acting on the bubble in table 4.5 suggests that it contributes to retarding the rise of large bubbles, as it does for smaller ones. Underlying mechanisms may however be different, and cannot be inferred from the present results. Specifically, the possible role played by the lift force in the biased sampling of the flow remains to be clarified. Last but not least, we stress that the conclusions drawn in this section are subject to caution: since the effect of the bubble on the flow cannot be categorically disentangled from that of preferential sampling, the proposed interpretation of the conditional averages is not unequivocal.

4.4 Conclusions

Interface-resolved numerical simulations of the rise of a finite-size bubble in otherwise homogeneous isotropic turbulence have been carried out for different values of the turbulence intensity β, defined as the root mean square of the liquid velocity fluctuations divided by the terminal velocity of the bubble in still liquid. These simulations were run over a time period long enough to allow a reasonable convergence of bubble Lagrangian and liquid Eulerian statistics.

The bubble kinematics has first been characterized, and similarities with that of fluid tracers and finite-size rigid particles have been highlighted. Specifically, the distributions of the bubble velocity components are approximately Gaussian, and the distribution of the bubble horizontal acceleration is log-normal. The distribution of the vertical acceleration also exhibits large tails, together with an additional feature: it is negatively skewed. This feature is believed to originate from the negative asymmetry in the bubble longitudinal acceleration distribution. This latter property, evidenced by our simulations, was only known for fluid tracers. It means that a finite-size bubble undergoes, on average, stronger deceleration than positive acceleration. Then, a physically-relevant definition of the liquid flow seen by the bubble, as it enters in usual models of the acceleration reaction force and of the lift force, has been proposed. Such a definition constitutes a first step toward the modeling of turbulent transport of finite-size bubbles. Finally, the present simulations show that the behavior of a bubble as large as the Taylor microscale is qualitatively similar to that of a small bubble, with a reduction of its rise velocity associated with a biased sampling of the turbulent flow. In particular, conditional averaging of the liquid flow in the bubble vicinity suggests that when $\beta \lesssim 1$, the bubble is more likely to reside in downflow regions of large extent, whereas when $\beta \gtrsim 1$, the bubble has a preference for large swirling zones. Underlying mechanisms however still need to be elucidated.

The above results have been obtained using a turbulence forcing which consists in including an artificial body force proportional to liquid velocity in the momentum conservation equation. Since the presence of the bubble modifies the flow in its surroundings, the bubble dynamics and more generally the flow physics may be affected by this extra term. As a further validation step, it would be desirable to reproduce the present simulations using a different forcing scheme. A possible alternative is the random forcing of Alvelius (1999) used by, e.g., Ten Cate, Derksen, Portela, and van den Akker (2004) for the simulation of interface-resolved particle-laden flow. In this scheme, the force is a divergence-free white noise signal generated in Fourier space and, after computing the inverse Fourier transform, is applied in the physical domain. Given the computational time required to gather sufficient statistics (each simulation cost around 800 000 CPU hours, and took nearly one year of real "human" time running on 144 Intel E5-2690 CPU cores), such a validation could not be undertaken as part of this thesis.

General conclusion

A number of original results pertaining to the dynamics and mixing properties of laminar bubbly suspensions and to the interaction between a finite-size bubble and a turbulent flow are presented in this thesis. Investigations have been carried out with the aid of interface-resolved direct numerical simulations of ordered and free arrays of bubbles. Here ordered arrays refer to simple cubic lattices of bubbles, and free arrays refer to freely evolving suspensions as represented by the periodic repetition of a unit cell containing a large number of freely moving bubbles. In these simulations, the bubble shapes are not prescribed but solved as part of the problem. Various shape regimes, including dimpled and skirted bubbles, have been considered. Numerical simulations have been complemented, when possible, by extensions of prior theoretical work on porous media and packed beds to idealized ordered bubbly suspensions.

Numerical simulations were performed using an in-house 3D parallelized code developed during the course of the present thesis. This code solves the three-dimensional incompressible Navier-Stokes equations in a two-phase fluid-fluid system within a periodic computational domain. A modified level-set method with strict mass conservation enforcement is employed to capture the interface, which allows simulations to be run over virtually infinitely long times. The motion of the fluids is driven by gravity, and possibly by an extra force used to sustain a turbulent background flow. The resolution of a scalar transport equation suitable for the computation of the system mixing properties is also implemented. This code has been validated against prior numerical simulations of laminar bubbly flows. Our simulations of forced turbulent bubbly flows and scalar dispersion are unique and are awaiting validation.

Before summarizing our main findings, we stress that these are restricted to flow regimes for which the motion of a single bubble in quiescent liquid is steady, vertical, and for which the bubble wake is steady and laminar. The simulation of bubbly flows in regimes for which a single bubble exhibits path instability would require substantially larger computational resources, rendering the cost of a systematic investigation prohibitive. In addition, as the onset of coalescence cannot be simulated accurately with our numerical approach, topological changes and polydispersity have not been considered in this study. Last but not least, the

bubbles considered in this work are perfectly clean. The presence of surfactants would modify the tangential stress balance at the gas-liquid interface through the generation of Marangoni stresses, which would substantially affect the bubble dynamics.

The first part of this thesis is concerned with the dynamics of laminar, homogeneous, buoyancy-driven bubbly flows. The long-standing issue of the bubble rise velocity at finite gas volume fraction has been addressed using a combination of direct numerical simulation and Oseen-flow analysis.

For ordered suspensions, the rise velocity has been demonstrated analytically and numerically to be a non-monotonic function of the gas volume fraction, first increasing and then decreasing, in the presence of liquid inertia. This nontrivial behavior results from the competition between cooperative wake interactions which increase the rise velocity and hindering viscous interactions which reduce it. The results have been summarized in a practical relation for the volume fraction dependence of the rise velocity, consistent with our numerical results even in the case of strongly deformed bubbles. Simulations also showed that ellipsoidal and skirted bubbles tend to become spherical when the volume fraction is increased. This observation has been explained using prior work on bubble pairs.

For certain parameter values, ordered arrays of bubbles do not rise vertically. The possibility of a steady oblique motion at low Reynolds number has been demonstrated analytically, and confirmed numerically. Steady oblique motion is shown to be essentially a wake-induced effect due to pair interactions between vertically-aligned bubbles, and is a precursor to oscillatory and chaotic oblique motions. The latter arises when longer-range nonlinear interactions with bubbles located in above horizontal planes come into play. A scenario explaining the transitions between these three regimes has been proposed.

Simulations of freely evolving bubbly suspensions revealed that these share some common properties with ordered ones. Specifically, free bubbles become more spherical upon increasing volume fraction, and the dependence of the bubble velocity on volume fraction is different in the limits of low and high volume fractions. This change in behavior is compatible with available experimental data, and is believed to be responsible for the confusion in the literature regarding the form of empirical correlations for the rise velocity. The similarities between ordered and freely evolving suspensions are explained by the fact that free bubbles keep the same neighbors for extended periods of time, or in other words, by the fact a certain degree of order is present in bubbly flows.

The second part of this work is devoted to the modeling of scalar mixing in laminar bubbly flows. In our approach, scalar dispersion is described by a macroscale version of Fick's law which involves an effective diffusivity tensor. Importantly, this model is restricted to homogeneous systems. Heterogeneity arising from, e.g., bubble clustering or wall effects, would preclude the modeling of scalar dispersion by an effective diffusivity (Koch & Brady, 1987a, 1988).

A consistent framework and a practical methodology have been proposed for the numerical computation of the effective diffusivity of homogeneous bubbly suspensions, and the behavior of the bubble-induced convective contribution to the effective diffusivity has been investigated.

Scalar dispersion in ordered suspensions of bubbles rising along a primary axis of the array has been studied analytically under the Oseen flow approximation, thereby extending prior work on ordered arrays of solid particles in the Stokes flow regime. In the limit of Stokes flow, bubble-induced scalar mixing occurs through convectively enhanced diffusion at low Péclet number, and through Taylor dispersion at high Péclet number. In the Taylor dispersion regime, convective mixing is conditioned on the presence of diffusive scalar transport across streamlines. Our analysis for Oseen flow revealed that these two dispersion regimes are qualitatively unchanged in the presence of inertial effects. Numerical simulations showed that theoretical predictions in the dilute limit yield the correct qualitative behavior of the effective diffusivity for a variety of flow regimes way beyond Oseen flow. A semi-empirical correction obtained from the simulations has been proposed to account for the effect of volume fraction.

Simulations of scalar transport in freely evolving bubbly suspensions at moderate Reynolds number were conducted for Péclet numbers ranging over six decades. At low Péclet number, diffusion contributes to bubble-induced scalar mixing, as for ordered arrays, resulting in identical scaling laws. At high Péclet number, bubble-induced scalar mixing is a purely advective process: whereas Taylor dispersion is obtained in ordered arrays, mechanical dispersion is obtained in arrays of freely moving bubbles, and the associated scaling laws are different. Despite the fact that free arrays of bubbles resemble ordered ones with respect to their dynamics, scalar dispersion at high Péclet number is extremely sensitive to the introduction of additional degrees of freedom, and fundamentally differs in perfectly ordered and weakly disordered suspensions. In addition, the convergence of the effective diffusivity with the system size seems very fast, although this last result would need to be confirmed.

It should be kept in mind that the results presented hereinabove are awaiting experimental validation. To date, experimental measurements of the effective diffusivity of bubbly suspensions are very sparse: they amount to those performed by Alméras et al. (2015) at very high Reynolds number and for a single value of the Péclet number. Experimental investigations of the effects of the Péclet number and of the flow regime on scalar mixing in bubbly flows are therefore highly desirable.

The third and last part of this thesis is a numerical exploration of the interaction between a finite-size bubble and turbulence. Direct numerical simulations of the statistically steady rise of an isolated bubble in an otherwise homogeneous isotropic turbulent flow were carried out. Unlike prior studies where spherical point bubbles were assumed, the bubble considered here is deformable and of size comparable to the Taylor microscale.

The bubble rise velocity is substantially reduced by turbulence, as is the case for much smaller bubbles. This reduction is maximum when the turbulence intensity is close to unity,

with the turbulence intensity defined as the magnitude of the liquid velocity fluctuations divided by the bubble terminal velocity in still liquid. The turbulence intensity alone may however not be sufficient to predict the rise velocity reduction, and further investigations are required to evaluate the role played by other dimensionless groups.

The present simulations also evidenced that a large bubble does not sample the flow uniformly. When the turbulence intensity is relatively low, the bubble shows a preference for downward velocity regions of large extent, whereas for higher turbulence intensity, the bubble preferentially resides in large swirling zones. This behavior, which is qualitatively similar to that of microbubbles, may explain the observed rise velocity reduction. The underlying mechanisms, in particular the possible role played by the lift force, remain to be clarified.

Besides, the bubble velocity and acceleration statistics share a number of common features with those of fluid tracers and inertial particulates. In particular, the componentwise velocity distributions are roughly Gaussian and the componentwise acceleration distributions exhibit large tails. Interestingly, the distribution of the bubble vertical acceleration is negatively skewed. This asymmetry is interpreted as a consequence of the preferential alignment of the bubble velocity with gravity and of the negative asymmetry of the bubble longitudinal acceleration distribution. This latter property, recently discovered for fluid tracers, has been evidenced by our simulations for the first time in the case of an inertial particulate. It means that the bubble undergoes, on average, stronger deceleration than positive acceleration.

Furthermore, the bubble acceleration has been shown to be correlated to appropriately defined liquid flow properties. Specifically, the liquid velocity and vorticity seen by the bubble, as they appear in usual expressions of the acceleration reaction force and of the lift force acting on a spherical bubble at moderate Reynolds number, can be defined in terms of shell-averages of the local flow. This work lays the first stone toward the formulation of a force balance, which should then be complemented by a torque balance, for finite-size deformable bubbles.

While nothing in our results suggests this, the deterministic forcing scheme used to sustain turbulence may substantially alter the flow physics. The next stage of the present study will consist in ensuring that our results can be reproduced using an alternative forcing method. If this validation test is passed, a direct perspective of this work is to include the effect of hydrodynamic interactions. Such a study is straightforward with our code, as it only requires introducing several bubbles in the computational domain. In addition, the computational cost of such simulations is expected to be lower than that of single-bubble simulations, as the size of the computational domain will be identical and the convergence of statistics will be comparatively faster.

Although this is beyond the scope of the present work, the properties of the carrier phase can readily be investigated with our code. Such a numerical study could actually be undertaken as a direct continuation of this thesis.

A number of experimental studies have been devoted to the characterization and modeling

of bubble-induced agitation in otherwise quiescent liquid (Cartellier & Rivière, 2001; Garnier et al., 2002; Martinez-Mercado et al., 2007; Cartellier et al., 2009; Riboux et al., 2010). On the numerical side, interface-resolved simulations were performed by Tryggvason and collaborators (Esmaeeli & Tryggvason, 1999, 2005; Bunner & Tryggvason, 2002b, 2003), who reported substantially weaker agitation than measured in the experiments. Possible explanations include the presence of weak shear in the experiments and a system that is not large enough in these early simulations. New simulations are therefore needed to solve this issue.

Besides, although there is ample evidence that bubbles can cause turbulence modulation in liquid flows (Lance & Bataille, 1991; Mazzitelli et al., 2003b; Lelouvetel et al., 2014), its mechanisms are poorly understood and are wide open for fundamental investigation (Balachandar & Eaton, 2010). Direct numerical simulations of turbulent bubbly flows at the bubble scale are now at our fingertips, and would certainly yield new insights into their physics.

Appendices

Contents

A Analytical solution for the rise of ordered arrays of particulates

In this appendix we derive the first effect of inertia on the steady drift velocity of an ordered suspension of spherical fluid particulates (bubbles or drops). The Reynolds number of the particulates $Re = \rho_c U d_b/\mu_c$ is assumed to be small so that the Navier-Stokes equations can be linearized. Since all the particulates move with the same velocity, this configuration is equivalent to that of a cubic array of fixed particulates immersed in a viscous fluid moving with an average mixture velocity $\langle \boldsymbol{u} \rangle = -\boldsymbol{U}$, and the problem becomes that of determining the hydrodynamic force, denoted $\boldsymbol{f}$, exerted by the ambient fluid on a representative particulate of the array.

It is customary to non-dimensionalize $\boldsymbol{f}$ with the magnitude of the Stokes-flow drag exerted on a single particulate in unbounded fluid to define a normalized force F:

$$F = \frac{f}{f_{0,\text{Stokes}}}, \tag{A.1}$$

where $f = |\boldsymbol{f}|$ and $\boldsymbol{f}_{0,\text{Stokes}}$ is the drag force exerted on an isolated spherical fluid particulate in Stokes flow (Hadamard, 1911; Rybczynski, 1911):

$$\boldsymbol{f}_{0,\text{Stokes}} = -2\pi\mu^*\mu_c d_b \boldsymbol{U} \qquad \text{with } \mu^* = \frac{\mu_c + 3/2\mu_d}{\mu_c + \mu_d}. \tag{A.2}$$

Deviations of F from unity are induced both by hydrodynamic interactions and by the external fluid inertia.

A.1 Derivation of the system of equations

Hill et al. (2001) obtained, under the assumption of $\phi \ll 1$, the first correction to F due to a small but non-zero Reynolds number for a cubic array of rigid spheres by matching the far-field fundamental periodic solution of the Oseen equations to the near-field solution of the Stokes equations past an isolated rigid sphere. Their derivation can be extended to cubic arrays of bubbles and drops by replacing the inner solution for a rigid sphere by that for a fluid sphere.

Consider the steady motion of an incompressible viscous fluid past a simple cubic array of spherical fluid particulates which centers are held fixed at

$$\boldsymbol{r_n} = n_1\boldsymbol{a}_1 + n_2\boldsymbol{a}_2 + n_3\boldsymbol{a}_3 \qquad n_1, n_2, n_3 = 0, \pm1, \pm2, \ldots \tag{A.3}$$

where $\boldsymbol{a}_i$ are the primitive vectors of the lattice. For simple cubic arrays as considered here, $\boldsymbol{a}_i = h\boldsymbol{e}_i$ where h is the lattice spacing and $\boldsymbol{e}_i$ are the unit basis vectors defining our Cartesian frame of reference which origin is located at the center of the reference particulate. Close to the obstacles (the "inner" region), the solution is approximated by that for Stokes flow past an isolated fluid particulate with a constant velocity $-\boldsymbol{U}^\infty$ far from the particulate, with $x = |\boldsymbol{x}|$:

$$\boldsymbol{u}_i(\boldsymbol{x}) = -\boldsymbol{U}^\infty \cdot \left\{ \boldsymbol{I} - \frac{1}{4(\mu_c+\mu_d)} \left[\left(\mu_c + \frac{3}{2}\mu_d \right) \frac{d_b}{x} + \frac{\mu_d}{8} \frac{d_b^3}{x^3} \right] \boldsymbol{I} \right.$$
$$\left. - \frac{1}{4(\mu_c+\mu_d)} \left[\left(\mu_c + \frac{3}{2}\mu_d \right) \frac{d_b}{x} - \frac{3}{8}\mu_d \frac{d_b^3}{x^3} \right] \frac{\boldsymbol{x}\boldsymbol{x}}{x^2} \right\} \quad \text{(A.4)}$$

(as found in standard textbooks, e.g., equation (6.7.47) in Pozrikidis (2011)). In the limit $x \to \infty$, this inner velocity reads

$$\lim_{x\to\infty} \boldsymbol{u}^{\text{in}}(\boldsymbol{x}) = -\boldsymbol{U}^\infty \cdot \left(\boldsymbol{I} - \frac{\mu^*}{4}\frac{d_b}{x}\boldsymbol{I} - \frac{\mu^*}{4}\frac{d_b}{x}\frac{\boldsymbol{x}\boldsymbol{x}}{x^2} \right). \quad \text{(A.5)}$$

At larger distances (the "outer" region), the particulates are represented by point forces acting on the fluid, and the Navier-Stokes equations can be approximated by the Oseen equations

$$\rho_c \boldsymbol{U} \cdot \boldsymbol{\nabla}\boldsymbol{u}^{\text{out}} + \mu_c \nabla^2 \boldsymbol{u}^{\text{out}} = \boldsymbol{\nabla} p + \boldsymbol{f} \sum_{\boldsymbol{n}} \delta(\boldsymbol{x} - \boldsymbol{r}_{\boldsymbol{n}}) \quad \text{and} \quad \boldsymbol{\nabla} \cdot \boldsymbol{u}^{\text{out}} = 0 \quad \text{(A.6)}$$

where δ denotes the Dirac delta function. The procedure to determine the outer velocity closely follows that of Hasimoto (1959). Taking into account the periodicity of the flow field the outer velocity is expanded in Fourier series

$$\boldsymbol{u}^{\text{out}}(\boldsymbol{x}) = -\boldsymbol{U} + \sum_{\boldsymbol{k}\neq\boldsymbol{0}} \hat{\boldsymbol{u}}^{\text{out}}(\boldsymbol{k}) \exp(-2\pi \mathrm{i} \boldsymbol{k}\cdot\boldsymbol{x}) \quad \text{(A.7)}$$

with the Fourier coefficients defined by

$$\hat{\boldsymbol{u}}^{\text{out}}(\boldsymbol{k}) = \frac{1}{V} \int_{\mathcal{V}} \boldsymbol{u}^{\text{out}}(\boldsymbol{x}) \exp(2\pi \mathrm{i} \boldsymbol{k}\cdot\boldsymbol{x}) \, \mathrm{d}\boldsymbol{x} \quad \text{(A.8)}$$

where V is the volume of the unit cell, $\mathcal{V}$ contains the point inside the cell, and where

$$\boldsymbol{k} = n_1\boldsymbol{b}_1 + n_2\boldsymbol{b}_2 + n_3\boldsymbol{b}_3 \quad \text{(A.9)}$$

are vectors in the reciprocal lattice defined by the primitive vectors $\boldsymbol{b}_i$. In particular, for simple cubic arrays, the reciprocal lattice and the physical one are defined by the same basis vectors and $\boldsymbol{b}_i = \boldsymbol{e}_i/h$. Taking the Fourier transform of (A.6) yields

$$\hat{\boldsymbol{u}}^{\text{out}}(\boldsymbol{k}) = \frac{\boldsymbol{f}\cdot(\boldsymbol{k}\boldsymbol{k}/k^2 - \boldsymbol{I})}{(2\pi k)^2 h^3 \mu_c + \mathrm{i}2\pi h^3 \rho_c \boldsymbol{U}\cdot\boldsymbol{k}} \qquad \boldsymbol{k} \neq \boldsymbol{0} \quad \text{(A.10)}$$

where $k = |\boldsymbol{k}|$. The outer solution only needs to be evaluated in the limit $x \to 0$. Following Hill et al. (2001) we first write the velocity in the form

$$\boldsymbol{u}^{\text{out}}(\boldsymbol{x}) = -\boldsymbol{U} + \boldsymbol{u}^{\text{out,Stokes}}(\boldsymbol{x}) + \boldsymbol{u}^{\text{out,Oseen}}(\boldsymbol{x}) \quad \text{(A.11)}$$

where the Stokes-flow and Oseen-flow velocity disturbances are given by

$$\boldsymbol{u}^{\text{out,Stokes}}(\boldsymbol{x}) = \sum_{\boldsymbol{k}\neq\boldsymbol{0}} \frac{\boldsymbol{f}\cdot(\boldsymbol{k}\boldsymbol{k}/k^2 - \boldsymbol{I})}{(2\pi k)^2 h^3 \mu_c} \exp(-2\pi \mathrm{i} \boldsymbol{k}\cdot\boldsymbol{x}) \quad \text{(A.12)}$$

and

$$\boldsymbol{u}^{\text{out,Oseen}}(\boldsymbol{x}) = \sum_{\boldsymbol{k}\neq\boldsymbol{0}} \frac{-\boldsymbol{f}\cdot(\boldsymbol{k}\boldsymbol{k}/k^2-\boldsymbol{I})\left[(2\pi\rho_c\boldsymbol{U}\cdot\boldsymbol{k})^2+\mathrm{i}(2\pi k)^2\mu_c(2\pi\rho_c\boldsymbol{U}\cdot\boldsymbol{k})\right]}{(2\pi k)^6h^3\mu_c^3+(2\pi k)^2h^3\mu_c(2\pi\rho_c\boldsymbol{U}\cdot\boldsymbol{k})^2}\exp(-2\pi\mathrm{i}\boldsymbol{k}\cdot\boldsymbol{x}). \tag{A.13}$$

The Stokes-flow disturbance has been calculated by Hasimoto (1959). For small values of x it reads

$$\lim_{x\to 0}\boldsymbol{u}^{\text{out,Stokes}}(\boldsymbol{x}) = \frac{1}{8\pi h\mu_c}\boldsymbol{f}\cdot\left(2.8373\frac{4}{3}\boldsymbol{I}-\frac{h}{x}\boldsymbol{I}-\frac{h}{x}\frac{\boldsymbol{x}\boldsymbol{x}}{x^2}\right). \tag{A.14}$$

In the limit of $x\to 0$, the Oseen-flow disturbance is independent of position and reduces to

$$\lim_{x\to 0}\boldsymbol{u}^{\text{out,Oseen}}(\boldsymbol{x}) = \frac{\boldsymbol{f}\cdot\boldsymbol{S}}{h\mu_c} \tag{A.15}$$

where $\boldsymbol{S}$ is the dimensionless symmetric tensor

$$\boldsymbol{S} = \sum_{\boldsymbol{k}^*\neq\boldsymbol{0}} \frac{Re_h^2(\boldsymbol{U}^*\cdot\boldsymbol{k}^*)^2(\boldsymbol{I}-\boldsymbol{k}^*\boldsymbol{k}^*/k^{*2})}{(2\pi)^4k^{*6}\left[1+\dfrac{Re_h^2}{(2\pi)^2k^{*4}}(\boldsymbol{U}^*\cdot\boldsymbol{k}^*)^2\right]} \tag{A.16}$$

with $\boldsymbol{U}^*=\boldsymbol{U}/U$, $\boldsymbol{k}^*=\boldsymbol{k}h$, and $Re_h=\rho_cUh/\mu_c$. The tensor $\boldsymbol{S}$ depends only on Re_h, and on the orientation of $\boldsymbol{U}$ relative to the array axes.

Matching the inner solution as $x\to\infty$ to the outer solution in the limit $x\to 0$ yields the following linear system from which $\boldsymbol{f}$ is determined:

$$\boldsymbol{f}-\frac{2.8373}{3}\mu^*\frac{d_b}{h}\boldsymbol{f}-2\pi\mu^*\frac{d_b}{h}\boldsymbol{f}\cdot\boldsymbol{S} = \boldsymbol{f}_{0,\text{Stokes}}. \tag{A.17}$$

Therefore, at finite Reynolds numbers, the hydrodynamic force exerted on the particulate and the drift velocity have, in general, different directions. Note that in the limit of $Re_h = O(\phi^{-1/3}Re)\to\infty$, that is, when $\phi\to 0$, it can be shown that (Hill et al., 2001)

$$\lim_{Re_h\to\infty} f_jS_{ji} = \frac{Re_h}{16\pi}f_i \tag{A.18}$$

so that one recovers the result of Brenner and Cox (1963) for the first inertial contribution to the normalized drag on a single fluid particulate translating in an unbounded fluid

$$\frac{1}{F} = 1-\frac{1}{8}\mu^*Re \qquad \text{for } \phi\to 0. \tag{A.19}$$

In the opposite limit $Re_h\to 0$, $\boldsymbol{S}$ grows linearly with Re_h^2, and using

$$\sum_{\boldsymbol{k}^*\neq\boldsymbol{0}}\frac{k_1^{*2}}{k^{*6}} = 5.51, \qquad \sum_{\boldsymbol{k}^*\neq\boldsymbol{0}}\frac{k_1^{*4}}{k^{*8}} = 3.98, \qquad \sum_{\boldsymbol{k}^*\neq\boldsymbol{0}}\frac{k_1^{*2}k_2^{*2}}{k^{*8}} = 0.765,$$

one finds, after some manipulations, the expression given by Hill et al. (2001)

$$\lim_{Re_h\to 0} f_jS_{ji} = \frac{Re_h^2}{(2\pi)^4}(4.75f_i-1.53f_jU_i^*U_j^*-1.69\delta_{ijkl}f_jU_k^*U_l^*) \tag{A.20}$$

where summation over repeated indices is implied, and where $\delta_{ijkl}=1$ when $i=j=k=l$ and $\delta_{ijkl}=0$ otherwise.

A.2 Particular solutions for the drift velocity

We now look for particular solutions for the drift velocity in the case where the system is buoyancy-driven. The problem is then reversed: the hydrodynamic force acting on the bubble is prescribed (it opposes buoyancy) and one wants to determine the drift velocity of the bubbles. We further assume that gravity is aligned with an axis of the lattice and writes $\boldsymbol{g} = -g\boldsymbol{e}_3$.

A.2.1 Vertical rise

We first consider the situation where the bubbles rise parallel to gravity. In that case the hydrodynamic force $\boldsymbol{f}$ is parallel to the drift velocity $\boldsymbol{U}$ and the off-diagonal components of $\boldsymbol{S}$ are zero. In the limit $Re_h \to 0$, the solution of (A.17) reads

$$\frac{1}{F} = 1 - 1.1734\mu^* \phi^{1/3} - 0.0050\mu^* Re^2 \phi^{-1/3} + O(Re_h^4) \qquad \text{for } \phi^{1/3} \gg O(Re). \tag{A.21}$$

For intermediate values of Re_h, the longitudinal component of $\boldsymbol{S}$, denoted $S_{\parallel} = \boldsymbol{U}^* \cdot \boldsymbol{S} \cdot \boldsymbol{U}^*$, is needed and can be computed numerically. In practice, the simple expression

$$S_{\parallel} \approx \frac{Re_h}{16\pi + \dfrac{(2\pi)^4}{1.53 Re_h}} \tag{A.22}$$

provides a reasonable estimate of $S_{\parallel}$ for any Re_h and F can be approximated at any volume fraction by

$$\frac{1}{F} \approx 1 - \frac{1}{8}\mu^* Re - 1.1734\mu^* \phi^{1/3} + \frac{25}{8}\mu^* \frac{Re\phi^{1/3}}{Re + 25\phi^{1/3}}. \tag{A.23}$$

Since the hydrodynamic force exerted by the fluid on the particulate is balanced with the buoyancy force, the solution of the sedimentation problem relates to F through the identity

$$\frac{U}{U_{0,\text{Stokes}}} = \frac{1}{F} \tag{A.24}$$

where $U_{0,\text{Stokes}}$ is given by (2.8).

A.2.2 Oblique rise

We now consider the (hypothetical) situation where bubbles rise obliquely with respect to gravity. In that case $\boldsymbol{U}$ is not parallel to $\boldsymbol{f}$. The buoyancy force is

$$\boldsymbol{f}_{\text{buoy}} = \frac{1}{6}\pi d_b^3 (\rho_c - \rho_d) g \boldsymbol{e}_3 = \frac{1}{6}\pi \frac{\mu_c^2}{\rho_c} Ar^2 \boldsymbol{e}_3. \tag{A.25}$$

Replacing $\boldsymbol{f} = -\boldsymbol{f}_{\text{buoy}}$ in (A.17) yields the following nonlinear system of dimensionless equations

$$U_1^* = \frac{1}{96\pi^3} Ar^2 Re_h s_{13} \tag{A.26a}$$

$$U_3^* = \frac{Ar^2}{12Re_h}\left(\frac{1}{\mu^*}\frac{h}{d_b} - \frac{2.8373}{3} - 2\pi\frac{Re_h^2}{(2\pi)^4}s_{33}\right) \tag{A.26b}$$

$$U_1^* + U_2^* + U_3^* = 1 \tag{A.26c}$$

where $s_{ij} = (2\pi)^4 S_{ij}/Re_h^2$ and from which $\boldsymbol{U} = U_i \boldsymbol{e}_i$ can be determined. We show in section 2.3.2 that this system possesses non-trivial (non-vertical) solutions for certain values of Ar and h.

B Derivation of an ensemble-averaged scalar transport equation

In this appendix we derive an ensemble-averaged scalar transport equation from local transport equations and interface boundary conditions. We proceed as follows:

(i) we derive a generalized local transport equation which applies to the entire suspension,

(ii) we ensemble average this generalized transport equation to obtain a conservation law for the average scalar field and an exact expression for the average scalar flux, the latter is then reorganized in order to highlight the origin of the various terms.

Subscripts d and c are used throughout to refer to the disperse and continuous phases, respectively.

B.1 Generalized local transport equation

We start by deriving a generalized equation that governs scalar transport through the entire suspension.

B.1.1 Indicator function and surface distribution

The suspension $\mathcal{V}$ consists of a disperse phase $\mathcal{V}_d$ and a continuous phase $\mathcal{V}_c$ separated by an interface $\mathcal{S}_i$. Each phase is identified using an discontinuous indicator function H which is 1 in the continuous phase and 0 in the disperse phase:

$$H(\boldsymbol{x}) = \begin{cases} 1 & \text{if } \boldsymbol{x} \in \mathcal{V}_c, \\ 0 & \text{if } \boldsymbol{x} \in \mathcal{V}_d. \end{cases} \tag{B.1}$$

As the interface moves, the shape of the region occupied by each fluid changes, but each fluid particle retains its identity. Thus, the material derivative of H is zero and we can write for each phase:

$$\frac{\partial H}{\partial t} + \boldsymbol{u}_c \cdot \boldsymbol{\nabla} H = 0 \quad \text{if } \boldsymbol{x} \in \mathcal{V}_c, \tag{B.2a}$$

$$\frac{\partial (1-H)}{\partial t} + \boldsymbol{u}_d \cdot \boldsymbol{\nabla} (1-H) = 0 \quad \text{if } \boldsymbol{x} \in \mathcal{V}_d, \tag{B.2b}$$

where $\boldsymbol{u}$ is the solenoidal velocity field.

The interface is defined by a non-zero gradient of the indicator function. When dealing with two-phase systems, it is customary to introduce a surface distribution δ_i which is concentrated on the interface just as the Dirac delta function is concentrated on a point:

$$\begin{cases} \delta_i(\boldsymbol{x}) \neq 0 & \text{if } \boldsymbol{x} \in \mathcal{S}_i, \\ \delta_i(\boldsymbol{x}) = 0 & \text{otherwise.} \end{cases} \tag{B.3}$$

For a detailed introduction to δ_i, the reader is referred to Appendix B in Tryggvason et al. (2011). This function has the property of changing volume integrals into surface integrals:

$$\int_{\mathcal{V}} \delta_i(\boldsymbol{x}) f(\boldsymbol{x})\,\mathrm{d}\boldsymbol{x} = \int_{\mathcal{S}_i} f(\boldsymbol{x})\,\mathrm{d}\boldsymbol{x} \tag{B.4}$$

where f is an arbitrary function. The gradient of the indicator function H is related to δ_i by

$$\boldsymbol{\nabla} H = \delta_i \boldsymbol{n} \tag{B.5}$$

where $\boldsymbol{n}$ is the unit vector normal to the interface and directed outward from the disperse phase.

B.1.2 Derivation of the generalized transport equation

We recall that the evolution of the scalar c is given by the conservation equation (with $n = \{c, d\}$ denoting either phases):

$$\frac{\partial c_n}{\partial t} + \boldsymbol{\nabla} \cdot \boldsymbol{q_n} = 0, \tag{B.6}$$

and that the flux of scalar $\boldsymbol{q}$ is given by the constitutive equation:

$$\boldsymbol{q}_n = \boldsymbol{u}_n c_n - D_n \boldsymbol{\nabla} c_n, \tag{B.7}$$

where D_n is a constant diffusivity. The transport equations are therefore:

$$\frac{\partial c_c}{\partial t} + \boldsymbol{\nabla} \cdot (\boldsymbol{u}_c c_c - D_c \boldsymbol{\nabla} c_c) = 0 \qquad \text{if } \boldsymbol{x} \in \mathcal{V}_c, \tag{B.8a}$$

$$\frac{\partial c_d}{\partial t} + \boldsymbol{\nabla} \cdot (\boldsymbol{u}_d c_d - D_d \boldsymbol{\nabla} c_d) = 0 \qquad \text{if } \boldsymbol{x} \in \mathcal{V}_d. \tag{B.8b}$$

They are coupled at the interface by the jump conditions:

$$D_c \boldsymbol{\nabla} c_c \cdot \boldsymbol{n} = D_d \boldsymbol{\nabla} c_d \cdot \boldsymbol{n} \qquad \text{if } \boldsymbol{x} \in \mathcal{S}_i, \tag{B.8c}$$

$$c_d = m c_c \qquad \text{if } \boldsymbol{x} \in \mathcal{S}_i, \tag{B.8d}$$

where m is a constant.

In order to obtain a transport equation valid everywhere, we first multiply (B.8a) by H:

$$H \frac{\partial c_c}{\partial t} + H \boldsymbol{\nabla} \cdot (\boldsymbol{u}_c c_c) - H \boldsymbol{\nabla} \cdot (D_c \boldsymbol{\nabla} c_c) = 0.$$

We wish to obtain a generalized equation in the form of a conservation law similar to (B.6). For that purpose we move the indicator function inside the time and space derivatives. Using the product rule we have, for the unsteady and convective terms, the identity:

$$H \frac{\partial c_c}{\partial t} + H \boldsymbol{\nabla} \cdot (\boldsymbol{u}_c c_c) = \frac{\partial H c_c}{\partial t} + \boldsymbol{\nabla} \cdot \big[H \boldsymbol{u}_c c_c \big] - c_c \Big(\frac{\partial H}{\partial t} + \boldsymbol{u}_c \cdot \boldsymbol{\nabla} H \Big).$$

Using (B.2) the last term on the right-hand side vanishes. Applying the product rule to the diffusive term yields the identity:

$$-H\boldsymbol{\nabla}\cdot(D_c\boldsymbol{\nabla}c_c) = -\boldsymbol{\nabla}\cdot\left[HD_c\boldsymbol{\nabla}c_c\right] + D_c\boldsymbol{\nabla}c_c\cdot\boldsymbol{\nabla}H = 0.$$

Finally we obtain:

$$\frac{\partial Hc_c}{\partial t} + \boldsymbol{\nabla}\cdot\left[H\boldsymbol{u}_c c_c\right] - \boldsymbol{\nabla}\cdot\left[HD_c\boldsymbol{\nabla}c_c\right] + D_c\boldsymbol{\nabla}c_c\cdot\boldsymbol{\nabla}H = 0. \tag{B.9}$$

Multiplying (B.8b) by $(1-H)$ yields, after similar manipulations:

$$\frac{\partial (1-H)c_d}{\partial t} + \boldsymbol{\nabla}\cdot\left[(1-H)\boldsymbol{u}_d c_d\right] - \boldsymbol{\nabla}\cdot\left[(1-H)D_d\boldsymbol{\nabla}c_d\right] - D_d\boldsymbol{\nabla}c_d\cdot\boldsymbol{\nabla}H = 0. \tag{B.10}$$

Since there is neither accumulation nor destruction of scalar at the interface, we can add (B.9) to (B.10) (otherwise an singular source or sink term multiplied by δ_i would be required). This leads to:

$$\begin{aligned}\frac{\partial Hc_c}{\partial t} + \boldsymbol{\nabla}\cdot\left[H\boldsymbol{u}_c c_c\right] - \boldsymbol{\nabla}\cdot\left[HD_c\boldsymbol{\nabla}c_c\right] \\ + \frac{\partial (1-H)c_d}{\partial t} + \boldsymbol{\nabla}\cdot\left[(1-H)\boldsymbol{u}_d c_d\right] - \boldsymbol{\nabla}\cdot\left[(1-H)D_d\boldsymbol{\nabla}c_d\right] \\ = \delta_i(-D_c\boldsymbol{\nabla}c_c\cdot\boldsymbol{n} + D_d\boldsymbol{\nabla}c_d\cdot\boldsymbol{n})\end{aligned}$$

where we have replaced $\boldsymbol{\nabla}H$ by its expression (B.5). The terms we have moved on the right-hand-side act only at the interface. Using the interface boundary condition (B.8c) these terms vanish. After reorganization we obtain a generalized local scalar transport which is valid everywhere:

$$\frac{\partial}{\partial t}\left[Hc_c + (1-H)c_d\right] + \boldsymbol{\nabla}\cdot\left[H\boldsymbol{u}_c c_c + (1-H)\boldsymbol{u}_d c_d - HD_c\boldsymbol{\nabla}c_c - (1-H)D_d\boldsymbol{\nabla}c_d\right] = 0. \tag{B.11}$$

B.2 Ensemble-averaged transport equation

We shall now proceed to the derivation of the macroscopic transport equation, which will be obtained by taking the ensemble average of the generalized local transport equation (B.11). The ensemble average operator is denoted $\langle\ \rangle$ and is formally defined as an integral over the configuration space

$$\langle f\rangle(\boldsymbol{x},t) = \int f(\boldsymbol{x},t:\mathcal{C})p(\mathcal{C})\,\mathrm{d}\mathcal{C} \tag{B.12}$$

where $f(\boldsymbol{x},t:\mathcal{C})$ is the value taken by $f(\boldsymbol{x},t)$ in configuration $\mathcal{C}$, and $p(\mathcal{C})$ is the probability density of configuration $\mathcal{C}$. Each configuration is determined by the detailed distribution of the disperse phase, including positions, sizes, shapes, orientations, velocities, etc, of individual particulates. By definition, the ensemble average operator is linear and satisfies the usual rules:

$$\langle\frac{\partial f}{\partial t}\rangle = \frac{\partial\langle f\rangle}{\partial t}, \qquad \langle\boldsymbol{\nabla}f\rangle = \boldsymbol{\nabla}\langle f\rangle, \qquad \langle\langle f\rangle g\rangle = \langle f\rangle\langle g\rangle.$$

We also introduce the volume fraction ϕ of the disperse phase. It is defined as the fraction of realizations for which the point $\boldsymbol{x}$ lies inside the disperse phase and relates, by definition, to the indicator function through

$$\phi(\boldsymbol{x},t) = \langle 1-H \rangle(\boldsymbol{x},t). \tag{B.13}$$

Using the indicator function, the average velocity field is defined as

$$\langle \boldsymbol{u} \rangle = \langle H\boldsymbol{u}_c + (1-H)\boldsymbol{u}_d \rangle \tag{B.14}$$

and the average scalar field is

$$\langle c \rangle = \langle Hc_c + (1-H)c_d \rangle. \tag{B.15}$$

Applying the ensemble average operator to the generalized transport equation (B.11) yields the average conservation law:

$$\frac{\partial \langle c \rangle}{\partial t} + \boldsymbol{\nabla} \cdot \langle \boldsymbol{q} \rangle = 0, \tag{B.16}$$

and the following definition of the average flux:

$$\langle \boldsymbol{q} \rangle = \langle H\boldsymbol{u}_c c_c + (1-H)\boldsymbol{u}_d c_d - HD_c \boldsymbol{\nabla} c_c - (1-H)D_d \boldsymbol{\nabla} c_d \rangle. \tag{B.17}$$

It is possible to reformulate (B.17) in a way that highlights the contributions of average and fluctuating advective and diffusive processes arising from the bulk and from the particulates. This is the purpose of the rest of this section. To facilitate the next stages of the derivation we split the average flux into convective and diffusive terms:

$$\langle \boldsymbol{q} \rangle = \langle \boldsymbol{q}_{\text{conv}} \rangle + \langle \boldsymbol{q}_{\text{diff}} \rangle \tag{B.18a}$$

$$\text{with } \langle \boldsymbol{q}_{\text{conv}} \rangle = \langle H\boldsymbol{u}_c c_c + (1-H)\boldsymbol{u}_d c_d \rangle \tag{B.18b}$$

$$\text{and } \langle \boldsymbol{q}_{\text{diff}} \rangle = -\langle HD_c \boldsymbol{\nabla} c_c + (1-H)D_d \boldsymbol{\nabla} c_d \rangle. \tag{B.18c}$$

B.2.1 Definitions of fluctuating fields

We can define the fluctuating velocity field $\boldsymbol{u}_n'$ in each phase by

$$\boldsymbol{u}_c' = \boldsymbol{u}_c - \langle \boldsymbol{u} \rangle \quad \text{and} \quad \boldsymbol{u}_d' = \boldsymbol{u}_d - \langle \boldsymbol{u} \rangle. \tag{B.19}$$

Note that

$$\langle H\boldsymbol{u}_c' + (1-H)\boldsymbol{u}_d' \rangle = 0 \tag{B.20}$$

is verified. An analogous definition could be used for the scalar fluctuations, as in, e.g., Koch and Brady (1985). An alternative choice will be made here, for the reason explained hereinafter.

Let us consider the equilibrium solution $c_{n,\mathrm{eq}}$ where the scalar fields are constant in each phase $n = \{c, d\}$. Since the solution must satisfy the jump condition (B.8d), $c_{c,\mathrm{eq}}$ and $c_{d,\mathrm{eq}}$ are not equal:

$$c_{d,\mathrm{eq}} = m c_{c,\mathrm{eq}}.$$

They are related to the average scalar field by

$$c_{c,\mathrm{eq}} = P\langle c\rangle \quad \text{and} \quad c_{d,\mathrm{eq}} = mP\langle c\rangle$$

where the P and mP give the equilibrium distribution of the scalar, with

$$P = \frac{1}{1+\phi(m-1)}. \tag{B.21}$$

We define the scalar fluctuation c_n' as the deviation from this equilibrium solution (a similar choice was made by Koch and Brady (1987b)):

$$c_c' = c_c - P\langle c\rangle \quad \text{and} \quad c_d' = c_d - mP\langle c\rangle. \tag{B.22}$$

Note that

$$\langle HP + (1-H)mP\rangle = 1 \tag{B.23}$$

and that

$$\langle Hc_c' + (1-H)c_d'\rangle = 0 \tag{B.24}$$

are verified. Definition (B.22) ensures that scalar fluctuations are zero in the absence of scalar gradients in both phases (obviously this would not be the case if we had used $c_n' = c_n - \langle c\rangle$). Note that this choice only matters when $m \neq 1$ (that is, when the scalar field is discontinuous across the interface), otherwise both definitions are identical.

B.2.2 Convective contribution

The velocity-induced part of the average flux (B.18b) is rewritten as

$$\langle \boldsymbol{q}_{\mathrm{conv}}\rangle = \boldsymbol{U}_s\langle c\rangle + \langle H\boldsymbol{u}_c'c_c' + (1-H)\boldsymbol{u}_d'c_d'\rangle \tag{B.25}$$

where $\boldsymbol{U}_s$ is the velocity at which the average scalar field is advected:

$$\boldsymbol{U}_s = \langle H\boldsymbol{u}_c P + (1-H)\boldsymbol{u}_d mP\rangle$$

which can be, after some manipulations, reformulated as

$$\boldsymbol{U}_s = \langle \boldsymbol{u}\rangle + \phi(m-1)P\boldsymbol{U} \tag{B.26}$$

where $\boldsymbol{U}$ is the average drift velocity of the disperse phase:

$$\phi\boldsymbol{U} = \langle (1-H)\boldsymbol{u}_d'\rangle \tag{B.27}$$

that is, the average velocity of the disperse phase relative to that of the entire system.

B.2.3 Diffusive contribution

The average diffusive flux (B.18c) may be written as

$$-\langle \boldsymbol{q}_{\text{diff}} \rangle = D_c \langle H \boldsymbol{\nabla} c_c + (1-H) \boldsymbol{\nabla} c_d \rangle + (D_d - D_c) \langle (1-H) \boldsymbol{\nabla} c_d \rangle.$$

Using the product rule, we have

$$\begin{aligned}
\langle H \boldsymbol{\nabla} c_c + (1-H) \boldsymbol{\nabla} c_d \rangle &= \langle \boldsymbol{\nabla} [H c_c + (1-H) c_d] + (c_d - c_c) \boldsymbol{\nabla} H \rangle \\
&= \boldsymbol{\nabla} \langle H c_c + (1-H) c_d \rangle + \langle (c_d - c_c) \boldsymbol{\nabla} H \rangle \\
&= \boldsymbol{\nabla} \langle c \rangle + \langle (c_d - c_c) \boldsymbol{\nabla} H \rangle \\
&= \boldsymbol{\nabla} \langle c \rangle + (1 - m^{-1}) \langle \delta_i c_d \boldsymbol{n} \rangle
\end{aligned}$$

where we made use of (B.5) and (B.8d) to step from the third line to the fourth line. We obtain the average diffusive flux:

$$-\langle \boldsymbol{q}_{\text{diff}} \rangle = D_c \boldsymbol{\nabla} \langle c \rangle + (D_d - D_c) \langle (1-H) \boldsymbol{\nabla} c_d \rangle + D_c (1 - m^{-1}) \langle \delta_i c_d \boldsymbol{n} \rangle, \tag{B.28}$$

where the first term on the right-hand-side is the diffusive flux in the absence of the particulates, and the other terms contain the effect of the particulates. Note that when $D_c = D_d$ and $m = 1$, $\langle \boldsymbol{q}_{\text{diff}} \rangle = -D_c \boldsymbol{\nabla} \langle c \rangle$.

A convenient feature of formulation (B.28) is that a configuration contributes to the unknown terms only if the point $\boldsymbol{x}$ lies either inside (second term) or at the surface (last term) of a particulate. This expression is therefore particularly suitable for a theoretical analysis in the dilute limit. It corresponds to the usual form of the diffusive flux found in prior theoretical work on the (heat or electricity) conduction problem in composite media (e.g., Maxwell (1873), Jeffrey (1973)). Indeed in this context only $m = 1$ is relevant, so the surface term vanishes. Then, under the homogeneity assumption, ensemble averages can be replaced by volume averages over a very large volume so that (B.28) is the same as equation (2.3) in Jeffrey (1973). In what follows we propose an alternative formulation which is more amenable to numerical computations.

Using the scalar field decomposition the average diffusive flux (B.18c) becomes:

$$-\langle \boldsymbol{q}_{\text{diff}} \rangle = \langle H D_c \boldsymbol{\nabla} (P \langle c \rangle) + (1-H) D_d \boldsymbol{\nabla} (m P \langle c \rangle) \rangle + \langle H D_c \boldsymbol{\nabla} c_c' + (1-H) D_d \boldsymbol{\nabla} c_d' \rangle.$$

One must be cautious with the first average term as it involves the gradient of a product. Using the product rule we have the equality:

$$\begin{aligned}
&\langle H D_c \boldsymbol{\nabla} (P \langle c \rangle) + (1-H) D_d \boldsymbol{\nabla} (m P \langle c \rangle) \rangle \\
&\qquad = \langle H D_c P + (1-H) D_d m P \rangle \boldsymbol{\nabla} \langle c \rangle + \langle H D_c \boldsymbol{\nabla} P + (1-H) D_d m \boldsymbol{\nabla} P \rangle \langle c \rangle.
\end{aligned}$$

Here $\boldsymbol{\nabla} P$ is obtained by taking the gradient of (B.21):

$$\boldsymbol{\nabla} P = -(m-1)P^2 \boldsymbol{\nabla}\phi .$$

We obtain for the average diffusive flux:

$$-\langle \boldsymbol{q}_{\text{diff}} \rangle = D_s \boldsymbol{\nabla}\langle c\rangle - (m-1)PD_s\langle c\rangle \boldsymbol{\nabla}\phi + \langle HD_c \boldsymbol{\nabla} c_c' + (1-H)D_d \boldsymbol{\nabla} c_d' \rangle \tag{B.29}$$

where D_s is

$$D_s = \langle HD_c P + (1-H)D_d mP \rangle$$

and can be reformulated as

$$D_s = D_c + \phi mP(D_d - D_c). \tag{B.30}$$

B.2.4 Phase average

It would be desirable to remove explicit references to the indicator function in the expression of the average flux. This is achieved by introducing (conditional) phase averages, that is, averages over the subset of realizations wherein $\boldsymbol{x}$ belong to a given phase. The disperse and continuous phase averages are denoted $\langle\,\rangle_d$ and $\langle\,\rangle_c$, respectively, and are defined by

$$\phi\langle f_d\rangle_d = \langle (1-H) f_d \rangle \tag{B.31a}$$

$$(1-\phi)\langle f_c\rangle_c = \langle H f_c \rangle \tag{B.31b}$$

where f_d and f_c are quantities pertaining to the disperse and continuous phases, respectively.

We emphasize that the ensemble (unconditional) average operator applies to variables defined everywhere with the aid of the indicator function, whereas phase averages apply to variables defined in a given phase. This is stressed here by the repetition of subscripts c and d on the left-hand-side of (B.31); to make the notation less cluttered this repetition is dropped hereinafter. A consequence is that gradient and phase average operators do not commute (this point is made clear in, e.g., Zhang and Prosperetti (1994)).

B.2.5 Final formulation of the average flux

We can now propose the following formulation of the average flux:

$$\begin{aligned}\langle \boldsymbol{q}\rangle = \boldsymbol{U}_s\langle c\rangle - D_s\boldsymbol{\nabla}\langle c\rangle + (m-1)PD_s\langle c\rangle\boldsymbol{\nabla}\phi \\ + (1-\phi)\langle \boldsymbol{u}'c'\rangle_c + \phi\langle \boldsymbol{u}'c'\rangle_d - (1-\phi)D_c\langle \boldsymbol{\nabla}c'\rangle_c - \phi D_d\langle \boldsymbol{\nabla}c'\rangle_d\end{aligned} \tag{B.32a}$$

with

$$P = \frac{1}{1+\phi(m-1)}, \tag{B.32b}$$

$$\boldsymbol{U}_s = \langle \boldsymbol{u} \rangle + \phi(m-1)P\boldsymbol{U}, \tag{B.32c}$$

$$D_s = D_c + \phi m P(D_d - D_c), \tag{B.32d}$$

and where the disperse phase drift velocity $\boldsymbol{U}$ defined in (B.27) can be written using phase averages as:

$$\boldsymbol{U} = \langle \boldsymbol{u} \rangle_d - \langle \boldsymbol{u} \rangle. \tag{B.32e}$$

These terms can be understood as follows:

- $\boldsymbol{U}_s \langle c \rangle$ is the advection of the average scalar field at an average velocity $\boldsymbol{U}_s$ which is, in general, different from $\langle \boldsymbol{u} \rangle$ because of the unequal partitioning ($m \neq 1$) of the scalar between the two phases and of the relative motion (the drift) between the disperse phase and the entire system;
- $-D_s \boldsymbol{\nabla} \langle c \rangle$ is the diffusion of the average scalar field with an average diffusivity D_s which is equal to the average diffusivity of the suspension weighted by the scalar equilibrium distribution; in particular, when $m = 1$, D_s is simply the average diffusivity (not to be confused with the *effective* diffusivity) of the suspension;
- $(m-1)PD_s \langle c \rangle \boldsymbol{\nabla} \phi$ is the average effect of a non-uniform volume fraction ($\boldsymbol{\nabla} \phi = 0$ in statistically homogeneous suspensions);
- $(1-\phi)\langle \boldsymbol{u}' c' \rangle_c + \phi \langle \boldsymbol{u}' c' \rangle_d$ corresponds to the advection of the scalar fluctuations by the velocity fluctuations in both phases;
- $-(1-\phi)D_c \langle \boldsymbol{\nabla} c' \rangle_c - \phi D_d \langle \boldsymbol{\nabla} c' \rangle_d$ is the diffusive flux due to the perturbation of the scalar field in both phases induced by the presence of the particulates.

Bibliography

Aboulhasanzadeh, B. & Tryggvason, G. (2014). Effect of bubble interactions on mass transfer in bubbly flow. *International Journal of Heat and Mass Transfer*, *79*, 390–396. (Cit. on pp. 20, 113).

Acrivos, A., Hinch, E. J., & Jeffrey, D. J. (1980, November). Heat transfer to a slowly moving fluid from a dilute fixed bed of heated spheres. *Journal of Fluid Mechanics*, *101*, 403–421. (Cit. on p. 113).

Aliseda, A. & Lasheras, J. C. (2011). Preferential concentration and rise velocity reduction of bubbles immersed in a homogeneous and isotropic turbulent flow. *Physics of Fluids*, *23*(9), 093301. (Cit. on pp. 124, 137).

Alméras, E., Risso, F., Roig, V., Cazin, S., Plais, C., & Augier, F. (2015). Mixing by bubble-induced turbulence. *Journal of Fluid Mechanics*, *776*, 458–474. (Cit. on pp. xiv, 79, 109, 111, 147).

Alvelius, K. (1999). Random forcing of three-dimensional homogeneous turbulence. *Physics of Fluids*, *11*(7), 1880–1889. (Cit. on p. 144).

Amoura, Z., Roig, V., Risso, F., & Billet, A.-M. (2010). Attenuation of the wake of a sphere in an intense incident turbulence with large length scales. *Physics of Fluids*, *22*(5), 055105. (Cit. on p. 119).

Auton, T. R. (1987). The lift force on a spherical body in a rotational flow. *Journal of Fluid Mechanics*, *183*, 199. (Cit. on p. 56).

Balachandar, S. & Eaton, J. K. (2010). Turbulent Dispersed Multiphase Flow. *Annual Review of Fluid Mechanics*, *42*, 111–133. (Cit. on pp. xviii, 116, 149).

Batchelor, G. K. (1972). Sedimentation in a dilute dispersion of spheres. *Journal of Fluid Mechanics*, *52*(02), 245–268. (Cit. on pp. xiii, 24).

Batchelor, G. K. (1974). Transport Properties of Two-Phase Materials with Random Structure. *Annual Review of Fluid Mechanics*, *6*, 227–255. (Cit. on pp. xv, 78, 83).

Bellani, G., Byron, M. L., Collignon, A. G., Meyer, C. R., & Variano, E. A. (2012). Shape effects on turbulent modulation by large nearly neutrally buoyant particles. *Journal of Fluid Mechanics*, *712*, 41–60. (Cit. on p. 116).

Bellani, G. & Variano, E. A. (2012). Slip velocity of large neutrally buoyant particles in turbulent flows. *New Journal of Physics*, *14*(12), 125009. (Cit. on p. 116).

Bhaga, D. & Weber, M. E. (1980). In-line interaction of a pair of bubbles in a viscous liquid. *Chemical Engineering Science*, *35*(12), 2467–2474. (Cit. on p. 62).

Bhaga, D. & Weber, M. E. (1981). Bubbles in viscous liquids: shapes, wakes and velocities. *Journal of Fluid Mechanics*, *105*, 61–85. (Cit. on pp. 29, 30, 49, 92).

Brackbill, J. U., Kothe, D. B., & Zemach, C. (1992). A continuum method for modeling surface tension. *Journal of Computational Physics*, *100*(2), 335–354. (Cit. on pp. xii, 4, 6, 30, 118).

Brenner, H. (1980). Dispersion Resulting from Flow through Spatially Periodic Porous Media. *Philosophical Transactions of the Royal Society A: Mathematical, Physical and Engineering Sciences*, *297*(1430), 81–133. (Cit. on pp. 79, 97).

Brenner, H. & Adler, P. M. (1982). Dispersion Resulting from Flow through Spatially Periodic Porous Media II. Surface and Intraparticle Transport. *Philosophical Transactions of the Royal Society A: Mathematical, Physical and Engineering Sciences*, *307*(1498), 149–200. (Cit. on p. 79).

Brenner, H. & Cox, R. G. (1963). The resistance to a particle of arbitrary shape in translational motion at small Reynolds numbers. *Journal of Fluid Mechanics*, *17*(04), 561–595. (Cit. on pp. 34, 95, 154).

Bunner, B. & Tryggvason, G. (2002a). Dynamics of homogeneous bubbly flows Part 1. Rise velocity and microstructure of the bubbles. *Journal of Fluid Mechanics*, *466*, 17–52. (Cit. on pp. 26, 40, 41, 59, 64, 66, 68, 69, 72, 73, 91).

Bunner, B. & Tryggvason, G. (2002b). Dynamics of homogeneous bubbly flows Part 2. Velocity fluctuations. *Journal of Fluid Mechanics*, *466*, 53–84. (Cit. on pp. xviii, 27, 74, 149).

Bunner, B. & Tryggvason, G. (2003). Effect of bubble deformation on the properties of bubbly flows. *Journal of Fluid Mechanics*, *495*, 77–118. (Cit. on pp. xiii, xviii, 25–27, 62, 66, 149).

Cantwell, B. J. (1992). Exact solution of a restricted Euler equation for the velocity gradient tensor. *Physics of Fluids A: Fluid Dynamics*, *4*(4), 782. (Cit. on p. 142).

Cartellier, A., Andreotti, M., & Sechet, P. (2009, December). Induced agitation in homogeneous bubbly flows at moderate particle Reynolds number. *Physical Review E*, *80*(6), 065301. (Cit. on pp. xviii, 68, 91, 149).

Cartellier, A. & Rivière, N. (2001). Bubble-induced agitation and microstructure in uniform bubbly flows at small to moderate particle Reynolds numbers. *Physics of Fluids*, *13*(8), 2165. (Cit. on pp. xviii, 26, 68, 91, 149).

Chorin, A. (1968). Numerical Solution of the Navier-Stokes Equations. *Mathematics of Computation*, *22*, 745–762. (Cit. on pp. xii, 9, 31, 87, 118).

Chouippe, A. & Uhlmann, M. (2015). Forcing homogeneous turbulence in direct numerical simulation of particulate flow with interface resolution and gravity. *Physics of Fluids*, *27*(12), 123301. (Cit. on pp. xvi, 116, 119, 120, 124, 126, 128).

Cisse, M., Homann, H., & Bec, J. (2013). Slipping motion of large neutrally buoyant particles in turbulence. *Journal of Fluid Mechanics*, *735*, R1. (Cit. on pp. xvi, 116, 131).

Clift, R., Grace, J. R., & Weber, M. E. (1978). *Bubbles, drops, and particles*. New York: Academic Press. (Cit. on p. 24).

Colombet, D., Legendre, D., Cockx, A., Guiraud, P., Risso, F., Daniel, C., & Galinat, S. (2011). Experimental study of mass transfer in a dense bubble swarm. *Chemical Engineering Science*, *66*(14), 3432–3440. (Cit. on p. 113).

Colombet, D., Legendre, D., Risso, F., Cockx, A., & Guiraud, P. (2015). Dynamics and mass transfer of rising bubbles in a homogenous swarm at large gas volume fraction. *Journal of Fluid Mechanics*, *763*, 254–285. (Cit. on pp. xiii, xiv, 24, 27, 70, 113).

Couderc, F. (2007). *Développement d'un code de calcul pour la simulation d'écoulements de fluides non miscibles. Application à la désintégration assistée d'un jet liquide par un courant gazeux.* (Doctoral dissertation, École nationale supérieure de l'aéronautique et de l'espace). (Cit. on p. 8).

Crabtree, J. R. & Bridgwater, J. (1971). Bubble coalescence in viscous liquids. *Chemical Engineering Science*, *26*(6), 839–851. (Cit. on p. 62).

Davis, R. H. & Acrivos, A. (1985). Sedimentation of Noncolloidal Particles at Low Reynolds Numbers. *Annual Review of Fluid Mechanics*, *17*, 91–118. (Cit. on p. 25).

Ding, H., Spelt, P. D. M., & Shu, C. (2007). Diffuse interface model for incompressible two-phase flows with large density ratios. *Journal of Computational Physics*, *226*(2), 2078–2095. (Cit. on p. 4).

Duret, B., Luret, G., Reveillon, J., Menard, T., Berlemont, A., & Demoulin, F. X. (2012). DNS analysis of turbulent mixing in two-phase flows. *International Journal of Multiphase Flow*, *40*, 93–105. (Cit. on pp. 119, 120).

Eames, I., Johnson, P. B., Roig, V., & Risso, F. (2011). Effect of turbulence on the downstream velocity deficit of a rigid sphere. *Physics of Fluids*, *23*(9), 095103. (Cit. on p. 119).

Ern, P., Risso, F., Fabre, D., & Magnaudet, J. (2012). Wake-Induced Oscillatory Paths of Bodies Freely Rising or Falling in Fluids. *Annual Review of Fluid Mechanics*, *44*, 97–121. (Cit. on p. 75).

Ervin, E. A. & Tryggvason, G. (1997). The Rise of Bubbles in a Vertical Shear Flow. *Journal of Fluids Engineering*, *119*(2), 443. (Cit. on p. 60).

Esmaeeli, A. & Tryggvason, G. (1998). Direct numerical simulations of bubbly flows. Part 1. Low Reynolds number arrays. *Journal of Fluid Mechanics*, *377*, 313–345. (Cit. on pp. xiii, 25–27).

Esmaeeli, A. & Tryggvason, G. (1999). Direct numerical simulations of bubbly flows. Part 2. Moderate Reynolds number arrays. *Journal of Fluid Mechanics*, *385*, 325–358. (Cit. on pp. xiii, xviii, 14–17, 26, 62, 68, 149).

Esmaeeli, A. & Tryggvason, G. (2005). A direct numerical simulation study of the buoyant rise of bubbles at O(100) Reynolds number. *Physics of Fluids*, *17*(9), 093303. (Cit. on pp. xviii, 26, 27, 59, 149).

Fedkiw, R. P., Aslam, T., Merriman, B., & Osher, S. (1999). A Non-oscillatory Eulerian Approach to Interfaces in Multimaterial Flows (the Ghost Fluid Method). *Journal of Computational Physics*, *152*(2), 457–492. (Cit. on p. 4).

Garnier, C., Lance, M., & Marié, J.-L. (2002). Measurement of local flow characteristics in buoyancy-driven bubbly flow at high void fraction. *Experimental Thermal and Fluid Science*, *26*(6-7), 811–815. (Cit. on pp. xiii, xiv, xviii, 24, 27, 70, 149).

Gillissen, J. J. J., Sundaresan, S., & van den Akker, H. E. A. (2011). A lattice Boltzmann study on the drag force in bubble swarms. *Journal of Fluid Mechanics*, *679*, 101–121. (Cit. on pp. 26, 27).

Gottlieb, S. & Shu, C.-W. (1998). Total variation diminishing Runge-Kutta schemes. *Mathematics of computation*, *67*(221), 73–85. (Cit. on p. 10).

Grace, J. R. (1973). Shapes and velocities of bubbles rising in infinite liquids. *Transactions of the Institution of Chemical Engineering*, *51*, 116–120. (Cit. on pp. 29, 30, 92).

Hadamard, J. (1911). Mouvement permanent lent d'une sphere liquide et visqueuse dans un liquide visqueux. *Comptes Rendus de l'Académie des Sciences*, *152*(25), 1735–1738. (Cit. on pp. 33, 95, 152).

Hallez, Y. & Legendre, D. (2011). Interaction between two spherical bubbles rising in a viscous liquid. *Journal of Fluid Mechanics*, *673*, 406–431. (Cit. on pp. xiii, 27, 39, 40, 47, 55, 56, 65).

Harfield, N. (1999). Conductivity calculation for a two-phase composite with spheroidal inclusions. *Journal of Physics D: Applied Physics*, *32*(10), 1104–1113. (Cit. on p. 79).

Harten, A., Engquist, B., Osher, S., & Chakravarthy, S. R. (1987). Uniformly high order accurate essentially non-oscillatory schemes, III. *Journal of Computational Physics*, *71*(2), 231–303. (Cit. on p. 11).

Hartmann, D., Meinke, M., & Schröder, W. (2008). Differential equation based constrained reinitialization for level set methods. *Journal of Computational Physics*, *227*(14), 6821–6845. (Cit. on p. 8).

Hartmann, D., Meinke, M., & Schröder, W. (2010). The constrained reinitialization equation for level set methods. *Journal of Computational Physics*, *229*(5), 1514–1535. (Cit. on p. 8).

Hasimoto, H. (1959). On the periodic fundamental solutions of the Stokes equations and their application to viscous flow past a cubic array of spheres. *Journal of Fluid Mechanics*, *5*(02), 317–328. (Cit. on pp. 153, 154).

Hill, R. J., Koch, D. L., & Ladd, A. J. C. (2001). The first effects of fluid inertia on flows in ordered and random arrays of spheres. *Journal of Fluid Mechanics*, *448*, 213–241. (Cit. on pp. 34, 152–154).

Hinch, E. J. (1977). An averaged-equation approach to particle interactions in a fluid suspension. *Journal of Fluid Mechanics*, *83*(04), 695–720. (Cit. on p. 79).

Hirt, C. W. & Nichols, B. D. (1981). Volume of fluid (VOF) method for the dynamics of free boundaries. *Journal of Computational Physics*, *39*(1), 201–225. (Cit. on p. 4).

Homann, H. & Bec, J. (2010). Finite-size effects in the dynamics of neutrally buoyant particles in turbulent flow. *Journal of Fluid Mechanics*, *651*, 81–91. (Cit. on pp. 116, 126, 128).

Hua, J., Stene, J. F., & Lin, P. (2008). Numerical simulation of 3D bubbles rising in viscous liquids using a front tracking method. *Journal of Computational Physics*, *227*(6), 3358–3382. (Cit. on pp. 29, 30, 49).

Ishii, M. & Zuber, N. (1979). Drag coefficient and relative velocity in bubbly, droplet or particulate flows. *AIChE Journal*, *25*(5), 843–855. (Cit. on p. 24).

Jacqmin, D. (1999). Calculation of Two-Phase Navier–Stokes Flows Using Phase-Field Modeling. *Journal of Computational Physics*, *155*(1), 96–127. (Cit. on p. 4).

Jeffrey, D. J. (1973). Conduction Through a Random Suspension of Spheres. *Proceedings of the Royal Society A: Mathematical, Physical and Engineering Sciences*, *335*(1602), 355–367. (Cit. on pp. 79, 83, 162).

Jiang, G.-S. & Peng, D. (2000). Weighted ENO Schemes for Hamilton-Jacobi Equations. *SIAM Journal on Scientific Computing*, *21*(6), 2126–2143. (Cit. on p. 87).

Jiang, G.-S. & Shu, C.-W. (1996). Efficient Implementation of Weighted ENO Schemes. *Journal of Computational Physics*, *126*, 202–228. (Cit. on p. 10).

Kang, I. S. & Leal, L. G. (1987). Numerical solution of axisymmetric, unsteady free-boundary problems at finite Reynolds number. I. Finite-difference scheme and its application to the deformation of a bubble in a uniaxial straining flow. *Physics of Fluids*, *30*(7), 1929. (Cit. on p. 4).

Kang, M., Fedkiw, R. P., & Liu, X.-D. (2000). A Boundary Condition Capturing Method for Multiphase Incompressible Flow. *Journal of Scientific Computing*, *15*(3), 323–360. (Cit. on p. 4).

Keh, H. J. & Tseng, Y. K. (1992, December). Slow motion of multiple droplets in arbitrary three-dimensional configurations. *AIChE Journal*, *38*(12), 1881–1904. (Cit. on pp. xiii, 25, 67).

Kim, J. & Moin, P. (1985, June). Application of a fractional-step method to incompressible Navier-Stokes equations. *Journal of Computational Physics*, *59*(2), 308–323. (Cit. on p. 13).

Klein, S., Gibert, M., Bérut, A., & Bodenschatz, E. (2013). Simultaneous 3D measurement of the translation and rotation of finite-size particles and the flow field in a fully developed turbulent water flow. *Measurement Science and Technology*, *24*(2), 024006. (Cit. on p. 116).

Koch, D. L. (1993). Hydrodynamic diffusion in dilute sedimenting suspensions at moderate Reynolds numbers. *Physics of Fluids A: Fluid Dynamics*, *5*(5), 1141. (Cit. on p. 59).

Koch, D. L. & Brady, J. F. (1985). Dispersion in fixed beds. *Journal of Fluid Mechanics*, *154*, 399–427. (Cit. on pp. xiv, xv, 78–80, 83, 105, 108, 111, 160).

Koch, D. L. & Brady, J. F. (1987a). A non-local description of advection-diffusion with application to dispersion in porous media. *Journal of Fluid Mechanics*, *180*, 387–403. (Cit. on p. 146).

Koch, D. L. & Brady, J. F. (1987b). The symmetry properties of the effective diffusivity tensor in anisotropic porous media. *Physics of Fluids*, *30*(3), 642. (Cit. on pp. xiv, xv, 78, 80, 83, 91, 161).

Koch, D. L. & Brady, J. F. (1988). Anomalous diffusion in heterogeneous porous media. *Physics of Fluids*, *31*(5), 965. (Cit. on p. 146).

Koch, D. L., Cox, R. G., Brenner, H., & Brady, J. F. (1989). The effect of order on dispersion in porous media. *Journal of Fluid Mechanics*, *200*, 173–188. (Cit. on pp. xiv, xv, 79, 91, 94, 95, 97, 99, 105, 112).

Kushch, V. I. (1997). Conductivity of a periodic particle composite with transversely isotropic phases. *Proceedings of the Royal Society A: Mathematical, Physical and Engineering Sciences*, *453*(1956), 65–76. (Cit. on p. 79).

Lance, M. & Bataille, J. (1991). Turbulence in the liquid phase of a uniform bubbly air–water flow. *Journal of Fluid Mechanics*, *222*, 95. (Cit. on pp. xviii, 149).

Legendre, D. & Magnaudet, J. (1998). The lift force on a spherical bubble in a viscous linear shear flow. *Journal of Fluid Mechanics*, *368*, 81–126. (Cit. on pp. 56, 134).

Legendre, D., Magnaudet, J., & Mougin, G. (2003). Hydrodynamic interactions between two spherical bubbles rising side by side in a viscous liquid. *Journal of Fluid Mechanics*, *497*, 133–166. (Cit. on pp. xiii, 27, 47).

Legendre, D., Merle, A., & Magnaudet, J. (2006). Wake of a spherical bubble or a solid sphere set fixed in a turbulent environment. *Physics of Fluids*, *18*(4), 048102. (Cit. on pp. xvi, 116, 119).

Lelouvetel, J., Tanaka, T., Sato, Y., & Hishida, K. (2014). Transport mechanisms of the turbulent energy cascade in upward/downward bubbly flows. *Journal of Fluid Mechanics*, *741*, 514–542. (Cit. on pp. xviii, 149).

Lévêque, E. & Naso, A. (2014). Introduction of longitudinal and transverse Lagrangian velocity increments in homogeneous and isotropic turbulence. *Europhysics Letters*, *108*(5), 54004. (Cit. on pp. xvii, 131).

Loth, E. (2008). Quasi-steady shape and drag of deformable bubbles and drops. *International Journal of Multiphase Flow*, *34*(6), 523–546. (Cit. on pp. 24, 30, 40, 42, 44, 45, 66, 70, 92, 137).

Lu, J. & Tryggvason, G. (2013, October). Dynamics of nearly spherical bubbles in a turbulent channel upflow. *Journal of Fluid Mechanics*, *732*(16), 166–189. (Cit. on p. 20).

Lundgren, T. S. (2003). Linearly forced isotropic turbulence. In *Annual research briefs* (pp. 461–473). Stanford: Center for Turbulence Research. (Cit. on pp. xvi, 119).

Luo, K., Shao, C., Yang, Y., & Fan, J. (2015). A mass conserving level set method for detailed numerical simulation of liquid atomization. *Journal of Computational Physics*, *298*, 495–519. (Cit. on p. 22).

Magnaudet, J. & Eames, I. (2000). The Motion of High-Reynolds-Number Bubbles in Inhomogeneous Flows. *Annual Review of Fluid Mechanics*, *32*, 659–708. (Cit. on pp. 75, 131, 132, 137).

Magnaudet, J., Takagi, S. H. U., & Legendre, D. (2003). Drag, deformation and lateral migration of a buoyant drop moving near a wall. *Journal of Fluid Mechanics*, *476*, 115–157. (Cit. on p. 60).

Mareuge, I. & Lance, M. (1995). Bubble Induced Dispersion of a Passive Scalar in Bubbly Flows. In *Proceedings of the 2nd international conference on multiphase flow* (pages). Kyoto, Japan. (Cit. on p. 79).

Martinez-Mercado, J., Palacios-Morales, C. A., & Zenit, R. (2007). Measurement of pseudo-turbulence intensity in monodispersed bubbly liquids for 10<Re<500. *Physics of Fluids*, *19*(10), 103302. (Cit. on pp. xiv, 27, 69, 70, 73, 74, 149).

Mathai, V., Prakash, V. N., Brons, J., Sun, C., & Lohse, D. (2015). Wake-Driven Dynamics of Finite-Sized Buoyant Spheres in Turbulence. *Physical Review Letters*, *115*(12), 124501. (Cit. on p. 116).

Maxey, M. R., Chang, E. J., & Wang, L.-P. (1994). Simulation of Interactions Between Microbubbles and Turbulent Flows. *Applied Mechanics Reviews*, *47*(6), S70–S74. (Cit. on pp. xvi, 116, 123, 137, 138).

Maxwell, J. C. (1873). *A treatise on electricity and magnetism*. Oxford: Clarendon Press. (Cit. on pp. 79, 83, 113, 162).

Mazzitelli, I. M., Lohse, D., & Toschi, F. (2003a). On the relevance of the lift force in bubbly turbulence. *Journal of Fluid Mechanics*, *488*, 283–313. (Cit. on pp. xvi, xvii, 116, 124, 137, 138).

Mazzitelli, I. M., Lohse, D., & Toschi, F. (2003b). The effect of microbubbles on developed turbulence. *Physics of Fluids*, *15*(1), L5. (Cit. on pp. xvi–xviii, 116, 124, 137, 138, 149).

McCaslin, J. O. & Desjardins, O. (2014). A localized re-initialization equation for the conservative level set method. *Journal of Computational Physics*, *262*, 408–426. (Cit. on pp. 8, 22).

Mei, R., Klausner, J. F., & Lawrence, C. J. (1994). A note on the history force on a spherical bubble at finite Reynolds number. *Physics of Fluids*, *6*(1), 418–420. (Cit. on pp. 30, 36, 40, 69, 70, 92, 117, 118, 123, 124, 137, 140).

Meland, R., Gran, I. R., Olsen, R., & Munkejord, S. T. (2007). Reduction of parasitic currents in level-set calculations with a consistent discretization of the surface-tension force for the CSF model. In P. Jacobs, T. McIntyre, M. Cleary, D. Buttsworth, D. Mee, R. Clements, R. Morgan, & C. Lemckert (Eds.), *16th australasian fluid mechanics conference (afmc)* (pp. 862–865). Gold Coast, Queensland, Australia: School of Engineering, The University of Queensland. (Cit. on p. 13).

Merle, A., Legendre, D., & Magnaudet, J. (2005). Forces on a high-Reynolds-number spherical bubble in a turbulent flow. *Journal of Fluid Mechanics*, *532*, 53–62. (Cit. on pp. xvi, 57, 116, 131).

Moore, D. W. (1959). The rise of a gas bubble in a viscous liquid. *Journal of Fluid Mechanics*, *6*(01), 113–130. (Cit. on p. 44).

Moore, D. W. (1963). The boundary layer on a spherical gas bubble. *Journal of Fluid Mechanics*, *16*(02), 161–176. (Cit. on pp. 134, 136).

Mordant, N., Crawford, A. M., & Bodenschatz, E. (2004). Three-dimensional structure of the Lagrangian acceleration in turbulent flows. *Physical Review Letters*, *93*(21), 214501. (Cit. on pp. xvii, 126).

Narayanan, S., Goossens, L. H. J., & Kossen, N. W. F. (1974). Coalescence of two bubbles rising in line at low Reynolds numbers. *Chemical Engineering Science*, *29*(10), 2071–2082. (Cit. on p. 62).

Naso, A. & Prosperetti, A. (2010). The interaction between a solid particle and a turbulent flow. *New Journal of Physics*, *12*(3), 033040. (Cit. on pp. xvi, 57, 116, 119, 120, 131, 132, 134).

Noh, W. F. & Woodward, P. R. (1976). SLIC (Simple Line Interface Calculation) method. In A. I. van Vooren & P. J. Zandbergen (Eds.), *Proceedings of the fifth international conference on numerical methods in fluid dynamics june 28–july 2, 1976 twente university, enschede* (pp. 330–340). (Cit. on p. 4).

Osher, S. & Sethian, J. A. (1988). Fronts propagating with curvature-dependent speed: Algorithms based on Hamilton-Jacobi formulations. *Journal of Computational Physics*, *79*(1), 12–49. (Cit. on pp. xii, 4, 7, 31).

Peskin, C. S. (1977). Numerical analysis of blood flow in the heart. *Journal of Computational Physics*, *25*(3), 220–252. (Cit. on p. 4).

Poorte, R. E. G. & Biesheuvel, A. (2002). Experiments on the motion of gas bubbles in turbulence generated by an active grid. *Journal of Fluid Mechanics*, *461*, 127–154. (Cit. on pp. 124, 126, 137).

Pozrikidis, C. (2011). *Introduction to Theoretical and Computational Fluid Dynamics* (2nd Editio). New York: Oxford University Press. (Cit. on p. 153).

Prakash, V. N., Tagawa, Y., Calzavarini, E., Mercado, J. M., Toschi, F., Lohse, D., & Sun, C. (2012). How gravity and size affect the acceleration statistics of bubbles in turbulence. *New Journal of Physics*, *14*(10), 105017. (Cit. on pp. xvi, 116, 124).

Prosperetti, A. & Tryggvason, G. (2007). *Computational Methods for Multiphase Flow*. Cambridge: Cambridge University Press. (Cit. on pp. 4, 6, 7).

Qureshi, N. M., Arrieta, U., Baudet, C., Cartellier, A., Gagne, Y., & Bourgoin, M. (2008). Acceleration statistics of inertial particles in turbulent flow. *European Physical Journal B*, *66*(4), 531–536. (Cit. on pp. xvii, 126).

Qureshi, N. M., Bourgoin, M., Baudet, C., Cartellier, A., & Gagne, Y. (2007). Turbulent Transport of Material Particles: An Experimental Study of Finite Size Effects. *Physical Review Letters*, *99*(18), 184502. (Cit. on p. 126).

Rastello, M., Marié, J.-L., & Lance, M. (2011). Drag and lift forces on clean spherical and ellipsoidal bubbles in a solid-body rotating flow. *Journal of Fluid Mechanics*, *682*, 434–459. (Cit. on p. 134).

Ravelet, F., Colin, C., & Risso, F. (2011). On the dynamics and breakup of a bubble rising in a turbulent flow. *Physics of Fluids*, *23*(10), 1–12. (Cit. on pp. xvi, 116).

Ray, B. & Prosperetti, A. (2014). On skirted drops in an immiscible liquid. *Chemical Engineering Science*, *108*, 213–222. (Cit. on p. 50).

Rayleigh, R. S. (1892). LVI. On the influence of obstacles arranged in rectangular order upon the properties of a medium. *Philosophical Magazine Series 5*, *34*(211), 481–502. (Cit. on p. 79).

Riboux, G., Risso, F., & Legendre, D. (2010). Experimental characterization of the agitation generated by bubbles rising at high Reynolds number. *Journal of Fluid Mechanics*, *643*, 509–539. (Cit. on pp. xiv, xviii, 27, 70, 149).

Richardson, J. & Zaki, W. (1954). Sedimentation and fluidisation: Part I. *Transactions of the Institution of Chemical Engineers*, *32*, 35–53. (Cit. on pp. 24, 42).

Rosales, C. & Meneveau, C. (2005). Linear forcing in numerical simulations of isotropic turbulence: Physical space implementations and convergence properties. *Physics of Fluids*, *17*(9), 095106. (Cit. on pp. 119, 120).

Russo, G. & Smereka, P. (2000). A remark on computing distance functions. *Journal of Computational Physics*, *163*(1), 51–67. (Cit. on pp. xii, 8, 9, 11, 22, 31, 87, 118).

Rybczynski, W. (1911). Uber die fortschreitende Bewegung einer flussigen Kugel in einem zahen Medium. *Bulletin International de l'Academie des Sciences de Cracovie Serie A*, *1*, 40–46. (Cit. on pp. 33, 95, 152).

Ryskin, G. & Leal, L. G. (1984a, November). Numerical solution of free-boundary problems in fluid mechanics. Part 1. The finite-difference technique. *Journal of Fluid Mechanics*, *148*, 1. (Cit. on p. 4).

Ryskin, G. & Leal, L. G. (1984b). Numerical solution of free-boundary problems in fluid mechanics. Part 2. Buoyancy-driven motion of a gas bubble through a quiescent liquid. *Journal of Fluid Mechanics*, *148*, 19–35. (Cit. on pp. 40, 44, 46, 47).

Sabelnikov, V., Ovsyannikov, A. Y., & Gorokhovski, M. (2014). Modified level set equation and its numerical assessment. *Journal of Computational Physics*, *278*, 1–30. (Cit. on pp. xii, 8, 9, 22, 31, 87, 118).

Salih, A. & Ghosh Moulic, S. (2009). Some numerical studies of interface advection properties of level set method. *Sadhana*, *34*(2), 271–298. (Cit. on pp. 10, 22).

Sangani, A. S. (1987). Sedimentation in ordered emulsions of drops at low Reynolds numbers. *Zeitschrift für angewandte Mathematik und Physik*, *38*(4), 542–556. (Cit. on pp. 25, 33, 34).

Sangani, A. S. & Acrivos, A. (1983a). Creeping flow through cubic arrays of spherical bubbles. *International Journal of Multiphase Flow*, *9*(2), 181–185. (Cit. on pp. 25, 27).

Sangani, A. S. & Acrivos, A. (1983b). The Effective Conductivity of a Periodic Array of Spheres. *Proceedings of the Royal Society A: Mathematical, Physical and Engineering Sciences*, *386*(1791), 263–275. (Cit. on p. 79).

Sankaranarayanan, K., Shan, X., Kevrekidis, I. G., & Sundaresan, S. (2002). Analysis of drag and virtual mass forces in bubbly suspensions using an implicit formulation of the lattice Boltzmann method. *Journal of Fluid Mechanics*, *452*, 61–96. (Cit. on pp. 26, 35, 36, 42, 47, 51, 60).

Sankaranarayanan, K. & Sundaresan, S. (2002). Lift force in bubbly suspensions. *Chemical Engineering Science*, *57*(17), 3521–3542. (Cit. on pp. 41, 51, 60).

Sene, K. J., Hunt, J. C. R., & Thomas, N. H. (1994). The role of coherent structures in bubble transport by turbulent shear flows. *Journal of Fluid Mechanics*, *259*, 219–240. (Cit. on p. 138).

Snyder, M. R., Knio, O. M., Katz, J., & Le Maître, O. P. (2007). Statistical analysis of small bubble dynamics in isotropic turbulence. *Physics of Fluids*, *19*(6), 065108. (Cit. on pp. xvi, 116, 124, 126, 137).

Spelt, P. D. M. (2005). A level-set approach for simulations of flows with multiple moving contact lines with hysteresis. *Journal of Computational Physics*, *207*(2), 389–404. (Cit. on p. 8).

Spelt, P. D. M. (2006). Shear flow past two-dimensional droplets pinned or moving on an adhering channel wall at moderate Reynolds numbers: a numerical study. *Journal of Fluid Mechanics*, *561*, 439. (Cit. on p. 8).

Spelt, P. D. M. & Biesheuvel, A. (1997). On the motion of gas bubbles in homogeneous isotropic turbulence. *Journal of Fluid Mechanics*, *336*, 221–244. (Cit. on pp. xvi, xvii, 116, 124, 126, 137, 138).

Spelt, P. D. M. & Sangani, A. S. (1998). Properties and Averaged Equations for Flows of Bubbly Liquids. *Applied Scientific Research*, *58*, 337–386. (Cit. on p. 25).

Sussman, M. & Fatemi, E. (1999). An efficient interface preserving level set redistancing algorithm and its application to interfacial incompressible fluid flow. *SIAM Journal of Scientific Computing*, *20*(4), 1165–1191. (Cit. on p. 8).

Sussman, M., Smereka, P., & Osher, S. (1994). A Level Set Approach for Computing Solutions to Incompressible Two-Phase Flow. *Journal of Computational Physics*, *114*(1), 146–159. (Cit. on pp. xii, 4, 7, 8, 31, 87).

Sussman, M. & Uto, S. (1998). A computational study of the spreading of oil underneath a sheet of ice. *UCLA Computational and Applied Mathematics Report*, *98*(32). (Cit. on pp. xii, 8, 22, 31, 119).

Takagi, S. & Matsumoto, Y. (2011). Surfactant Effects on Bubble Motion and Bubbly Flows. *Annual Review of Fluid Mechanics*, *43*(1), 615–636. (Cit. on p. 75).

Taylor, G. I. (1922). Diffusion by Continuous Movements. *Proceedings of the London Mathematical Society*, *s2-20*(1), 196–212. (Cit. on p. 79).

Taylor, T. D. & Acrivos, A. (1964). On the deformation and drag of a falling viscous drop at low Reynolds number. *Journal of Fluid Mechanics*, *18*(03), 466–476. (Cit. on p. 44).

Ten Cate, A., Derksen, J. J., Portela, L. M., & van den Akker, H. E. A. (2004). Fully resolved simulations of colliding monodisperse spheres in forced isotropic turbulence. *Journal of Fluid Mechanics*, *519*, 233–271. (Cit. on p. 144).

Theodoropoulos, C., Sankaranarayanan, K., Sundaresan, S., & Kevrekidis, I. (2004). Coarse bifurcation studies of bubble flow lattice Boltzmann simulations. *Chemical Engineering Science*, *59*(12), 2357–2362. (Cit. on p. 51).

Tomiyama, A., Tamai, H., Zun, I., & Hosokawa, S. (2002). Transverse migration of single bubbles in simple shear flows. *Chemical Engineering Science*, *57*(11), 1849–1858. (Cit. on p. 60).

Toschi, F. & Bodenschatz, E. (2009). Lagrangian Properties of Particles in Turbulence. *Annual Review of Fluid Mechanics*, *41*, 375–404. (Cit. on pp. xvii, 126).

Tryggvason, G., Scardovelli, R., & Zaleski, S. (2011). *Direct Numerical Simulations of Gas-Liquid Multiphase Flows*. Cambridge: Cambridge University Press. (Cit. on pp. 4, 20, 158).

Unverdi, S. O. & Tryggvason, G. (1992). A front-tracking method for viscous, incompressible, multi-fluid flows. *Journal of Computational Physics*, *100*(1), 25–37. (Cit. on p. 4).

Veldhuis, C. H. J. (2007). *Leonardo's Paradox : path and shape instabilities of particles and bubbles* (Doctoral dissertation, University of Twente). (Cit. on p. 75).

Volk, R., Calzavarini, E., Leveque, E., & Pinton, J.-F. (2011). Dynamics of inertial particles in a turbulent von Kármán flow. *Journal of Fluid Mechanics*, *668*, 223–235. (Cit. on p. 116).

Volk, R., Calzavarini, E., Verhille, G., Lohse, D., Mordant, N., Pinton, J.-F., & Toschi, F. (2008). Acceleration of heavy and light particles in turbulence: Comparison between experiments and direct numerical simulations. *Physica D: Nonlinear Phenomena*, *237*(14), 2084–2089. (Cit. on pp. xvi, 116).

Wang, L.-P. & Maxey, M. R. (1993). The motion of microbubbles in a forced isotropic and homogeneous turbulence. *Applied Scientific Research*, *51*, 291–296. (Cit. on pp. xvi, 116, 123, 137, 138).

Yin, X. & Koch, D. L. (2008). Lattice-Boltzmann simulation of finite Reynolds number buoyancy-driven bubbly flows in periodic and wall-bounded domains. *Physics of Fluids*, *20*(10), 103304. (Cit. on pp. xiii, 26, 59, 68, 69, 91).

Zenit, R., Koch, D. L., & Sangani, A. S. (2001). Measurements of the average properties of a suspension of bubbles rising in a vertical channel. *Journal of Fluid Mechanics*, *429*(01), 307–342. (Cit. on pp. xiii, 24, 26, 27, 70).

Zhang, D. Z. & Prosperetti, A. (1994). Averaged equations for inviscid disperse two-phase flow. *Journal of Fluid Mechanics*, *267*, 185–219. (Cit. on p. 163).

Zimmermann, R., Gasteuil, Y., Bourgoin, M., Volk, R., Pumir, A., & Pinton, J.-F. (2011). Rotational Intermittency and Turbulence Induced Lift Experienced by Large Particles in a Turbulent Flow. *Physical Review Letters*, *106*(15), 154501. (Cit. on p. 116).